ADVANCING OCEAN OBSERVING TECHNOLOGY AND INDUSTRY - SCIENCE PARTNERSHIPS FOR THE FUTURE OF OCEAN SCIENCE

EDITED BY: Ole Mikkelsen, Paula Bontempi, Alex Nimmo-Smith, Wayne Homer Slade and Ho Kyung Ha

PUBLISHED IN: Frontiers in Marine Science

frontiers Research Topics

frontiers

ISSN 1664-8714
ISBN 978-2-88974-403-9
DOI 10.3389/978-2-88974-403-9

About Frontiers

Frontiers is more than just an open-access publisher of scholarly articles: it is a pioneering approach to the world of academia, radically improving the way scholarly research is managed. The grand vision of Frontiers is a world where all people have an equal opportunity to seek, share and generate knowledge. Frontiers provides immediate and permanent online open access to all its publications, but this alone is not enough to realize our grand goals.

Frontiers Journal Series

The Frontiers Journal Series is a multi-tier and interdisciplinary set of open-access, online journals, promising a paradigm shift from the current review, selection and dissemination processes in academic publishing. All Frontiers journals are driven by researchers for researchers; therefore, they constitute a service to the scholarly community. At the same time, the Frontiers Journal Series operates on a revolutionary invention, the tiered publishing system, initially addressing specific communities of scholars, and gradually climbing up to broader public understanding, thus serving the interests of the lay society, too.

Dedication to Quality

Each Frontiers article is a landmark of the highest quality, thanks to genuinely collaborative interactions between authors and review editors, who include some of the world's best academicians. Research must be certified by peers before entering a stream of knowledge that may eventually reach the public - and shape society; therefore, Frontiers only applies the most rigorous and unbiased reviews.
Frontiers revolutionizes research publishing by freely delivering the most outstanding research, evaluated with no bias from both the academic and social point of view. By applying the most advanced information technologies, Frontiers is catapulting scholarly publishing into a new generation.

What are Frontiers Research Topics?

Frontiers Research Topics are very popular trademarks of the Frontiers Journals Series: they are collections of at least ten articles, all centered on a particular subject. With their unique mix of varied contributions from Original Research to Review Articles, Frontiers Research Topics unify the most influential researchers, the latest key findings and historical advances in a hot research area! Find out more on how to host your own Frontiers Research Topic or contribute to one as an author by contacting the Frontiers Editorial Office: frontiersin.org/about/contact

ADVANCING OCEAN OBSERVING TECHNOLOGY AND INDUSTRY - SCIENCE PARTNERSHIPS FOR THE FUTURE OF OCEAN SCIENCE

Topic Editors:
Ole Mikkelsen, Sequoia Scientific (United States), United States
Paula Bontempi, National Aeronautics and Space Administration (NASA), United States
Alex Nimmo-Smith, University of Plymouth, United Kingdom
Wayne Homer Slade, Sequoia Scientific (United States), United States
Ho Kyung Ha, Inha University, South Korea

Citation: Mikkelsen, O., Bontempi, P., Nimmo-Smith, A., Slade, W. H., Ha, H. K., eds. (2022). Advancing Ocean Observing Technology and Industry - Science Partnerships for the Future of Ocean Science. Lausanne: Frontiers Media SA. doi: 10.3389/978-2-88974-403-9

Table of Contents

frontiers in Marine Science

ORIGINAL RESEARCH
published: 21 April 2021
doi: 10.3389/fmars.2021.668733

Coastal Observation Using a Vertical Profiling System at the Southern Coast of Korea

Young-Gyu Park[1], Seongbong Seo[1], Dong Guk Kim[1], Joocheul Noh[1,2] and Hyuk Min Park[3]*

[1] Ocean Circulation Research Center, Korea Institute of Ocean Science and Technology, Busan, South Korea, [2] School of Earth and Environmental Sciences, Seoul National University, Seoul, South Korea, [3] Marine Bigdata Center, Korea Institute of Ocean Science and Technology, Busan, South Korea

At a coastal station near the southern coast of Korea, the vertical profiles of temperature salinity dissolved oxygen and velocity were obtained using a vertical profiler, Aqualog, every summer from 2016 to 2020. At the site, fishing activity was not allowed, and it was possible to maintain the profiler continuously and stably. It was set to travel every one or 2 h for two to 4 months. Thus, we were able to observe the variations of the water properties from hourly to monthly scales. The sensors were contaminated much less than we expected, and the data could be used without correction at least for our coastal applications. The main phenomena we observed are tides, coastal warming, fresh water, and responses to typhoons. On the daily time scale, the most prominent phenomenon is semi-diurnal tides, with which the thickness and temperature of coastal warm waters changed. The warm water also showed fluctuations between 10 and 15 days. The data also revealed that the tide showed strong seasonality. In summer, when the water is strongly stratified, the tidal current is baroclinic, while in winter, when the water is well mixed, the current is barotropic. Responses to typhoon induced winds were rather complicated. In one case, increase in the upper mixed layer was observed. The thick mixed layer disappeared in about a day due to advection. In another case the upper mixed layer became thinner, while the wind became stronger due the advection of the offshore water. Hydrographic observations conducted every 2 months, of course, or point measurement at a surface buoy could not show such continuous changes. More and more local fishermen are showing interest in oceanographic information, and data from the profiler could be of much use to them.

Keywords: coastal mooring, Aqualog, vertical profiling system, coastal warming, typhoon

OPEN ACCESS

Edited by:
Ho Kyung Ha,
Inha University, South Korea

Reviewed by:
Yang Ding,
Ocean University of China, China
Chen Wei-Bo,
National Science and Technology Center for Disaster Reduction (NCDR), Taiwan

****Correspondence:***
Young-Gyu Park
ypark@kiost.ac.kr

Specialty section:
This article was submitted to Ocean Observation, a section of the journal Frontiers in Marine Science

Received: *17 February 2021*
Accepted: *22 March 2021*
Published: *21 April 2021*

Citation:
Park Y-G, Seo S, Kim DG, Noh J and Park HM (2021) Coastal Observation Using a Vertical Profiling System at the Southern Coast of Korea. Front. Mar. Sci. 8:668733. doi: 10.3389/fmars.2021.668733

INTRODUCTION

Many socio-economic activities are actively taking place on coastal areas, and it is important to understand and predict coastal environments (Rixen et al., 2009). However, since phenomena of various spatiotemporal scales appear, neither coastal observation nor prediction is easy (Weller et al., 2019). To obtain time series buoy systems could be used. One could install diverse sensors to a buoy to obtain diverse time series, but data are from the depths at which the sensors are installed.

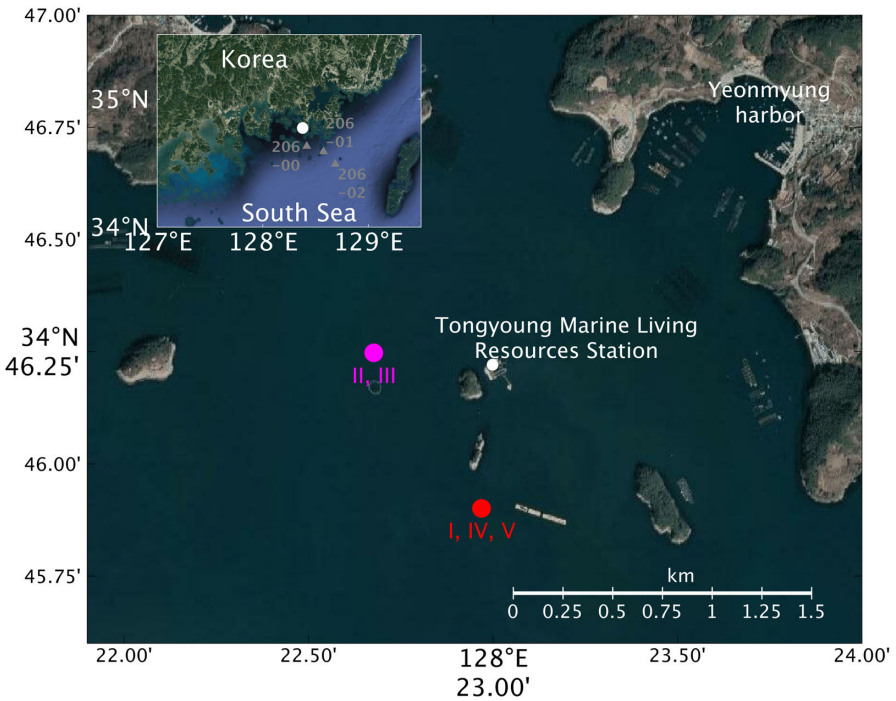

FIGURE 1 | Map of study area (Image: Google Earth, accessed 29 March, 2021). The numbers in the inserted panel are for hydrographic stations used in **Figure 8** for comparison.

A profiling system is an instrument that is designed to measure the vertical structure of a water column at a fixed time interval. Broadly speaking there are two types of profiling systems (Carlson et al., 2013). One is an underwater winch installed to a bottom mooring (Forrester et al., 1997; Von Alt et al., 1997). The winch pays out a profiling buoy in which diverse sensors are attached for a predetermined distance at predetermined times using the positive buoyancy of the buoy. The winch then winds the line back to the starting point with torque. By installing a winch to a surface buoy or a structure, a similar profiling system could be constructed (Dunne et al., 2002; Kolding and Sagstad, 2013). Another type of profiling system is based on a taut mooring line maintained by a subsurface buoy and a weight. In this type, a carrier in which instruments are attached travels along the line at a predetermined interval. With a profiling system of this type, Aqualog (Ostrovskii et al., 2010, 2013; Ostrovskii and Zatsepin, 2011; Fayman et al., 2019), we have been monitoring southern coastal water of Korea since 2016 (**Figure 1**).

Maintaining a mooring system at a coastal area is challenging because of high fishing activity and rapid contamination, although the data from the system is useful to the local fisheries. At our observation site fishing activity is not allowed and it has been possible to maintain the system continuously and stably. Our two attempts at other sites prior to 2016 could not be continued more than 2 weeks due to fishing activities. In 2016, the system was maintained from summer to winter, and it was possible to quantify bio-fouling, which turned out to be less than what we expected. Although the site is about two kilometers away from the coast, there is no river, and the data from the site represent more of open ocean waters than local coastal waters. With the profiling system that collected data every one or 2 h, we were able to observe tides, coastal warm water events, and responses to typhoons. There were expected structures such as dominance of the semi-diurnal tide as well as unexpected features such as strong baroclinicity in tidal currents during summer daily variation in the thickness of warm water. Here, we mainly focus on our experience with the system rather than the dynamics of the phenomena. The profiler has not always been working perfectly, and the proper working condition is also explained.

PROFILING SYSTEM AND OBSERVATION

The southern coast areas of Korea are heavily populated with aquafarms and fishing equipment and vessels. Thus, oceanographic data obtained in these areas could be of much use to local fisheries (Chang et al., 2020), but for the same reason it is not easy to maintain a mooring system. There, however, is a small area, the Tongyoung Marine Living Resources Station, reserved only for scientific research activity by the Korean Government (**Figure 1**). Since any commercial fishing activity is not allowed there, we have been maintaining a profiling system safely and continuously since 2016. The station is approximately two kilometers away from a pier and easily

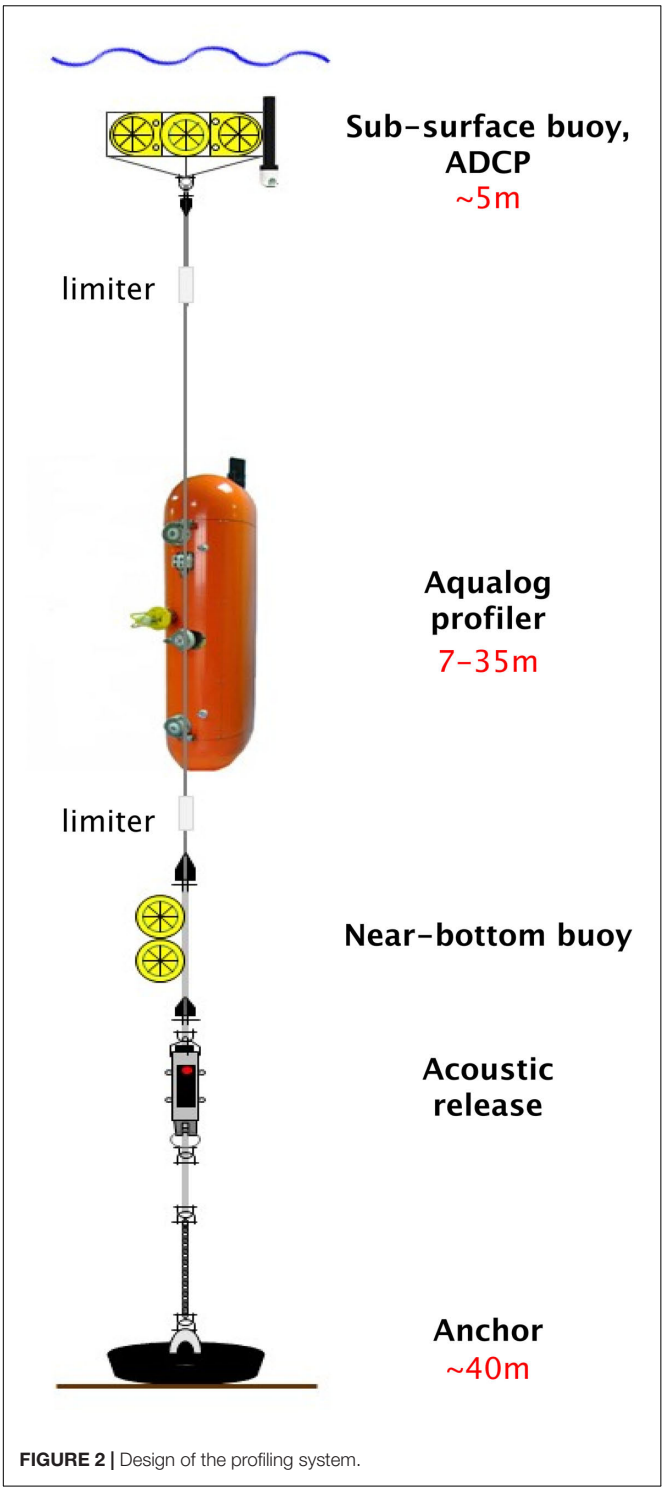

FIGURE 2 | Design of the profiling system.

accessible by a small boat. In addition, at the station that is constructed over a barge one can prepare instruments and download the data. This facility has helped us to maintain the mooring system easily. The proximity to a pier was at the same time was a concern because the data may just show local coastal water, rather than open water, properties. As we explain later, this turned out not to be the case. Previously we deployed a profiling system near an island in the East Sea. It did not take a week before the instrument entangled with traps installed by a local shrimp fisherman and damaged. Even a system deployed in a protected area in open water it did not take more than 2 weeks before being destroyed, presumably by fishing gear. In this particular case, a profiling system using an underwater winch, which is considered safer because the line was not in water except during profiling, was used.

The design of the profiling system is shown in **Figure 2**. A profiling carrier manufactured by the Aqualog Ltd., Aqualog (Ostrovskii et al., 2010), is used. It traverses vertically with an average speed of 0.25 m/s at predetermined time along a taut mooring line between the subsurface buoy and the anchor. Sensors such as Conductivity-Temperature-Depth (CTD) and Acoustic Doppler Current Profiler (ADCP) can be installed to the Aqualog. The utilized sensors are listed in **Table 1**. The ADCP installed to the profiler did not have an Inertial Measurement Unit (IMU), and unfortunately did not produce high quality data. There was another ADCP, Nortek Aquadopp 400 kHz current profiler, mounted to the subsurface buoy and produced stable current data. Of course one could obtain continuous velocity profiles using any ADCP installed on a buoy, but not continuous vertical profiles of temperature and salinity. The total weight of Aqualog was adjusted to have neutral buoyancy in a water tank to reduce battery consumption. One magnet, a limiter, is installed below the subsurface buoy and another above the anchor to limit the vertical range of the carrier. At predetermined times, the carrier starts to ascent from the parking depth. Upon touching the upper limiter, the carrier starts to descend while making measurement. On reaching the lower limiter, the carrier goes to sleep mode until the next profiling. Although the ADCP did not produce good data while the carrier was moving, it produced good data at the parking depth. The profiler is designed to travel about 100 km with 24 alkaline batteries. Typically, during our 2-month-long deployment, it traveled 80∼90 km.

From August 2016 to October 2020, there were five deployments. During Deployment I, which lasted for about 7 months, there were five Segments and four maintenances during which the battery and mooring line were replaced and the carrier was cleaned. During Deployments II and III, there were two segments and one maintenance. From Deployments I through III, it was found that during winter and spring the water was relatively homogeneous, and Deployments IV and V were conducted only during summer without any maintenance, while increasing the sampling interval from one to 2 h. Since this area has been used as a test bed, once in a while the mooring system became entangled with other instrument and the profiling system did not work properly. After Deployment IV, we found that the shaft and pulley of the motor in the carrier were corroded and replaced them. To collaborate or coordinate with other mooring systems deployed into the area, the profiling system

TABLE 1 | Summary of deployments.

Deployment	Period	Interval (hr)	Profiling range (m)	Sensors	Mean subsurface buoy depth (m)
I	2016. 08. 04 ~ 2016. 08. 24	1	15.98–40.18	SBE 19plus, RINKO3	14.64
	2016. 08. 25 ~ 2016. 10. 10		7.47–39.30		6.13
	2016. 10. 12 ~ 2016. 11. 22		6.61–37.29		5.96
	2016. 11. 24 ~ 2017. 01. 19		9.22–39.17		8.37
	2017. 01. 24 ~ 2017. 03. 14		7.15–39.51		5.94
II	2017. 07. 21 ~ 2017. 09. 21	1	6.25–36.74	SBE 52MP, SBE	5.50
	2017. 09. 22 ~ 2017. 12. 28	2	6.90–41.65	43F	6.25
III	2018. 07. 24 ~ 2018. 09. 18	2	6.79–41.14		5.80
	2018. 09. 19 ~ 2018. 12. 12		4.90–41.98		4.57
IV	2019. 07. 12 ~ 2019. 10. 10	2	7.63–39.99		6.38
V	2020. 06. 26 ~ 2020. 10. 21	2	8.05–41.56		7.48

FIGURE 3 | Biofouling and cleaning.

was not always kept the same location, as depicted in **Figure 1**.

BIOFOULING AND CLEANING

Since this coastal area is highly productive, biofouling was a major concern. In **Figure 3**, the conditions of the subsurface buoy and the profiler after 2-month-long deployment are shown. The subsurface buoy that was placed about 5 meters below the surface was contaminated more than the profiler. The line was clean because the profiler moved regularly. The inside of the profiler was also contaminated. These organisms were removed on site by water jets, and if necessary the system was moored again. Even though the profiler was parked 5 m above the bottom, there were sediments inside the carrier due to the tidal currents.

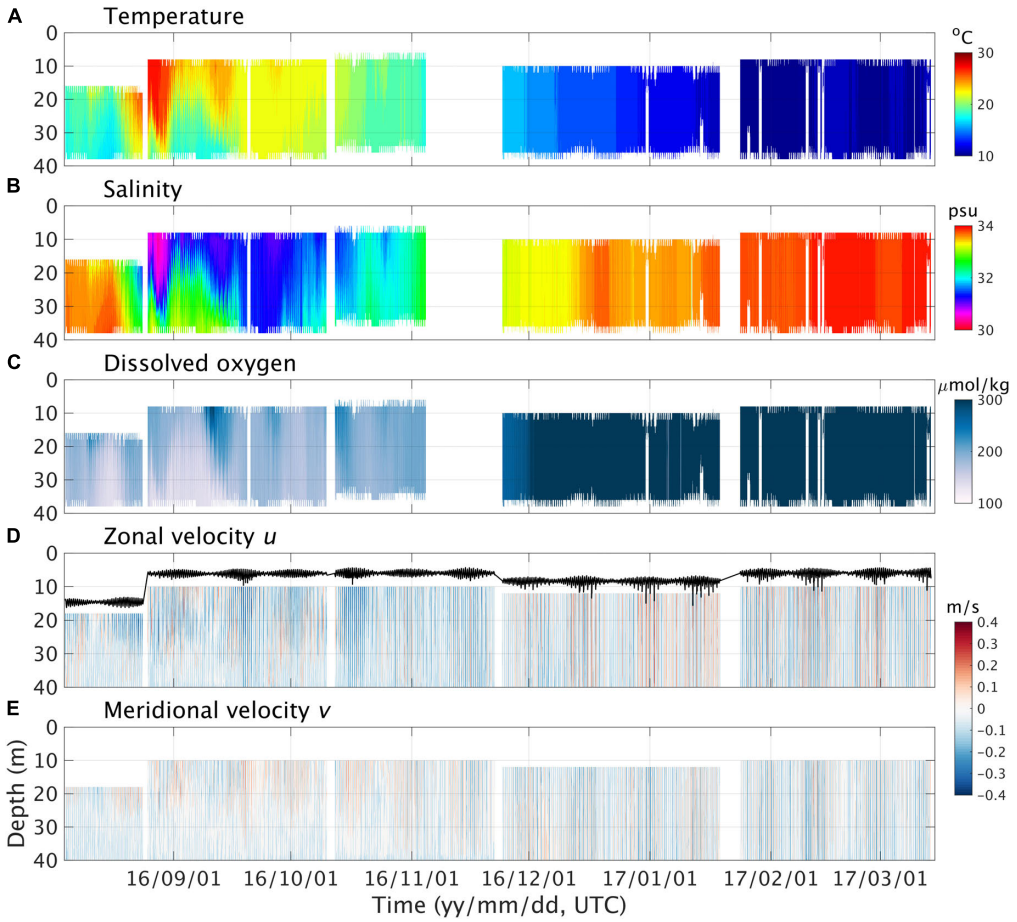

FIGURE 4 | Data from the profiling system **(A)** temperature, **(B)** salinity, **(C)** dissolved oxygen, and **(D)** zonal, *u*, and **(E)** meridional velocity, *v*, from the Aquadopp installed to the subsurface buoy. The solid line in **(D)** is pressure from the Aquadopp and shows the depth of the subsurface buoy.

As explained later biofouling, however, did not degrade the CTD data, at least for our coastal applications.

RESULTS

In **Figure 4**, the data collected during Deployment I are displayed. The prominent signals are tide and coastal warm/fresh water events as explained more in detail later. Since mid-September the amount of the fresh water from the Yangtze River decreased, and the salinity was increased. The area had been hit by typhoons a few times and the responses of the water to the typhoons were also recorded. From November 1 to late November, there was not enough battery power, and the profiler stopped. We miscalculated the remaining battery life, and did not replace the battery pack during the maintenance. During Segment 1, due to security concern the subsurface buoy was placed rather deep and the profile stopped at 15 m below the surface. During the first maintenance, the subsurface buoy was raised to about 5 m and the profile was obtained up to about 8 m.

Under a strong flow, the mooring line could be drooped so that the profiler may not be able to move properly. Between August 4, 2016 and March 11, 2017 there were five of such events. Using pressure data from the ADCP installed at the subsurface buoy, the angle between the mooring line and the vertical line was estimated during those events (**Figure 5**). It was found that when the angle was less than about 22 degrees or the ambient current was 0.6 m/s, the profiler worked properly. If the angel was less than 20 degrees, the profiler worked properly even at higher speed, as suggested by the manufacturer. Even after the mooring line became vertical, it took several cycles for the profiler to function properly probably again due to the misalignment between the rollers and the mooring line. Since the surface current is stronger it is more likely to have this problem as the subsurface buoy was raised.

Validation of Data

Since the instruments were deployed more than 6 months, the quality of the data must be verified first. Temperature and salinity were verified by comparing with the hydrographic observations made just before the deployments of the mooring system in **Figure 6**. Temperature showed an offset of about 0.02 but not

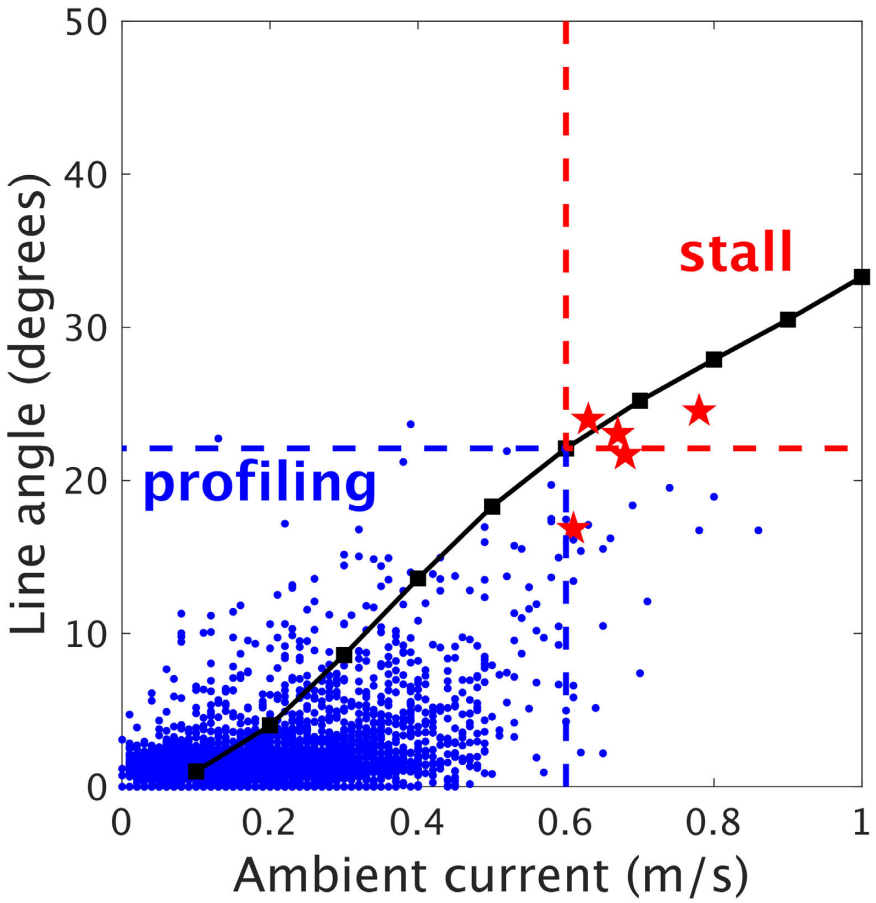

FIGURE 5 | Range for profiling.

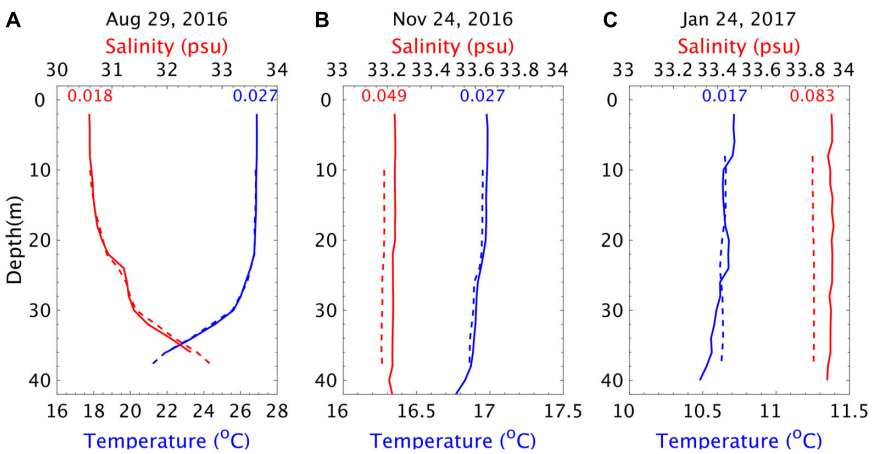

FIGURE 6 | Comparisons of temperature and salinity from the profiler and hydrographic data on three different days on **(A)** August 29, 2016, which is 25 days, **(B)** November 24, 2016, 112 days, and **(C)** January 24, 2017, 173 days after the first deployment. The dashed line is for the profiler and the solid one for the hydrographic observations. The numbers in the figure represent the difference between the two within upper mixed layer in each case. The time difference between the profiler and the hydrographic cast is less than 1.5 h in all three.

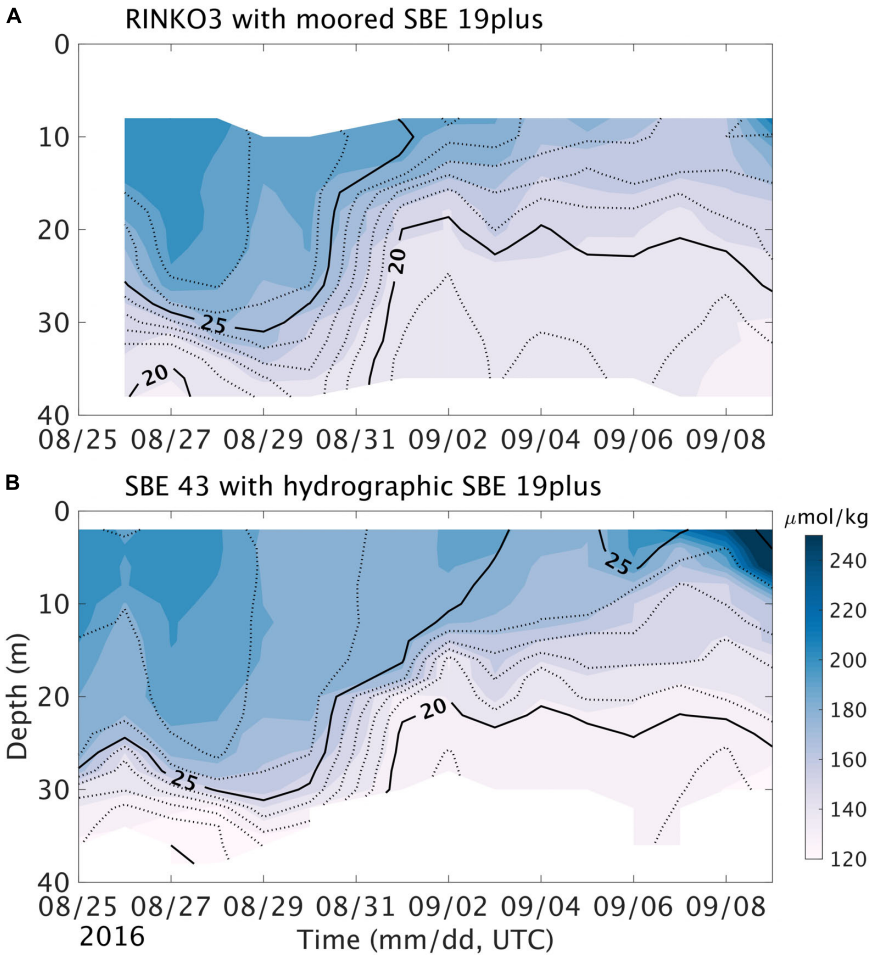

FIGURE 7 | Dissolved oxygen (shading) and temperature (contours) from **(A)** the profiler and **(B)** daily hydrographic casts made at the research station. The time difference between the two data set is less than an hour.

a drift. Salinity, however, was reduced by approximately 0.01 psu/month. This is highly productive costal area and we were expecting rather rapid contamination but it was less than what we expected. The profiler was parked below euphotic zone and must therefore be contaminated less than expected. The drift was rather linear and could be corrected using the hydrographic data. This amount of drift would be substantial for an open ocean and must be corrected (Ando et al., 2005), but in this coastal area it was much smaller compared to the daily or seasonal changes in salinity and the correction was not made. Instead we calibrate the sensor once a year, typically.

Using another CTD, SBE19plus equipped with SBE43F dissolved oxygen, daily hydrographic casts were also conducted at the research station from August 26, 2016 to September 9, and compared with DO from the profiler as shown in **Figure 7**. In general, the two data sets are consistent. DO data from other period is within a comparable range except for winters when air-sea interaction was active, and we can conclude that the DO sensor installed to the profiler was not contaminated seriously. One interesting feature from the data is that temperature and DO are positively correlated. At the particular site a warm water event is not causing hypoxia on the contrary to common belief. The cause and the structure of the warm water will be reported in a separate paper.

The site is close to a pier and easily accessible, but at the same is too close to the coast so that the data may just show local properties. There is no river around the site that is located over the headland. Thus it is rather unlikely that our data just show local structure. To verify our assumption, in **Figure 8** the data from the profiler shown in **Figure 4** are compared with hydrographic data taken by the Korea Oceanographic Data Center (KODC, 2017) at stations shown in **Figure 1**, 206-00, 206-01 and 206-02 which are 15, 26, and 41 km away from the mooring site, respectively. Except for the relatively salty (>34 psu) affected by Tsushima Warm Current water (Hyun et al., 1996; Pang et al., 1996) found further offshore, the profiler captured the warm and fresh upper and subsurface water found in the southern part of the Korea. The cold and salty winter coastal water was also well observed during Segment 5 (green dots).

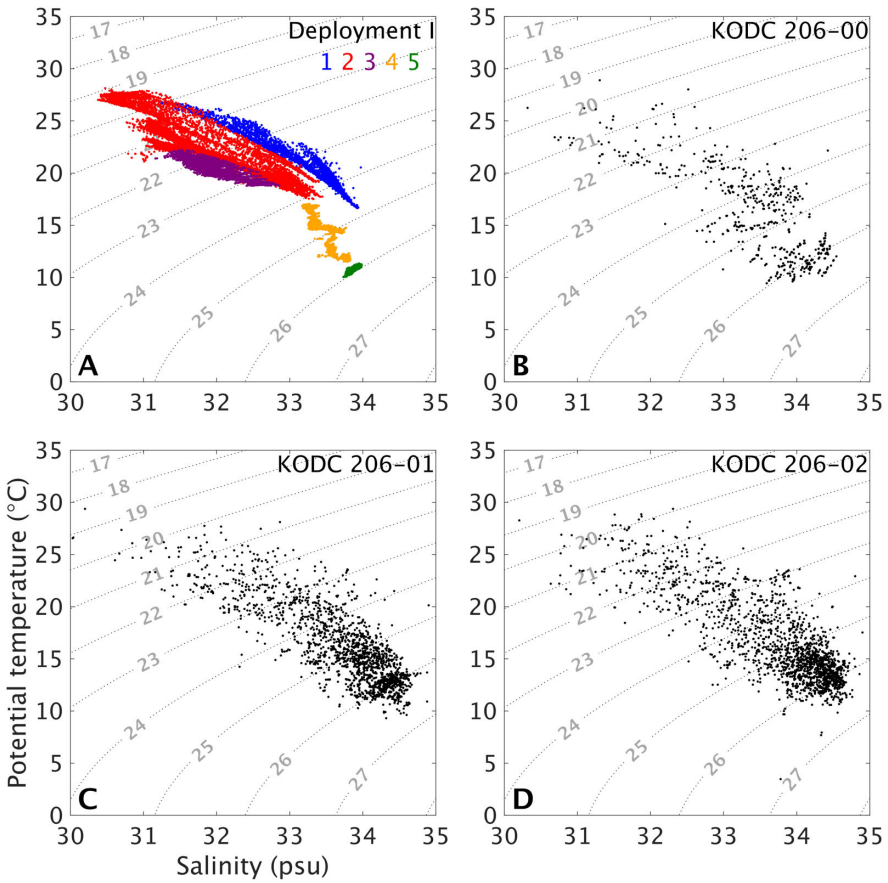

FIGURE 8 | T-S diagrams using data **(A)** from Deployment I, and hydrographic data from **(B)** KODC 206-00, **(C)** KODC 206-01, and **(D)** KODC 206-02 sites shown in **Figure 1**. The different colors in **(A)** represent different segments during Deployment I.

Tide

As in other southern Korean coastal areas (Teague et al., 2001) the most dominant signal from the current is M_2, followed by S_2 and then K_1, as well as from the pressure obtained at the subsurface buoy. In **Figure 9**, the tide during August 2016 when the water was well stratified and that in December 2016 when the water was well mixed, are shown. During August, the tidal current was strongly baroclinic while during December barotropic. Seasonality in barotropic tide is known (Kang et al., 1995), but such a change in vertical structure has not been reported previously. In this area, due to the strong stratification, the Richardson Number is >0.25, and the velocity shear would not be able to induce vertical mixing. Whether the baroclinicity is limited to this coastal area or common to other parts is a topic for future studies.

Warm Water Event

Warm water events were observed every summer. Explaining the structure of this warm water itself is beyond the scope of this study and here we want describe the basic structure and the benefits of using continuous measurement. The shortest time scale of the warm water event is due to the diurnal tide (**Figure 9**). The warm water is not produced locally but remotely. During the flood tide warm and fresh water flows from northwest and fills the area so that the amount of the warm and fresh water becomes greatest during high tide. During the ebb the warm and fresh water retreats. The warm water also shows variations between 10 and 15 days due to onshore advection (**Figure 10**). The dynamics behind the onshore advection is yet to be studied. One may conclude that this time scale is tied to the spring-neap cycle, but close investigation using all the data shows that they are not correlated. Since this warm water event is due to freshwater from the Yangtze River (Park et al., 2011; Kako et al., 2016; Moon et al., 2019), temperature and salinity are negatively correlated. In Korea, there are surface buoys measuring surface temperature, but the vertical extent of the warm water cannot be estimated with such data. This large change in the vertical extent would be useful information to local aquafarms. In open ocean, there is no data showing temporal variation and we used model outputs. Warm water events are rather continuous and do not show the variation observed with the profiler, suggesting that the temporal structure is limited to this coastal area. If this applies to other coastal area, more specific warning system taking into account vertical extent and duration is required. Around Korea, hydrographic observations have been made every 2 months. These data are

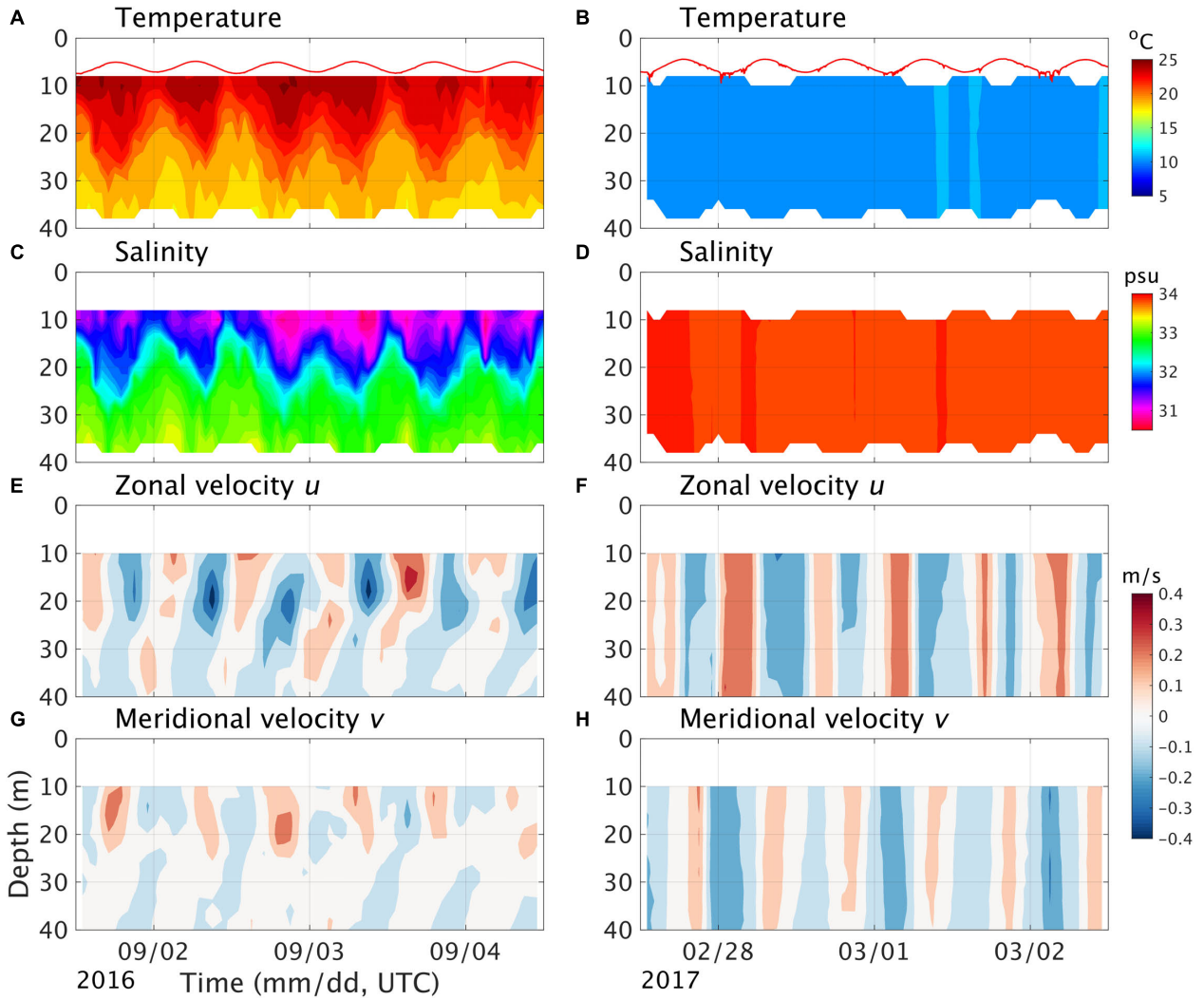

FIGURE 9 | Temperature **(A,B)**, salinity **(C,D)**, zonal velocity *u* **(E,F)**, and meridional velocity *v* **(G,H)** during summer (left column) and winter (right column).

useful in studying the long term changes and the mean state, but naturally cannot resolve the warm water events.

Response to Typhoons

During the deployment, six typhoons passed by the observation site as displayed in **Figure 11**, and the data provide us with a rare opportunity to investigate the response of the coastal water to typhoons. In open oceans, a typhoon enhances vertical mixing to mix warm surface water with the cooler subsurface layer, causing a deeper mixed layer and cold wake at the surface (Price, 1981). In coastal waters, due to topography and lateral boundaries, the response could be different from that in open ocean.

During Typhoons Chaba in 2016 and Maisak and Haisen in 2020, the mooring site was hit by winds of about 20 m/s or stronger. Since the mooring was under the water, it produced nice data without any damage. In the case of Chaba 2016, as the wind became stronger salty and cold water was advected toward the observation site, the stratification between 20∼30 m levels became stronger (**Figure 12**). This tendency continued until 10 h after the wind speed reached the maximum, after which mixed water started to appear. This observation suggests that the effect of advection was stronger than local mixing. During Typhoon Maysak on September 1st 2020, as the wind intensified, the mixed layer became deeper. Note that since we are lacking data for the upper 10 m, the mixed layer depth cannot be defined strictly. Instead, the 24°C isotherm was used as a proxy for the mixed layer depth. The mixed layer became deepest when the wind was strongest (**Figure 13**). It was possible to reproduce this deepening tendency using a 1-D mixed layer model such as GTOM (Burchard, 1999, available at[1]). In a mixed layer model, the initial upper layer stratification governs the subsequent evolution of temperature. In this case, the upper layer structure is unknown, and by assuming a rather strong stratification within upper 10 m, it

[1]www.gotm.net

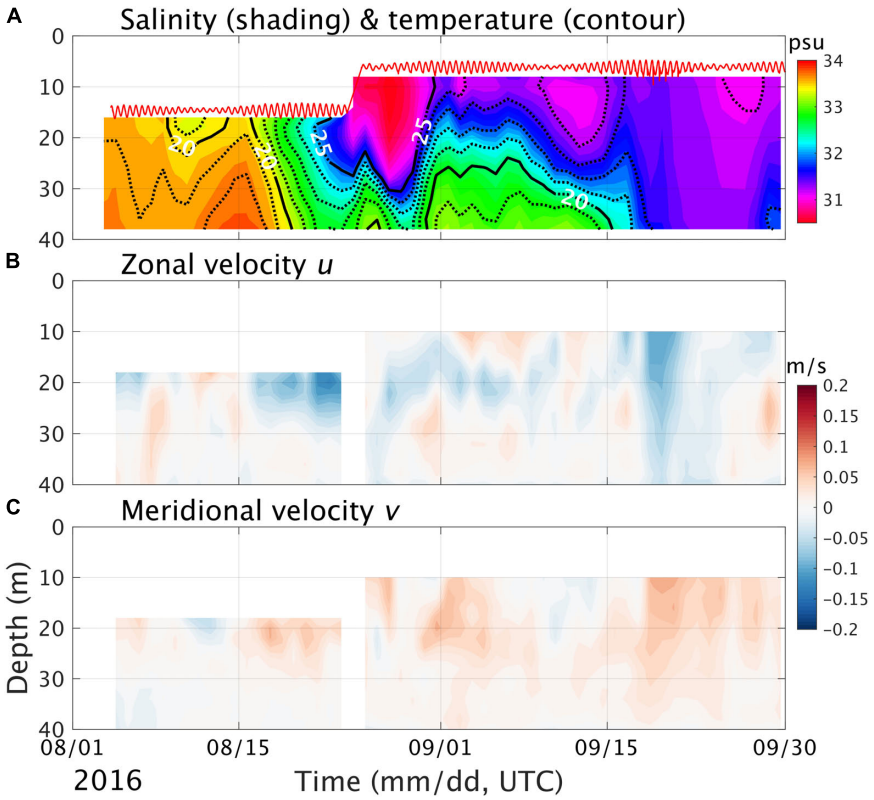

FIGURE 10 | Warm water events in summer 2016. Daily mean **(A)** salinity (shading) and temperature (contour), **(B)** zonal velocity, *u*, and **(C)** meridional velocity, *v*.

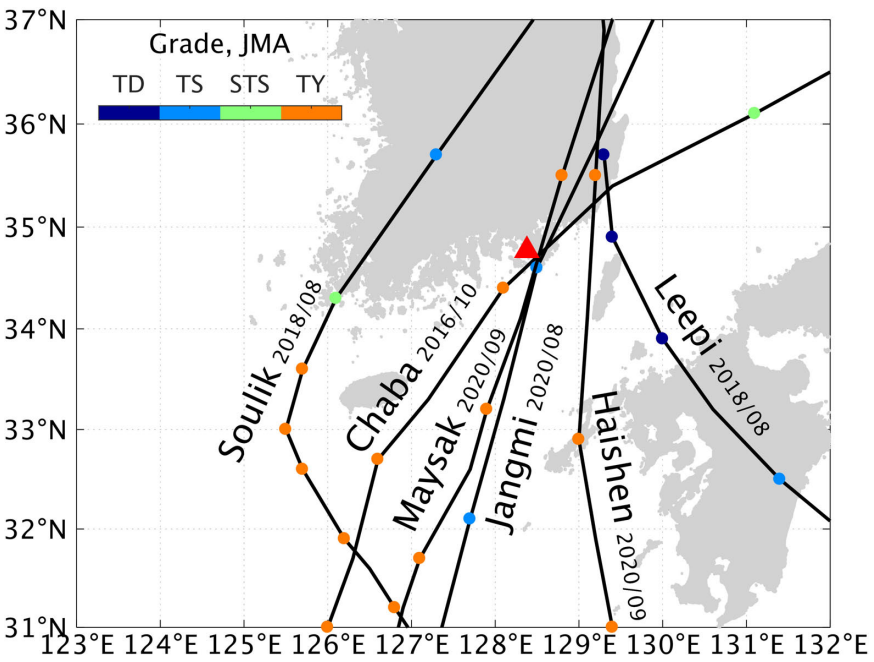

FIGURE 11 | Tracks of the typhoons passed by the observation site (red triangle) at 6-h intervals. The color bar in the upper left corner represents the typhoon category. Tropical Depression (TD), Tropical Storm (TS), Severe Tropical Storm (STS), Typhoon (TY).

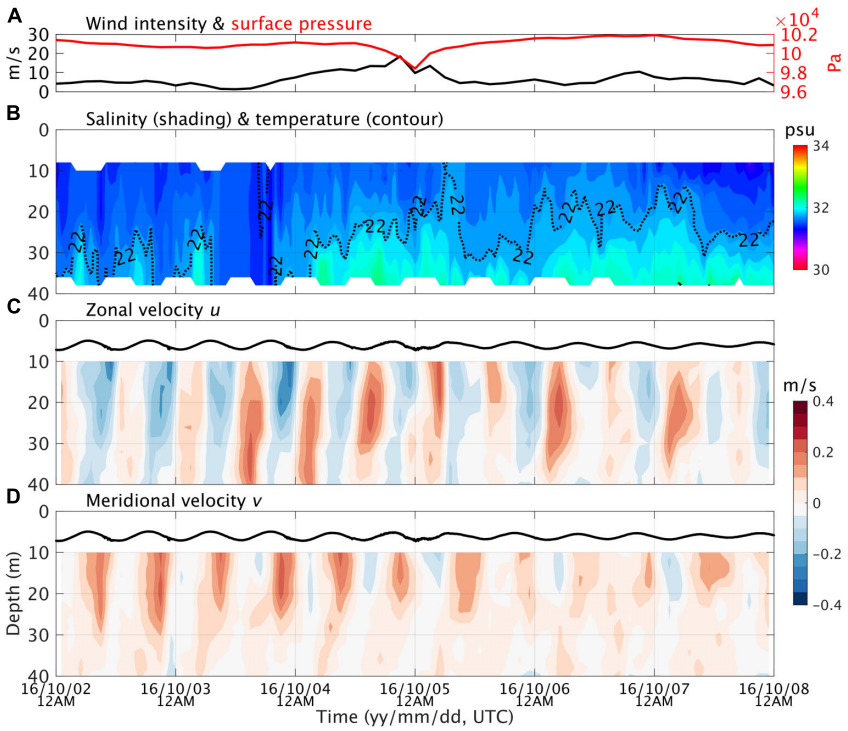

FIGURE 12 | Responses to Typhoon Chaba. **(A)** wind strength (back line) and surface pressure (red line) from European Centre for Medium-Range Weather Forecasts (ECMWF) ERA5 (Hersbach et al., 2020), **(B)** salinity (shading) and temperature (contour), **(C)** zonal velocity, *u*, and **(D)** meridional velocity, *v*.

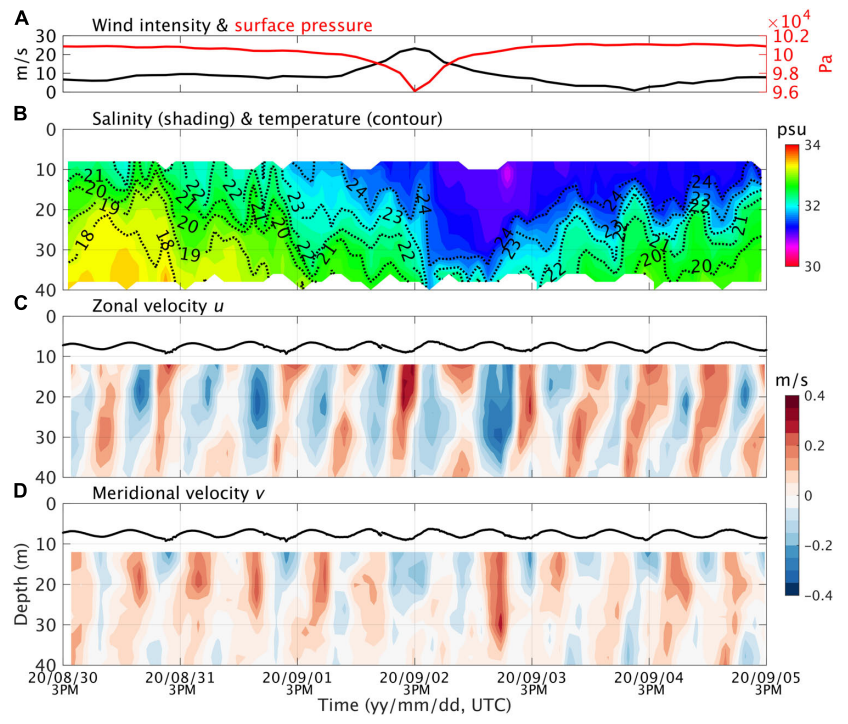

FIGURE 13 | The same as **Figure 12** except for Typhoon Maysak.

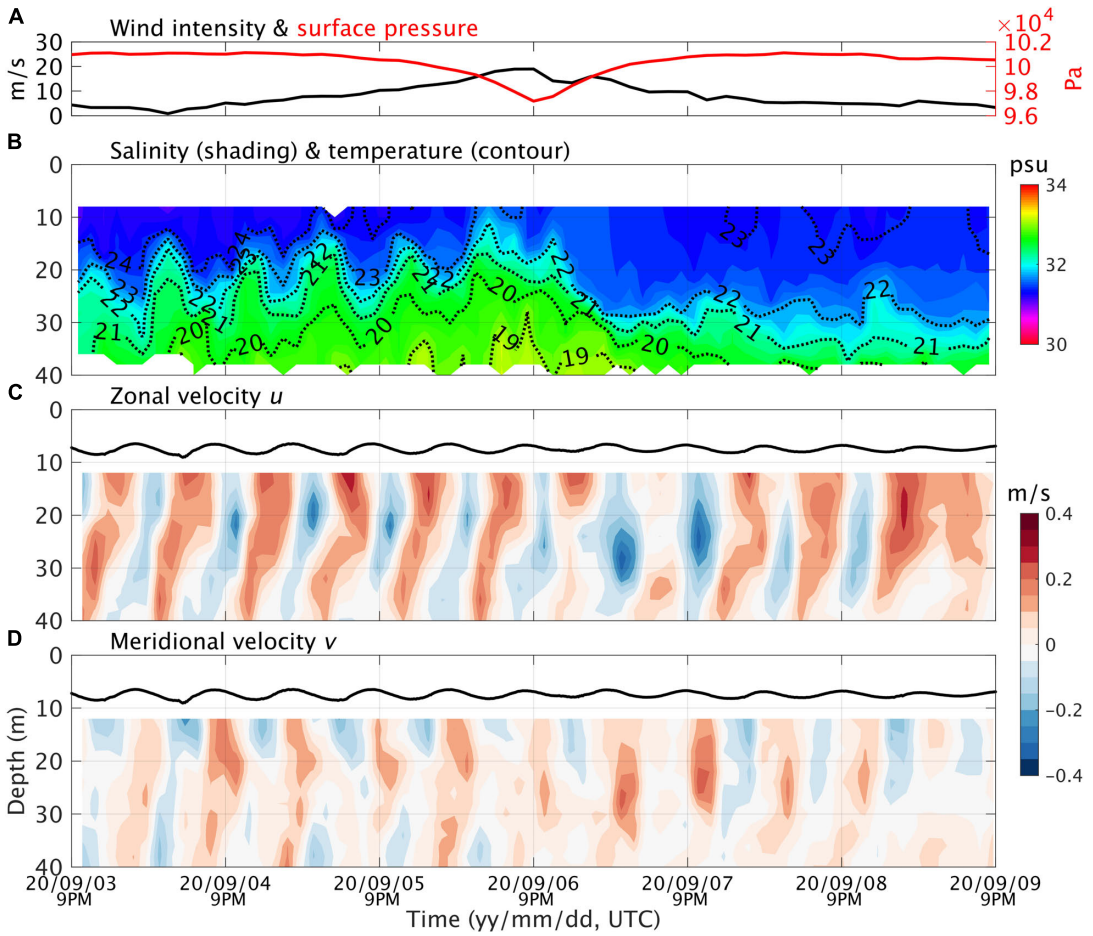

FIGURE 14 | The same as **Figure 12** except for Typhoon Haishen.

was possible to reproduce the deepening of the 24°C isotherm (not shown). The mixed layer disappeared within less than a day due to subsurface advection of cold and salty water from south. The 1-D mixed layer model was not able to reproduce the disappearance of the mixed layer, however. The global analysis field from the HYbrid Coordinate Ocean Model (HYCOM, GOFS 3.1[2]) whose horizontal resolution is 1/12° was able to reproduce the deepening of the mixed layer due to the typhoon. The disappearance of the mixed layer was not reproduced probably because the horizontal resolution is not high enough to resolve the coastal circulation properly. During Typhoon Haisen, which arrived about 4 days after Typhoon Maysak, the water column does not show notable response to the increasing wind until a few hours before the peak wind (**Figure 14**). Then, the mixed layer started to thicken rather slowly and became thickest about 12 h after the peak wind. The thick mixed layer was maintained for a few days. Tidal currents were strong but the two typhoons homogenized water around the observation site and the water remain homogeneous.

[2]https://www.hycom.org

SUMMARIES AND CONCLUSION

At a coastal research station located at the southern coastal area of Korea, a vertical profiling system measuring temperature, salinity, dissolved oxygen, and velocity has been successfully maintained every summer from 2016 to 2020. Around the station, fishing activity is not allowed, and it has thus been possible to maintain the profiler continuously and stably. Comparisons with hydrographic data show that the sensors were contaminated much less than we expected during 2- to 6-month-long deployments probably because the sensors were located below the euphotic zone. Therefore, the data could be used without correction for our coastal applications. Even though the station is within 2 km of the land, there is no river and the profiler observed the warm and fresh southern coastal water of Korea well. When the profiler did not operate properly, this was because the flow was stronger than about 0.6 m/s so that mooring line was inclined from the vertical by more than 20 degrees.

The profiling system recorded continuous spatiotemporal variations that cannot be measured using hydrographic surveys or point measurements at a surface buoy. The semi-diurnal tides were the most prominent phenomenon, as in other coastal

areas around Korea. It was found for the first time that in summer, when the water is strongly stratified, the tidal current is baroclinic, while in winter, when the water is well mixed, the current is barotropic. The baroclinicity was not strong enough to overcome the stratification sufficiently to induce vertical mixing, however. The strong seasonality calls for a further study on the dynamics and its effect on coastal environments. Coastal warm water events were also prominent. On the daily time scale, the semi-diurnal tide was the main driver. During the flood, warm and fresh water was transported from the offshore while during the ebb retreated to the offshore. The warm water also showed fluctuations between 10 and 15 days due to northward advection from the offshore. Numerical model results show that such variations do not occur in offshore waters. The profiling system deployed underwater recorded the responses to typhoon-induced winds without any damage. Both lateral advection and wind-induced vertical mixing were important.

The collected time series can be used in verifying coastal ocean circulation models as well as for data assimilation once real-time data become available. There are diverse types of aquafarms in the study area, and the data help the stake holders in selecting the optimal site for such farms as demonstrated in Chang et al. (2020). Coastal warm water events are becoming serious concerns to aquafarms. The variability and characteristics of the warm water events we reported would be of much help in establishing effective countermeasures.

The main limitation with the profiling system is real-time communication, and the data have not been used for real-time prediction so far. Another limitation is the lack of surface data. The upper most temperature from the profiler was lower by 5 to 2°C than surface temperature obtained from a nearby surface buoy. To overcome these deficiencies, we plan to upgrade the profiling system using a surface buoy equipped with a temperature sensor and a real-time communication system utilizing an acoustic modem and a cellular modem.

DATA AVAILABILITY STATEMENT

The raw data supporting the conclusions of this article will be made available by the authors, without undue reservation.

AUTHOR CONTRIBUTIONS

Y-GP led the project, interpreted the data, and wrote the manuscript. SS performed data analysis and visualization. DK contributed to the design of the mooring, data acquisition, and processing. DK, SS, JN, and HP contributed to the maintenance of the mooring system and instruments, data acquisition, and processing. All authors contributed to manuscript revision, and approved the submitted version.

FUNDING

This work was funded through the projects "Investigation and prediction system development of marine heatwave around the Korean Peninsula originated from the subarctic and western Pacific (20190344)" from the Ministry of Oceans and Fisheries, Korea, and "Building Conceptual Design for Mid-size Integrated CCS Demonstration (20214710100060)" from the Korea Institute of Energy Technology Evaluation and Planning.

ACKNOWLEDGMENTS

We would like to thank Yong-Joo Park and the members of Tongyoung Marine Living Resources Station for their support.

REFERENCES

Ando, K., Matsumoto, T., Nagahama, T., Ueki, I., Takatsuki, Y., and Kuroda, Y. (2005). Drift characteristics of a moored conductivity-temperature-depth sensor and correction of salinity data. *J. Atmos. Ocean Technol.* 22, 282–291. doi: 10.1175/jtech1704.1

Burchard, H. (1999). Recalculation of surface slopes as forcing for numerical water column models of tidal flow. *Appl. Math. Model.* 23, 737–755. doi: 10.1016/s0307-904x(99)00008-6

Carlson, D. F., Ostrovskii, A., Kebkal, K., and Gildor, H. (2013). "Moored automatic mobile profilers and their applications," in *Advances in Marine Robotics*, ed. G. Oren (Riga: LAP Lambert Academic Publishing), 169–206.

Chang, Y. S., Jin, J., Choi, J. Y., Jeong, W. M., Hyun, S. K., Chung, C. S., et al. (2020). Three dimensional numerical modeling using a multi-level nesting system for identifying a Water layer suitable for scallop farming in Tongyeong, Korea. *Aquac. Eng.* 89:102058. doi: 10.1016/j.aquaeng.2020.102058

Dunne, J. P., Devol, A. H., and Emerson, S. (2002). The oceanic remote chemical/optical analyzer (ORCA)—an autonomous moored profiler. *J. Atmos. Ocean Technol.* 19, 1709–1721. doi: 10.1175/1520-0426(2002)019<1709:torcoa>2.0.co;2

Fayman, P., Ostrovskii, A., Lobanov, V., Park, J. H., Park, Y. G., and Sergeev, A. (2019). Submesoscale eddies in Peter the Great Bay of the Japan/East Sea in winter. *Ocean Dyn.* 69, 443–462. doi: 10.1007/s10236-019-01252-8

Forrester, N., Stokey, R. P., Von Alt, C., Allen, B. G., Goldsborough, R. G., Purcell, M. J., et al. (1997). "The LEO-15 long-term ecosystem observatory: design and installation," in *Proceedings of the Oceans '97 Conference MTS/IEEE*, Halifax, NS.

Hersbach, H., Bell, B., Berrisford, P., Hirahara, S., Horányi, A., Muñoz-Sabater, J., et al. (2020). The ERA5 global reanalysis. *Q. J. R. Meteorol. Soc.* 146, 1999–2049.

Hyun, K. H., Pang, I. C., and Rho, H. K. (1996). The seasonal circulation in the South and West Seas and the inflow of warm waters into the West Sea in summer. *Bull. Mar. Res. Inst. Cheju Nat. Univ.* 20, 17–30.

Kako, S. I., Nakagawa, T., Takayama, K., Hirose, N., and Isobe, A. (2016). Impact of Changjiang River discharge on sea surface temperature in the East China Sea. *J. Phys. Oceanog.* 46, 1735–1750. doi: 10.1175/jpo-d-15-0167.1

Kang, S. K., Chung, J. Y., Lee, S. R., and Yum, K. D. (1995). Seasonal variability of the M2 tide in the seas adjacent to Korea. *Cont. Shelf Res.* 15, 1087–1113. doi: 10.1016/0278-4343(94)00066-v

KODC (2017). *Korea Oceanographic Data Center*. Available online at: http://kodc.nfrdi.re.kr (accessed April 1, 2017).

Kolding, M. S., and Sagstad, B. (2013). Cable-free automatic profiling buoy. *Sea Technol.* 54, 10–12.

Moon, J. H., Kim, T., Son, Y. B., Hong, J. S., Lee, J. H., Chang, P. H., et al. (2019). Contribution of low-salinity water to sea surface warming of the East China Sea in the summer of 2016. *Prog. Oceanogr.* 175, 68–80. doi: 10.1016/j.pocean.2019.03.012

Ostrovskii, A. G., and Zatsepin, A. G. (2011). Short-term hydrophysical and biological variability over the northeastern Black Sea continental slope as inferred from multiparametric tethered profiler surveys. *Ocean Dyn.* 61, 797–806. doi: 10.1007/s10236-011-0400-0

Ostrovskii, A. G., Zatsepin, A. G., Shvoev, D. A., and Soloviev, V. A. (2010). "Underwater anchored profiler Aqualog for ocean environmental monitoring," in *Advances in Environmental Research*, ed. J. A. Daniels (New York, NY: Nova Science Publishers, Inc), 179–196.

Ostrovskii, A. G., Zatsepin, A. G., Soloviev, V. A., Tsibulsky, A. L., and Shvoev, D. A. (2013). Autonomous system for vertical profiling of the marine environment at a moored station. *Oceanology* 53, 233–242. doi: 10.1134/s0001437013020124

Pang, I. C., Rho, H. K., Lee, J. H., and Lie, H. J. (1996). Water mass distribution and seasonal circulation northwest of Cheju Island in 1994. *Korean J. Fish. Aquat. Sci.* 29, 862–875.

Park, T., Jang, C. J., Jungclaus, J. H., Haak, H., and Park, W. (2011). Effects of the Changjiang river discharge on sea surface warming in the Yellow and East China Seas in summer. *Cont. Shelf Res.* 31, 15–22. doi: 10.1016/j.csr.2010.10.012

Price, J. F. (1981). Upper ocean response to a hurricane. *J. Phys. Oceanogr.* 11, 153–175. doi: 10.1175/1520-0485(1981)011<0153:uortah>2.0.co;2

Rixen, M., Book, J. W., and Orlic, M. (2009). Coastal processes: challenges for monitoring and prediction. *J. Mar. Syst.* 78, S1–S2.

Teague, W. J., Perkins, H. T., Jacobs, J. W., and Book, J. W. (2001). Tide observation in the Korea-Tsushima Strait. *Cont. Shelf Res.* 21, 545–561. doi: 10.1016/s0278-4343(00)00110-2

Von Alt, C., De Luca, M. P., Glenn, S. M., Grassle, J. F., and Haidvogel, D. B. (1997). LEO-15: monitoring and managing coastal resources. *Sea Technol.* 38, 10–16.

Weller, R. A., Baker, D. J., Glackin, M. M., Roberts, S. J., Schmitt, R. W., Twigg, E. S., et al. (2019). The challenge of sustaining ocean observations. *Front. Mar. Sci.* 6:105. doi: 10.3389/fmars.2019.00105

Conflict of Interest: The authors declare that the research was conducted in the absence of any commercial or financial relationships that could be construed as a potential conflict of interest.

frontiers in Marine Science

ORIGINAL RESEARCH
published: 07 July 2021
doi: 10.3389/fmars.2021.695510

Practical Method to Screen Contaminated Holograms of Flocs Using Light Intensity

*Sun Min Choi[1], Jun Young Seo[1], Guan-hong Lee[1], Xiaoteng Shen[2] and Ho Kyung Ha[1]**

[1] Department of Ocean Sciences, Inha University, Incheon, South Korea, [2] College of Harbour, Coastal and Offshore Engineering, Hohai University, Nanjing, China

Submergible digital holographic camera can measure the *in situ* size and shape of suspended particles, such as complex flocs and biological organisms, without disturbance. As the number of particles in the water column increases, overlapping concentric rings (interference patterns) can contaminate the holographic images. Using light intensity (LI), this study proposes a practical method to assess the degree of contamination and screen out contaminated images. The outcomes from image processing support that LI normalized on a gray scale of 0 (black) to 255 (white) can be a reliable criterion for defining the contamination boundary. Results found that as LI increased, the shape of the particle size distribution shifted from a positively skewed to a normal distribution. When LI was lower than approximately 80, owing to the distortion of particle properties, the settling velocities derived from the contaminated holograms with mosaic patterns were underestimated compared to those from the uncontaminated holograms. The proposed method can contribute to a more accurate estimation of the transport and behavior of cohesive sediments in shallow estuarine environments.

Keywords: hologram, floc, light intensity, contamination, interference

OPEN ACCESS

Edited by:
Oscar Schofield, Rutgers, The State University of New Jersey, United States

Reviewed by:
Kyle Strom, Virginia Tech, United States
Byung Joon Lee, Kyungpook National University, South Korea

****Correspondence:***
Ho Kyung Ha
hahk@inha.ac.kr;
hokyung.ha@gmail.com

Specialty section:
This article was submitted to Ocean Observation, a section of the journal Frontiers in Marine Science

Received: *15 April 2021*
Accepted: *14 June 2021*
Published: *07 July 2021*

Citation:
Choi SM, Seo JY, Lee G, Shen X and Ha HK (2021) Practical Method to Screen Contaminated Holograms of Flocs Using Light Intensity. Front. Mar. Sci. 8:695510. doi: 10.3389/fmars.2021.695510

INTRODUCTION

Digital holography is an imaging method that records holograms using a charge-coupled device (CCD) camera. The reconstruction of such images is numerically performed using digitized interferograms (Mills and Yamaguchi, 2005). Since the introduction of holography into the scientific community in the 1940s (Gabor, 1948), it has become an indispensable technique used in various fields of fluid mechanics, metrology, and medical imaging (Nayak et al., 2021). Because holography is a proven method that enables the provision of a solution to the limitations of the focal plane, the marine science community has recently adopted it to collect information on the three-dimensional properties of particulate matter (e.g., sediment and plankton) suspended in a water column (e.g., Graham and Nimmo-Smith, 2010; Choi et al., 2018; Nayak et al., 2019; Giering et al., 2020).

The application of holographic techniques to cohesive sediments distributed in coastal environments has been somewhat limited. It is because the high concentration of fine-grained suspended particles greatly reduces the optical transmittance within the water column (Sun et al., 2002). For instance, flocculated cohesive sediments are readily settled and deposited on the bed during slack tides, and then resuspended into the overlying layer during tidal acceleration periods. Such cyclic behaviors form a high-concentration (greater than hundreds of mg l^{-1}) near-bed layer,

which makes it hard to meet the optical transmittance required to acquire the proper hologram and conduct post-processing for image analysis. To overcome this technical problem, several studies have developed a post-processing procedure for background correction and modified segmentation sequences, and suggested the maximum theoretical suspended sediment concentration (SSC) for measurable operation (e.g., Sequoia, 2014; Giering et al., 2020). However, the threshold for capturing proper hologram varies with the local bed properties because the SSC greatly depends on the size and shape of particles (Davies-Colley et al., 2014; Merten et al., 2014), causing difficulties in the accurate detection of complex cohesive sediments.

Owing to the aforementioned technical issues, there is a need to define a widely applicable criterion to assess the degree of contamination and then screen out the contaminated images. Therefore, the main objectives of this study were to: (1) identify a criterion to screen contaminated holograms and (2) evaluate the associated practical method in the view of behaviors (e.g., settling) of flocs in cohesive sediment dynamics.

MATERIALS AND METHODS

Study Sites and Data Collection

Two study sites representing a tide-dominated estuarine system were selected on the west coast of Korea (**Figure 1A**): Ganghwa Tidal Flat (GTF) and Geum River Estuary (GRE). In both sites, the bed sediments predominantly consist of fine-grained sediments (clay and silt) supplied from the river. Under a hypertidal regime with a tidal range of up to 10.2 m, the suspended sediments in the water column are repetitively resuspended and settled by tidal currents. Such a dynamic condition is optimal for investigating *in situ* holograms of fine-grained particles.

The GTF lies in the estuary of the Han River (**Figure 1B**). The total surface area of the tidal flats is 302.4 km^2, and its southern part contains 86% of them extending up to 6 km from the coastline (Woo and Je, 2002). Within the GTF, the mixed (sand and mud) flat is widely distributed, and median particle size (d_{50}) was approximately 17.5 μm, which was measured by a particle-sizing instrument (Malvern, Mastersizer 2000S) in a dispersed state (**Table 1**). The imaging data were obtained using a submergible digital holographic camera (LISST-Holo, Sequoia Inc.). By installing a path reduction module, the optical path length was reduced from 50 to 10 mm to extend the upper limit of the measurable SSC. The LISST-Holo attached to a H-frame system was deployed at 0.15 m above the bed in the upper tidal flat during October 12–20, 2019. For the analysis, two typical tidal cycles (October 12 and 16) were chosen based on the SSC varying from 53 to 221 mg l^{-1}.

The GRE is a 396-km-long drowned river valley with the watershed area of 9,836 km^2 (**Figure 1C**; Kim et al., 2006;

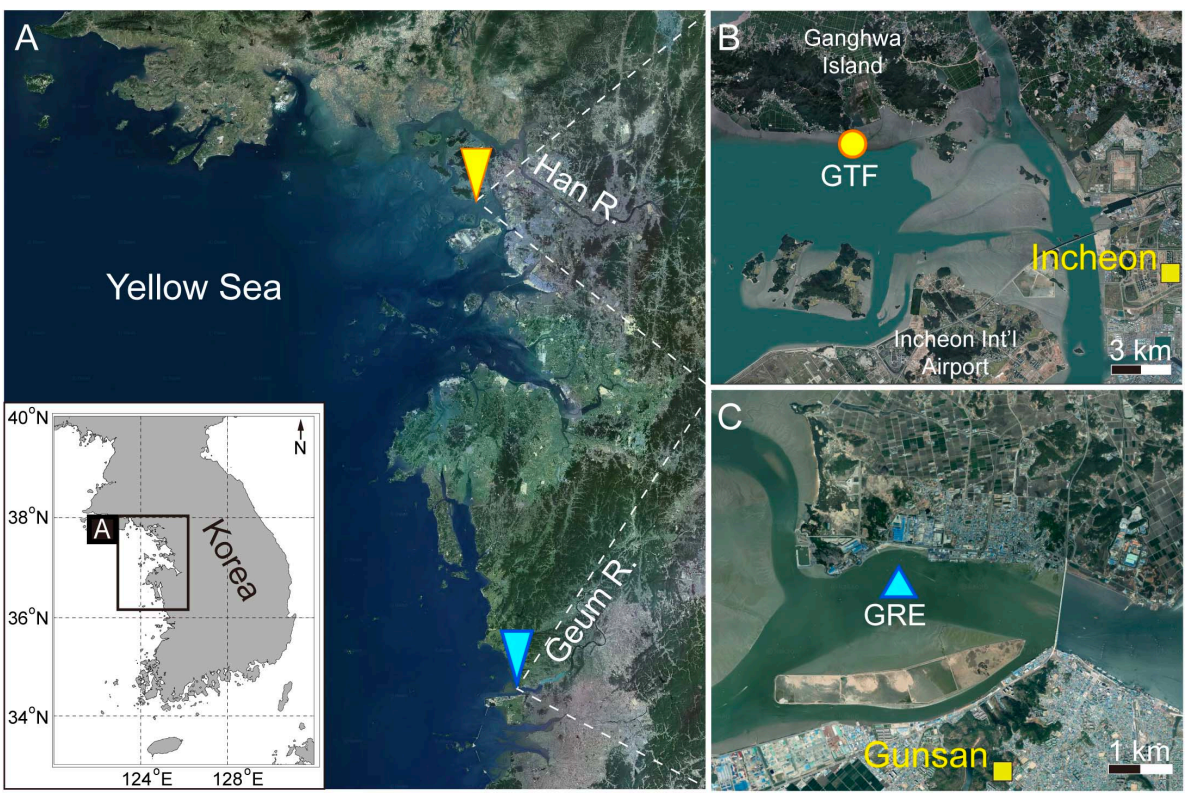

FIGURE 1 | (A) Satellite image showing the study area in Korean Peninsula: **(B)** Ganghwa tidal flat (GTF) and **(C)** Geum river estuary (GRE). Sampling stations are marked by the yellow circle in panel **(B)** and the cyan triangle in panel **(C)**. All satellite images were downloaded from https://map.kakao.com/.

TABLE 1 | Summary on hydrodynamics and sediment properties for Ganghwa Tidal Flat (GTF) and Geum River Estuary (GRE).

	GTF	GRE
Median particle size (μm)	17.5	30.7
Mean current velocity (m s^{-1})	0.02	0.5
SSC ranges (mg l^{-1})	53–221	1.9–45.3
Number of holograms used	2,224	776

Figueroa et al., 2019). In the GRE, the sediment was sandy-silt and d_{50} was 14–58 μm (Ministry of Oceans and Fisheries, 2019). The mean current velocity reached approximately 0.5 m s^{-1} during the spring tide (Figueroa et al., 2020). The optical backscattering sensor and LISST-Holo were profiled at intervals of 30 min for 12 h on September 2, 2016, to collect the particle information. With cyclic tidal phases, the SSC in the water column varied in the range of 2–45.3 mg l^{-1}.

The laboratory water tank experiments have been conducted to convince the *in situ* results. We used a suspension of known particle size and shape with varying concentration. Details on laboratory experiments are given in **Supplementary Figures 1–3**.

LISST-Holo

The LISST-Holo is a device designed to measure the properties (e.g., size, number, shape, and volume concentration) of suspended particles (Sequoia, 2014). This device is capable of capturing *in situ* size (20–2,000 μm) and shape for suspended particles such as complex aggregates and biological organisms (Graham and Nimmo-Smith, 2010; Graham et al., 2012). To visualize the holograms generated from LISST-Holo, several parameters such as exposure, shutter, brightness, gain, and laser power should be balanced. In this study, each parameter was set as the default value suggested by Sequoia Inc. A detailed description of the settings is provided next. The exposure and shutter indicate the amount of light per unit area reaching the surface of the electronic image sensor and of the passed light for a determined period, respectively. Thus, the observed holograms could be contaminated depending on the exposure values modulated by the shutter speed and lens aperture (Sequoia, 2014). In a condition where the suspended particles are freely transported in the water column, the longer the shutter time, the blurrier the hologram. This is because a few microseconds are required to capture the hologram image. If suspended particles move more than half a pixel during that time, the captured image includes the trajectories of the particles, resulting in a blurry hologram. Sequoia (2014) recommended that the current velocity should be lower than 0.5 m s^{-1} with a camera shutter of 30 ms and a pixel of 4.4 μm. The brightness is an attribute of visual perception in which a source appears to be radiating or reflecting light. The gain is a process of increasing the optical power by transferring the medium's energy to the emitted electromagnetic radiation to obtain an appropriate intensity of the hologram. Adding more voltage to the pixels in CCD causes the pixels to

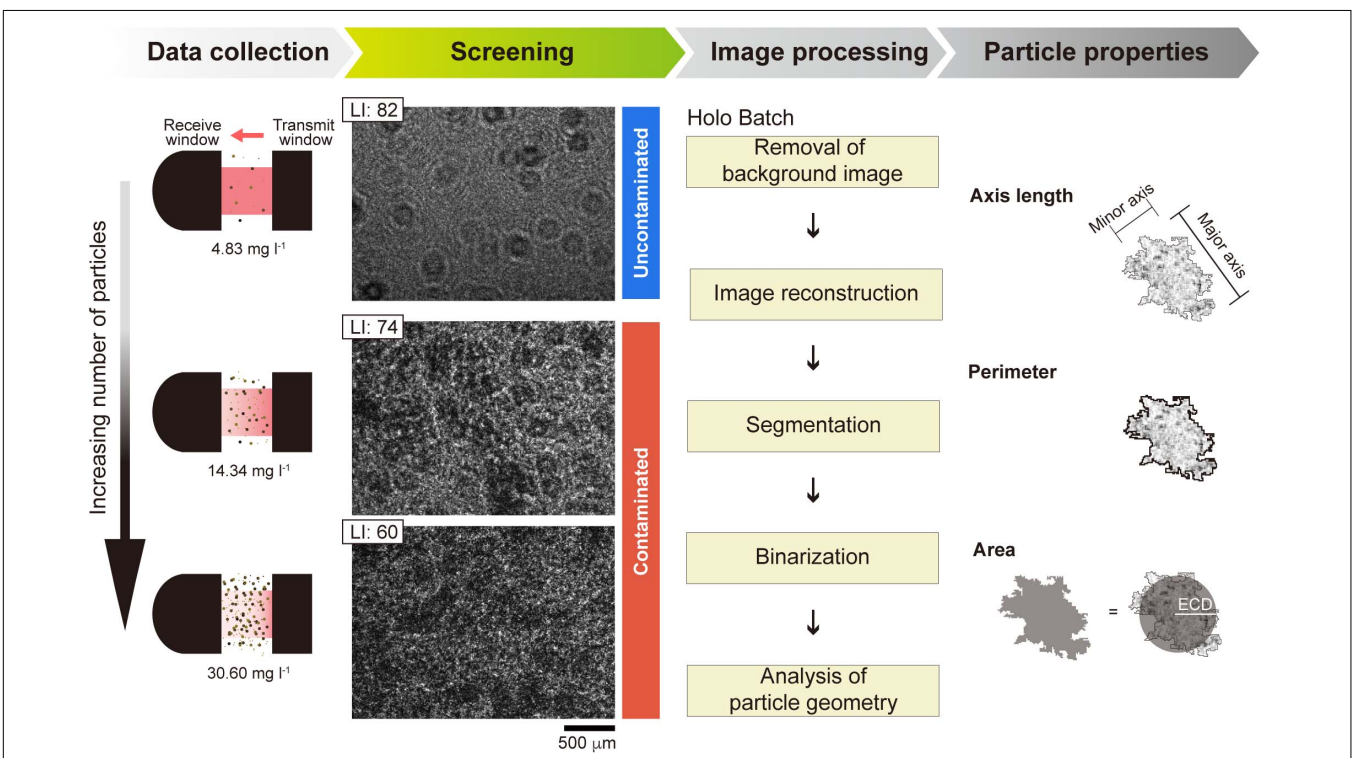

FIGURE 2 | Conceptual flow chart for hologram image analysis (modified after Many et al., 2019). Light intensity (LI) normalized on a gray scale of 0 (black) to 255 (white) can be a reliable criterion for defining the contamination boundary. The holograms follow sequential steps to generate the Euclidean geometry of particles such as axis length, perimeter, area, and equivalent circular diameter (ECD).

amplify the intensity, and thus brighten the hologram image. Higher-voltage pixels can also determine the light reflection and intensity of acquired images in the ranges of 0–255 (for brightness) and 56–739 (for gain) but cannot determine the brightness when measuring the image.

These parameters are balanced to best capture clear images, and the properties of suspended particles on the hologram are saved in the format of a portable gray map (file extension name: PGM). The interference patterns of the particles are displayed as concentric rings in a rectangular image (1,600 × 1,200 pixels) with a gray scale from 0 (black) to 255 (white). The concentric rings contain information about the phase and amplitude of the diffracted wave, representing characteristics such as size and position of suspended particles, so that their shapes and intensities are all different (Graham and Nimmo-Smith, 2010; Katz and Sheng, 2010; Davies et al., 2015). The intensities of them decrease (dark) or increase (bright), depending on the size, shape, and distance from the CCD of suspended particles within the sample volume. Each concentric ring with several fringes on the hologram generally had a peak of intensity at the center, and the intensity decayed with distance from the center of the concentric ring (Katz and Sheng, 2010). The light intensity (LI) refers to the average of all intensities in a hologram, which represents the degree of darkness or brightness of the hologram.

The hologram analysis followed the workflow from data collection to the extraction of particle properties (**Figure 2**). A digital hologram was created on a 7 mm × 5 mm-sized CCD by a collimated beam (659-nm solid state diode laser) being scattered when passed through a water sample with particles. The interference between the collimated and scattered lasers is usually visually represented as a pattern of concentric rings on the hologram. Such patterns with different fringe spacings contain unique information of the phase and amplitude to deduce the size and position of suspended particles (Graham and Nimmo-Smith, 2010). The interference patterns on the hologram were reconstructed using Holo Batch® software (Sequoia Inc.) (Owen and Zozulya, 2000; Graham and Nimmo-Smith, 2010; Choi et al., 2018; Giering et al., 2020). The noise and stationary particles on the image were removed by reapplying the collimated beam to the hologram. This creates a virtual image of the object positions behind the hologram (Graham and Nimmo-Smith, 2010). Segmentation was then applied to derive the particle parameters of interest. The particles located within a three-dimensional volume along the path length (typically 3–50 mm, 10 mm in this study) are shown as in-focus monochrome (binary) images with a high pixel resolution (1 pixel = 4.4 μm × 4.4 μm). Using image analysis, Euclidian and fractal geometry parameters for each binarized particle were determined as follows: perimeter (P), area (A), major (a), and minor (b) axis lengths (Olson, 2011; Choi et al., 2018; Many et al., 2019), where P is the total length surrounding the projected particle area, A is the extent converted from pixels occupied by the projected two-dimensional area of the particle, a is the axis passing through the center of the particle corresponding to the minimum rotational energy of the shape, and b is the perpendicular axis to a (Olson, 2011).

RESULTS AND DISCUSSION

Light Intensity as a Practical Criterion

In image processing for extracting particle properties, the evaluation of whether a hologram is contaminated is relatively subjective; further, the definition of the criterion for determining the contamination is not clear. This is because hologram contamination is primarily related to out-of-range SSC (i.e., SSC lower than the lower limit or higher than the upper limit of the instrument) during LISST-Holo measurements (Zhao et al., 2018). A critical SSC that generates mosaic patterns on a hologram depends on the particle size and beam attenuation with path length, as follows (Agrawal et al., 2008):

$$c = -\ln t/L \quad (1)$$

$$SSC = c \times d_{50}/1.13 \quad (2)$$

where c is the beam attenuation coefficient (m^{-1}), t is the optical transmission (0.8), and L is the path length (m). The maximum SSC, in which the LISST-Holo captures a hologram with identifiable concentric rings, has a wide range from 8 to 16,456 mg l^{-1} (**Table 2**; Sequoia, 2014). Because finer particles increase the beam scattering, the measurable range of SSC greatly

TABLE 2 | Maximum theoretical suspended sediment concentration (SSC) as a function of particle size and sample path length (L) of LISST-Holo.

Median particle diameter		Wentworth grades	*Maximum theoretical SSC (mg l^{-1})				
μm	phi		L = 50	L = 25	L = 10	L = 5	L = 3
2	9	Clay	8	15	39	77	128
3.9	8	Very Fine Silt	15	31	77	154	257
7.8	7	Fine Silt	31	62	154	308	513
15.6	6	Medium Silt	62	123	308	616	1,027
31.3	5	Coarse Silt	123	247	617	1,234	2,057
62.5	4	Very Fine Sand	247	494	1,234	2,468	4,114
125	3	Fine Sand	494	987	2,468	4,937	8,228
250	2	Medium Sand	987	1,975	4,937	9,874	16,456

Calculated by Eqs 1 and 2.
The gray-shaded column indicates L used for this study.

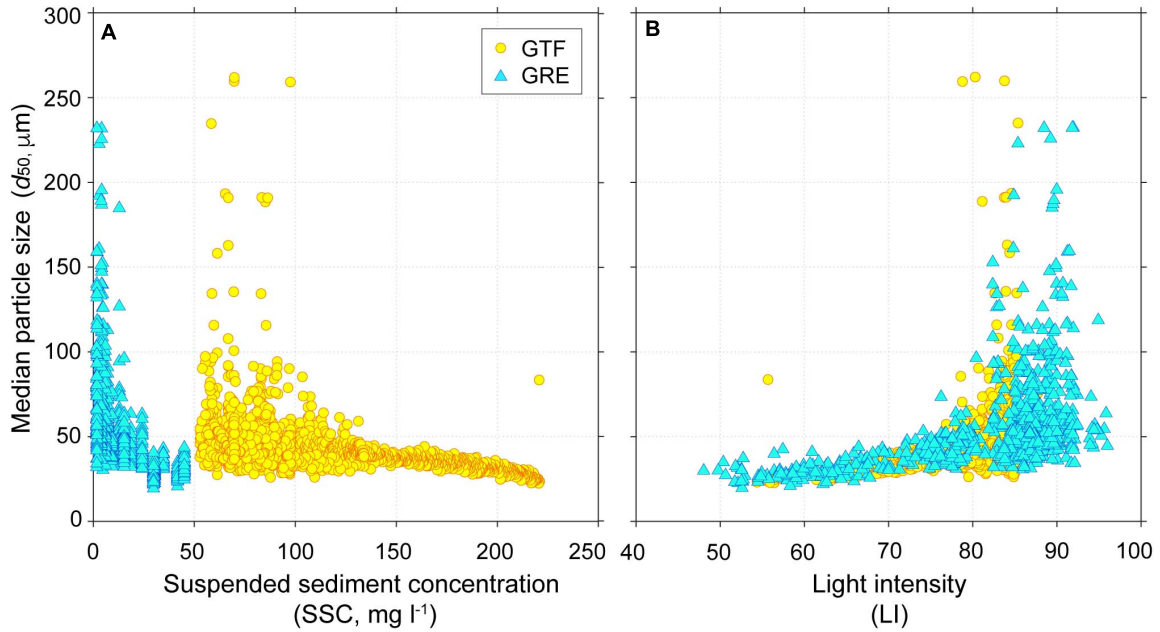

FIGURE 3 | Variations in median particle size (d_{50}) by **(A)** suspended sediment concentration (SSC) and **(B)** light intensity (LI).

decreases according to the reduced optical transmission (Agrawal et al., 2008). For the GTF and GRE, the identification of the concentric rings on the hologram distinctly varied depending on the SSC variability. Because the d_{50}'s of bed sediments at both sites were 17.5 (medium silt) and 30.7 μm (coarse silt), respectively, and L was fixed at 10 mm (see the shaded column in **Table 2**), the theoretical SSCs that the LISST-Holo would be able to measure were 308 and 617 mg l^{-1} for GTF and GRE, respectively (**Table 2**). Both theoretical values were high enough to cover *in situ* SSCs measured at GTF (53–221 mg l^{-1}) and GRE (2–45.3 mg l^{-1}) without any hologram contamination.

The LISST-Holo detected different sized particles ranging from 19.7 to 261.8 μm in GTF and GRE (**Figure 3A**). However, the distributions of d_{50} decreased logarithmically as SSC increased. The d_{50} eventually converged to approximately 30 μm above a specific SSC (GTF: 150 mg l^{-1}; GRE 30 mg l^{-1}). This made it appear as if only suspended sediments of uniform particle size existed in high-SSC conditions (see **Supplementary Figure 1** for laboratory results). Even though the SSCs for GTF and GRE did not exceed the maximum theoretical SSC (**Table 2**), the holograms at SSCs above 69.9 (GTF) and 14.3 mg l^{-1} (GRE) already included the mosaic patterns not suitable for image processing (see the holograms in **Figure 2**). This suggests that the actual upper limit of SSC may have differed from the maximum theoretical SSC because of the various local sediment properties (e.g., particle shape and composition) (Andrews et al., 2010; Graham et al., 2012). Such contradictory results between theoretical and actual conditions made it difficult to distinguish whether the hologram was contaminated. On the other hands, the LIs were similarly modulated in the range of 40–100, despite the difference in SSCs between GTF and GRE (**Figure 3B**). As the LI decreased (i.e., SSC increased), the d_{50} for GTF and GRE also decreased to converge toward approximately 30 μm (see **Supplementary Figure 1** for laboratory results). Unlike the maximum theoretical SSC that depends on local sediment characteristics, the LI allowed quantitative comparison of the overlapping degree of the concentric rings. The LI represents how intense (or dark) the gray shade of concentric rings is on a gray scale (Nakadate, 1986). Whether the hologram is contaminated is determined by the distinguishability of its interference patterns (concentric rings). In low-SSC conditions, for instance, concentric rings separated by certain distance from others can be identified. As the SSC increased, the overlap of bright and dark areas between the concentric rings limited the separation of the individual rings. This turned the hologram into a dark mosaic plane, which was a hindrance to detect particles with high accuracy (Murata and Yasuda, 2000).

Particle Properties Distorted by Contaminated Holograms

Many concentric rings with different fringe spacings were produced on the holograms at the GTF and GRE. Following the procedure presented in **Figure 2**, each hologram including spatially incoherent particles within a sample volume was reconstructed at in-focused planes with an interval of 0.5 mm. The montage of the particles from the planes was visualized in the reconstructed image (file extension name: tiff) (**Figure 4**). For the GTF and GRE, the number of particles counted in the reconstructed images was in the range of 0–1,800 (**Figure 5**). In uncontaminated holograms with LI > 80, particles of less than 1,000 were reconstructed. As the LI decreased from 80 to 70, however, the number of particles with small A of 199.4–386.7 μm^2 abruptly increased, as shown in **Figure 4**. Their

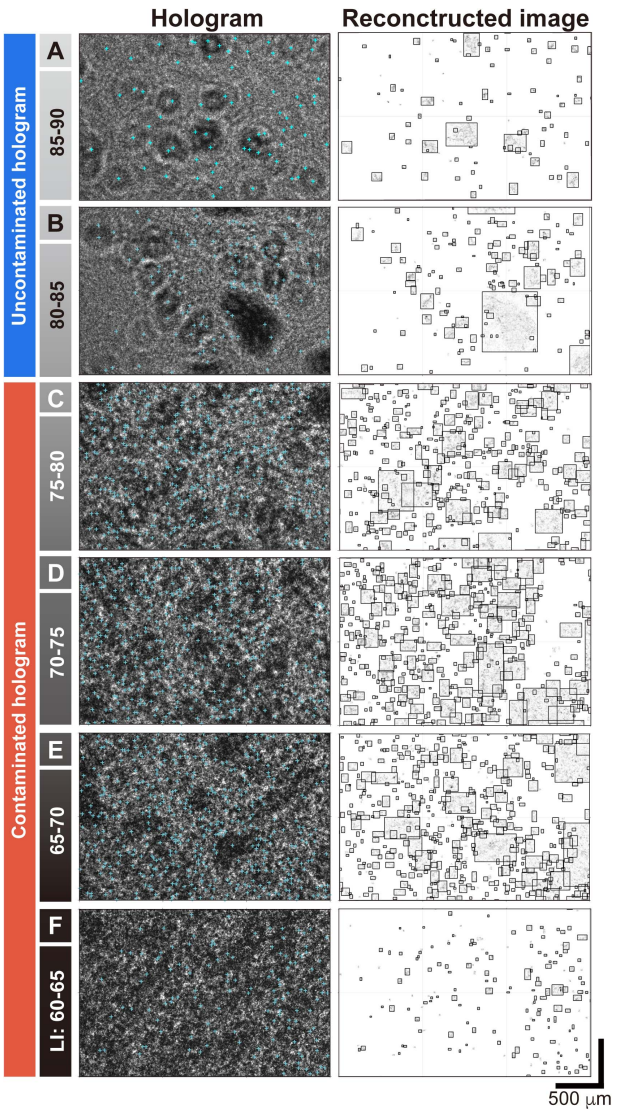

FIGURE 4 | Representative holograms (left) and montages of reconstructed images (right) with different LIs. Cyan crosses on the hologram denote the centroids of particle area. Black bounding boxes on the reconstructed images exhibit the smallest area containing individual particles. Based on the LI, the holograms can be classified into uncontaminated [concentric rings, **(A,B)**] and contaminated [mosaic patterns, **(C–F)**].

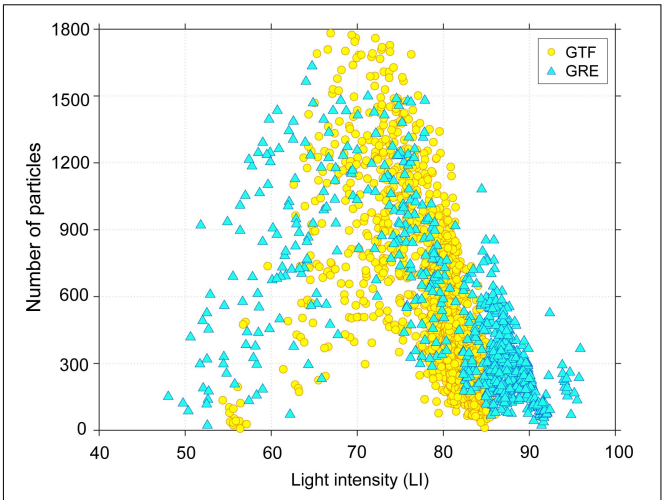

FIGURE 5 | Changes in the number of particles under the various LI conditions.

number, consequently, had reached up to 1,800 at LI = 70 with increasing SSCs to 191.7 (GTF) and 45.3 mg l^{-1} (GRE). While LI decreased from 70 to 40, the number of particles approached nearly zero, even though the SSCs still increased. Considering the mosaic pattern on holograms with LI < 80 (**Figures 4C–F**), an abnormally large number of particles was derived from contamination. This is because the excessive number of suspended particles in the sample volume caused the concentric rings to overlap with each other (Brunnhofer et al., 2020). Therefore, the possibility of false extraction of particle properties on the reconstructed image was enhanced, resulting in increasing the number of small particles.

For GTF and GRE, the particle size distribution (PSD) extracted from the contaminated hologram (LI < 80) had a positive skewness with d_{50} of 30 μm (**Figures 6A,B**). The silt-sized particles lower than 64 μm accounted for approximately 96% (GTF) and 93% (GRE). As LI increased, the shape of the PSD shifted from a positively skewed (d_{50} = 30 μm) to a normal distribution (d_{50} = 56 μm). When LI was higher than 80, for GTF and GRE, the population of particles less than 64 μm decreased to account for approximately 61% and 46%, respectively, and the d_{50} increased to 48.2 and 63.3 μm, respectively (see **Supplementary Figure 2** for laboratory results). Moreover, the particle shapes (e.g., *A* and *P*) visualized in the reconstructed image were distorted (**Figure 6C**). Such particle shapes are usually represented as a combination of monochrome pixels in the reconstructed image. Furthermore, it was found that fine particles developed into irregularly shaped particles through flocculation. The cross-section of the particles had an uneven arrangement of pixels within *A* in the range of 279–1,305.1 μm^2. Depending on the local properties of bed sediments, the *P* of GRE was approximately 1.47 times higher than that of GTF in the equivalent particle area, because of the elongated or irregular shape by more flocculation. The *A* at GTF and GRE was greatly reduced to 423.2 and 400.8 μm^2, respectively, owing to the generation of 30 μm-sized distorted particles as the LI decreased. Meanwhile, *P* was slightly higher (approximately 10 μm) compared to the particles of equivalent *A* on uncontaminated holograms, leading to an increase in particle irregularity.

Implications for Cohesive Sediment Transport

Contaminated holograms with distorted properties should be screened to derive accurate particle properties. In general, the three-dimensional structures of flocs expressed as a shape factor (e.g., *A* and *P*) of particles are irregular because of the repetitive flocculation and breakage (Jarvis et al., 2005; Maggi, 2013). In

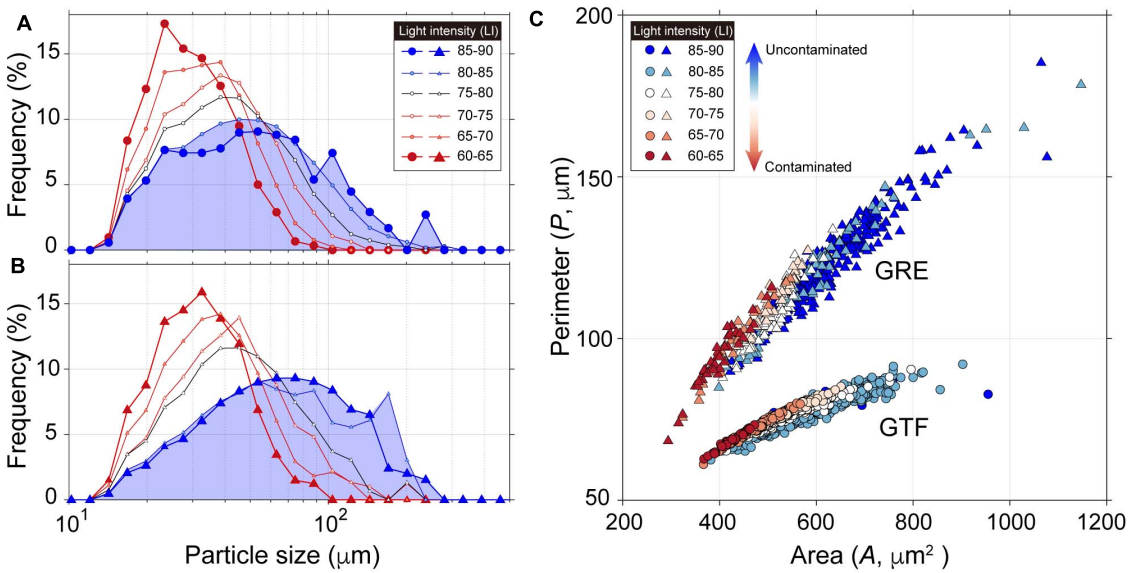

FIGURE 6 | Particle size distribution (PSD) at **(A)** GTF (circles) and **(B)** GRE (triangles) under various LI conditions. **(C)** Relationship between perimeter and area of particles. Note that the PSD shifted from the positively skewed to normal distribution (blue shaded area for LI: 80–90), as the LI increased. The particles with smaller area and longer perimeters were mostly measured from the contaminated holograms.

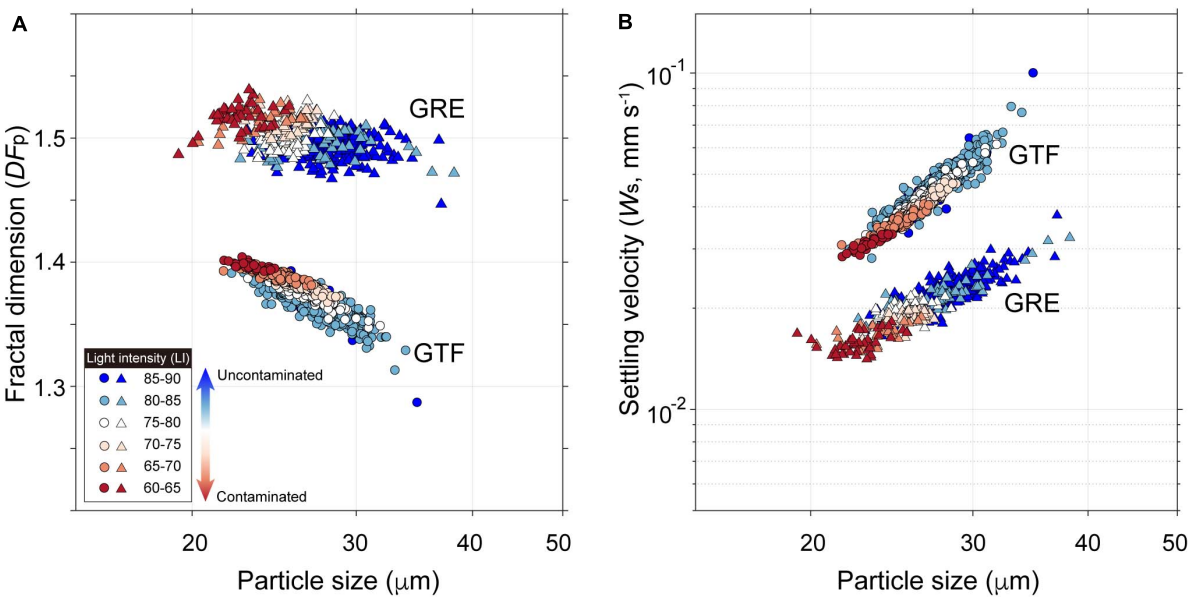

FIGURE 7 | (A) Perimeter-based fractal dimension (DF_p) and **(B)** settling velocity (W_s) determined by the particle size. Note that the W_s derived from the contaminated holograms was lower than that from the uncontaminated.

sediment dynamics, the shape factor is essential to determine the irregularity and settling velocity (W_s) of particles using the following equations (Maggi, 2007):

$$DF_p = 2\frac{\log(P)}{\log(A)} \quad (3)$$

$$DF_{3D} = -1.63DF_p + 4.6 \quad (4)$$

$$W_s = \frac{a}{18b}\frac{(\rho_p - \rho_w)\,g}{\mu} d_p^{3-DF_{3D}} \frac{d_f^{DF_{3D}-1}}{1 + 0.15R^{0.687}} \quad (5)$$

where the perimeter-based fractal dimension (DF_p), modulated in the range of 1 (sphericity) to 2 (irregularity), is derived based on the relationship between A and P of individual flocs under the assumption of $A = P^{2/DFp}$ (Maggi and Winterwerp, 2004). In Eq. 4, three-dimensional fractal dimension (DF_{3D}) is calculated

in the range of 1.34 (irregularity) to 2.97 (sphericity) according to the DF_p (Lee and Kramer, 2004; Many et al., 2019). The ratio of a and b indicates the eccentricity of particles, ρ_p denotes the density of the primary particle (2,650 kg m^{-3}), μ is the dynamic viscosity of seawater (1.08×10^{-3} Pa s), g is the gravitational acceleration (9.81 m s^{-2}), d_p is the primary particle diameter (1 μm), d_f is the floc diameter (μm), and R is the floc Reynolds number [$R = W_s \times d_f/\nu$, where ν is the kinematic viscosity of seawater (1.05×10^{-6} m^{-2} s^{-1})] (Winterwerp, 1998).

The DF_p was distributed in the range of 1.28–1.41 (GTF) and 1.45–1.54 (GRE) (**Figure 7A**). As the particle size and LI decreased, DF_p gradually increased. The DF_p derived from contaminated holograms was overestimated by up to 2% compared to that from uncontaminated holograms (see **Supplementary Figure 3** for laboratory results). Because the irregular shape of flocs resulted from flocculation, the distorted particles appeared to be highly flocculated compared to normal particles. This can be further extended to the subsequent determination of W_s which is essential to predict settling flux of fine sediments (**Figure 7B**). The irregularity of the floc shape normally contributes to the drag force on the flow through the suspended particles (Dietrich, 1982; Vahedi and Gorczyca, 2011; Maggi, 2013). Compared to flocs with circular shapes, flocs with irregular shapes have a lower W_s (Droppo et al., 2005). As the distortion of floc size and shape for GTF and GRE was enhanced, W_s decreased by approximately 0.01–0.04 mm s^{-1} (**Figure 7B**; see the **Supplementary Figure 3** for laboratory results). This was an underestimation of W_s since the increase of SSC as a concomitant of the strong current velocities contaminated holograms. However, it could be misunderstood as the flocs being broken into smaller flocs or primary particles with lower W_s by the strong current velocities (Winterwerp et al., 2006). The contaminated holograms, therefore, should be properly screened using our proposed method to prevent confusion.

Limitations

The practical method proposed in this study can be applied before performing image processing in the workflow (see **Figure 2**). This work reduces the labor and time required to determine whether a hologram is contaminated. Using LI, nonetheless, itself has inherent uncertainties. The LI could increase, for example, if suspended particles within the sample volume move faster than the recommended speed (up to 0.5 m s^{-1}) (Sequoia, 2014). Assuming that the particle moving velocity is close to the current velocity, a drastic increase in current velocity caused by natural forcing or artificial disturbances would lead to concentric rings of particles to be stretched. Such rings would appear as long bright lines along the trajectory of the particles, which could eventually increase the LI of the hologram.

The LI screening method is optimized for a high-SSC environment where frequent resuspension of cohesive sediments is observed. In offshore areas (e.g., Ha et al., 2015; Many et al., 2019), where the sediment supply is significantly limited, the possibility of hologram contamination caused by the overlapping concentric rings would be considerably low. In this case, the criterion of LI to screen the contamination might be higher than that proposed in this study. Therefore, the screening method requires additional post-processing (filtering and segmentation) suitable for each environment to extract the accurate particle information.

CONCLUSION

A practical method was proposed to screen holograms contaminated by overlapping interference patterns. The distorted particle properties of contaminated holograms were quantitatively estimated. The conclusions drawn from this study can be summarized as follows.

(1) The LI, which can be normalized on a gray scale of 0 (black) to 255 (white), is a reliable criterion for determining the contamination of holograms on the basis of the overlapping degree of concentric rings.
(2) Based on LI as a contamination boundary, the holograms were classified into contaminated images (LI < *ca.* 80) with mosaic patterns and uncontaminated images (LI > *ca.* 80) with identifiable concentric rings.
(3) The shape of the PSD shifted from a positively skewed to a normal distribution as the LI increased from the contaminated to uncontaminated holograms.
(4) Owing to the distortion of particle properties, the settling velocities derived from the contaminated holograms with mosaic patterns were underestimated compared to those derived from the uncontaminated holograms. Therefore, by screening the contamination, the proposed method can contribute to a more accurate estimation of the transport and behavior of cohesive sediments in shallow estuarine environments.

DATA AVAILABILITY STATEMENT

The raw data supporting the conclusions of this article will be made available by the authors, without undue reservation.

AUTHOR CONTRIBUTIONS

SC and JS conceived and designed the project, participated in data collection and processing, and wrote manuscript with contribution from all authors. GL and XS reviewed the manuscript. HH conceived and supervised the project and reviewed the manuscript. All authors contributed to the article and approved the submitted version.

FUNDING

The authors would like to acknowledge the funding support from the International Cooperation Program managed by the National Research Foundation of Korea (2020K2A9A2A06036472,

FY2020), and the National Natural Science Foundation of China (51909068 and 52011540388). It was also supported by the project entitled "Development of Advanced Science and Technology for Marine Environmental Impact Assessment" (20210427), funded by the Ministry of Oceans and Fisheries of Korea (MOF).

SUPPLEMENTARY MATERIAL

The Supplementary Material for this article can be found online at: https://www.frontiersin.org/articles/10.3389/fmars.2021.695510/full#supplementary-material

REFERENCES

Agrawal, Y. C., Whitmire, A., Mikkelsen, O. A., and Pottsmith, H. C. (2008). Light scattering by random shaped particles and consequences on measuring suspended sediments by laser diffraction. *J. Geophys. Res. Oceans* 113:C04023. doi: 10.1029/2007JC004403

Andrews, S., Nover, D., and Schladow, S. G. (2010). Using laser diffraction data to obtain accurate particle size distributions: the role of particle composition. *Limnol. Oceanogr. Methods* 8, 507–526. doi: 10.4319/lom.2010.8.507

Brunnhofer, G., Hinterleitner, I., Bergmann, A., and Kraft, M. (2020). A comparison of different counting methods for a holographic particle counter: designs, validations and results. *Sensors* 20:3006. doi: 10.3390/s20103006

Choi, S. M., Seo, J. Y., Ha, H. K., and Lee, G. H. (2018). Estimating effective density of cohesive sediment using shape factors from holographic images. *Estuar. Coast. Shelf Sci.* 215, 144–151. doi: 10.1016/j.ecss.2018.10.008

Davies, E. J., Buscombe, D., Graham, G. W., and Nimmo-Smith, W. A. M. (2015). Evaluating unsupervised methods to size and classify suspended particles using digital in-line holography. *J. Atmos. Oceanic Technol.* 32, 1241–1256. doi: 10.1175/JTECH-D-14-00157.1

Davies-Colley, R. J., Ballantine, D. J., Elliott, S. H., Swales, A., Hughes, A. O., and Gall, M. P. (2014). Light attenuation-a more effective basis for the management of fine suspended sediment than mass concentration? *Water Sci. Technol.* 69, 1867–1874. doi: 10.2166/wst.2014.096

Dietrich, W. E. (1982). Settling velocity of natural particles. *Water Res. Res.* 18, 1615–1626. doi: 10.1029/WR018i006p01615

Droppo, I. G., Nackaerts, K., Walling, D. E., and Williams, N. (2005). Can flocs and water stable soil aggregates be differentiated within fluvial systems? *Catena* 60, 1–18. doi: 10.1016/j.catena.2004.11.002

Figueroa, S. M., Lee, G. H., and Shin, H. J. (2019). The effect of periodic stratification on floc size distribution and its tidal and vertical variability: Geum Estuary, South Korea. *Mar. Geol.* 412, 187–198. doi: 10.1016/j.margeo.2019.03.009

Figueroa, S. M., Lee, G. H., and Shin, H. J. (2020). Effects of an estuarine dam on sediment flux mechanisms in a shallow, macrotidal estuary. *Estuar. Coast. Shelf Sci.* 238:106718. doi: 10.1016/j.ecss.2020.106718

Gabor, D. (1948). A new microscopic principle. *Nature* 161, 777–778. doi: 10.1038/161777a0

Giering, S. L., Hosking, B., Briggs, N., and Iversen, M. H. (2020). The interpretation of particle size, shape, and carbon flux of marine particle images is strongly affected by the choice of particle detection algorithm. *Front. Mar. Sci.* 7:564. doi: 10.3389/fmars.2020.00564

Graham, G. W., Davies, E. J., Nimmo-Smith, W. A. M., Bowers, D. G., and Braithwaite, K. M. (2012). Interpreting LISST-100X measurements of particles with complex shape using digital in-line holography. *J. Geophys. Res. Oceans* 117:C05034. doi: 10.1029/2011JC007613

Graham, G. W., and Nimmo-Smith, W. A. M. (2010). The application of holography to the analysis of size and settling velocity of suspended cohesive sediments. *Limnol. Oceanogr. Methods* 8, 1–15. doi: 10.4319/lom.2010.8.1

Ha, H. K., Kim, Y. H., Lee, H. J., Hwang, B., and Joo, H. M. (2015). Under-ice measurements of suspended particulate matters using ADCP and LISST-Holo. *Ocean Sci. J.* 50, 97–108. doi: 10.1007/s12601-015-0008-2

Jarvis, P., Jefferson, B., and Parsons, S. A. (2005). Measuring floc structural characteristics. *Rev. Environ. Sci. Biotechnol.* 4, 1–18. doi: 10.1007/s11157-005-7092-1

Katz, J., and Sheng, J. (2010). Applications of holography in fluid mechanics and particle dynamics. *Annu. Rev. Fluid Mech.* 42, 531–555. doi: 10.1146/ANNUREV-FLUID-121108-145508

Kim, T. I., Choi, B. H., and Lee, S. W. (2006). Hydrodynamics and sedimentation induced by large-scale coastal developments in the Keum River Estuary, Korea. *Estuar. Coast. Shelf Sci.* 68, 515–528. doi: 10.1016/j.ecss.2006.03.003

Lee, C., and Kramer, T. A. (2004). Prediction of three-dimensional fractal dimensions using the two-dimensional properties of fractal aggregates. *Adv. Colloid Interface Sci.* 112, 49–57. doi: 10.1016/j.cis.2004.07.001

Maggi, F. (2007). Variable fractal dimension: a major control for floc structure and flocculation kinematics of suspended cohesive sediment. *J. Geophys. Res. Oceans* 112:C07012. doi: 10.1029/2006JC003951

Maggi, F. (2013). The settling velocity of mineral, biomineral, and biological particles and aggregates in water. *J. Geophys. Res. Oceans* 118, 2118–2132. doi: 10.1002/jgrc.20086

Maggi, F., and Winterwerp, J. C. (2004). Method for computing the three-dimensional capacity dimension from two-dimensional projections of fractal aggregates. *Phys. Rev. E Stat. Nonlin. Soft. Matter Phys.* 69(Pt 1):011405. doi: 10.1103/PhysRevE.69.011405

Many, G., de Madron, X. D., Verney, R., Bourin, F., Renosh, P. R., Jourdin, F., et al. (2019). Geometry, fractal dimension and settling velocity of flocs during flooding conditions in the Rhônee ROFI. *Estuar. Coast. Shelf Sci.* 219, 1–13. doi: 10.1016/j.ecss.2019.01.017

Merten, G. H., Capel, P. D., and Minella, J. P. (2014). Effects of suspended sediment concentration and grain size on three optical turbidity sensors. *J. Soils Sedim.* 14, 1235–1241. doi: 10.1007/s11368-013-0813-0

Mills, G. A., and Yamaguchi, I. (2005). Effects of quantization in phase-shifting digital holography. *Appl. Opt.* 44, 1216–1225. doi: 10.1364/AO.44.001216

Ministry of Oceans and Fisheries (2019). *Investigation of Hydrodynamic Variability in Geum River estuary. Final Report*. Sejong-si: Ministry of Oceans and Fisheries, 700.

Murata, S., and Yasuda, N. (2000). Potential of digital holography in particle measurement. *Opt. Laser Technol.* 32, 567–574. doi: 10.1016/S0030-3992(00)00088-8

Nakadate, S. (1986). Vibration measurement using phase-shifting time-average holographic interferometry. *Appl. Opt.* 25, 4155–4161. doi: 10.1364/AO.25.004155

Nayak, A. R., Malkiel, E., McFarland, M. N., Twardowski, M. S., and Sullivan, J. M. (2021). A review of holography in the aquatic sciences: in situ characterization of particles, plankton, and small scale biophysical interactions. *Front. Mar. Sci.* 7:1256. doi: 10.3389/fmars.2020.572147

Nayak, A. R., McFarland, M. N., Twardowski, M. S., Sullivan, J. M., Moore, T. S., and Dalgleish, F. R. (2019). "Using digital holography to characterize thin layers and harmful algal blooms in aquatic environments," in *Proceedings of the Digital Holography and Three-Dimensional Imaging*, (Bordeaux: Optical Society of America). doi: 10.1364/DH.2019.Th4A.4

Olson, E. (2011). Particle shape factors and their use in image analysis-Part 1: theory. *J. GXP Compl.* 15:85.

Owen, R. B., and Zozulya, A. A. (2000). In-line digital holographic sensor for monitoring and characterizing marine particulates. *Opt. Eng.* 39, 2187–2197. doi: 10.1117/1.1305542

Sequoia (2014). *LISST-HOLO User's Guide*. Bellevue, WA: Sequoia Scientific Inc, 73.

Sun, H., Dong, H., Player, M. A., Watson, J., Paterson, D. M., and Perkins, R. (2002). In-line digital video holography for the study of erosion processes in sediments. *Meas. Sci. Technol.* 13, L7–L12. doi: 10.1088/0957-0233/13/10/101

Vahedi, A., and Gorczyca, B. (2011). Application of fractal dimensions to study the structure of flocs formed in lime softening process. *Water Res.* 45, 545–556. doi: 10.1016/j.watres.2010.09.014

Winterwerp, J. C. (1998). A simple model for turbulence induced flocculation of cohesive sediment. *J. Hydraul. Res.* 36, 309–326. doi: 10.1080/00221689809498621

Winterwerp, J. C., Manning, A. J., Martens, C., De Mulder, T., and Vanlede, J. (2006). A heuristic formula for turbulence-induced flocculation of cohesive sediment. *Estuar. Coast. Shelf Sci.* 68, 195–207. doi: 10.1016/j.ecss.2006.02.003

Woo, H. J., and Je, J. G. (2002). Changes of sedimentary environments in the southern tidal flat of Kanghwa island (Korean ed.). *Ocean Polar Res.* 24, 331–343. doi: 10.4217/OPR.2002.24.4.331

Zhao, L., Boufadel, M. C., King, T., Robinson, B., Conmy, R., and Lee, K. (2018). Impact of particle concentration and out-of-range sizes on the measurements of the LISST. *Meas. Sci. Technol.* 29:055302. doi: 10.1088/1361-6501/aab83d

Conflict of Interest: The authors declare that the research was conducted in the absence of any commercial or financial relationships that could be construed as a potential conflict of interest.

frontiers in Marine Science

ORIGINAL RESEARCH
published: 13 July 2021
doi: 10.3389/fmars.2021.698102

Exploring Ocean Biogeochemistry Using a Lab-on-Chip Phosphate Analyser on an Underwater Glider

Antony J. Birchill[1,2], A. D. Beaton[2]*, Tom Hull[3], Jan Kaiser[3], Matt Mowlem[2], R. Pascal[2], A. Schaap[2], Yoana G. Voynova[4], C. Williams[5] and M. Palmer[5]*

[1] School of Geography Earth and Environmental Sciences, University of Plymouth, Plymouth, United Kingdom, [2] Ocean Technology and Engineering, National Oceanography Centre, Southampton, United Kingdom, [3] School of Environmental Sciences, University of East Anglia, Norwich, United Kingdom, [4] Institute of Coastal Ocean Dynamics, Helmholtz Zentrum Hereon, Geesthacht, Germany, [5] Marine Physics and Ocean Climate, National Oceanography Centre, Liverpool, United Kingdom

The ability to make measurements of phosphate (PO_4^{3-}) concentrations at temporal and spatial scales beyond those offered by shipboard observations offers new opportunities for investigations of the marine phosphorus cycle. We here report the first *in situ* PO_4^{3-} dataset from an underwater glider (Kongsberg Seaglider) equipped with a PO_4^{3-} Lab-on-Chip (LoC) analyser. Over 44 days, a 120 km transect was conducted in the northern North Sea during late summer (August and September). Surface depletion of PO_4^{3-} (<0.2 μM) was observed above a seasonal thermocline, with elevated, but variable concentrations within the bottom layer (0.30–0.65 μM). Part of the variability in the bottom layer is attributed to the regional circulation and across shelf exchange, with the highest PO_4^{3-} concentrations being associated with elevated salinities in northernmost regions, consistent with nutrient rich North Atlantic water intruding onto the shelf. Our study represents a significant step forward in autonomous underwater vehicle sensor capabilities and presents new capability to extend research into the marine phosphorous cycle and, when combined with other recent LoC developments, nutrient stoichiometry.

Keywords: Seaglider observations, phosphate, lab on a chip (LoC), North Sea, shelf sea biogeochemistry, autonomous and remotely operated underwater vehicle

OPEN ACCESS

Edited by:
Ole Mikkelsen, Sequoia Scientific, United States

Reviewed by:
Ellen Briggs, University of Hawai'i at Mānoa, United States
Yanhui Wang, Tianjin University, China

****Correspondence:***
Antony J. Birchill
antony.birchill@plymouth.ac.uk
A. D. Beaton
a.beaton@noc.ac.uk

Specialty section:
This article was submitted to Ocean Observation, a section of the journal Frontiers in Marine Science

Received: *20 April 2021*
Accepted: *07 June 2021*
Published: *13 July 2021*

Citation:
Birchill AJ, Beaton AD, Hull T, Kaiser J, Mowlem M, Pascal R, Schaap A, Voynova YG, Williams C and Palmer M (2021) Exploring Ocean Biogeochemistry Using a Lab-on-Chip Phosphate Analyser on an Underwater Glider. Front. Mar. Sci. 8:698102. doi: 10.3389/fmars.2021.698102

INTRODUCTION

The ocean phosphorus biogeochemical cycle is intrinsically linked with the cycles of carbon, oxygen, nitrogen, sulfur, silicon, and trace metals (Moore et al., 2013; Karl, 2014). The temporal scales of the processes acting upon the ocean phosphorus cycle range from hours to weeks (e.g., gene expression and microbial growth), months to decades (e.g., biological carbon pump and ocean circulation), and hundreds of years to millennia (e.g., tectonics and sedimentation) (Moore et al., 2013; Karl, 2014). Therefore, in order to understand and quantify the processes acting upon the ocean phosphorus cycle, oceanographers must make accurate and precise measurements over a range of temporal and spatial scales.

In oceanographic studies, the most commonly measured chemical form of phosphorus is phosphate (PO_4^{3-}). PO_4^{3-} concentrations are traditionally determined following manual

sampling of seawater; water is collected at known times and depths, filtered (0.20 or 0.45 μm), and then preserved for laboratory analysis on board ships or on land (Jońca et al., 2013). There are numerous sample preservation approaches available for nutrient analysis; these include filtration, heating, pasteurisation, refrigeration, freezing and chemical poisoning, with diverse recommendations found in the literature (Clementson and Wayte, 1992; Dore et al., 1996; Aminot and Kérouel, 1997; Kattner, 1999; Gardolinski et al., 2001). Consequently, selecting an appropriate preservation method is non-trivial, and has been shown to be dependent upon the physico-chemical properties of the sample (e.g., salinity, calcium content, organic matter content) (Burton, 1973; Gardolinski et al., 2001). The most common method for measuring PO_4^{3-} is coupling the phosphomolybdenum blue (PMB) spectrophotometric assay with a gas-segmented continuous-flow analyser (Murphy and Riley, 1962; Hydes et al., 2010; Worsfold et al., 2016).

In situ techniques enhance the spatial and temporal resolution and coverage, providing marine chemists with a more detailed insight into biogeochemical cycling, and enhance monitoring capabilities (Daniel et al., 2020). Additionally, *in situ* techniques remove the need for sample preservation (Nightingale et al., 2015), which is a considerable advantage. Several attempts have been made to develop *in situ* systems capable of measuring PO_4^{3-} in natural waters using compact flow injection manifolds and microfluidic Lab-on-Chip (LoC) analysers (Lyddy-Meaney et al., 2002; Thouron et al., 2003; Adornato et al., 2007; Slater et al., 2010; Legiret et al., 2013; Clinton-Bailey et al., 2017; Grand et al., 2017) and electrochemical techniques (Jońca et al., 2011; Barus et al., 2016). Flow injection systems utilising miniaturised peristaltic pumps may suffer from drifting flow rates as tubing wears out and mechanical parts fail during prolonged usage. These systems require relatively large power sources, limiting them either to short deployments or deployments at locations with an external power supply (Nightingale et al., 2015). Electrochemical PO_4^{3-} sensor prototypes under development have the potential to offer small, low power, and reagent free detection. However, current prototypes are not sufficiently developed for large scale use (Jońca et al., 2013; Daniel et al., 2020; Wei et al., 2021).

Microfluidic technology involves the miniaturisation of analytical methods, typically using channels with cross-sectional dimensions below 1 mm and low flow rates (μL/min to mL/min). Their characteristic low volumes reduce the consumption of reagents and generation of waste and require little power to actuate the movement of fluids. LoC nutrient analysers with power consumption below 2 W have been demonstrated (Cleary et al., 2010; Beaton et al., 2011, 2012; Clinton-Bailey et al., 2017; Grand et al., 2017). Currently the application of PO_4^{3-} measuring microfluidic technology has been largely restricted to fluvial, waste water or estuarine environments (Cleary et al., 2010; Cohen et al., 2013; Gilbert et al., 2013; Clinton-Bailey et al., 2017). Marine deployments have been reported on fixed moorings, underway ship pumped systems, and a YOYO profiler (Thouron et al., 2003; Legiret et al., 2013; Grand et al., 2017).

In this study, we integrate a microfluidic LoC PO_4^{3-} analyser into an underwater glider (Kongsberg Seaglider) to determine PO_4^{3-} concentrations in the northern North Sea as part of the AlterEco programme (*An alternative framework to assess marine ecosystem functioning in shelf seas, NERC reference NE/P013902/2*). The LoC analyser used in this study was developed at the National Oceanography Centre (NOC), United Kingdom (Clinton-Bailey et al., 2017; Grand et al., 2017). A comparison of the specifications of the NOC analyser and the commercially available Sea-Bird Scientific HydroCycle-PO_4 is presented in **Table 1**. A number of features make the NOC analyser ideal for integration with gliders or other autonomous underwater vehicles (AUVs); the relatively compact size and small waste generation require minimal payload space; its pressure compensating housing permits regular profiling over depth, down to 6,000 m; low power requirements provide

TABLE 1 | Comparison of Sea-Bird Scientific HydroCycle-PO4 commercially available analyser and the National Oceanographic Centre, Lab-on-Chip analyser (AUV integration set up specifications).

		Sea-Bird Scientific HydroCycle-PO4	National Oceanographic Centre Lab-on-Chip
Mechanical	Diameter (cm)	18	15
	Height (cm)	56	17
	Weight in air with reagents (kg)	6.8	6.5
	Operating temperature range (°C)	0–35	5–35
	Depth rating (m)	200	6,000
Electrical	Continuous sampling frequency (h^{-1})	2	5
	Input voltage (V DC)	10.5–18	12
	Average current draw (mA)	115	155
	Max current draw (mA)	3,000	390
	Data output	RS232/SDI-12	RS232/RS485
	Data memory (GB)	1	8
Optical	LED wavelength (nm)	870	700
	Path length (cm)	5	9.14[1], 3.44, 0.25
Analytical	Limit of detection (μM)	0.075[2]	0.030, 0.040[3]
	Limit of quantification (μM)	0.25	0.14
	Limit of linearity (μM)	9.68	10
	Precision (RSD%)	1.9[4]	1.8[4]
	Runs per reagent set	>1,500	3,600
	Demonstrated reagent life span (months)	5	2[5]
	Waste generation 720 samples, 180 in situ calibrations (L)	25.52	0.43

Specifications for Sea-Bird Scientific HydroCycle-PO4 accessed from HydroMet (2020).

[1]*Long (9.14 cm) path used in this study, limit of detection estimates made using this path length, limit of linearity and precision using short (0.25 cm) path.*

[2]*In ultra-high purity water (UHP) (>18.2 MΩ cm).*

[3]*In UHP water and low nutrient seawater.*

[4]*Precision demonstrated at concentration of 2.6 μM for Sea-Bird Scientific HydroCycle-PO4 and 2.5 μM for National Oceanographic Centre LoC.*

[5]*Demonstrated reagent longevity, likely longer.*

maximum endurance; high sampling frequency (5 samples per hour in the Seaglider configuration described here) allows for resolution of changes in nutrient concentrations occurring over small spatial scales, such as across a thermocline. The analytical figures of merit (accuracy, precision, limit of detection, and quantification) allow for the determination of PO_4^{3-} concentrations in all but the most oligotrophic regions of the ocean, and *in situ* results have been validated using water samplers and benchtop spectrophotometric reference methods (Grand et al., 2017). The combined (random and systematic uncertainty) measurement uncertainty associated with LoC PO_4^{3-} measurements from multiple LoC analysers was estimated to be 6.1% (u_c) (Birchill et al., 2019a).

To our knowledge, this study is the first report of *in situ* ocean PO_4^{3-} measurements conducted using an AUV. The potential for long term deployments make the LoC-glider approach appealing to both academic and marine management communities, enabling resolution of spatial and temporal scales that would be difficult and comparatively expensive to replicate using traditional shipboard studies (Liblik et al., 2016; Rudnick, 2016; Vincent et al., 2018). This manuscript provides a critical assessment of the first *in situ* PO_4^{3-} LoC–AUV deployment, considers potential future applications, and highlights development priorities.

MATERIALS AND METHODS

Phosphomolybdenum Blue Spectrophotometric Assay

The PMB spectrophotometric assay is often coupled with gas-segmented continuous-flow analysers to make PO_4^{3-} concentration measurements in oceanographic studies (Hydes et al., 2010; Worsfold et al., 2016). The PO_4^{3-} LoC analyser used in this study also utilises the PMB assay. The PMB reaction follows two steps; (1) the formation of a Keggin ion around the analyte anion, and (2) the reduction of this heteropoly acid to form a blue coloured product (Nagul et al., 2015) (Eqs 1, 2).

$$PO_4^{3-} + 12MoO_4^{2-} + 27H^+ \rightarrow H_3PO_4\,(MoO_3)_{12} + 12H_2O \quad (1)$$

$$H_3PO_4\left(Mo^{VI}O_3\right)_{12} + 4\,e^- + H^+ \rightarrow \left[H_4PMo_8^{VI}Mo_4^{V}O_{40}\right]^{3-} \quad (2)$$

The key parameters to consider when utilising this colourimetric reaction are the molybdate and acid concentrations and choice of acid and reductant. Measurements made using this approach are commonly reported as orthophosphate (PO_4^{3-}, which also includes HPO_4^{2-}, $H_2PO_4^-$, and H_3PO_4; the dominant form in seawater at pH = 8 is HPO_4^{2-}) measurements. However, it is well established that the PMB complex may also be formed with acid labile, molybdate reactive organic P species, condensed polyphosphates and colloidal P (Burton, 1973; Nagul et al., 2015; Worsfold et al., 2016), thus the fraction accessed is more accurately defined as "soluble (molybdate) reactive phosphorus." Magnesium coprecipitation allows for the isolation and concentration of inorganic P species prior to acidification. Detection following magnesium concentration therefore reduces the analytical interference caused by hydrolysis of organic P compounds. Application of the magnesium coprecipitation method to oligotrophic Pacific Ocean surface seawater consistently resulted in lower PO_4^{3-} concentrations (up to 50%) than concurrent analysis by traditional gas-segmented-continuous-flow techniques (Thomson-Bulldis and Karl, 1998). Consequently, a significant fraction of the apparent PO_4^{3-} signal observed in oligotrophic surface waters by result from P species other than PO_4^{3-}. Here, we refer to this operationally defined fraction as PO_4^{3-} to avoid confusion with the wider oceanographic literature.

Lab-on-Chip Analyser Description

The LoC PO_4^{3-} analyser used in this study was designed and fabricated at the National Oceanography Centre, United Kingdom (**Figure 1**). It is a slightly modified version (see section "Lab-on-Chip Analytical Cycle") of the sensor that is described by Grand et al. (2017) and Clinton-Bailey et al. (2017). A detailed technical description can be found in the supporting information. Briefly, the LoC analyser is composed of a three layer poly(methyl methacrylate) chip with precision milled microchannels, mixers, and optical components consisting of light emitting diodes and photodiodes, electronics, solenoid valves, and syringe pumps mounted on the chip. The chip forms the end cap of a dark watertight pressure compensating PVC housing, which is rated to 6,000 dbar. Previous studies using the same LoC analyser as in this study demonstrated good agreement between *in situ* values and traditional shipboard and laboratory measurement techniques, with a limit of detection (3σ of 10 blank measurements) of 0.04 μM and limit of quantification (10σ of 10 blank measurements) of 0.14 μM (Clinton-Bailey et al., 2017; Grand et al., 2017).

The system is automated using a 32 bit microcontroller-based electronics package with 18-bit analogue to digital inputs and can stream raw data (1 Hz) over USB, as well as store data on a 8 GB flash memory card. Provided with the values of the on-board standards, the LoC analyser is capable of outputting processed data (μM PO_4^{3-}) over RS232 or RS485 interfaces. Transmitting only the processed data (i.e., not the raw data) reduces the size of near-real time data files, lessening the transmission duration and cost for satellite communications during an AUV deployment. Raw data is stored on an internal flash memory card, providing backup and access upon recovery.

Lab-on-Chip Reagent Preparation and Storage

Ultra-high purity water (UHP; 18.2 MΩ cm) was used for artificial seawater (ASW) standards and reagents. All plastic and glassware used to prepare reagents and standards was cleaned in 10% hydrochloric acid for 24 h, rinsed with UHP water and dried before use. All working solutions, including waste, were stored in flexible bags (FlexBoy, Sartorius-Stedim) inside the Ogive faring of the Seaglider during deployment.

The reagent preparation followed the procedure detailed by Grand et al. (2017). Briefly, the molybdate reagent (reagent 1) was made up of ammonium heptamolybdate tetrahydrate

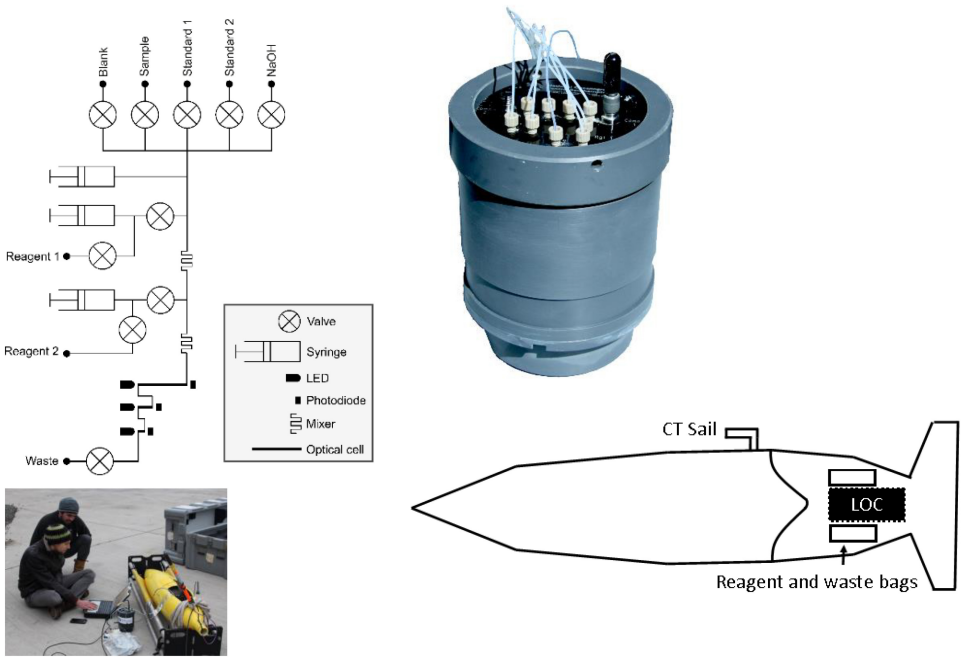

FIGURE 1 | Fluidic diagram of the phosphate Lab-on-Chip analyser, picture of integration into glider Ogive faring, schematic showing location of analyser and reagent bags with the Seaglider (not to scale) and a close-up picture of the Lab-on-Chip analyser in pressure compensating housing.

(0.45 mM), sulfuric acid (120 mM) and potassium antimonyl tartrate (0.06 mM). The reagent 1 storage bag was covered with opaque tape to prevent photodegradation of the chemicals before deployment inside the glider. The reducing reagent (reagent 2) was made up of L-ascorbic acid (0.057 M) and polyvinylpyrrolidone (0.1 g/L). The wash solution was made up of sodium hydroxide (NaOH; 0.01 M).

Blank and standard solutions were prepared in ASW to match the refractive index of seawater. ASW was prepared by dissolving sodium chloride (NaCl; 0.60 M; VWR, ACS reagent) and sodium bicarbonate ($NaHCO_3$; 0.006 M; Fisher, analytical grade reagent) in UHP water. To maintain PO_3^{4-} in solution whilst in the storage bags, blank, and standard solutions were acidified with sulfuric acid (H_2SO_4; 0.016 M; Fluka) (Clinton-Bailey et al., 2017). To prepare the standard solutions, a known amount of PO_4^{3-} was added. First, a 1 mM PO_4^{3-} stock was prepared by dissolving potassium phosphate monobasic salt (KH_2PO_4; 99+%, extra pure, Acros Organics) in UHP water. The salt had been dried at 105°C for >1 h and left to cool in a desiccator prior to use. The stock was stored in an opaque high-density polyethylene bottle. Standard solutions were made up volumetrically by addition of the PO_4^{3-} stock to acidified ASW. Upon recovery, subsamples of the blanks and standards, as well as a certified reference material, were analysed by a standard gas-segmented-flow spectrophotometric technique (QuAAtro, Seal Analytical); the results are displayed in **Table 2**.

Lab-on-Chip Analytical Cycle

The LoC analyser is a stop flow system whereby reagents and sample/blank/standard are delivered into the absorbance flow cell and then left to react and form colour. All solutions are mixed in a 1:1:1 volume ratio (reagent 1: reagent 2: blank/standard/sample). In this version of the LoC analyser, reagent 1 is added to the sample and these two fluids are mixed, prior to the addition of reagent 2. The flow of the mixed solution is stopped to react for 145 s, and the average reading of the long channel photodiodes during the next 5 s (145–150 s) was used to calculate absorbance (Clinton-Bailey et al., 2017; Grand et al., 2017). The LoC analyser was configured to begin an analytical cycle whenever powered on by the Seaglider. The LoC analyser ran through the following cycle each time it was powered on: (a) Blank, (b) Blank, (c) Standard 1, (d) Standard 2, (e) NaOH wash, (f) Sample, (g) NaOH wash, (h) Sample, (i) NaOH wash, and (j) Sample... until powered off. The first blank was treated as a conditioning sample and was not used in any subsequent computations. This analytical cycle meant that the analyser was

TABLE 2 | The concentration of blank and standard solutions determined by gas-segmented flow techniques upon recovery.

Solution (nominal or certified concentration, μM)	Concentration determined (μM)
Blank (0.00)	<0.01 (n = 2)
Standard 1 (0.50)	0.46 ± 0.04 (n = 2)
Standard 2 (1.00)	1.00 ± 0.01 (n = 2)
KANSO CD 1515 (0.46 ± 0.01)	0.46 ± 0.01 (n = 4, *1 S.D.*)

KANSO CD 1515 is a natural seawater certified reference material (http://www.kanso.co.jp/eng/index.html), the analysis of blank and standard solutions was bracketed with duplicate CRM analyses.

calibrated during the downcast of each dive, allowing the upcast to be used for continuous measurements. It took 23 min from the LoC analyser being powered on to the beginning of first sample measurement. Each sample measurement took 8 min. Calibration on each dive allowed compensation for any drift occurring during the deployment.

Raw voltages were converted to absorbance (A) using a modified Beer-Lambert-Bouguer law (Eq. 3; Grand et al., 2017):

$$A = -\log_{10}(V_S/V_{BLK} \times I_{BLK}/I_S) \quad (3)$$

The second blank (BLK) from each dive was used to calculate the absorbance of standards and samples (S). V_S and V_{BLK} are the mean voltages from the measurement photodiode of the standard or sample and blank during the 5 s measurement. I_{BLK} and I_S are the mean voltages of the monitoring photodiodes during this period, which measures LED output during the measurement state of blanks, standards, and samples. Thus I_{BLK}/I_S is a scaling factor used to correct for drift in LED intensity that may occur from the start of an analytical cycle (blank measurement) to the end (sample measurements).

Seaglider Salinity and Temperature Measurements, Lab-on-Chip Integration and Deployment Details

The LoC PO_4^{3-} analyser was integrated within the science bay of a Kongsberg Seaglider using an ogive fairing to provide required space. The Seaglider is an autonomous buoyancy driven underwater vehicle capable of deployments down to 1,000 m depth and range and endurance of 4,000 km and several months. Positive Buoyancy is managed by transferring oil from inside the pressure hull to an external bladder, increasing the displacement and causing it to rise though the water column. Removing oil from the bladder has the opposite effect and alternating this pumping cycle produces yo-yo profiling of the glider. Horizontal motion is generated through a combination of body drag and shifting ballast and small wings provide added stability of the platform (Eriksen and Perry, 2009; Meyer, 2016; Rudnick, 2016).

The range of LoC analysers available at NOC use common hardware and software, therefore the physical and electrical integration of the PO_4^{3-} LoC analyser into the Seaglider followed the procedure described by Vincent et al. (2018), which presents the first LoC glider deployment using a nitrate + nitrite LoC analyser. The sample inlet tube, located on the surface of the payload bay, was fitted with a 0.45 μm poly(ether-sulfone) luer lock syringe filter (MERCK, Millipore, United States). The LoC analyser received power from the Seaglider, and linked via a RS232 serial communication. The Seaglider software uses a CNF file that contains the configuration for each on-board instrument and a CMD file that provides mission parameters. The CNF file enables communication between the Seaglider and the LoC PO_4^{3-} analyser. The LoC PO_4^{3-} analyser is set to "logger" mode in the CNF file, which enables the glider to send a number of commands. These commands allow the Seaglider to send and receive data to and from the analyser. Commands include: "clock-set," used only at the start of each dive, but which enables the analyser to store any time offset between glider and analyser, "status," which sends the analyser depth every 5 s, and "download," sent at the end of each dive requesting the sensor to send both ascent and descent data files of processed PO_4^{3-} values. The sensor transmits only processed data, raw data are accessed upon recovery.

The mission was supported by the *MRV Scotia*, a Marine Scotland research vessel that managed glider deployment, while conducting a fisheries survey in the northern North Sea, approximately 170 km from the east coast of Scotland (**Figure 2A**). The Seaglider followed a prescribed south-east to north-west transect approximately 120 km in length, before being piloted to the south-west for recovery. The Seaglider conducted 1,555 dives from 15/08/2018 to 28/09/2018, with 71 dives including PO_4^{3-} measurements providing 353 individual PO_4^{3-} measurements. Bidirectional communication between the Seaglider and base station, through an Iridium satellite connection, allowed dive configurations to be modified once deployed and near-real time processed data to be viewed at the base station. The glider operated in two flight modes, "*standard*" and "*loiter*" following methods described by Vincent et al. (2018; **Figures 2B,C**). *Standard* flight mode adjusts pitch and buoyancy to maintain a uniform glide slope and speed during descent and ascent and was used to transit efficiently between deployment, waypoint and recovery locations. The short duration of profiles in *standard* flight mode allowed for a maximum of 2 PO_4^{3-} measurements per dive, and sometimes zero. A *loiter* flight mode was adopted to lengthen the duration of a dive by reducing the angle of ascent for 30 min following the Seaglider reaching its maximum dive depth. *Loiter* flight mode was used during high resolution PO_4^{3-} transects and increased sampling to 6 or 7 PO_4^{3-} measurements per ascending profile.

In addition to PO_4^{3-}, the Seaglider measured conductivity, temperature (non-pumped Sea-Bird CT Sail, Seabird Electronics) and pressure (Paine Electronics). The CT sail consists of separate (non-ducted) thermistor and conductivity sensor, the latter inside a protective metal housing. Temperature and conductivity data were extracted and processed using the University of East Anglia Glider Toolbox (Queste, 2013) and arithmetic means calculated for 1 m depth bins. Conductivity is dependent on water temperature as well as ionic strength. The conductivity sensor on the CT sail has a thermal lag response issue when passing through strong temperature gradients due to heat stored in sensor materials. Heat dissipation is affected by the water flow rate through the sensor. While *loiter* flight mode increases LoC sampling, it also produces slow and variable Seaglider ascent speeds (**Figure 2B**), and subsequently variable flow rates through the conductivity sensor, which makes thermal inertia corrections difficult and, in this instance unresolvable. Consequently, temperature and salinity data were used from descending profiles for analysis.

Lab-on-Chip Data Screening and Comparison With Nearby Ship-Based Measurements and Climatological Data

It is important to understand the quality of any analytical data. For laboratory analyses, this can be achieved routinely

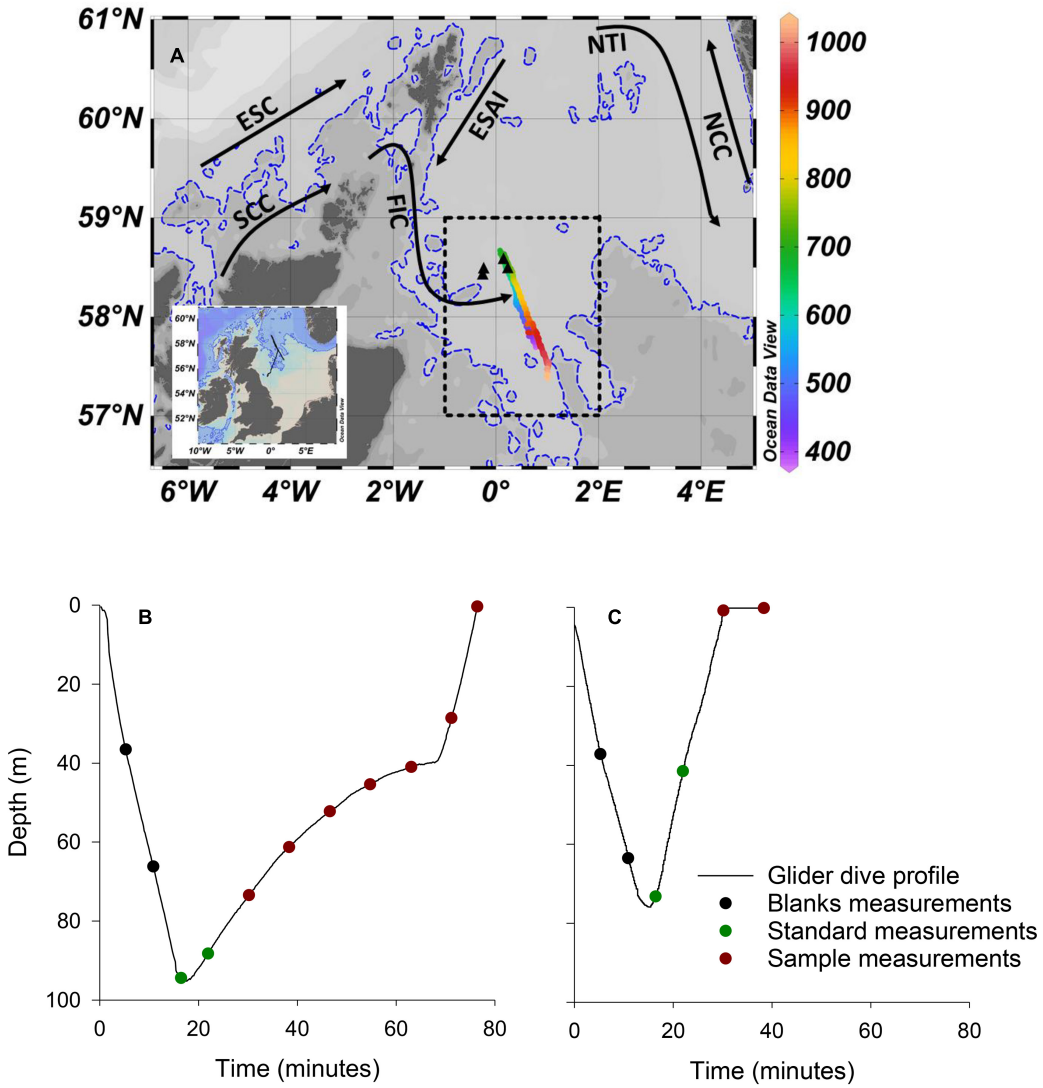

FIGURE 2 | Deployment location and dive profiles. **(A)** Map of the study area with complete Seaglider track shown on inset map. The colour bar represents the dive number. Dives <379 and >1,034, which included minimal PO_4^{3-} sampling as the glider was piloted toward deployment and recovery locations, respectively, and are not shown on main figure. Transect 1 included dives numbered 390–690. Transect 2 included dives numbered 691–1,034. The dashed rectangle encompasses the area of the North Sea Biogeochemical Climatology used for comparison (see text for details). Black triangles are the location of 4 *RV Heincke* sampling stations used for comparison (see text for details). Dashed blue line is the 100 m isobath. Black arrows are approximate paths of the Fair Isle Current (FIC), East Shetland Atlantic Inflow (ESAI), Scottish Coastal Current (SCC), European Slope Current (ESC), Norwegian Trench Inflow (NTI), and Norwegian Coastal Current (NCC). **(B)** An example of a "*loiter*" dive profile. **(C)** An example of a "*standard*" dive profile.

by analysing a series of blanks, standards, and certified reference materials. In addition, the analyst is regularly performing quality control by observing the output of the instrument (e.g., peak shapes and baseline shifts). Clearly, the same degree of constant attention cannot be applied to field deployable autonomous measurement technology; therefore, raw data (353 measurements) retrieved from the analyser upon recovery was subject to the following screening procedure.

(1) Identifying and removing data generated from poor LoC analyser calibrations.
(2) Identifying and removing data that are considered extreme (>1 μM) for this study region.
(3) Identifying and removing extreme negative concentrations (<−0.2 μM).
(4) Identifying data that are below the limit of detection (0.04 μM) and replacing them with a value of half the limit of detection (0.02 μM).

Validation here is defined as the assurance that the generated data meets the need of the end user, in this case oceanographers studying marine biogeochemistry. Two approaches are adopted to assess the validity of the dataset: (1) a comparison with 4 depth

profiles, that were collected by partners Hereon from *RV Heincke* on 30th August 2018 nearby our survey area and (2) comparison with the North Sea Biogeochemical Climatology dataset.

Seawater samples were collected on board the *RV Heincke* using a sampling rosette (**Figure 2**). Seawater samples were analysed using a gas segmented flow manifold, Seal AA3 (Norderstedt, Germany), combined with a standard spectrophotometric technique (molybdenum blue) (Hydes et al., 2010). The chemistry is almost identical to that used in the LoC analyser, and previous studies have demonstrated that data generated via gas segmented flow analysis is directly comparable to that generated via LoC analysers (Clinton-Bailey et al., 2017; Grand et al., 2017; Birchill et al., 2019a). The limit of detection for gas segmented flow analysis is 0.01 μM in seawater (SEAL-Analytical, 2019). Every year between 2017 and 2019 the SEAL AA3 HR performance was verified through analysis of QUASIMEME reference samples for estuarine and seawater (Aminot et al., 1997). For PO_4^{3-}, the Seal AA3 consistently reproduced the expected reference values (z-scores < 1).

The results of the LoC analyser were also compared with version 1.1 of the "North Sea Biogeochemical Climatology" (Laane et al., 1996a; Hinrichs et al., 2017a). This is a 0.25° × 0.25° gridded monthly climatologies of biogeochemical parameters, which covers the region from 47 to 65°N and from 15°W to 15°E. It includes observations from 1960 to 2014. Level 2 data was used in this study. Level 2 data is quality-controlled bin-averaged gridded fields and gaps left where data were missing (i.e., level 2 data is not interpolated between grids). For more details see University of Hamburg technical report (Hinrichs et al., 2017b). We selected the region covering 57 to 59°N and 1°W to 2°E (**Figure 2**), and calculated a mean profile for this region using the depth bins at 0, 5, 10, 15, 20, 25, 30, 35, 42, 50, 62, 78, and 98 m, defined in the climatology for the months of August and September. Mean values were calculated from a minimum and maximum of 16 and 52 data points, respectively.

RESULTS AND DISCUSSION

Lab-on-Chip Long Term Performance and Data Screening

The mean voltage output of the photodiode during 5-s measurement periods of the blank, 0.46 and 1.00 μM standard solutions throughout the deployment is displayed in **Figure 3**. Over the duration of the deployment, a decrease in voltage output was observed, with noticeable step changes. Importantly, these changes occur proportionally across the blank and standard solutions. By converting raw voltages to absorbance values, it is evident that the shifts in photodiode voltage are not associated with shifts in the sensitivity ($\Delta A/\Delta c$) of the analyser during deployment (**Figures 4A–C**). Anecdotally, we report that after passing weak cleaning agent (diluted Deacon 90) through the analyser upon recovery, the raw photodiode voltages returned to initial values. Therefore, the decrease in voltage is likely due to staining of the measurement cell. In this instance the decreasing output of the photodiode did not prevent the analyser from making measurements (i.e., there was always sufficient signal from which to measure absorbance). For longer duration deployments this could become an issue. Therefore, the first recommendation we make for future deployments is to include additional NaOH flushes in the analytical procedure to clean the optical cells.

The sensitivity of the analyser ($\Delta A/\Delta c$) showed some variability but no systematic increase or decrease during the course of the deployment (**Figures 4A–C**), indicating that reagent, blank and standard solutions remained stable under the storage conditions of the deployment, in the dark and at the temperature of the summer North Sea (6–16°C, see **Figure 7**). A plot of the residual values associated with the linear regression calibration slope exhibited no systematic trend, indicating that a linear regression was appropriate (**Figures 4D–G**). This is consistent with previous laboratory testing, which demonstrated that the limit of linearity ranged from the limit of quantification to 10 μM (Clinton-Bailey et al., 2017). The calibration procedure required forcing the calibration curve through the origin, because the absorption of both standard points is defined against the "zero" point of the blank. This manipulation resulted in a <1% change in the gradient of the calibration slope. Out of the 71 dives where PO_4^{3-} was measured, there were three calibrations that were clearly of poor quality (**Figures 4D–F**). Since only three of 71 calibrations were considered unreliable, containing nine data points, no attempt was made to apply any correction factor (e.g., applying a deployment average calibration slope). Instead, the nine sample data associated with these dives was omitted from the final analyses (**Figures 5A,B**). A further nine extreme values (>1.0 μM) were removed as likely analytical artefacts (**Figure 5C**). Although PO_4^{3-} concentrations in excess of 1 μM are found in North Sea coastal waters (Radach and Pätsch, 1997; Frank et al., 2006), our study location was in the central northern North Sea, where concentrations are typically <1 μM (see validation section below). Moreover, concentrations in excess of 1 μM were distributed randomly suggesting that they resulted from an unidentified source of random error. Similarly, profiles with extreme negative concentrations (<–0.2 μM) were removed from the dataset (six measurements; **Figure 5D**). In total 24 out 353 measurements, or 7%, were removed from the final dataset before further analysis (**Figure 5E**).

Surface PO_4^{3-} concentrations were depleted and consequently 68 PO_4^{3-} measurements were below the limit of quantification (0.14 μM), with 19 of these below the limit of detection (0.04 μM), representing 6% of the dataset. Whilst non-detects do not provide a point measure of PO_4^{3-} concentration, they do inform us that their PO_4^{3-} concentration was between 0 and 0.04 μM. The methods available to deal with non-detects include substitution and distribution-based imputation methods, which are recommended when a large proportion of the total observations are non-detects (Baccarelli et al., 2005). Although based on judgment and without statistical basis, substitution methods are simpler and represent a pragmatic approach that is suitable when the proportion of non-detects in the overall dataset is low [e.g., less than 15% (EPA, 2000)]. Consequently, replacing values below the limit of detection with a value equal to half the

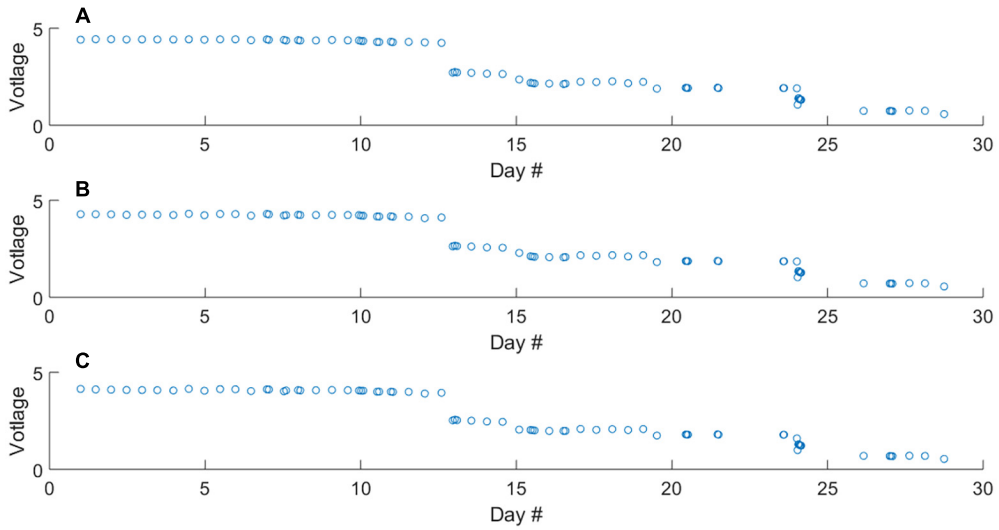

FIGURE 3 | Raw voltage output of the measurement photodiode throughout the deployment during the measurement of the blank **(A)**, 0.46 μM standard **(B)**, and 1.00 μM standard **(C)** solutions. The differences in raw voltage for respective blank and standard measurements are too small to see, **Figure 4** contains absorbance values.

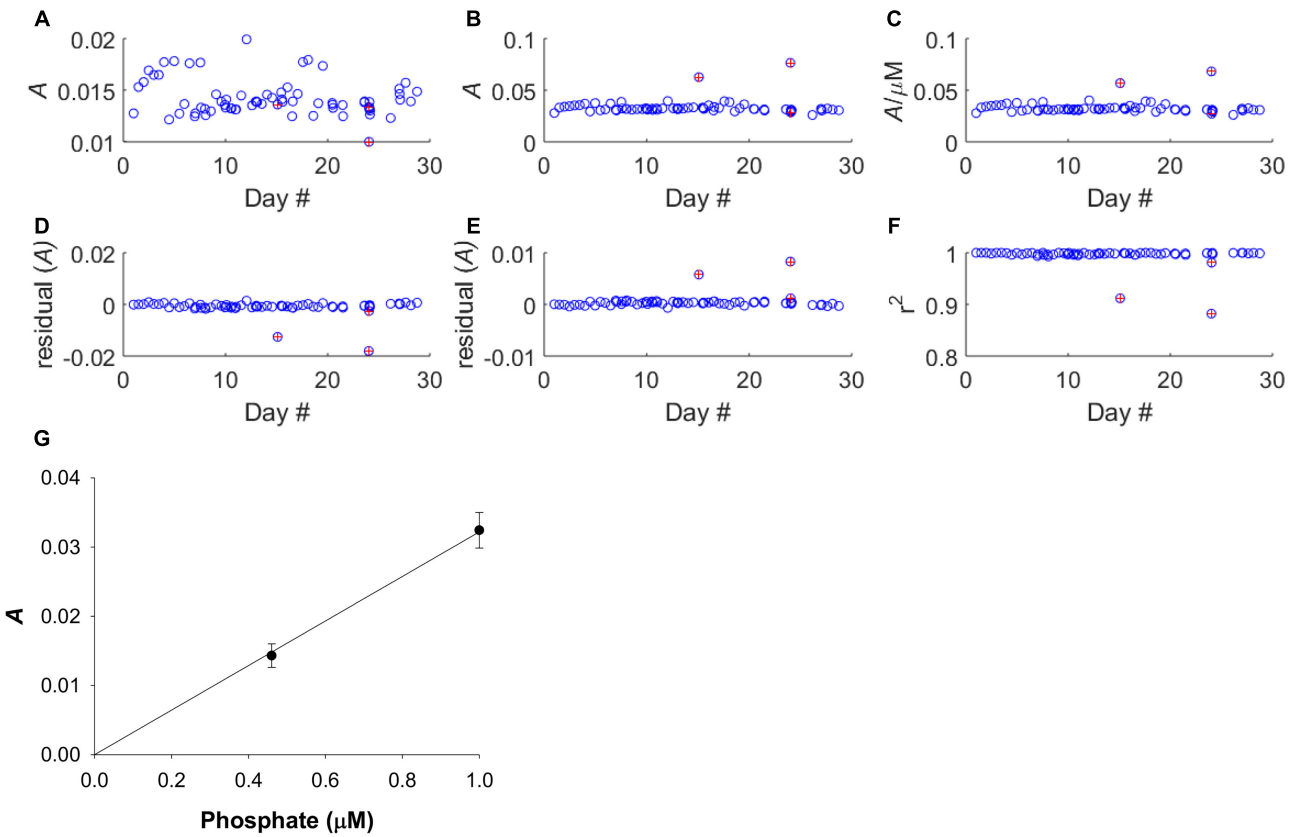

FIGURE 4 | Calibration performance of LoC analyser throughout the deployment. Red markers indicate poor calibrations and data from these dives was removed before further analyses. **(A)** The absorbance of the 0.46 μM standard. **(B)** The absorbance of the 1.00 μM standard. **(C)** Sensitivity of analyser. **(D)** Residual values for 0.46 μM standard. **(E)** Residual values for 1.00 μM standard. **(F)** Correlation co-efficient of regression slope. **(G)** Average calibration slope for all deployment dives, except those with poor calibrations, with linear fit forced through the zero intercept. The linear fit was based on a mean 0.46 μM PO_4^{3-} standard absorbance of 0.0143 ± 0.0017, and a mean 1.00 μM PO_4^{3-} standard absorbance of 0.0324 ± 0.0026. The mean regression slope was 0.0322 ± 0.0027.

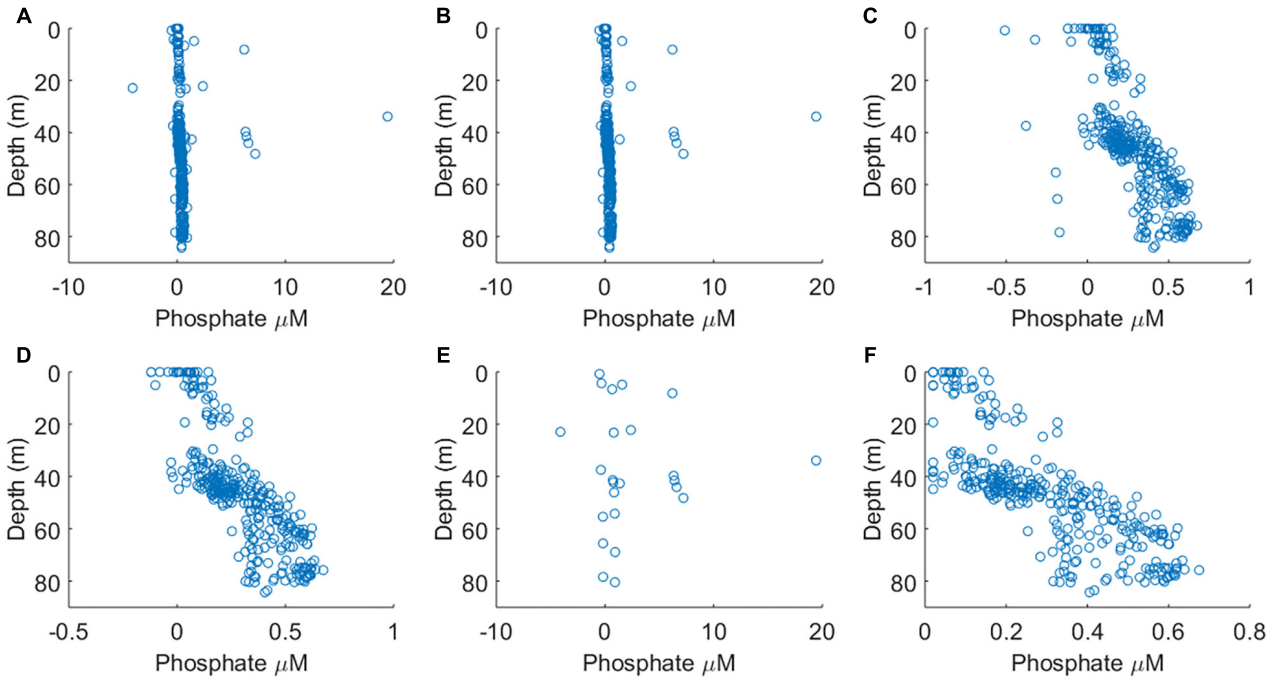

FIGURE 5 | The results of data screening steps carried out, panels **(A–D)** are in sequence. Note changing horizontal axis scales. **(A)** The complete dataset. **(B)** Dataset after the removal of data generated from poor calibrations (see **Figure 4**). **(C)** Dataset after the removal of concentrations >1 μM PO_4^{3-}. **(D)** Dataset after the removal concentrations <–0.20 μM. **(E)** All outliers and data resulting from poor calibrations, which were removed from final dataset. **(F)** The quality controlled data product.

limit of detection is an approach commonly adopted in studies of environmental chemistry (Vitaliano and Zdanowicz, 1992; Tajimi et al., 2005; García-Fernández et al., 2009). If the scientific outcomes of a study are affected by the treatment of non-detects, the choice of treatment takes on greater importance. Here we simply characterise surface waters as oligotrophic low nutrient environments, therefore the scientific findings are not impacted by the choice of non-detect treatment. Hence, we adopted a simple substitution method. While the oceanographic community is working toward harmonising the use of *in situ* nutrient sensors, including providing recommendations for defining the limit of detection (Daniel et al., 2020), it is not yet providing recommendations for non-detect treatment. We suggest that treatment of non-detects be clearly defined, particularly when working in oligotrophic waters.

Prior to substitution with LoD/2, some surface values had apparent negative concentrations, as a result of a negative sample absorbance. A negative sample absorbance has no physical meaning and results from a larger voltage generated at the photodiode during the sample measurement than during the blank measurement. A typical cause would be PO_4^{3-} contamination of the blank solution. However, the blank solution was subsampled upon recovery and found to contain <0.01 μM PO_4^{3-} (**Table 2**). Alternatively, it might be caused by sample fluorescence or phosphorescence, or simply be analytical noise resulting from measuring the absorbance of two solutions (blank, low concentration sample) with a small signal.

Comparison With Ship-Based *in situ* Phosphate Data

To illustrate general trends present in the final data product, the LoC–AUV data was binned into 5 m depth intervals and the arithmetic mean of each depth bin was calculated (**Figures 6A,B**). The imprint of seasonal stratification is clear within the dataset; low nutrient concentrations characterised surface waters, with a mean PO_4^{3-} concentration of 0.06 ± 0.04 μM at 0–5 m depth. Between 40 and 60 m depth, there was an increase in the mean concentration of PO_4^{3-} from 0.17 ± 0.09 to 0.45 ± 0.10 μM, consistent with a seasonal thermocline and remineralisation of sinking organic matter. Below 60 m, the mean PO_4^{3-} concentration ranged from 0.42 to 0.54 μM. Whilst the imprint of seasonal stratification is clear, the high standard deviation of each depth bin indicate that other processes in addition to seasonal cycling must drive variability.

The vertical distribution and range of PO_4^{3-} concentrations determined by LoC–AUV are consistent with traditional shipboard observations made at several depths in the study area on 30th August 30th 2018 (**Figure 6A**). It is noteworthy that the shipboard observations at 40 m depth were collected at four locations in relatively close proximity (**Figure 2**), but produced

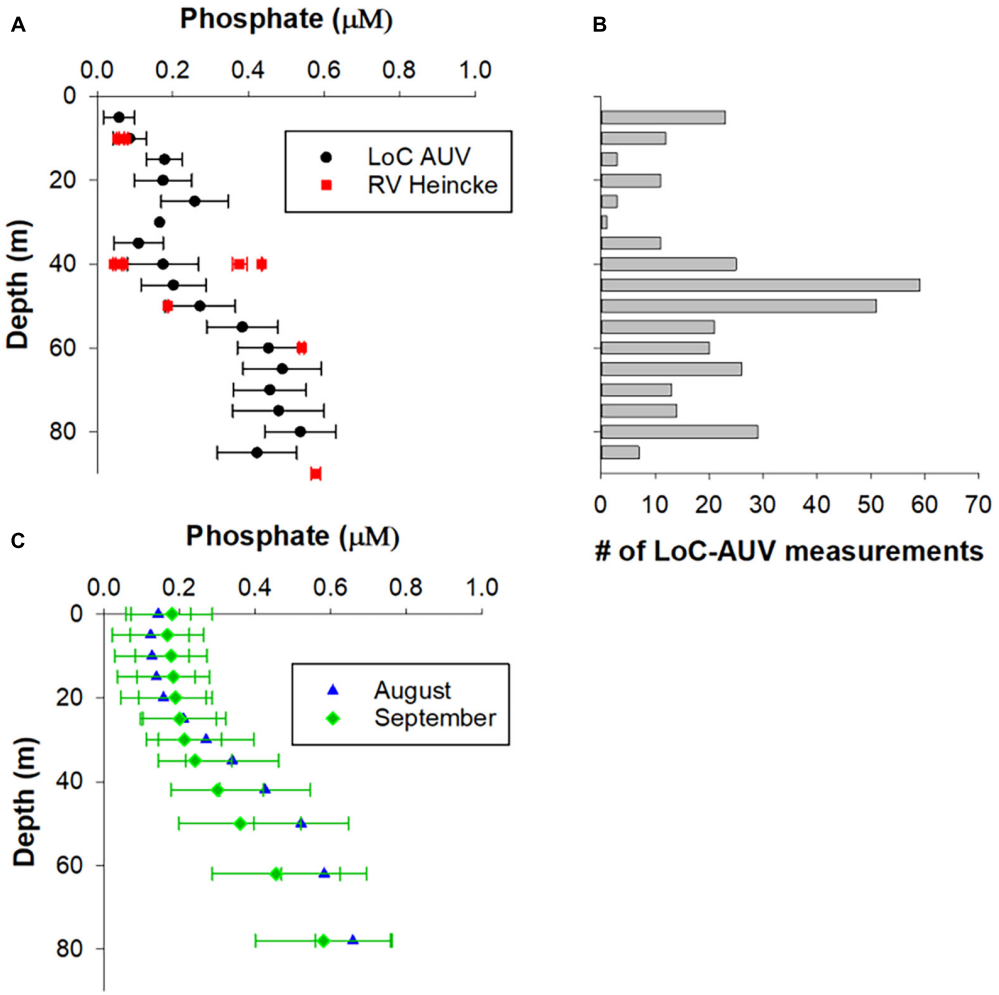

FIGURE 6 | Validation of phosphate LoC–AUV results. **(A)** LoC–AUV are binned into 5 depth bins and presented as arithmetic mean ± 1 SD. The data from *RV* Heincke were collected at four locations at the northern end of our transect (see **Figure 2** for locations). **(B)** The number of LoC–AUV measurements within each depth bin. **(C)** Arithmetic mean ± 1 SD of phosphate concentrations for August and September from the North Sea Biogeochemical Climatology.

a PO_4^{3-} concentration range of 0.06–0.44 μM, suggesting large nutrient variability in a relatively small region of the North Sea. Similarly, the mean PO_4^{3-} concentrations from climatology data for months August and September show surface PO_4^{3-} depletion in surface waters: 0.11 ± 0.08 μM for August and 0.19 ± 0.12 μM for September, with increasing PO_4^{3-} concentrations at depth (0.36–0.74 μM, for depth range 42–98 m) (**Figure 6C**). In agreement with both the LoC–AUV and shipboard observations, the climatology shows considerable variability in PO_4^{3-} distribution with depth.

In addition to producing accurate and precise PO_4^{3-} concentrations, LoC–AUV needs to provide oceanographers with spatial and temporal coverage to resolve biogeochemical processes. To provide sufficient resolution to produce a PO_4^{3-} depth profile, the glider must operate in loiter flight mode (**Figure 2**). During loiter mode, the reduction in vertical speed of the Seaglider allows for high-resolution measurements through the phosphocline (**Figure 6**). However, biogeochemical parameters are nearly always interpreted alongside hydrographic data; therefore, it is essential that LoC–AUV provide reliable temperature and salinity measurements. During the upcast of a loiter dive the shallow angle of climb causes slow and variable seawater flow rates through the conductivity cell on the CT sail, thus loiter flight mode is a sub-optimal mode of operation for producing high quality salinity data. Pumped and ducted Conductivity-Temperature-Depth payloads would help mitigate this problem, which have been used on the Seaglider (Janzen and Creed, 2011), and are available on other ocean glider platforms, although the payload requirements for the LoC analyser made the Ogive fairing fitted Seaglider the only viable choice at the time of this study. Increasing the sampling rate of the LoC PO_4^{3-} analyser would also reduce the need to operate in loiter flight mode. However, the sampling rate is limited by the calibration procedure at the start of each dive, and the reaction rate of the

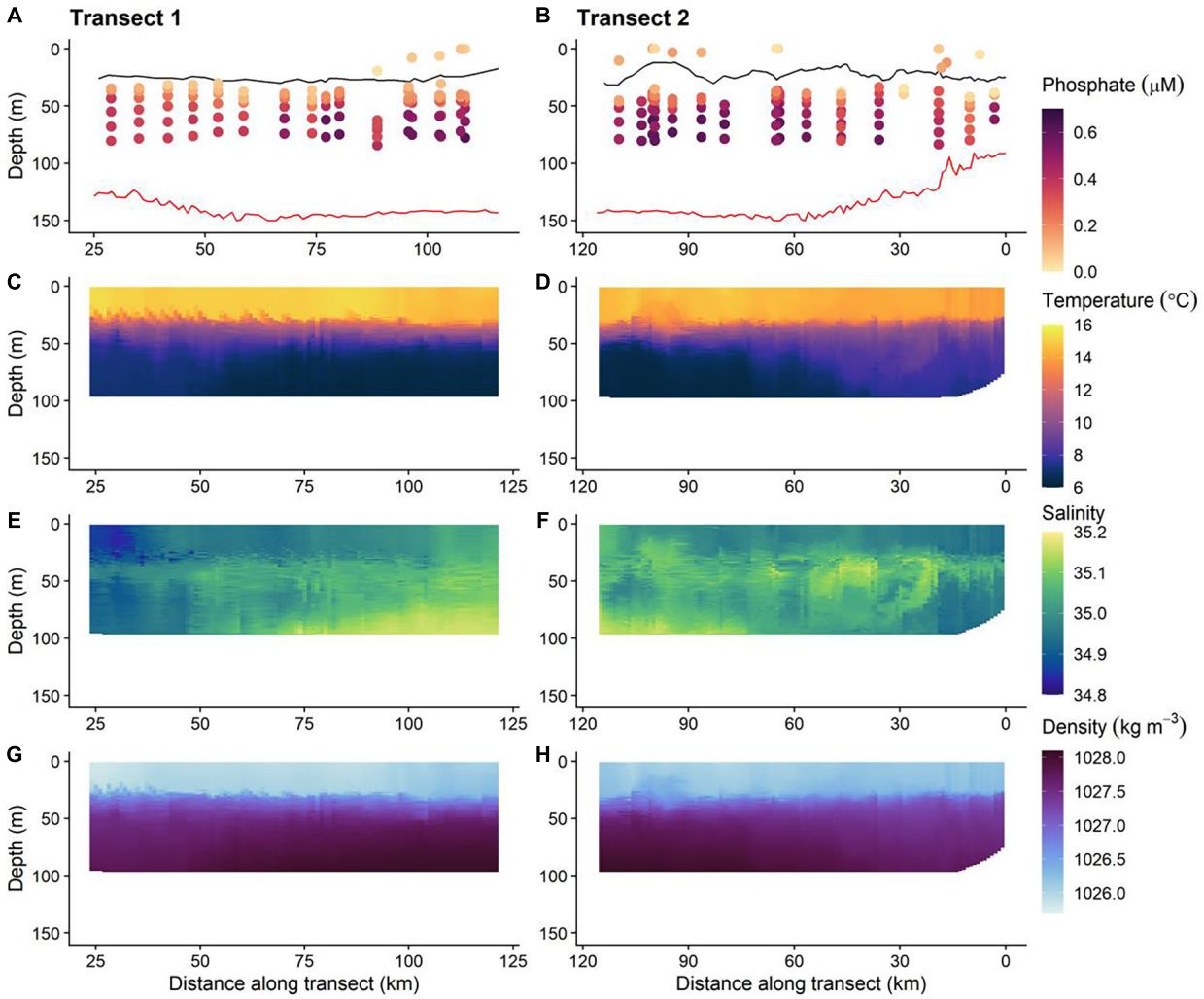

FIGURE 7 | The physical and biogeochemical *in situ* glider dataset; 0 km is the start transect 1 and the end of transect 2 (i.e., time runs left to right along the horizontal axis). Red and black lines on phosphate plots **(A,B)** are the GEBCO bathymetry and thermocline, respectively. The location of the thermocline is defined as a 0.03 kg m^{-3} density increase relative to that at 10 m depth (de Boyer Montégut et al., 2004). **(C,D)** Temperature, **(E,F)** salinity, and **(G,H)** density.

molybdenum blue assay meaning there is a requirement for a 150 s period of colour formation for each blank, standard, and sample measurement.

In situ Measurements of Phosphate in the Northern North Sea

Plots of *in situ* PO_4^{3-} concentration, temperature, salinity and density for each transect are presented in **Figure 7**. There are three primary features evident in the dataset, which are presented and discussed in turn. These are (1) Nutrient depletion in surface waters with enrichment below the seasonal thermocline; (2) The presence of relatively cold, salty bottom layer waters with elevated PO_4^{3-} concentrations at the northern end of our transect; (3) Horizontally heterogeneous, or "patchy" PO_4^{3-} distribution.

The concentration of PO_4^{3-} was depleted (typically < 0.20 μM) in waters above the seasonal thermocline. PO_4^{3-} concentrations increased to ≈0.30–0.65 μM in bottom layer waters (**Figures 7A,B**). The stratification of nutrient concentration corresponds with the location and structure of the thermocline (**Figures 7C,D**), with low PO_4^{3-} concentration within warmer surface waters ≈14–16°C and high concentration in bottom layer waters, where temperatures were cold ≈6–9°C. Summer surface nutrient depletion is typical for seasonally stratifying shelf seas, such as the northern North Sea (Painter et al., 2018). This nutrient depletion is a result of uptake by primary producers and export via sinking organic matter during the spring bloom and summer months, coupled with inefficient resupply from nutrient enriched bottom waters due to low levels of vertical mixing across the seasonal thermocline. When estimating the magnitude of seasonal productivity in

stratified shelf seas it is important to estimate the diapycnal diffusive flux of nutrients through the thermocline:

$$F_{\mathrm{d}} = K_z \frac{\Delta c}{\Delta z} \quad (4)$$

Where K_z is the eddy diffusivity, Δc is the nutrient concentration gradient through the thermocline, and Δz is the thickness of the thermocline. Shipbased research conducted in the Celtic Sea demonstrated significant variation of the diapycnal nutrient flux (daily mean values of 0.04–2.6 mmol PO_4^{3-} m^{-2} day^{-1} with 95% confidence intervals for these mean estimates ranging from 0.00 to 9.0 mmol m^{-2} day^{-1}) (Tweddle et al., 2013). Variability of the diapycnal nutrient flux is driven by the gradient of PO_4^{3-} through the thermocline, which varied by over an order of magnitude within a 25-h period at a single location, and the variability of K_z, which for example is affected by tidal forces and bathymetry (Sharples et al., 2007; Tweddle et al., 2013). Research ships are ideal for targeted studies, but provide only limited spatial and temporal coverage. Gliders can now be equipped with microstructure turbulence profilers (Palmer et al., 2015) and nutrient analysers (this study; Vincent et al., 2018). Here we demonstrate that LoC–AUV can be used to observe the distribution of PO_4^{3-} concentrations through the thermocline (**Figure 8**). Consequently, it is now possible to autonomously collect all the information required to calculate the terms in the vertical diffusive flux equation (Eq. 4) at a greater resolution than shipboard observations. Therefore, autonomous techniques could be used to provide a better constraint of this important rate limiting flux.

Relatively cool, salty bottom layer water found to the northern end of the transect, coincided with the largest observed PO_4^{3-} concentrations (**Figure 7**). This suggests that the phosphate-rich deep waters most likely came from the Atlantic Ocean. Inflow from the Atlantic Ocean into the northern North Sea occurs primarily through the Norwegian Trench Inflow (1.2 Sv, 1 Sv = 10^6 m^3 s^{-1}), Fair Isle Current (FIC; 0.5 Sv) and the East Shetland Atlantic Inflow (ESAF; 0.5 Sv) (Winther and Johannessen, 2006). The Norwegian Trench Inflow largely retroflects with the Norwegian Trench leaving the FIC and ESAF to have the greatest influence on the hydrographic conditions of the northern North Sea (**Figure 2**). The inflow of Atlantic water via the FIC and ESAF has been shown to be a source of nutrients to the shelf (Laane et al., 1996b; Große et al., 2017), and so natural variability of such transport will lead to an associated variability of inflowing nutrients. Consequently, discrete sampling may not provide a comprehensive representation of seasonal or interannual conditions. Assessment of the current state of shelf sea nutrients is therefore challenging and requires consideration of a range of temporal and spatial scales to suitably capture the temporally and spatially varying drivers that modify observed nutrient data. Observations from AUVs, moorings, shipboard studies and drifters have allowed variability of the physical characteristics of the North Atlantic inflow to the North Sea to be quantified over weekly, seasonal, yearly and decadal timescales (Marsh et al., 2017; Sheehan et al., 2017, 2020; Porter et al., 2018). In contrast, nutrient data are collected at a much coarser resolution via discrete sampling during ship based surveys. Sustained LoC–AUV observations therefore offer the potential to increase the spatial and temporal frequency over which nutrient observations are made and to help extend this physical understanding of shelf seas to include biogeochemical pathways and ecosystem function.

In addition to the general vertical and horizontal trends discussed above, there was noticeable heterogeneity within the PO_4^{3-} concentrations (**Figures 7A,B**). This patchiness may be a result of natural variability but may also indicate low levels of precision from the LoC analyser. To evaluate LoC analyser precision, PO_4^{3-} concentrations were determined during three sequential dives, thereby minimising the effects of natural spatial and temporal variability. Broadly, PO_4^{3-} concentrations measured at similar depths on sequential dives were within the combined analytical uncertainty determined by laboratory testing (**Figure 9A**). It is most informative to make direct comparisons at deeper depths where the vertical gradient of PO_4^{3-} concentration was less steep. Measurements were made at around 75 and 60 m on each of the three dives. The mean PO_4^{3-} concentrations at the two depths were 0.60 ± 0.01 and 0.53 ± 0.03 μM (1 SD), respectively. Moreover, a significant inverse correlation between temperature and PO_4^{3-} concentration was observed (**Figure 9B**), characteristic of seasonally stratified shelf seas (Tweddle et al., 2013). We conclude therefore that the LoC analyser field performance was in line with laboratory testing (u_c = 6.1%), and thus the variation of PO_4^{3-} concentrations observed in bottom waters (0.30–0.65 μM) was driven by natural variability. Similar variability within macronutrient distributions has been seen in the Hebridean Sea (PO_4^{3-} concentrations ranging from 0.2 to 0.5 μM within a degree of latitude), and such variability has been identified as an environmental driver of macrophytoplankton distributions (Siemering et al., 2016; Birchill et al., 2019b). In the central northern North Sea, localised patches of elevated summer surface PO_4^{3-} (>0.5 μM) have been reported by ship based observations (Painter et al., 2018). Repeated observations at two locations in the Celtic Sea showed that the concentration of PO_4^{3-} in bottom waters ranged from 0.4 to 0.8 μM within a 25-days period (Tweddle et al., 2013). In summary, the patchiness observed in northern North Sea (**Figures 7A,B**) is characteristic of nutrient distributions in waters overlying the north west European shelf. Shelf seas are dynamic environments impacted by hydrographic and biogeochemical processes occurring over a range of temporal and spatial scales (e.g., phytoplankton blooms, semi diurnal tides and tidal interaction with uneven topography, spring-neap cycles, internal tides, storms, seasonal stratification, and complex regional circulation), which impact phosphorus distributions (Davis et al., 2014; Poulton et al., 2019). When viewed in this context, the observed variability of PO_4^{3-} concentrations is expected. It is important that future shelf sea deployments of LoC–AUVs are designed with this variability in mind.

Assessing the Extent to Which This Research Has Expanded Glider Sensor Capabilities for Oceanographic Research

The oceanographic research community is experiencing a dramatic increase in capability as autonomous technologies

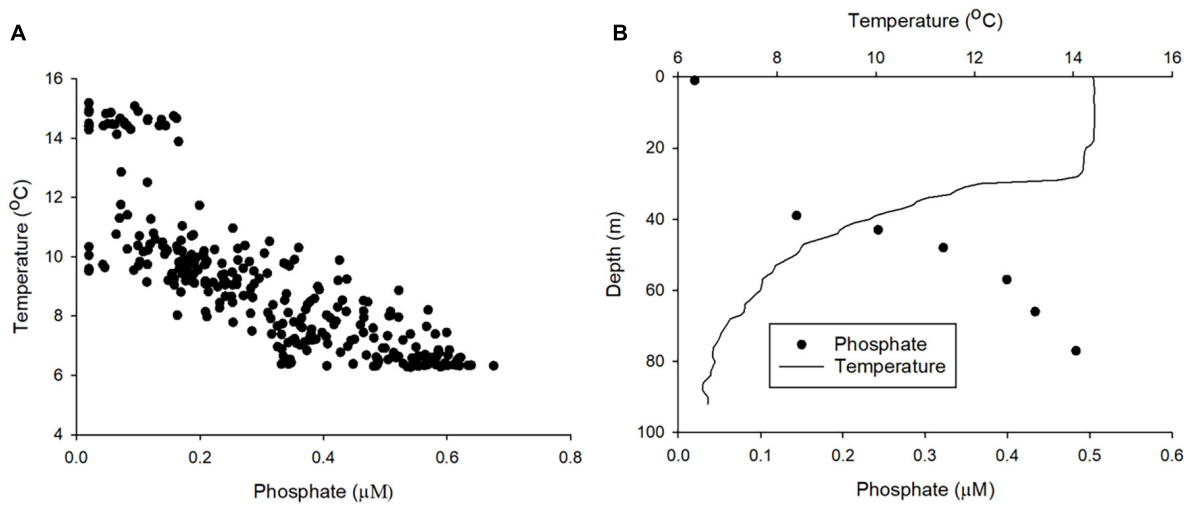

FIGURE 8 | (A) The relationship between phosphate and temperature for the entire dataset. **(B)** An example depth profile of phosphate and temperature (dive number 883 conducted on 23/08/2018).

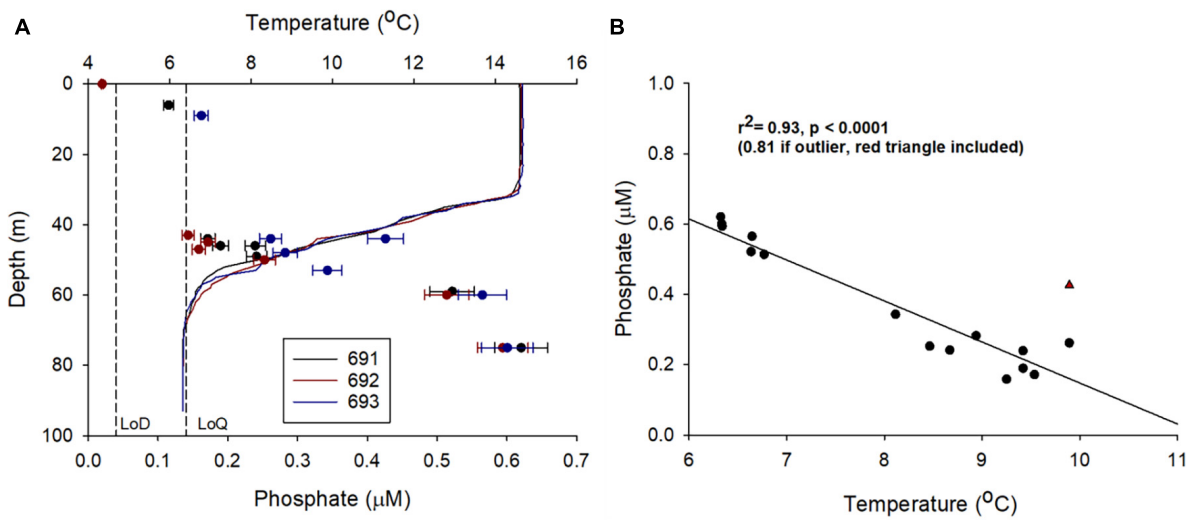

FIGURE 9 | Examining LoC analyser field precision by conducting PO_4^{3-} analysis during three sequential Seaglider dives (691, 692, and 693), first and last sample separated by 1.98 km and 4.00 h. **(A)** Depth profiles of temperature and PO_4^{3-} concentration. Vertical dashed lines are laboratory estimates of the limit of detection (LoD) and limit of quantification (LoQ) (Clinton-Bailey et al., 2017; Grand et al., 2017). Error bars are laboratory estimates of combined (random + systematic) relative uncertainty (Birchill et al., 2019a). **(B)** Statistically significant inverse linear correlation between temperature and PO_4^{3-} concentration from dives 691, 692, and 693 for samples collected below 40 m.

become more accessible (Johnson et al., 2009; Roemmich et al., 2010; Beaton et al., 2012; Heslop et al., 2012; Liblik et al., 2016; Hendry et al., 2019). This study represents the first ever *in situ* PO_4^{3-} dataset obtained using an underwater glider and, for that matter, actually any AUV. Therefore, this represents a significant advance in marine biogeochemical capabilities (Jońca et al., 2013). Glider observations are already making an a major contribution to Global Ocean Observing Systems (Testor et al., 2019) and provide a valuable tool to investigate the range of sub-mesoscale phenomena that typify shelf seas and shelf break regions (Roemmich et al., 2010; Liblik et al., 2016). The data presented here provides evidence in support of this assertion, demonstrating the potential of coupling physical and chemical sensors to investigate marine biogeochemical processes. Importantly, an opportunity now exists to combine existing capability to measure NO_3^- and NO_2^- on AUVs (Vincent et al., 2018) with the PO_4^{3-} LoC–AUV capability demonstrated here. Understanding the controls on nutrient stoichiometry in the ocean has been a central topic of marine research for almost as long as oceanography has existed as a modern scientific discipline, and it remains so to the present day (Redfield, 1934; Moore et al., 2013). It is now a realistic goal to attempt to

capture the inorganic N:P stoichiometry of marine systems via simultaneous glider deployments. With current LoC payload requirements this could not happen on a single Seaglider.

In order to put our PO_4^{3-} LoC–AUV research into the context of wider glider-sensor developments we adopt the Gliders for Research, Ocean Observation and Management (GROOM) approach to sensor development classification (**Supplementary Table 1**). The GROOM approach utilises two measures of sensor development, Ocean Sciences Technology Readiness Levels (OS-TRL) defined by Waldmann et al. (2010) and Development Status defined by Johnson et al. (2000). To fulfil OS-TRL 3, the sensor must be a commercial product and "*Actual systems completed and mission qualified through test and demonstration*". The corresponding Development Status is "*III Early stage of development with successful short-term deployments in the marine environment.*" We assert that results of the deployment detailed in this manuscript, in combination with recent commercial availability[1], satisfy these requirements and thus PO_4^{3-} LoC–AUV has fulfilled the requirements of OS-TRL 3 and Development Status II.

LoC–AUV as a Tool for Environmental Management of Regional Seas?

At present, the LoC–AUV technology presented here is used exclusively as a research tool. However, given that now both PO_4^{3-} and $NO_3^- + NO_2^-$ can be measured by LoC–AUV, and both sensors and platforms are commercially available, it is worth considering the potential applications beyond oceanographic research. Nutrient cycles in coastal waters have been greatly modified by anthropogenic activity. For example riverine phosphorus fluxes have increased 50–300% upon pre-industrial levels (Cordell et al., 2009). Eutrophication of coastal waters can result from anthropogenic nutrient inputs, which can have adverse effects on coastal sea ecosystems such as deoxygenation and increased frequency of harmful algal blooms (Jickells, 1998; Moore et al., 2013; Karl, 2014; Breitburg et al., 2018). Policy at national and international levels has been implemented, which is related, either directly or indirectly, to the issue of eutrophication in the marine environment. The ability to assess the effectiveness of these policies is to a large extent dependent upon sustained observations of inorganic nutrients over timescales of years to decades. As an example, both phosphate and nitrate + nitrite + ammonia are core set indicators (core set indicator 21) used by the European Environment Agency to address policy questions. Current data coverage is geographically biased toward particular regions such as the Baltic Sea, with data coverage in regions such as offshore parts of the Bay of Biscay, Black Sea, and Mediterranean Sea deemed "unsatisfactory" (European-Environment-Agency, 2019). Future ocean observing systems will likely include the capability to autonomously measure macronutrients in the marine environment, and thus will potentially provide data to environmental management agencies with the expanded temporal and spatial resolution they require. The North Sea is an example of an economically important regional sea that is heavily influenced by anthropogenic activity (Emeis et al., 2015), and where various national and international regulation measures are in place (EU, 2008). The nature of this deployment, from a routine fisheries survey, highlights the plausibility that LoC–AUV technology could be readily integrated into existing observing system infrastructure for coastal ocean monitoring.

[1]http://www.clearwatersensors.com/

RECOMMENDATIONS AND CONCLUSION

Recommendations for Further Development

The potential development pathways for new technology are almost infinite, whereas the resources available for this technology development are limited. We therefore take the opportunity to analyse the lessons learned from this and other recent LoC–AUV developments (Vincent et al., 2018) to highlight what we consider important development priorities, besides the ever-present incentive to reduce costs, size, power demand, reagent consumption, and increase sampling frequency.

PO_4^{3-} LoC–AUV Specific Development Priorities

We consider what criteria remain outstanding in order to fulfil the requirement of OS-TRL 4 (**Supplementary Table 1**; *Actual system proven through successful mission operations* and *currently operational and available commercially available*). A critical step in assessing sensor (or microfluidic analyser) performance is independent validation of *in situ* results (Waldmann et al., 2010). In this study, we achieve a semi-quantitative validation using data generated from traditional measurement approaches, collected nearby in space and time, and by using a North Sea climatological dataset. Whilst this is sufficient to conclude that we have generated an oceanographically consistent dataset, it does not allow for a robust quantitative validation of the *in situ* dataset, such as that achieved by Vincent et al. (2018) when deploying a $NO_3^- + NO_2^-$ LoC analyser on a Seaglider in the Celtic Sea. Throughout the field campaign reported by Vincent et al. (2018), water samples were collected using traditional water sampler techniques, followed by traditional benchtop spectrophotometric analysis, allowing for a direct comparison with LoC–AUV data. In order to progress to OS-TRL 4, long-term PO_4^{3-} LoC–AUV deployments with robust validation are a development priority. Given typical glider speeds ($\approx$25 cm s^{-1}) and deployment lengths (months) and spatial scales (100–1,000 s km), simultaneous or sequential LoC–AUV deployments may be required to obtain the resolution suitable to study oceanographic processes. To be considered "*mission proved*," multiple long-term (>1 month; **Supplementary Table 1**) deployments that produce valid datasets are required. Glider missions are typically used in conjunction with other measurement platforms (e.g., satellites, research vessels, moored platforms) (Roemmich et al., 2010; Liblik et al., 2016). For unequivocal proof of mission readiness, future PO_4^{3-} LoC–AUV deployments should be placed within the context of a novel oceanographic observing network (i.e., coordinated to target an oceanographic process) (Hendry et al., 2019).

Expansion of LoC–AUV Parameter Capability

Currently, LoC analysers are available to measure $NO_3^- + NO_2^-$ (Vincent et al., 2018) and PO_4^{3-} using a LoC–AUV approach. A strength of the LoC technology is that standard hardware and software is used across the range of analysers in development. At NOC these include silicic acid, pH, dissolved inorganic carbon, total alkalinity, ammonia and iron. As the future LoC analyser technology matures, physical and electrical integration with autonomous platforms, such as the Seaglider used in this study, can follow already established procedures (this study; Vincent et al., 2018). Being able to collect concurrent measurements of multiple important chemical parameters will expand research horizons. Ideally, size and power requirements would permit this to occur on a single platform, presently larger AUV platforms should be considered or objectives may be met using multiple simultaneous AUV deployments.

Expansion of Platform Integration

There are multiple autonomous platforms available, which each offer different advantages and disadvantages. There are different types of glider (e.g., Seaglider, Slocum, and Spray) available, whose merits have been reviewed in detail elsewhere (Meyer, 2016; Rudnick, 2016). Some differences pertinent to LoC integration are highlighted here. The Slocum Electric's buoyancy engine and tail fin rudder give it a tight turning circle (7 m), making it well suited to shallow water (30–200 m) operations, such as the deployments presented here and by Vincent et al. (2018). Additionally, an optional propulsion system means it can generate horizontal as well as vertical motion, allowing it to pass through strong pycnoclines and currents, common in shelf seas. However, the payload requirements of the LoC analyser restricts internal housing of the sensor to the Ogive modified Seaglider for ocean glider deployments at the time of writing. Further NOC developments are currently being trialled with a Slocum glider that will enable external housing of the LoC analyser, which would expand the range of platforms suitable for integration.

Deep ocean exploration typically uses a range of larger AUVs (e.g., WHOI's Sentry and the NOC Autosub). Integration of LoC analysers onto such platforms offers the opportunity to extend biogeochemical capability to deep ocean environments enabling, for instance, monitoring impacts of deep-sea mining or investigating the influence of hydrothermal exchange on deep ocean biogeochemistry. Autosub offers the possibility to house up to 9 LoC analysers simultaneously and research is ongoing to integrate LoC analysers into Autosub (A. Schaap, personal communication, August 2020). For the PO_4^{3-} LoC analyser specifically, the current minimum operating temperature of 5°C (**Table 1**) would limit deep ocean observations. Integration into an ever-expanding fleet of autonomous surface vehicles would offer an opportunity to study the surface ocean in detail, where primary production and air-sea gas exchange occurs.

Conclusion

We report the integration of a PO_4^{3-} LoC analyser into a Seaglider, successfully deployed in the northern North Sea for a period of 44 days to measure PO_4^{3-} concentrations along a 120 km transect (surveyed twice). Validation of *in situ* data was achieved through comparison with nearby ship board measurements and climatology data, demonstrating our ability to produce high quality, oceanographically consistent, *in situ* measurements. As the first demonstration of *in situ* PO_4^{3-} measurements using an AUV, this study represents a step forward in glider-sensor capabilities opening up new research horizons. More broadly, LoC–AUV offers the exciting possibility to autonomously observe a range of important chemical parameters *in situ* and can make important contributions to the global effort to leave the era of ocean data scarcity behind. Thus, LoC–AUV should be considered in the design of future ocean observing systems.

DATA AVAILABILITY STATEMENT

The datasets presented in this study can be found in online repositories. The names of the repository/repositories and accession number(s) can be found below: British Oceanographic Data Centre, doi: 10.5285/bf632e43-d8e9-43ab-e053-6c86abc0ab7a.

ETHICS STATEMENT

Written informed consent was obtained from the individual(s) for the publication of any potentially identifiable images or data included in this article.

AUTHOR CONTRIBUTIONS

MP, ADB, AJB, AS, RP, MM, CW, TH, and JK contributed to the conception and design of the study. AJB, processed Lab-on-Chip data and wrote the first draft of the manuscript. TH processed CT sail data. YV provided macronutrient analysis. All co-authors contributed to the manuscript revision and approved the submitted version.

FUNDING

This research was funded by the National Environment Research Council AlterEco Grant (Grant No. NE/P013899/1). This provided funding for the bulk of the work-deployment of seaglider and fabrication and testing of lab-on-chip analyser. Funding for Heincke cruise was awarded to Rüdiger Röttgers and Holger Brix (Hereon), for project ShelfVal. Hereon funding was provided by the Helmholtz Association PACES II Program: Polar regions and coasts in the changing earth system.

ACKNOWLEDGMENTS

We thank the captain and crew of *MRV Scotia* and the *RV Heincke*. We thank John Walk (Ocean Technology and Engineering, National Oceanography Centre), Michael Smart and Steven Woodward (Marine Autonomous Robotic Systems,

National Oceanography Centre) for their invaluable input during LoC analyser Seaglider integration and deploying, piloting and recovering the Seaglider. We also thank Christian Ahlers, Alina Zacharzewski, and Tanja Pieplow (Helmholtz-Zentrum Hereon) for helping to collect and analyze discrete nutrient samples.

SUPPLEMENTARY MATERIAL

The Supplementary Material for this article can be found online at: https://www.frontiersin.org/articles/10.3389/fmars.2021.698102/full#supplementary-material

REFERENCES

Adornato, L. R., Kaltenbacher, E. A., Greenhow, D. R., and Byrne, R. H. (2007). High-resolution in situ analysis of nitrate and phosphate in the oligotrophic ocean. *Environ. Sc. Technol.* 41, 4045–4052. doi: 10.1021/es0700855

Aminot, A., and Kérouel, R. (1997). Assessment of heat treatment for nutrient preservation in seawater samples. *Anal. Chim. Acta* 351, 299–309. doi: 10.1016/S0003-2670(97)00366-8

Aminot, A., Kirkwood, D., and Carlberg, S. (1997). The QUASIMEME laboratory performance studies (1993–1995): overview of the nutrients section. *Mari. Pollut. Bull.* 35, 28–41. doi: 10.1016/S0025-326X(97)80876-4

Baccarelli, A., Pfeiffer, R., Consonni, D., Pesatori, A. C., Bonzini, M., Patterson, D. G., et al. (2005). Handling of dioxin measurement data in the presence of non-detectable values: overview of available methods and their application in the *Seveso chloracne* study. *Chemosphere* 60, 898–906. doi: 10.1016/j.chemosphere.2005.01.055

Barus, C., Romanytsia, I., Striebig, N., and Garçon, V. (2016). Toward an in situ phosphate sensor in seawater using Square Wave Voltammetry. *Talanta* 160, 417–424. doi: 10.1016/j.talanta.2016.07.057

Beaton, A. D., Cardwell, C. L., Thomas, R. S., Sieben, V. J., Legiret, F.-E., Waugh, E. M., et al. (2012). Lab-on-chip measurement of nitrate and nitrite for in situ analysis of natural waters. *Environ. Sci. Technol.* 46, 9548–9556.

Beaton, A. D., Sieben, V. J., Floquet, C. F., Waugh, E. M., Bey, S. A. K. I, Ogilvie, R., et al. (2011). An automated microfluidic colourimetric sensor applied in situ to determine nitrite concentration. *Sensors Actuat. B Chem.* 156, 1009–1014.

Birchill, A. J., Clinton-Bailey, G., Hanz, R., Mawji, E., Cariou, T., White, C., et al. (2019a). Realistic measurement uncertainties for marine macronutrient measurements conducted using gas segmented flow and Lab-on-Chip techniques. *Talanta* 200, 228–235.

Birchill, A. J., Hartner, N., Kunde, K., Siemering, B., Daniels, C., Gonzalez-Santana, D., et al. (2019b). The eastern extent of seasonal iron limitation in the high latitude North Atlantic Ocean. *Sci. Rep.* 9, 1–12.

Breitburg, D., Levin, L. A., Oschlies, A., Grégoire, M., Chavez, F. P., Conley, D. J., et al. (2018). Declining oxygen in the global ocean and coastal waters. *Science* 359:eaam7240. doi: 10.1126/science.aam7240

Burton, J. D. (1973). Problems in the analysis of phosphorus compounds. *Water Res.* 7, 291–307. doi: 10.1016/0043-1354(73)90170-X

Cleary, J., Maher, D., Slater, C., and Diamond, D. (2010). "In situ monitoring of environmental water quality using an autonomous microfluidic sensor," in *Proceeding Ofpaper Presented at 2010 IEEE Sensors Applications Symposium (SAS)*, 23–25.

Clementson, L. A., and Wayte, S. E. (1992). The effect of frozen storage of open-ocean seawater samples on the concentration of dissolved phosphate and nitrate. *Water Res.* 26, 1171–1176. doi: 10.1016/0043-1354(92)90177-6

Clinton-Bailey, G. S., Grand, M. M., Beaton, A. D., Nightingale, A. M., Owsianka, D. R., Slavik, G. J., et al. (2017). A lab-on-chip analyzer for in situ measurement of soluble reactive phosphate: improved phosphate blue assay and application to fluvial monitoring. *Environ. Sci. Technol.* 51, 9989–9995. doi: 10.1021/acs.est.7b01581

Cohen, M. J., Kurz, M. J., Heffernan, J. B., Martin, J. B., Douglass, R. L., Foster, C. R., et al. (2013). Diel phosphorus variation and the stoichiometry of ecosystem metabolism in a large spring-fed river. *Ecol. Monog.* 83, 155–176. doi: 10.1890/12-1497.1

Cordell, D., Drangert, J.-O., and White, S. (2009). The story of phosphorus: global food security and food for thought. *Global Environ. Change* 19, 292–305. doi: 10.1016/j.gloenvcha.2008.10.009

Daniel, A., Laës-Huon, A., Barus, C., Beaton, A. D., Blandfort, D., Guigues, N., et al. (2020). Toward a harmonization for using in situ nutrient sensors in the marine environment. *Front. Mari. Sci.* 6:773. doi: 10.3389/fmars.2019.00773

Davis, C. E., Mahaffey, C., Wolff, G. A., and Sharples, J. (2014). A storm in a shelf sea: Variation in phosphorus distribution and organic matter stoichiometry. *Geophys. Res. Lett.* 41, 8452–8459. 10.1002/2014GL061949

de Boyer Montégut, C., Madec, G., Fischer, A. S., Lazar, A., and Iudicone, D. (2004). Mixed layer depth over the global ocean: an examination of profile data and a profile-based climatology. *J. Geophys. Res. Oceans* 109:C12003. doi: 10.1029/2004JC002378

Dore, J. E., Houlihan, T., Hebel, D. V., Tien, G., Tupas, L., and Karl, D. M. (1996). Freezing as a method of sample preservation for the analysis of dissolved inorganic nutrients in seawater. *Mari. Chem.* 53, 173–185. doi: 10.1016/0304-4203(96)00004-7

Emeis, K.-C., van Beusekom, J. E. E., Callies, U., Ebinghaus, R., Kannen, A., Kraus, G., et al. (2015). The north seaa shelf sea in the anthropocene. *J. Mari. Syst.* 141, 18–33. doi: 10.1016/j.jmarsys.2014.03.012

EPA (2000). *Guidance for Data Quality Assessment Practical Methods for Data Analysis EPA QA/G-9Rep., Office of Environmental Information*. Washington DC: USA.

Eriksen, C. C., and Perry, M. J. (2009). The nurturing of seagliders by the national oceanographic partnership program. *Oceanography* 22, 146–157. doi: 10.5670/oceanog.2009.45

EU (2008). Directive 2008/56/EC of the european parliament and of the council. *Offi. J. Eur. Union*.

European-Environment-Agency (2019). *Nutrient Enrichment and Eutrophication in Europe's Seas: Moving Towards A Healthy Marine Environmentrep*. Luxembourg: European Union.

Frank, C., Schroeder, F., Ebinghaus, R., and Ruck, W. (2006). Using sequential injection analysis for fast determination of phosphate in coastal waters. *Talanta* 70, 513–517. doi: 10.1016/j.talanta.2005.12.055

García-Fernández, A. J., Gómez-Ramírez, P., Martínez-López, E., Hernández-García, A., María-Mojica, P., Romero, D., et al. (2009). Heavy metals in tissues from loggerhead turtles (*Caretta caretta*) from the southwestern Mediterranean (Spain). *Ecotoxicol. Environ. Safety* 72, 557–563. doi: 10.1016/j.ecoenv.2008.05.003

Gardolinski, P. C., Hanrahan, G., Achterberg, E. P., Gledhill, M., Tappin, A. D., House, W. A., et al. (2001). Comparison of sample storage protocols for the determination of nutrients in natural waters. *Water Res.* 35, 3670–3678. doi: 10.1016/S0043-1354(01)00088-4

Gilbert, M., Needoba, J., Koch, C., Barnard, A., and Baptista, A. (2013). Nutrient loading and transformations in the columbia river estuary determined by high-resolution in situ sensors. *Estuar. Coasts* 36, 708–727. doi: 10.1007/s12237-013-9597-0

Grand, M. M., Clinton-Bailey, G. S., Beaton, A. D., Schaap, A. M., Johengen, T. H., Tamburri, M. N., et al. (2017). A lab-on-chip phosphate analyzer for long-term in situ monitoring at fixed observatories: optimization and performance evaluation in estuarine and oligotrophic coastal waters. *Front. Mari. Sci.* 4:255. doi: 10.3389/fmars.2017.00255

Große, F., Kreus, M., Lenhart, H.-J., Pätsch, J., and Pohlmann, T. (2017). A novel modeling approach to quantify the influence of nitrogen inputs on the oxygen dynamics of the North Sea. *Front. Mari. Sci.* 4:383. doi: 10.3389/fmars.2017.00383

Hendry, K. R., Huvenne, V. A. I., Robinson, L. F., Annett, A., Badger, M., Jacobe, A. W., et al. (2019). The biogeochemical impact of glacial meltwater from southwest greenland. *Prog. Oceanog.* 176:102126. doi: 10.1016/j.pocean.2019.102126

Heslop, E. E., Ruiz, S., Allen, J., ópez-Jurado, J. L. L., Renault, L., and Tintoré, J. (2012). Autonomous underwater gliders monitoring variability at "choke points" in our ocean system: a case study in the Western Mediterranean Sea. *Geophys. Res. Lett.* 39:L20604. doi: 10.1029/2012gl053717

Hinrichs, I., Gouretski, V., Pätsch, J., Emeis, K., and Stammer, D. (2017b). *North Sea Biogeochemical Climatology Technical ReportRep*. Germany: CEN (Center for Earth System Research and Sustainability).

Hinrichs, I., Gouretski, V., Pätsch, J., Emeis, K.-C., and Stammer, D. (2017a). *North Sea Biogeochemical Climatology (Version 1.0)*. Hamburg, World Data Center for Climate (WDCC) at DKRZ, doi: 10.1594/WDCC/NSBClim_v1.0.

Hydes, D., Aoyama, M., Aminot, A., Bakker, K., Becker, S., Coverly, S., et al. (2010). "Determination of dissolved nutrients (N, P, SI) in seawater with high precision and inter-comparability using gas-segmented continuous flow analysers," in *The GO-SHIP Repeat Hydrography Manual: A Collection of Expert Reports and Guidelines. Version 1. IOCCP Report Number 14, ICPO Publication Series Number 134,* eds E. M. Hood, C. L. Sabine, and B. M. Sloyan, doi: 10.25607/OBP-15, Available online at: http://www.go-ship.org/HydroMan.html

HydroMet, O. (2020). *Technical Data Sea-Bird Scientific HydroCycle-PO4 Phosphate Sensor*. OTT. Available online at: https://www.ott.com/en-uk/products/water-quality-2/sea-bird-scientific-hydrocycle-po4-phosphate-sensor-1528/productAction/outputAsPdf/ (accessed April 2020).

Janzen, C. D., and Creed, E. L. (2011). "Physical oceanographic data from Seaglider trials in stratified coastal waters using a new pumped payload CTD," in *Proceeding of the Paper Presented at OCEANS'11 MTS/IEEE KONA*, 19–22.

Jickells, T. (1998). Nutrient biogeochemistry of the coastal zone. *Science* 281, 217–222. doi: 10.1126/science.281.5374.217

Johnson, K., Byrne, B., Balch, B., Bender, M., Benner, R., Bishop, J., et al. (2000). *Modern observing sytems working group summary*. New York: NY, OCTET.

Johnson, K. S., Berelson, W. M., Boss, E. S., Chase, Z., Claustre, H., Emerson, S. R., et al. (2009). Observing biogeochemical cycles at global scales with profiling floats and gliders: prospects for a global array. *Oceanography* 22, 216–225. doi: 10.5670/oceanog.2009.81

Jońca, J., Comtat, M., and Garçon, V. (2013). "Smart sensors for real-time water quality monitoring. smart sensors," in *Measurement and Instrumentation*, eds S. C. Mukhopadhyay and A. Mason (Berlin: Springer), doi: 10.1007/978-3-642-37006-9_2

Jońca, J., León Fernández, V., Thouron, D., Paulmier, A., Graco, M., and Garçon, V. (2011). Phosphate determination in seawater: toward an autonomous electrochemical method. *Talanta* 87, 161–167. doi: 10.1016/j.talanta.2011.09.056

Karl, D. M. (2014). Microbially mediated transformations of phosphorus in the sea: new views of an old cycle. *Ann. Rev. Mari. Sci.* 6, 279–337. doi: 10.1146/annurev-marine-010213-135046

Kattner, G. (1999). Storage of dissolved inorganic nutrients in seawater: poisoning with mercuric chloride. *Mari. Chem.* 67, 61–66. doi: 10.1016/S0304-4203(99)00049-3

Laane, R., van Leussen, W., Radach, G., Berlamont, J., Sündermann, J., van Raaphorst, W., et al. (1996a). North-west European shelf programme (NOWESP): an overview. *Deutsche Hydrografische Zeitschrift* 48, 217–229.

Laane, R. W., Svendsen, E., Radach, G., Groeneveld, G., Damm, P., PÄtsch, J., et al. (1996b). Variability in fluxes of nutrients (N, P, Si) into the North Sea from the atlantic ocean and skagerrak caused by variability in water flow. *Deutsche Hydrografische Zeitschrift* 48, 401–419.

Legiret, F.-E., Sieben, V. J., Woodward, E. M. S., Abi Kaed Bey, S. K., Mowlem, M. C., Connelly, D. P., et al. (2013). A high performance microfluidic analyser for phosphate measurements in marine waters using the vanadomolybdate method. *Talanta* 116, 382–387. doi: 10.1016/j.talanta.2013.05.004

Liblik, T., Karstensen, J., Testor, P., Alenius, P., Hayes, D., Ruiz, S., et al. (2016). Potential for an underwater glider component as part of the global ocean observing system. *Methods Oceanog.* 17, 50–82. doi: 10.1016/j.mio.2016.05.001

Lyddy-Meaney, A. J., Ellis, P. S., Worsfold, P. J., Butler, E. C., and McKelvie, I. D. (2002). A compact flow injection analysis system for surface mapping of phosphate in marine waters. *Talanta* 58, 1043–1053. doi: 10.1016/S0039-9140(02)00428-9

Marsh, R. I, Haigh, D., Cunningham, S. A., Inall, M. E., Porter, M., and Moat, B. I. (2017). Large-scale forcing of the European slope current and associated inflows to the north sea. *Ocean Sci.* 13, 315–335. doi: 10.5194/os-13-315-2017

Meyer, D. (2016). Glider technology for ocean observations: a review. *Ocean Sci. Dis.* 2016, 1–26.

Moore, C., Mills, M., Arrigo, K., Berman-Frank, I., Bopp, L., Boyd, P., et al. (2013). Processes and patterns of oceanic nutrient limitation. *Nat. Geosci.* 6, 701–710. doi: 10.1038/ngeo1765

Murphy, J., and Riley, J. P. (1962). A modified single solution method for the determination of phosphate in natural waters. *Anal. Chim. Acta* 27, 31–36. doi: 10.1016/S0003-2670(00)88444-5

Nagul, E. A. I, McKelvie, D., Worsfold, P., and Kolev, S. D. (2015). The molybdenum blue reaction for the determination of orthophosphate revisited: opening the black box. *Anal. Chim. Acta* 890, 60–82. doi: 10.1016/j.aca.2015.07.030

Nightingale, A. M., Beaton, A. D., and Mowlem, M. C. (2015). Trends in microfluidic systems for in situ chemical analysis of natural waters. *Sensors Actuat. B Chem.* 221, 1398–1405. doi: 10.1016/j.snb.2015.07.091

Painter, S. C., Lapworth, D. J., Woodward, E. M. S., Kroeger, S., Evans, C. D., Mayor, D. J., et al. (2018). Terrestrial dissolved organic matter distribution in the north sea. *Sci. Total Environ.* 630, 630–647. doi: 10.1016/j.scitotenv.2018.02.237

Palmer, M. R., Stephenson, G. R., Inall, M. E., Balfour, C., Düsterhus, A., and Green, J. (2015). Turbulence and mixing by internal waves in the Celtic Sea determined from ocean glider microstructure measurements. *J. Mari. Syst.* 144, 57–69. doi: 10.1016/j.jmarsys.2014.11.005

Porter, M., Dale, A., Jones, S., Siemering, B., and Inall, M. (2018). Cross-slope flow in the atlantic inflow current driven by the on-shelf deflection of a slope current. *Deep Sea Res. Part I Oceanog. Res. Papers* 140, 173–185. doi: 10.1016/j.dsr.2018.09.002

Poulton, A. J., Davis, C. E., Daniels, C. J., Mayers, K. M. J., Harris, C., Tarran, G. A., et al. (2019). Seasonal phosphorus and carbon dynamics in a temperate shelf sea (Celtic Sea). *Prog. Oceanog.* 177:101872. doi: 10.1016/j.pocean.2017.11.001

Queste, B. (2013). *Hydrographic Observations of Oxygen and Related Physical Variables in the North Sea and Western Ross Sea Polynya: Investigations Using Seagliders, Historical Observations and Numerical Modelling*. Norwich, University of East Anglia.

Radach, G., and Pätsch, J. (1997). Climatological annual cycles of nutrients and chlorophyll in the North Sea. *J. Sea Res.* 38, 231–248. doi: 10.1016/S1385-1101(97)00048-8

Redfield, A. C. (1934). "On the proportions of organic derivatives in sea water and their relation to the composition of plankton," in *James Johnstone memorial* (Liverpool: Univ. Press), 176–192.

Roemmich, D., Boehme, L., Claustre, H., Freeland, H., Fukasawa, M., Goni, G., et al. (2010). Integrating the ocean observing system: mobile platforms. *Proc. OceanObs* 9:33.

Rudnick, D. L. (2016). Ocean research enabled by underwater gliders. *Ann. Rev. Mari. Sci.* 8, 519–541. doi: 10.1146/annurev-marine-122414-033913

SEAL-Analytical (2019). *AA3 P04 Application Notes*. Germany: Porvair.

Sharples, J., Tweddle, J. F., Mattias Green, J., Palmer, M. R., Kim, Y.-N., Hickman, A. E., et al. (2007). Spring-neap modulation of internal tide mixing and vertical nitrate fluxes at a shelf edge in summer. *Limnol. Oceanog.* 52, 1735–1747. doi: 10.4319/lo.2007.52.5.1735

Sheehan, P. M., Berx, B., Gallego, A., Hall, R. A., Heywood, K. J., and Hughes, S. L. (2017). Thermohaline forcing and interannual variability of northwestern inflows into the northern North Sea. *Continental Shelf Res.* 138, 120–131. doi: 10.1016/j.csr.2017.01.016

Sheehan, P. M., Berx, B., Gallego, A., Hall, R. A., Heywood, K. J., and Queste, B. Y. (2020). Weekly variability of hydrography and transport of northwestern inflows into the northern North Sea. *J. Mari. Syst.* 204:103288. doi: 10.1016/j.jmarsys.2019.103288

Siemering, B., Bresnan, E., Painter, S. C., Daniels, C. J., Inall, M., and Davidson, K. (2016). Phytoplankton distribution in relation to environmental drivers on the north west european shelf sea. *PLoS One* 11:e0164482. doi: 10.1371/journal.pone.0164482

Slater, C., Cleary, J., Lau, K.-T., Snakenborg, D., Corcoran, B., Kutter, J. P., et al. (2010). Validation of a fully autonomous phosphate analyser based on a microfluidic lab-on-a-chip. *Water Sci. Technol.* 61, 1811–1818. doi: 10.2166/wst.2010.069

Tajimi, M., Uehara, R., Watanabe, M., Oki, I., Ojima, T., and Nakamura, Y. (2005). Correlation coefficients between the dioxin levels in mother's milk and the distances to the nearest waste incinerator which was the largest source of dioxins from each mother's place of residence in Tokyo, Japan. *Chemosphere* 61, 1256–1262. doi: 10.1016/j.chemosphere.2005.03.096

Testor, P., de Young, B., Rudnick, D. L., Glenn, S., Hayes, D., Lee, C. M., et al. (2019). OceanGliders: a component of the integrated GOOS. *Front. Mari. Sci.* 6:422. doi: 10.3389/fmars.2019.00422

Thomson-Bulldis, A., and Karl, D. (1998). Application of a novel method for phosphorus determinations in the oligotrophic North Pacific Ocean. *Limnol. Oceanog.* 43, 1565–1577. doi: 10.4319/lo.1998.43.7.1565

Thouron, D., Vuillemin, R., Philippon, X., Lourenço, A., Provost, C., Cruzado, A., et al. (2003). An autonomous nutrient analyzer for oceanic long-term in situ biogeochemical monitoring. *Anal. Chem.* 75, 2601–2609. doi: 10.1021/ac020696

Tweddle, J. F., Sharples, J., Palmer, M. R., Davidson, K., and McNeill, S. (2013). Enhanced nutrient fluxes at the shelf sea seasonal thermocline caused by stratified flow over a bank. *Prog. Oceanog.* 117, 37–47. doi: 10.1016/j.pocean.2013.06.018

Vincent, A. G., Pascal, R. W., Beaton, A. D., Walk, J., Hopkins, J. E., Woodward, E. M. S., et al. (2018). Nitrate drawdown during a shelf sea spring bloom revealed using a novel microfluidic in situ chemical sensor deployed within an autonomous underwater glider. *Mari. Chem.* 205, 29–36. doi: 10.1016/j.marchem.2018.07.005

Vitaliano, J. J., and Zdanowicz, V. S. (1992). Trace metals in eggs of winter flounder from boston harbor, a contaminated North American estuary. *Mari. Pollut. Bull.* 24, 364–367. doi: 10.1016/0025-326X(92)90374-F

Waldmann, C., Tamburri, M., Prien, R., and Fietzek, P. (2010). Assessment of sensor performance. *Ocean Sci.* 6, 235–245. doi: 10.5194/os-6-235-2010

Wei, H., Pan, D., and Han, H. (2021). Electrochemical monitoring of marine nutrients: from principle to application. *TrAC Trends Anal. Chem.* 138:116242. doi: 10.1016/j.trac.2021.116242

Winther, N. G., and Johannessen, J. A. (2006). North sea circulation: atlantic inflow and its destination. *J. Geophys. Res. Oceans* 111. doi: 10.1029/2005JC003310

Worsfold, P., McKelvie, I., and Monbet, P. (2016). Determination of phosphorus in natural waters: a historical review. *Anal. Chim. Acta* 918, 8–20. doi: 10.1016/j.aca.2016.02.047

Conflict of Interest: MM, ADB, and RP are co-founders and employees of Clearwater Sensors.

The remaining authors declare that the research was conducted in the absence of any commercial or financial relationships that could be construed as a potential conflict of interest.

frontiers in Marine Science

METHODS
published: 21 July 2021
doi: 10.3389/fmars.2021.679534

Advanced Remote Data Acquisition Using a Pop-Up Data Shuttle (PDS) to Report Data From Current- and Pressure-Recording Inverted Echo Sounders (CPIES)

Chanhyung Jeon[1,2], Jae-Hun Park[3], Maureen Kennelly[4], Erran Sousa[4], D. Randolph Watts[4], Eun-Joo Lee[3], Taewook Park[5] and Thomas Peacock[1]*

[1] Department of Mechanical Engineering, Massachusetts Institute of Technology, Cambridge, MA, United States, [2] Department of Oceanography, Pusan National University, Busan, South Korea, [3] Department of Ocean Sciences, Inha University, Incheon, South Korea, [4] Graduate School of Oceanography, University of Rhode Island, Narragansett, RI, United States, [5] Korea Polar Research Institute, Incheon, South Korea

OPEN ACCESS

Edited by:
Alex Nimmo-Smith, University of Plymouth, United Kingdom

Reviewed by:
Antoine De Ramon N'Yeurt, University of the South Pacific, Fiji
Xiao-Hua Zhu, Second Institute of Oceanography, Ministry of Natural Resources, China

***Correspondence:**
Jae-Hun Park
jaehunpark@inha.ac.kr

Specialty section:
This article was submitted to Ocean Observation, a section of the journal Frontiers in Marine Science

Received: 12 March 2021
Accepted: 23 June 2021
Published: 21 July 2021

Citation:
Jeon C, Park J-H, Kennelly M, Sousa E, Watts DR, Lee E-J, Park T and Peacock T (2021) Advanced Remote Data Acquisition Using a Pop-Up Data Shuttle (PDS) to Report Data From Current- and Pressure-Recording Inverted Echo Sounders (CPIES). Front. Mar. Sci. 8:679534. doi: 10.3389/fmars.2021.679534

A current- and pressure-recording inverted echo sounder (CPIES) placed on the sea floor monitors aspects of the physical ocean environment for periods of months to years. Until recently, acoustic telemetry of daily-processed data was the existing method for data acquisition from CPIES without full instrument recovery. However, this approach, which requires positioning a ship at the mooring site and operator time, is expensive and time-consuming. Here, we introduce a new method of obtaining data remotely from CPIES using a popup-data-shuttle (PDS), which enables straightforward data acquisition without a ship. The PDS data subsampled from CPIES has 30–60 min temporal resolution. The PDS has a scheduled pop-up-type release system, so each data pod floats to the sea surface at a user-specified date and relays the recorded data via the Iridium satellite system. We demonstrated the capability of an array of PDS-CPIES via two successful field experiments in the Arctic Ocean. The data acquired through the PDS were in agreement with the fully recovered datasets. An example of the data retrieved from the PDS shows that time-varying signals of tides and high-frequency internal waves were well captured. GPS-tracked trajectories of the PDS floating free at the sea surface can provide insights into ice drift or ocean surface currents. This PDS technology provides an alternative method for remote deep-ocean mooring data acquisition.

Keywords: pop-up data shuttle, remote data acquisition, advanced technology, temporal high-resolution data, deep-ocean mooring

INTRODUCTION

Deep-sea mooring, an Eulerian method, is typically used to measure oceanic variables at a fixed location. A pressure-recording inverted echo sounder (PIES) or PIES with a current sensor (CPIES), installed on the sea floor, is a well-established and highly reliable tool for long-term monitoring of large-scale ocean flows and has been successfully used in the world's oceans (Sun and Watts, 2001; Watts et al., 2001b; Book et al., 2002; Zhu et al., 2003; Park et al., 2005; Andres et al., 2008, 2015;

Donohue et al., 2010). The CPIES measures the current 50 m above the bottom, as well as bottom pressure and round-trip acoustic travel time from the sea floor to the sea surface (τ).

The PIES or CPIES-measured variables have been used to investigate oceanic barotropic and baroclinic variabilities. For example, in low- and mid-latitude oceans, acoustic travel time has been used to estimate, with remarkable accuracy, time-varying vertical profiles of temperature (Watts and Rossby, 1977; Watts et al., 2001a; Park et al., 2005) and geopotential height (Chiswell et al., 1988; Baker-Yeboah et al., 2009; Park et al., 2012; Behnisch et al., 2013; Donohue et al., 2016; Jeon et al., 2018; Andres et al., 2020). Moreover, a recent field experiment in Sermilik Fjord in Greenland showed the possibility of detecting ice thickness variations using τ (Andres et al., 2015). Observations of bottom pressure conveys a variety of information such as tides, barotropic responses to wind forcing (Park and Watts, 2005b, 2006a; Na et al., 2012, 2016; Zhao et al., 2017; Zheng et al., 2020), and gravity anomalies at the sea bottom (Park et al., 2008). A two-dimensional array of appropriately spaced CPIES can enable the visualization of two- or three-dimensional structures of geostrophic currents and eddies (Tracey et al., 1997; Meinen, 2001; Mitchell et al., 2005; Park et al., 2005; Donohue et al., 2010; Na et al., 2014; Zhao et al., 2020) as well as linear and nonlinear internal wave fields (Park and Watts, 2005a, 2006b; Alford et al., 2015; Zhao et al., 2018; Ramp et al., 2019). Current records allow the investigation of abyssal currents and waves in the deep ocean (Watts et al., 2001b; Park and Watts, 2005a; Park et al., 2010), and bottom pressures and deep currents can both provide referencing to make velocity profiles absolute.

The PIES or CPIES can carry out measurements in the range of approximately 500–6,700 m water depths from periods of months up to 5 years, depending on the measurement schedule and the depth (Donohue et al., 2010). For data acquisition without full instrument recovery, an existing method is acoustic telemetry of *in situ* processed data, which involves onsite ship surveys (e.g., Chaplin, 1990). That approach requires ship and operator times, skilled techniques, laborious tasks, and substantial costs and thus is costly and time-consuming. As an alternative approach, the University of Rhode Island (URI) has newly developed a cost- and time-effective advanced remote data acquisition method using pop-up data shuttle (PDS) capability (**Figure 1**). Here, we introduce this PDS system and present its performance through two field experiments conducted in 2017 and 2018 in the western Arctic Ocean. The methodology and economic benefits of the PDS data acquisition system are described, and illustrations are given of the scientific data and broadened applications.

POP-UP DATA SHUTTLE CURRENT- AND PRESSURE-RECORDING INVERTED ECHO SOUNDER (PDS-CPIES) FIELD EXPERIMENTS IN THE ARCTIC OCEAN

PDS

The PDS is an add-on device designed for use with PIES or CPIES to retrieve the data remotely (**Figure 1A**) with a deployment capability of 7,000 m in depth and 4 years in maximum time (deployment capability of PIES or CPIES is 6,700 m in depth and 5 years in maximum time). The PDS using alkaline batteries has no measurement sensors of its own but receives the hourly data broadcast from the PIES or CPIES and floats to the sea surface at a time programmed by the user. Once on the surface, the PDS transmits the recorded data via the Iridium satellite constellation to an email server ashore (**Figure 1B**). At the sea floor, the PIES or CPIES and a cluster of PDS capsules within a short-range (<2 m) are linked wirelessly through a magnetic field (**Figure 1C**, copied from the Popeye Data Shuttle User's Manual, 2021). Data are broadcast from the PIES or CPIES to all PDS capsules within range as time-delay encoded amplitude modulations of the magnetic field. The PIES or CPIES generates a magnetic field by driving a series-tuned ferrite-coil antenna that is mounted inside the PIES or CPIES glass housing. Each PDS capsule is equipped with a magnetic field detector to convert the amplitude modulations of the field into digital signals. For high-quality response, broadcast and receiving antennas are designed as narrow-band pairs, optimizing error-free reception. The received signals at each PDS are decoded and logged to a memory card. For robust performance in ocean environments, the communication is one-way (from PIES or CPIES to PDS) that includes checksum error detection. If an error is detected by the PDS, the received data will still be logged but flagged as failing the checksum validation. This allows the PDS system, which includes the broadcast hardware in the PIES or CPIES and the PDS itself, to be simple (inexpensive and expendable) yet highly reliable. Each PDS has a burn-wire release system that is activated when PDS system time matches the user programmed release time. In addition, the PDS has an Iridium Short Burst Data (SBD) modem to transmit the data to the Iridium satellite constellation and a GPS receiver. Once on the surface, the PDS can be commanded via the Iridium connection to acquire and transmit GPS positions at selected intervals ranging from several minutes up to a week.

Field Experiments

Two field experiments using PDS-CPIES were conducted from 2017/2018 through 2020 in the western Arctic Ocean to monitor heat content changes over the water column, sea-ice thickness, and internal wave activity. These experiments facilitated scientific data capture and PDS performance analysis in extreme circumstances. A total of six sets of PDS-CPIES were deployed in the Arctic Ocean: AES1–AES3 in the Northwind Abyssal Plain (NAP) in August 2017 and AES4–AES6 on the Chukchi shelf slope of the Canada Basin in September 2018 (**Figure 2A**). All CPIES were deployed with either 3 or 4 PDS. The earliest scheduled release of PDS was ∼1 month after the deployment to confirm the capability of PDS and CPIES operation and to be free from the interference of freezing sea-ice in October. Other PDSs were programmed to release after 1 or 2 years to obtain long-term data. The PDS release schedules are indicated in **Figure 2B** with gray triangles. One recovery cruise with the icebreaker RV *Araon* occurred in late August 2020, during which all six CPIES were successfully recovered, along with full data records.

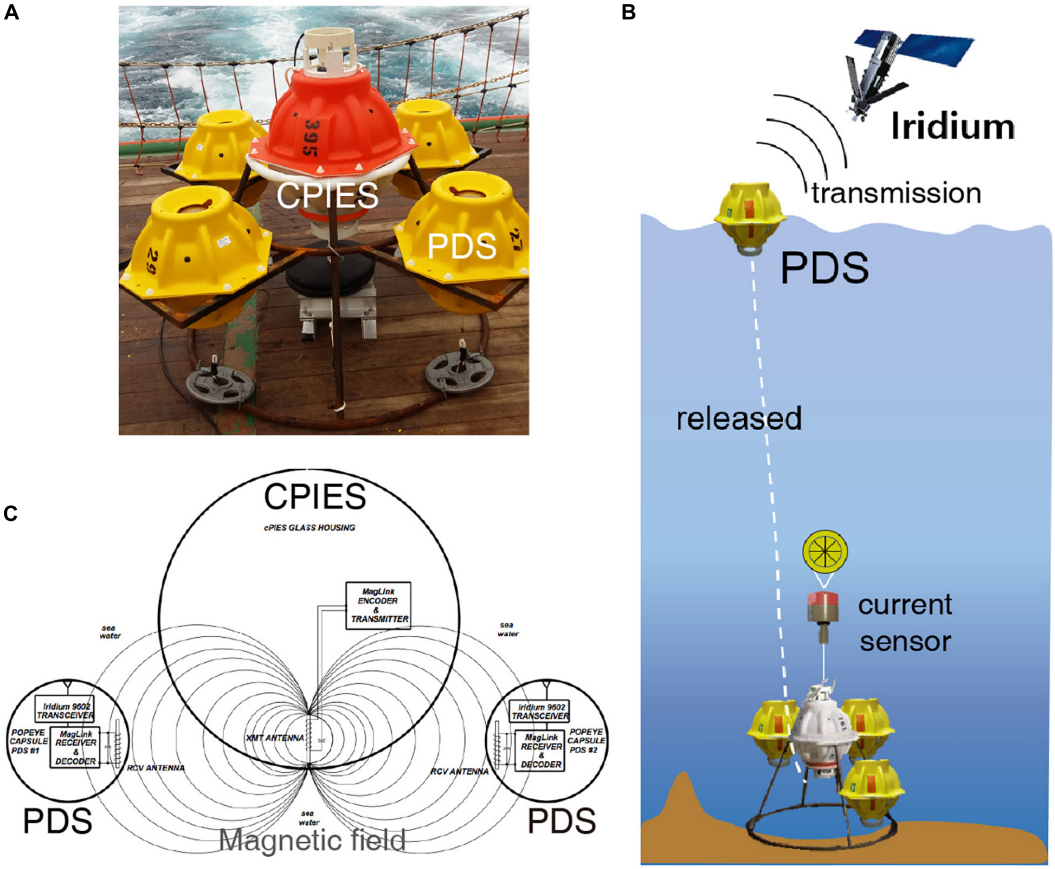

FIGURE 1 | (A) Assembled PDS-CPIES on RV *Araon*. **(B)** Concept of PDS operation. **(C)** Concept of subsea wireless link using magnetic field between CPIES and PDS (selected from PDS manual). PDS, pop-up data shuttle; CPIES, current- and pressure-recording inverted echo sounder.

The measurement settings of the deployed CPIES are as follows: τ measured 96 pings per hour with an accuracy of 0.05 ms, whereas the current and bottom pressure values were measured every 30 min. The Aanderaa Doppler current-meter (ZPulse model 4930 DW; Aanderaa Data Instruments, Bergen, Norway) has a speed range of 0–300 cm s^{-1} in a detected direction. The pressure sensor was a Paroscientific Digiquartz model 410K-101 with an accuracy of ±0.01% FS and 0.001 dbar (Paroscientific, Inc., Redmond Washington). The obtained PDS data consisted of hourly τ (1st quartile value after windowing outliers) and 30-min-interval current and bottom pressure readings.

PERFORMANCE OF THE PDS SYSTEM

PDS Release System

First Deployments in 2017

A total of 12 Model 3F PDSs were deployed during the first (i.e., 2017) experiment (**Figure 2B**) after successful prelaunch tests. The PDS includes a feature that it will start the release process if it does not receive valid data from the host CPIES for six successive hours. This feature affected 6 of the 2017 deployed PDSs (inverted yellow triangles in **Figure 2B**): four popped up within 3 days of the deployment and two additional PDSs were released within 30 days of deployment, hence 6 of 12 were much earlier than programmed. In addition, two PDSs on AES2 did not send any signals even after the time of the CPIES recovery (inverted red triangles). Four PDSs released on time (inverted blue and cyan triangles), and we remotely acquired the CPIES-transmitted data from three of those. The fourth PDS had system reset issues on the surface and no useful data were recovered. The data are transmitted Last In First Out (LIFO). When the PDS resets, the file pointer is lost and the PDS repeats data previously transmitted. A command was transmitted to the PDS via Iridium to stop further data transmission. Due to the problems of communication between the CPIES and PDSs at depth and subsequent early release in the first (i.e., 2017) experiment, technical issues were identified and addressed by upgrading firmware and hardware on both the PDS and the transmitting hardware mounted inside of the CPIES.

Second Deployments in 2018

After the firmware and hardware modifications of the PDS-CPIES, an array of three PDS-CPIES with a total of 11 Model 3G PDSs were deployed during the second (i.e., 2018) experiment

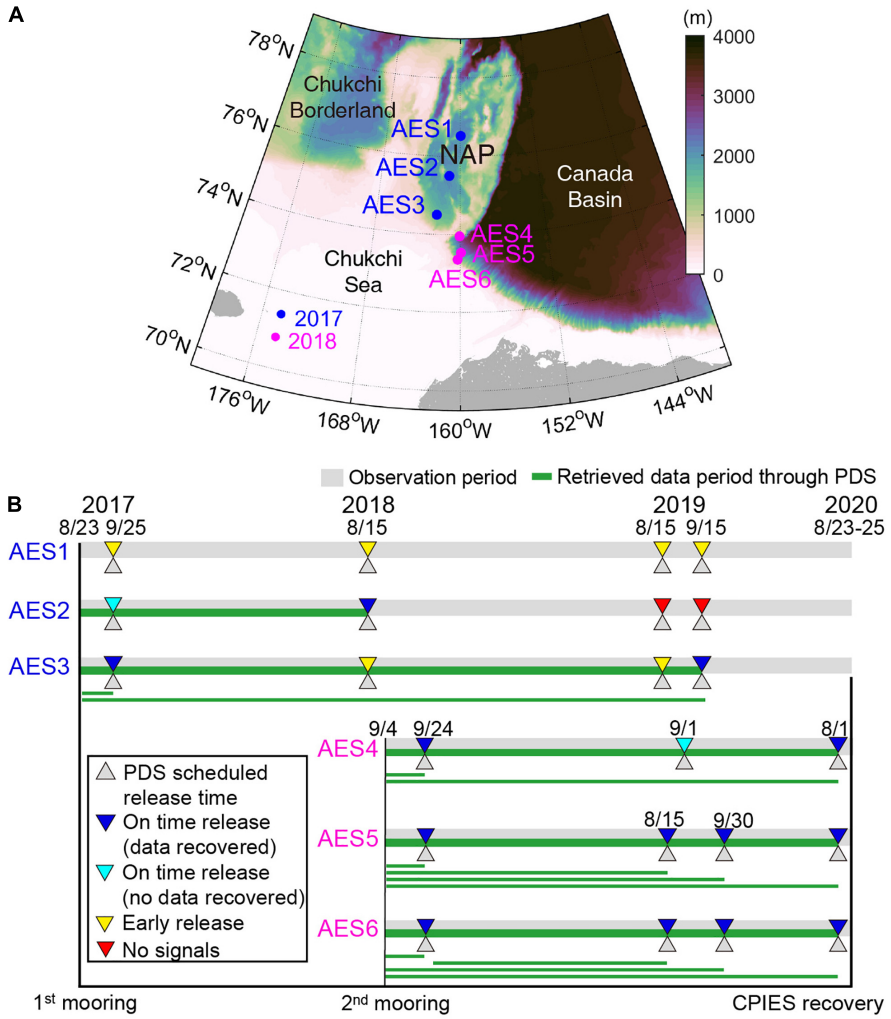

FIGURE 2 | (A) Location of PDS-CPIES deployment in the western Arctic Ocean. Blue and magenta circles indicate locations in 2017 and 2018, respectively. Background colors indicate bathymetry every 100 m. NAP: Northwind Abyssal Plain. **(B)** Timeline of CPIES observation and PDS operation time. Gray and green lines indicate the duration of CPIES observation and retrieved data period through PDS, respectively. Thin green lines indicate the retrieved data period through individual PDSs. Triangles indicate PDS-related information; gray triangles are the scheduled PDS release time, whereas inverted blue (and cyan) triangles indicate on-time PDS release with success (and failure) of remote data retrieval. Inverted yellow (and red) triangles indicate the failure of on-time release of PDS with early release (and no signals). Substantial system-upgrades addressed problems observed with the 2017 deployment, producing much better performance in 2018.

(**Figure 2B**). All PDSs released as scheduled, although one PDS did not successfully send its data due to repeated resets on the sea surface. Based on the results of the two experiments, the PDS system has been further improved for robustness and reliability.

Data Transmission and Acquisition

To examine the data transmission performance from CPIES to the email server ashore, we calculated the data acquisition rate through comparison of the internally saved data in CPIES (after recovery and processed as described in Kennelly et al., 2007) and the remotely retrieved data (via PDS). Bottom pressure and current time series were used for this comparison, because although τ was properly recorded in the CPIES, the internal processing of τ for transmittal to the PDS was only done correctly in the 2018 experiment. **Figure 3A** presents the averaged data acquisition rates in the first and second experiments. For this calculation, we selected the PDSs that released as programmed and for which data were recovered (blue triangles in **Figure 2**); thus, 3 and 10 sets of PDS datasets were used in the first and second experiments, respectively. The acquisition rates were higher than 99.9% (99.94 and 99.98% in the first and second experiments, respectively). Prior to CPIES recovery, users also can confirm the success or failure of data transmission from CPIES to PDS using the recorded checksum flag. **Figure 3B** shows the average percentage of good versus bad data in the PDS time series. The percentage good data was 99.7% (99.4% in minimum) and 99.9% in first and second experiments, respectively. The acquisition rate and percentage of suitable τ data reached 99.9% in the 2018 experiment as in the pressure and current data. These demonstrate that the

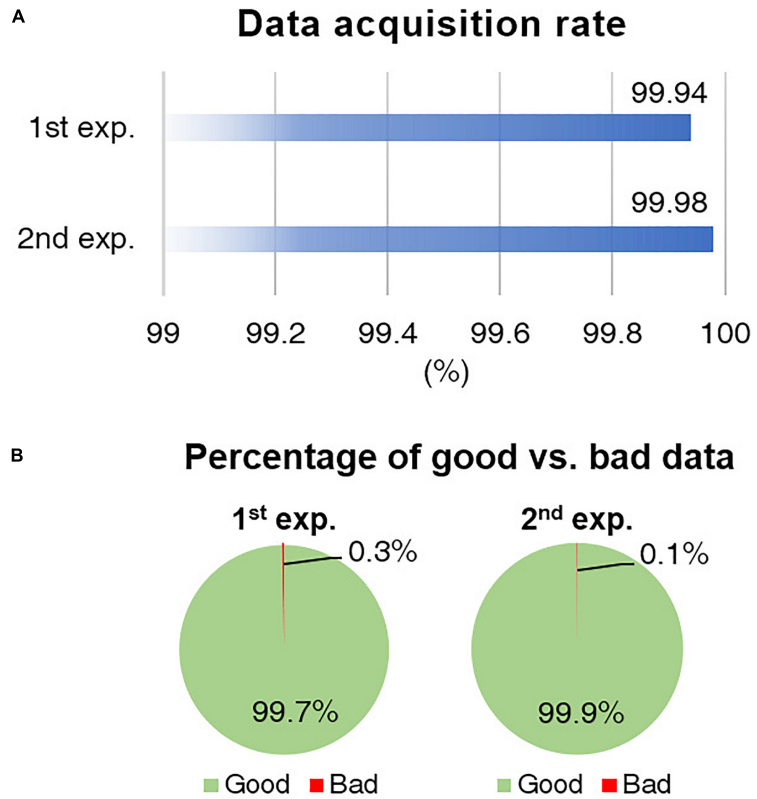

FIGURE 3 | (A) Data acquisition rate calculated through the comparison of internally saved and remotely retrieved data. **(B)** Percentage of good versus bad data in remotely retrieved dataset.

process of data transmission from CPIES to the email server ashore worked well.

Example of Remotely Acquired Data Using PDS

The existing method in the PIES or CPIES using *in situ* shipboard acoustic pulse delay telemetry (PDT) provides processed daily values; however, data acquired from the PDS consist of hourly τ and 30-min-interval single-depth current and bottom pressure values. **Figure 4** shows an example time series of all variables at the AES4 site of second experiment for the period of October 9–22, 2019 (14 days). The 14-day-long example highlights the hour-to-day variabilities which would be averaged out using daily processed data in the previously existing shipboard PDT method.

Tide-induced variation was predominant in the bottom pressure time series (**Figure 4A**). Semidiurnal and diurnal tides were dominant; hence, mixed tidal cycle and diurnal inequality were seen in the time series. The τ in polar oceans can be affected by changes in temperature, salinity, sea surface height, and sea-ice thickness; hence, the obtained τ values showed many fluctuations at various time scales (**Figure 4B**). Overall, changes larger than 0.0015 s were rare in the τ records, yet a notable ∼0.002 s early echo was observed on October 19, probably due to the ∼1.5-m thickness of sea-ice, in that, 0.75-m sea-ice thickness is known to cause a 1-ms early echo time in τ. We may guess the size of sea-ice with the early echo signal under following simple assumptions. If the sea-ice moves with a speed of 0.05–0.1 m s^{-1} on average in the same direction for 16 h and the shape is close to a circle, the diameter reaches roughly 2.9–5.8 km; and thus, this floating ice is indeed hard to be resolved in current satellite-based products such as daily sea-ice products with 25-km (e.g., Cavalieri et al., 1996; Brodzik and Stewart, 2016) and 4-km (Fetterer et al., 2015) spatial resolutions. The near-bottom zonal and meridional velocities showed highly fluctuating patterns (**Figure 4C**). The average current speed was 0.027 m s^{-1}, although sometimes it reached ∼0.1 m s^{-1}. Another notable feature is a periodicity of the current from October 13 through 20, i.e., a 30–50-h period. This motion may have been caused by bottom-trapped topographic Rossby waves that existed in regions of abrupt bathymetric change at these latitudes of the Arctic Ocean (Ku et al., 2020).

Location Reporting System

The PDS, once adrift on the sea surface, transmitted its location regularly. The initial setting of the location reporting was once per day. Two PDS trajectories released at AES4 are plotted in **Figure 5**; one for September 24, 2018 (1st PDS) and the other for August 1, 2020 (3rd PDS). The 2nd PDS from site AES4 failed to report location. Based on the reported locations, including the error range of the longitude and latitude, we omitted erroneous values (∼5% in total).

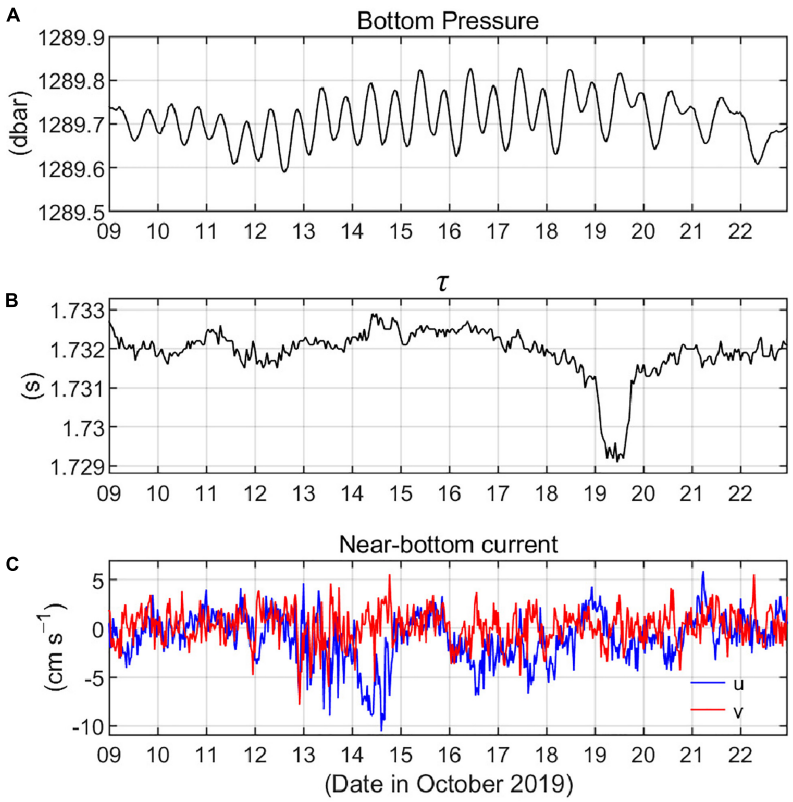

FIGURE 4 | Example of time series acquired from PDS at site AES4. **(A)** Bottom pressure, **(B)** τ, and **(C)** zonal and meridional velocities for the 14-day period of October 9–22, 2019.

The 1st PDS moved to the east initially and switched its direction to the north on September 29, 2018. It drifted to the north continuously, and the last signal of 2018 was reported on December 19. It resumed its location reporting on January 18, 2019 but was lost again on January 30 and had no more reports in 2019. The PDS resumed its location reporting on January 18, 2020, in the Canada Basin, and the final signal was on October 9, 2020. The location signals were intermittent between October 19, 2018 and August 29, 2020, presumably due to interference or confinement by the sea-ice. Nevertheless, the 1st PDS endured longer than 2 years in the extreme circumstances of the Arctic Ocean, thus demonstrating its durability and usability.

The 3rd PDS drifted to the northwest for ∼30 days and then moved north/northeastward after wandering. The PDS has an antenna enabling two-way communication with the Iridium satellite; hence, we could control the data transmission and the time interval of location reporting. We switched the time interval to 6 h on August 8, 2020 as indicated by red dots along the black solid line in **Figure 5**. The temporally high-resolution PDS trajectory, to a certain extent, can provide some insights into ice drift or ocean surface current.

Economic Benefits of PDS System

Here we compare the economic costs for remote data acquisition between the new (PDS) and the existing (acoustic telemetry) methods (**Figure 6**). The existing method requires approximately 14,500 USD for one-site ship operation for navigation from one site to another and for data recovery using acoustic telemetry. Note that this is a minimal assumption that the ship is already operating in the area, avoiding long transit costs to and from the site. The ship cost estimation is based on the Korean icebreaker RV *Araon* (50,000 USD per day) that conducted the first deployment and CPIES recovery cruise. Additionally, the existing method demanded skilled technicians, equipment, and ship operations, accompanied by travel and shipping costs (at least 4,500 USD). The new method using the PDS requires a budget of 5,000 USD for one PDS capsule and 400 USD for one antenna embedded inside PIES or CPIES glass-housing to transmit the measured data. A year's worth of CPIES data costs 460.5 USD due to Iridium service, as the 1-year-long data payload is 307 kilobytes (Popeye Data Shuttle User's Manual, 2021). This method requires no ship operation. Therefore, the new method saves ∼70% of the cost compared to the previous shipboard PDT method.

CONCLUSION AND SUMMARY

We introduce a newly developed remote data acquisition method using PDS to support CPIES, a type of deep-sea

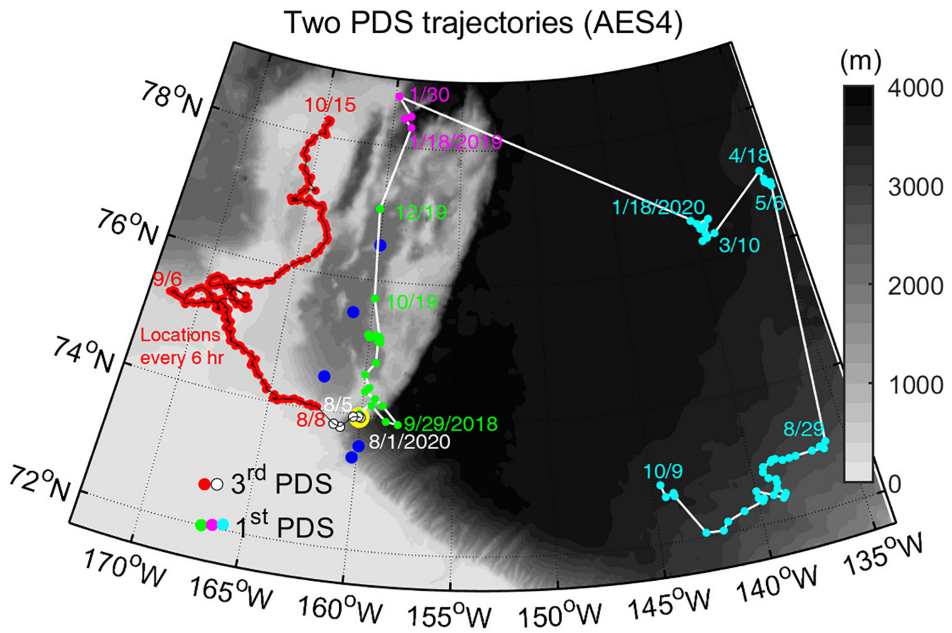

FIGURE 5 | Two PDS trajectories released at AES4 site on September 24, 2018 (1st PDS) and August 1, 2020 (3rd PDS). White line indicates the 1st PDS trajectory with the green, magenta, and cyan dots along the line denoting daily locations in the years 2018–2020, respectively. Black line indicates the 3rd PDS trajectory with the white and red dots along the line denoting locations every day and 6 h, respectively. Note that bad locations (~5%) are not shown. Yellow (AES4) and blue (AES 1–3, 5, 6) dots indicate CPIES sites as in **Figure 2**. Dots at certain locations with mm/dd or mm/dd/yyyy date designations mark the PDS positions at 00 h GMT on those dates.

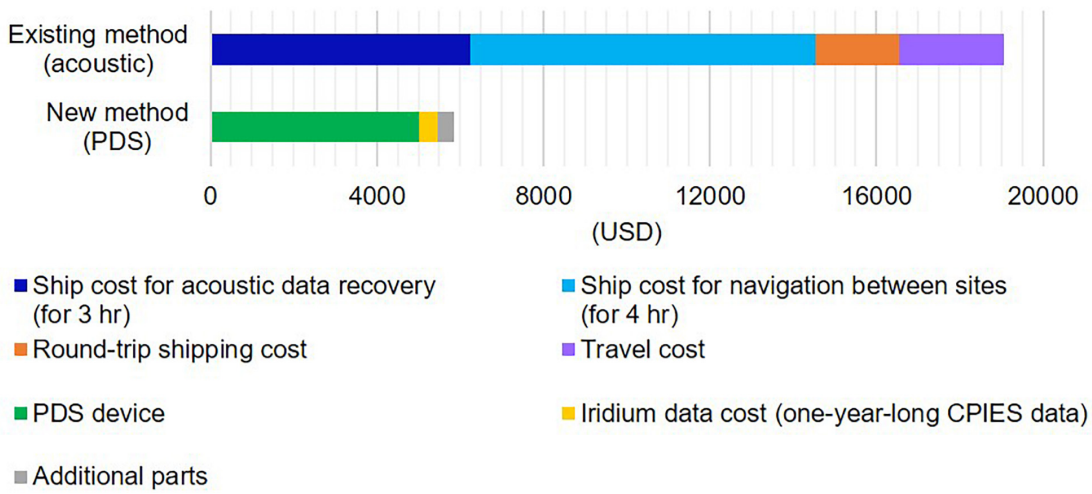

FIGURE 6 | Cost comparison for data acquisition between the existing and the new methods. Note that the ship cost estimation is based on the Korean icebreaker RV *Araon* (50,000 USD per day) used in the first deployment and CPIES recovery cruises.

mooring instrument to measure barotropic and baroclinic oceanic variabilities. Prior to this development, for data acquisition prior to recovery, the PIES or CPIES used acoustic telemetry, which involves positioning a ship at the mooring site; thus, that method requires ship and operator times which are both costly. In contrast, the new method utilizing PDS capability enables a more straightforward data acquisition without ship operation.

Scientific benefits arise because the PDS transmits high temporal-resolution data, and logistical benefits arise from its scheduled pop-up-type release system—the data pod floats to the surface at a user-chosen time to transmit the recorded data via the Iridium constellation of satellites to an email server ashore. The high temporal-resolution PDS data, well representing time-varying signals from hour timescale, enable rapid resolution of scientific questions.

The performance of the PDS system was verified in two field experiments conducted in the western Arctic Ocean. Substantial system hardware and firmware upgrades were made prior to the second deployment to address problems that were discovered in the first deployment. This produced great reliability in the PDS release system, data transmission and acquisition, and data quality. Further, the PDS system can save valuable cost and time and represents a secure and reliable method of advanced remote data acquisition. Hence, this novel method provides a robust capability for remote deep-ocean mooring data acquisition, which has not been readily feasible with autonomous data relay technologies.

DATA AVAILABILITY STATEMENT

The original contributions presented in the study are publicly available. This data can be found here: https://github.com/PADOLab1/PDS_Paper_Data.git.

AUTHOR CONTRIBUTIONS

CJ: primary writing, *in situ* moorings, and calculations. J-HP and TPe: *in situ* moorings, overall coordination, and discussion. MK, ES, and DW: writing, discussion, and development of PDS-CPIES. E-JL and TPa: data collection, processing, and discussion. All authors modify the manuscript.

FUNDING

This study was supported by ONR "Stratified Ocean Dynamics of the Arctic" Grant number N000141612450 and the ONR Global grant (N62909-17-1-2041). Supports for this research were also provided by "Test of long-term monitoring system installation for oceanic environmental changes caused by accelerated sea-ice melting in the Chukchi Sea (20210540)" funded by the MOF, and Basic Science Research Program through the National Research Foundation of Korea (NRF) funded by the Ministry of Education (2021R1I1A305799311).

ACKNOWLEDGMENTS

An array of six PDS-CPIES deployments and CTD hydrocasts were conducted by RV *Araon* and RV *Sikuliaq*; we would like to express our deepest gratitude to the crew and scientists for their dedicated help. We wish to acknowledge and give highest thanks to Mr. Gerard Chaplin, who prior to his retirement from URI was Project Engineer and led in the conceptualization and initial development of the PDS system for PIES.

REFERENCES

Alford, M. H., Peacock, T., Mackinnon, J. A., Nash, J. D., Buijsman, M. C., Centuroni, L. R., et al. (2015). The formation and fate of internal waves in the South China Sea. *Nature* 521, 65–69. doi: 10.1038/nature14399

Andres, M., Musgrave, R. C., Rudnick, D. L., Zeiden, K. L., Peacock, T., and Park, J.-H. (2020). On the predictability of sea surface height around Palau. *J. Phys. Oceanogr.* 50, 1–76. doi: 10.1175/jpo-d-19-0310.1

Andres, M., Silvano, A., Straneo, F., and Watts, D. R. (2015). Icebergs and sea ice detected with inverted echo sounders. *J. Atmospheric Oceanic Technol.* 32, 1042–1057. doi: 10.1175/JTECH-D-14-00161.1

Andres, M., Wimbush, M., Park, J.-H., Chang, K.-I., Lim, B.-H., Watts, D. R., et al. (2008). Observations of Kuroshio flow variations in the East China Sea. *J. Geophys. Res.* 113:C05013. doi: 10.1029/2007JC004200

Baker-Yeboah, S., Watts, D. R., and Byrne, D. A. (2009). Measurements of sea surface height variability in the eastern South Atlantic from pressure sensor-equipped inverted echo sounders: Baroclinic and barotropic components. *J. Atmospheric Oceanic Technol.* 26, 2593–2609. doi: 10.1175/2009JTECHO659.1

Behnisch, M., Macrander, A., Boebel, O., Wolff, J. O., and Schröter, J. (2013). Barotropic and deep-referenced baroclinic SSH variability derived from Pressure Inverted Echo Sounders (PIES) south of Africa. *J. Geophys. Res. Oceans* 118, 3046–3058. doi: 10.1002/jgrc.20195

Book, J. W., Wimbush, M., Imawaki, S., Ichikawa, H., Uchida, H., and Kinoshita, H. (2002). Kuroshio temporal and spatial variations South of Japan determined from inverted echo sounder measurements. *J. Geophys. Res. Oceans* 107, 4.1–4.12. doi: 10.1029/2001jc000795

Brodzik, M. J., and Stewart, J. S. (2016). *Near-Real-Time SSM/I-SSMIS EASE-Grid Daily Global Ice Concentration and Snow Extent, Version 5*. Boulder, Colorado: NASA National Snow and Ice Data Center Distributed Active Archive Center.

Cavalieri, D. J., Parkinson, C. L., Gloersen, P., and Zwally, H. J. (1996). *Sea Ice Concentrations from Nimbus-7 SMMR and DMSP SSM/I-SSMIS Passive Microwave Data, Version 1*. Boulder, Colorado: NASA National Snow and Ice Data Center Distributed Active Archive Center.

Chaplin, G. F. (1990). *Acoustic telemetry system for real-time monitoring of the Gulf Stream path*. Washington, DC: IEEE, 46–51.

Chiswell, S. M., Wimbush, M., and Lukas, R. (1988). Comparison of dynamic height measurements from an inverted echo sounder and an island tide gauge in the central Pacific. *J. Geophys. Res.* 93:2277. doi: 10.1029/jc093ic03p02277

Donohue, K. A., Kennelly, M. A., and Cutting, A. (2016). Sea surface height variability in drake passage. *J. Atmos. Ocean. Technol.* 33, 669–683. doi: 10.1175/JTECH-D-15-0249.1

Donohue, K. A., Watts, D. R., Tracey, K. L., Greene, A. D., and Kennelly, M. (2010). Mapping circulation in the Kuroshio Extension with an array of current and pressure recording inverted echo sounders. *J. Atmospheric Oceanic Technol.* 27, 507–527. doi: 10.1175/2009JTECHO686.1

Fetterer, F., Stewart, J. S., and Meier, W. N. (2015). *MASAM2: Daily 4 km Arctic Sea Ice Concentration, Version 1*. Boulder, Colorado: National Snow and Ice Data Center.

Jeon, C., Park, J.-H., Kim, D. G., Kim, E., and Jeon, D. (2018). Comparison of measurements from pressure-recording inverted echo sounders and satellite altimetry in the north equatorial current region of the Western Pacific. *Ocean Sci. J.* 53, 207–213. doi: 10.1007/s12601-018-0012-4

Kennelly, M., Tracey, K. L., and Watts, D. R. (2007). *Inverted echo sounder data processing manual*.

Ku, A., Seung, Y. H., Jeon, C., Choi, Y., Yoshizawa, E., Shimada, K., et al. (2020). Observation of bottom-trapped topographic rossby waves on the shelf break of the Chukchi Sea. *J. Geophys. Res. Oceans* 125, 1–14. doi: 10.1029/2019JC015436

Meinen, C. S. (2001). Structure of the North Atlantic current in stream-coordinates and the circulation in the Newfoundland basin. *Deep-Sea Res. I* 48, 1553–1580. doi: 10.1016/S0967-0637(00)00103-5

Mitchell, D. A., Teague, W. J., Wimbush, M., Watts, D. R., and Sutyrin, G. G. (2005). The dok cold Eddy. *J. Phys. Oceanogr.* 35, 273–288. doi: 10.1175/JPO-2684.1

Na, H., Park, J.-H., Randolph Watts, D., Donohue, K. A., and Lee, H. J. (2012). Near 13 day barotropic ocean response to the atmospheric forcing in the North Pacific. *J. Geophys. Res. Oceans* 117, 1–12. doi: 10.1029/2012JC008211

Na, H., Watts, D. R., Park, J.-H., Jeon, C., Lee, H. J., Nonaka, M., et al. (2016). Bottom pressure variability in the Kuroshio Extension driven by the atmosphere and ocean instabilities. *J. Geophys. Res. Oceans* 121, 6507–6519. doi: 10.1002/2016JC012097

Na, H., Wimbush, M., Park, J.-H., Nakamura, H., and Nishina, A. (2014). Observations of flow variability through the Kerama gap between the East China Sea and the Northwestern Pacific. *J. Geophys. Res. Oceans* 119, 689–703. doi: 10.1002/2013JC008899

Park, J.-H., Donohue, K. A., Watts, D. R., and Rainville, L. (2010). Distribution of deep near-inertial waves observed in the Kuroshio Extension. *J. Oceanogr.* 66, 709–717. doi: 10.1007/s10872-010-0058-0

Park, J.-H., and Watts, D. R. (2005a). Near-inertial oscillations interacting with mesoscale circulation in the southwestern Japan/East Sea. *Geophys. Res. Lett.* 32, 1–4. doi: 10.1029/2005GL022936

Park, J.-H., and Watts, D. R. (2005b). Response of the southwestern Japan/East Sea to atmospheric pressure. *Deep-Sea Res. II* 52, 1671–1683. doi: 10.1016/j.dsr2.2003.08.007

Park, J.-H., and Watts, D. R. (2006a). Near 5-day nonisostatic response of the Atlantic Ocean to atmospheric surface pressure deduced from sub-surface and bottom pressure measurements. *Geophys. Res. Lett.* 33, 1–5. doi: 10.1029/2006GL026304

Park, J.-H., and Watts, D. R. (2006b). Internal tides in the southwestern Japan/East Sea. *J. Phys. Oceanogr.* 36, 22–34. doi: 10.1175/JPO2846.1

Park, J.-H., Watts, D. R., Donohue, K. A., and Jayne, S. R. (2008). A comparison of in situ bottom pressure array measurements with GRACE estimates in the Kuroshio Extension. *Geophys. Res. Lett.* 35, 1–5. doi: 10.1029/2008GL034778

Park, J.-H., Watts, D. R., Donohue, K. A., and Tracey, K. L. (2012). Comparisons of sea surface height variability observed by pressure-recording inverted echo sounders and satellite altimetry in the Kuroshio Extension. *J. Oceanogr.* 68, 401–416. doi: 10.1007/s10872-012-0108-x

Park, J.-H., Watts, D. R., Tracey, K. L., and Mitchell, D. A. (2005). A multi-index GEM technique and its application to the southwestern Japan/East Sea. *J. Atmospheric Oceanic Technol.* 22, 1282–1293. doi: 10.1175/JTECH-1668.1

Popeye Data Shuttle User's Manual. (2021). *Graduate School of Oceanography*. Narragansett, RI: University of Rhode Island.

Ramp, S. R., Park, J.-H., Yang, Y. J., Bahr, F. L., and Jeon, C. (2019). Latitudinal structure of solitons in the South China Sea. *J. Phys. Oceanogr.* 49, 1747–1767. doi: 10.1175/jpo-d-18-0071.1

Sun, C., and Watts, D. R. (2001). A circumpolar gravest empirical mode for the Southern Ocean hydrography. *J. Geophys. Res. Oceans* 106, 2833–2855. doi: 10.1029/2000jc900112

Tracey, K. L., Howden, S. D., and Watts, D. R. (1997). IES calibration and mapping procedures. *J. Atmospheric Oceanic Technol.* 14, 1483–1493. doi: 10.1175/1520-04261997014<1483:ICAMP<2.0.CO;2

Watts, D. R., and Rossby, H. T. (1977). Measuring dynamic heights with inverted echo sounders: results from MODE. *J. Phys. Oceanogr.* 7, 345–358. doi: 10.1175/1520-04851977007<0345:MDHWIE<2.0.CO;2

Watts, D. R., Sun, C., and Rintoul, S. (2001a). A two-dimensional gravest empirical mode determined from hydrographic observations in the subantarctic front. *J. Phys. Oceanogr.* 31, 2186–2209. doi: 10.1175/1520-04852001031<2186:ATDGEM<2.0.CO;2

Watts, D. R., Qian, X., and Tracey, K. L. (2001b). Mapping abyssal current and pressure fields under the meandering gulf stream. *J. Atmospheric Oceanic Technol.* 18, 1052–1067. doi: 10.1175/1520-04262001018<1052:MACAPF<2.0.CO;2

Zhao, R., Nakamura, H., Zhu, X. H., Park, J.-H., Nishina, A., Zhang, C., et al. (2020). Tempo-spatial variations of the Ryukyu current southeast of Miyakojima Island determined from mooring observations. *Sci. Rep.* 10, 1–10. doi: 10.1038/s41598-020-63836-5

Zhao, R., Zhu, X.-H., and Park, J.-H. (2017). Near 5-Day nonisostatic response to atmospheric surface pressure and coastal-trapped waves observed in the Northern South China Sea. *J. Phys. Oceanogr.* 47, 2291–2303. doi: 10.1175/JPO-D-17-0013.1

Zhao, R., Zhu, X. H., Park, J.-H., and Li, Q. (2018). Internal tides in the northwestern South China Sea observed by pressure-recording inverted echo sounders. *Prog. Oceanogr.* 168, 112–122. doi: 10.1016/j.pocean.2018.09.019

Zheng, H., Zhu, X. H., Nakamura, H., Park, J.-H., Jeon, C., Zhao, R., et al. (2020). Generation and propagation of 21-day bottom pressure variability driven by wind stress curl in the East China Sea. *Acta Oceanol. Sinica* 39, 91–106. doi: 10.1007/s13131-020-1603-3

Zhu, X. H., Han, I. S., Park, J.-H., Ichikawa, H., Murakami, K., Kaneko, A., et al. (2003). The Northeastward current southeast of Okinawa Island observed during November 2000 to August 2001. *Geophys. Res. Lett.* 30, 3–6. doi: 10.1029/2002GL015867

Conflict of Interest: The authors declare that the research was conducted in the absence of any commercial or financial relationships that could be construed as a potential conflict of interest.

frontiers in Marine Science

ORIGINAL RESEARCH
published: 11 August 2021
doi: 10.3389/fmars.2021.681265

A Standard Criterion for Measuring Turbulence Quantities Using the Four-Receiver Acoustic Doppler Velocimetry

Hyoungchul Park[1] *and Jin Hwan Hwang*[1,2]*

[1] *Department of Civil and Environmental Engineering, Seoul National University, Seoul, South Korea,* [2] *Institute of Construction and Environmental Engineering, Seoul National University, Seoul, South Korea*

Acoustic Doppler velocimetry (ADV) enables three-dimensional turbulent flow fields to be obtained with high spatial and temporal resolutions in the laboratory, rivers, and oceans. Although such advantages have led ADV to become a typical approach for analyzing various fluid dynamics mechanisms, the vagueness of ADV system operation methods has reduced its accuracy and efficiency. Accordingly, the present work suggests a proper measurement strategy for a four-receiver ADV system to obtain reliable turbulence quantities by performing laboratory experiments under two flow conditions. Firstly, in still water, the magnitude of noises was evaluated and a proper operation method was developed to obtain the Reynolds stress with lower noises. Secondly, in channel flows, an optimal sampling period was determined based on the integral time scale by applying the bootstrap sampling method and reverse arrangement test. The results reveal that the noises of the streamwise and transverse velocity components are an order of magnitude larger than those of the vertical velocity components. The orthogonally paired receivers enable the estimation of almost-error-free Reynolds stresses and the optimal sampling period is 150–200 times the integral time scale, regardless of the measurement conditions.

Keywords: turbulence, acoustic velocimeter, sampling times, integral time scales, sampling error reduction

OPEN ACCESS

Edited by:
Ho Kyung Ha,
Inha University, South Korea

Reviewed by:
Prashanth Hanmaiahgari,
Indian Institute of Technology Kharagpur, India
Jun Choi,
Pukyong National University, South Korea

***Correspondence:**
Jin Hwan Hwang
jinhwang@snu.ac.kr

Specialty section:
This article was submitted to Ocean Observation, a section of the journal Frontiers in Marine Science

Received: *16 March 2021*
Accepted: *23 July 2021*
Published: *11 August 2021*

Citation:
Park H and Hwang JH (2021) A Standard Criterion for Measuring Turbulence Quantities Using the Four-Receiver Acoustic Doppler Velocimetry. Front. Mar. Sci. 8:681265. doi: 10.3389/fmars.2021.681265

INTRODUCTION

Acoustic Doppler velocimetry (ADV) is one of the most popular instruments for measuring three-dimensional flow velocities in research related to water resources. It easily obtains velocity fields with high sampling rates for small sampling volumes and little data contamination. These advantages have led to the use of ADV in numerous studies to analyze the various physical mechanisms observed in the laboratory as well as in field studies (e.g., Kim et al., 2000; Reidenbach et al., 2006; Nystrom et al., 2007; Wang et al., 2012; Salim et al., 2017; Park and Hwang, 2019). For example, Reidenbach et al. (2006) investigated the turbulence and flow structure in a boundary layer over a coral reef in field observations using ADV, and Park and Hwang (2019) used this approach in the laboratory to elucidate the mechanisms within a vegetated channel.

Although ADV is a robust and user-friendly technique, it has several limitations. First, the velocity data inevitably include measurement noises inherently produced by the measurement

system itself or poor external conditions as fluctuations (Doroudian et al., 2010). Such noises are negligible in the mean-field estimates but still influences turbulence quantities such as the turbulence intensity and the Reynolds shear stress, which are the most important physical variables in turbulent flows (McLelland and Nicholas, 2000). Accordingly, several researchers have evaluated such noises from the ADV measurements by conducting laboratory experiments in still water (e.g., Nikora and Goring, 1998; Voulgaris and Trowbridge, 1998; McLelland and Nicholas, 2000). However, because these researchers mainly considered ADV using three receivers, the ADV having four receivers, which was more recently introduced, has not been sufficiently investigated even though it is used popularly.

The second limit is that the strategy and standard method of determining a proper sampling time have not been well known so far, which makes users lack confidence about their measurements and raises doubts about the reliability of the measured data, particularly turbulence quantities. A short data recording period can cause a loss of information about low-frequency motions, which constitute a dominant factor causing errors in turbulence quantities (Soulsby, 1980). Meanwhile, excessively long and redundant records result in ineffective measurement and the inability to capture spatial flow fields with high spatial resolution owing to the limited time. Nevertheless, the sampling period has been determined only by the experience or judgment of the researchers without any definite standard in many cases.

Hence, several researchers have proposed criteria for the optimal measurement period based on statistical methods (e.g., Sukhodolov and Rhoads, 2001; Buffin-Bélanger and Roy, 2005; Chanson et al., 2007; Chanson, 2008). Buffin-Bélanger and Roy (2005) reported that the interval 60–90 s is the optimal sampling time range to describe most turbulence statistics, whereas Chanson (2008) demonstrated that the sampling duration should be at least 10 min to obtain the proper Reynolds stresses. However, the most critical drawback of such studies is that the proposed sampling period depends considerably on the scale of the experiment and the flow conditions of the target area and thus is not suitable as a measurement criterion.

To overcome this limitation, Lesht (1980) and Petrie et al. (2013) quantified the sampling time based on the integral time scale representing the time scale of the largest turbulent eddies and concluded that the measurement period should exceed 20 times the integral time scale to achieve stationarity of the mean velocity. Because the integral time scale can reflect the flow characteristics under diverse conditions and in various locations, this method can be recommended as an appropriate technique for determining the sampling period. However, the previous researchers only considered the mean velocity rather than other hydraulic parameters and lack of verification whether the optimal record length is sufficient to describe the physical characteristics of long-time-series data.

Therefore, the main objective of this study is to develop an ADV measurement strategy using four receivers to obtain reliable turbulent quantities. Experiments were conducted under two flow conditions: (1) in still water and (2) in an open channel flow. In the still water experiment, the magnitude of the Doppler noises was evaluated and a proper ADV operation method is suggested to obtain the turbulence quantities with less noises. In the open channel experiment, the optimal sampling period based on the integral time scale was determined under various flow conditions by applying the non-parametric bootstrap method and reverse arrangement test. The results obtained from the velocity data collected during the optimal sampling period in each case were verified by comparing them with those computed based on velocity data measured for a sufficiently long time, which could be assumed as ground truth values.

MATERIALS AND METHODS

Description of ADV

ADV is a bistatic acoustic instrument that measures three velocity components over a small sampling volume. This instrument consists of one transmitter and several receivers and operates theoretically based on the Doppler shift effect. A transmitter located in the middle of the receivers which are deployed separately emits acoustic pulses into the water flow and each receiver detects the pulses scattered back from suspended particles within the sampling volume (**Figure 1**). The movement of particles shifts the phase of the emitted acoustic pulses to the back-scattered pulses due to the Doppler effect, and this shifted phase is converted into the radial flow velocity (V_i) based on the following equation (Lane et al., 1998):

$$V_i = \frac{c}{4\pi f_{\mathrm{ADV}}} \cdot \frac{d\phi}{dt}, \tag{1}$$

where the subscript i can be from 1 to 4 and denotes the component in each receiver, c is the speed of sound in water, f_{ADV} is the frequency of sound emitted by the ADV device, and $d\phi/dt$ is the phase difference given by

$$\frac{d\phi}{dt} = \frac{1}{\Delta t} \tan^{-1} \left[\frac{\sin\left[\phi\left(t\right)\right] \cos\left[\phi\left(t+\Delta t\right)\right] - \sin\left[\phi\left(t+\Delta t\right)\right] \cos\left[\phi\left(t\right)\right]}{\cos\left[\phi\left(t\right)\right] \cos\left[\phi\left(t+\Delta t\right)\right] + \sin\left[\phi\left(t\right)\right] \sin\left[\phi\left(t+\Delta t\right)\right]} \right], \tag{2}$$

where ϕ is the signal phase in radians, t is the time, and Δt is the time difference between transmissions.

The ADV device (Vectrino+) used in this study is a point measurement instrument having a downward-looking probe with four receivers. In this four-receiver configuration, all receivers are orthogonal to each other and surrounding the transmitter. Two receivers deployed in the longitudinal direction (R1 and R3 in **Figure 1B**) measure the streamwise velocity, u and vertical velocity, w_1, whereas the remaining two receivers that are arranged in the transverse direction (R2 and R4 in **Figure 1B**) measure the transverse velocity, v, and vertical velocity, w_2. Here, the vertical velocities, w_1 and w_2, are measured redundantly but independently, and this arrangement can be utilized for noise analysis (Doroudian et al., 2010).

The radial flow velocity components along each receiver axis (V_1, V_2, V_3, and V_4) are obtained by the Eq. 1 and then

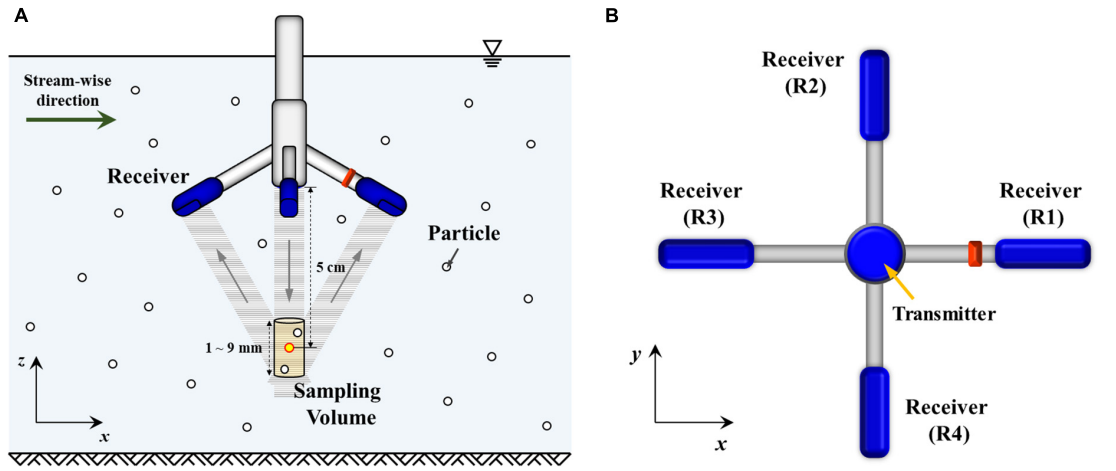

FIGURE 1 | Schematic diagram of ADV system: **(A)** Side view; **(B)** top view.

transformed into the Cartesian coordinate system (u, v, w_1, and w_2) by multiplying the 4×4 transformation matrix T_m as follows:

$$\begin{bmatrix} u \\ v \\ w_1 \\ w_2 \end{bmatrix} = \underbrace{\begin{bmatrix} a_{11} & a_{12} & a_{13} & a_{14} \\ a_{21} & a_{22} & a_{23} & a_{24} \\ a_{31} & a_{32} & a_{33} & a_{34} \\ a_{41} & a_{42} & a_{43} & a_{44} \end{bmatrix}}_{T_m} \cdot \begin{bmatrix} V_1 \\ V_2 \\ V_3 \\ V_4 \end{bmatrix}, \tag{3}$$

The transformation matrix elements are determined based on the geometric relationship between the transmitter and receivers during the calibration process by the manufacturer. Accordingly, each ADV device has its transformation matrix, as introduced in **Table 1**, which remains invariant unless the equipment undergoes physical deformation (Voulgaris and Trowbridge, 1998).

Experimental Setup

Two kinds of laboratory experiments were performed in the Hydraulic and Coastal Engineering Laboratory of Seoul National University. The first kind of experiment was conducted in still water to evaluate the system and surrounding noises of the ADV device in the various velocity ranges and sample volumes for setup. Still water conditions were created by filling water with seeding particles into a bucket, and the velocity was measured 12 cm away from the bottom when no movement was observed at the water surface. Data were collected in a total of 125 cases by changing five transmit length (0.3, 0.6, 1.2, 1.8, and 2.4 mm), five heights of sampling volume determined depending on the transmit length, and five nominal velocity ranges (± 0.03, 0.1, 0.3, 1.0, and 2.5 m/s). The velocity was measured at 100 Hz for 100 s in each case.

The second kind of experiments was performed in a 6.5-m-long, 0.15-m-wide, and 0.3-m-deep glass-walled recirculating flume to evaluate the proper sampling duration required to collect the various turbulence statistics. As presented in **Table 2**, the present work analyzed eight flow conditions with cross-sectional averaged streamwise velocities (U) ranging from 0.10 to 0.37 m/s. The vertical profile of the turbulent statistics was obtained from measurements taken at several locations over the acrylic bed for each flow condition. The data acquisition period lasted approximately 1 h for each measurement depth at 30 Hz to ensure that the data were sufficiently long to describe the turbulence field in the open channel as Chanson (2008) suggests. In the time series of the velocity data, the spikes that can overestimate the turbulence statistics were excluded and replaced following the phase-space threshold method suggested by Goring and Nikora (2002).

Determination of Record Length

When turbulence quantities are measured in a flow, the proper sampling duration needs to be selected carefully because a shorter sampling time loses the lower-frequency turbulent motions, whereas an excessive sampling time reduces the efficiency of the experimental procedures and does not allow to have the required spatial resolution. To determine the proper sampling duration, the non-parametric bootstrap sampling method and reverse arrangement test were applied in the present work. **Supplementary Figure A.1** illustrates the overall procedures, and each process can be described as follows. The first step is to compute the integral time scale characterizing the time scale of the largest eddies from the measured velocities based on the following equation (Nystrom et al., 2007):

$$T_i \equiv \int_0^{t_0} R_i(\tau)\, d\tau, \tag{4}$$

where τ is a time lag between two points in time series data, t_0 is the time of the first zero-crossing in the normalized autocorrelation function (O'Neill et al., 2004). $R_i(\tau)$ can be calculated as follows:

$$R_i(\tau) \equiv \frac{\langle u_i(t)\, u_i(t+\tau) \rangle}{\langle u_i(t)^2 \rangle}, \tag{5}$$

here, $u_i(t)$ is the velocity component, and the subscript i denotes the x, y, or z direction. The integral time scale is calculated for

TABLE 1 | Specification of ADV.

Description	Values
Operating frequency	10 MHz
Sampling rate	1–200 Hz
Number of receivers	4
Distance of sampling volume from transmitter	0.05 m
Sampling volume diameter	6 mm
Sampling volume height	1–9.1 mm
Transmit length	0.3, 0.6, 1.2, 1.8, 2.4 mm
Velocity ranges	± 0.03, 0.1, 0.3, 1.0, 2.5, 4.0 m/s
Accuracy	± 0.5% of measured value ± 1.0 mm/s
Transformation matrix	$\begin{bmatrix} 1.9841 & 0 & -1.9797 & 0 \\ 0 & 2.0205 & 0 & -2.0034 \\ 0.5081 & 0 & 0.5251 & 0 \\ 0 & 0.4829 & 0 & 0.5491 \end{bmatrix}$

TABLE 2 | Experimental conditions.

Case	Q (m^3/s)	H (m)	U (m/s)	z/H	n_p	$\overline{u}$ (m/s)	u_* (m/s)	T (sec)
1	1.42×10^{-3}	0.09	1.05×10^{-1}	0.12 ∼ 0.39	7	9.99×10^{-2} ∼ 1.05×10^{-1}	3.32×10^{-3}	0.33 ∼ 0.61
2	2.00×10^{-3}	9.50×10^{-2}	1.40×10^{-1}	0.04 ∼ 0.37	7	1.34×10^{-1} ∼ 1.50×10^{-1}	3.36×10^{-3}	0.30 ∼ 0.40
3	1.67×10^{-3}	0.07	1.59×10^{-1}	0.04 ∼ 0.24	6	1.48×10^{-1} ∼ 1.70×10^{-1}	5.70×10^{-3}	0.33 ∼ 0.44
4	2.50×10^{-3}	7.80×10^{-2}	2.14×10^{-1}	0.04 ∼ 0.32	8	1.95×10^{-1} ∼ 2.20×10^{-1}	5.99×10^{-3}	0.26 ∼ 0.40
5	3.33×10^{-3}	8.50×10^{-2}	2.61×10^{-1}	0.03 ∼ 0.39	10	2.33×10^{-1} ∼ 2.60×10^{-1}	5.86×10^{-3}	0.19 ∼ 0.34
6	4.17×10^{-3}	9.30×10^{-2}	2.99×10^{-1}	0.03 ∼ 0.44	12	2.65×10^{-1} ∼ 2.94×10^{-1}	6.36×10^{-3}	0.16 ∼ 0.30
7	5.00×10^{-3}	0.10	3.33×10^{-2}	0.03 ∼ 0.37	11	2.94×10^{-1} ∼ 3.25×10^{-1}	6.56×10^{-3}	0.15 ∼ 0.27
8	5.00×10^{-3}	0.09	3.70×10^{-2}	0.02 ∼ 0.40	9	3.16×10^{-1} ∼ 3.63×10^{-1}	8.12×10^{-3}	0.14 ∼ 0.22

each direction, and the maximum value among them becomes the representative integral time scale (T).

The next step is sampling data sequentially within the entire time series dataset based on the bootstrap sampling method. To elaborate, 1000 subsamples with a length of the integral time scale were extracted at a random location and five hydraulic parameters representing the flow characteristics such as the temporal-averaged stream-wise velocity ($\bar{u}$), the stream-wise and vertical turbulence intensities (u'_{rms} and w'_{rms}), the Reynolds shear stress ($\overline{u'w'}$), and the turbulent kinetic energy (k) were computed for all subsamples. And then the standard error was calculated from the following equation:

$$\varepsilon_X = \sqrt{\frac{\sum_{m=0}^{m=N} (X_m - \langle X \rangle)^2}{N-1}}, \tag{6}$$

where, ε_X is the standard error of the hydraulic parameter, N is the number of subsamples fixed as 1000 in this work, X is one of the five hydraulic parameters and $\langle X \rangle$ is the ensemble average of the selected parameter over 1000 subsamples. Once ε_X for the subsamples with a length of the integral time scale are computed, the next step is to repeat the above procedure by changing the length of subsample. The length of the subsample was determined as 1–1000 times of the integral time scale and the standard error of each case is represented by $\varepsilon_{\alpha,X}$. Here, α ranging from 1 to 1000 means the length of the subsample. As an example, $\varepsilon_{1,X}$ and $\varepsilon_{1000,X}$ are the standard errors of subsample having a length of 1 and 1000 times the integral time scale, respectively.

When we set X equal to u'_{rms} , the variation of the standard error for u'_{rms} with α can be represented in **Figure 2**. According to **Figure 2**, the slope of the standard error (ε'_X ($= d\varepsilon_X/d\alpha$)) approaches zero with increasing α and eventually converges. This means that when the sample length exceeds a critical value, the hydraulic parameter changes no longer. To define the starting point of convergence (α_c), the reverse arrangement test allowing us to quantify whether a significant trend in the dataset (Beck et al., 2006) was applied to ε'_X . Firstly, a sequence of n observations of ε'_X was extracted, where the observations are denoted as $\varepsilon'_{p,X}$ and p is from α to α+n-1 (e.g., α = 1, n = 3: observations = $\varepsilon'_{1,X}$, $\varepsilon'_{2,X}$, $\varepsilon'_{3,X}$). In the present study, n was determined to be 100, which is long enough to represent the overall trend of the dataset. The second step was counting the number of times that $\varepsilon'_{p,X} > \varepsilon'_{q,X}$ for $p < q$ and to compute A based on the following equation:

$$A = \sum_{p=1}^{n-1} \sum_{q=p+1}^{n} h_{pq}, \tag{7}$$

where

$$h_{pq} = \begin{cases} 1 & \text{if } \varepsilon'_{p,X} > \varepsilon'_{q,X} \\ 0 & \text{otherwise} \end{cases}, \tag{8}$$

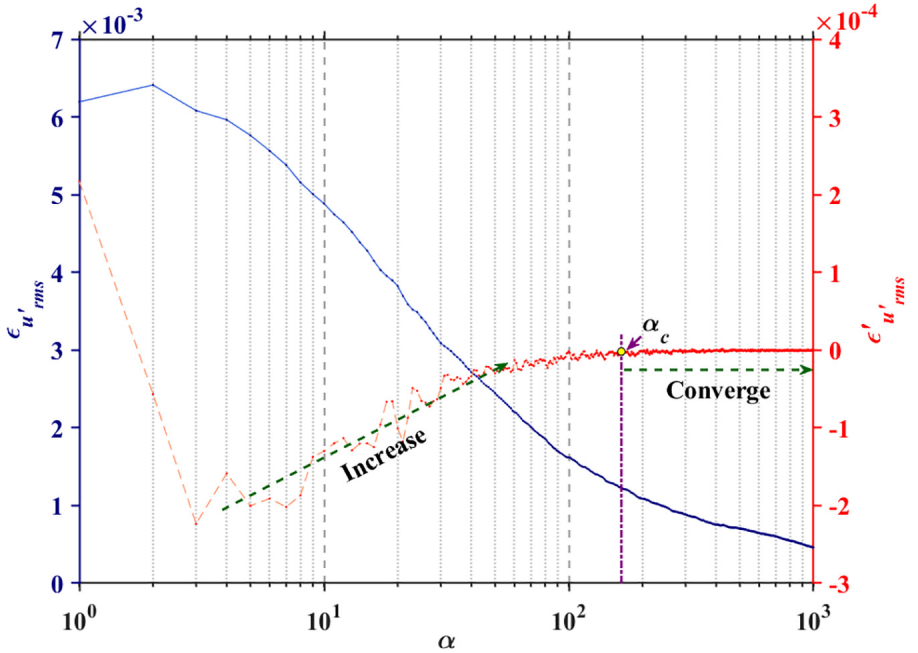

FIGURE 2 | Variation of $\varepsilon_{U'_{rms}}$ and $\varepsilon'_{U'_{rms}}$ with the sample length, α.

The third step is evaluating a z-score by using the following equation and performing a hypothesis test with a significance level of 0.05:

$$z = \frac{A - \left[\frac{n(n-1)}{4}\right]}{\sqrt{\frac{2n^3+3n^2-5n}{72}}}, \quad (9)$$

Our null hypothesis was that there is no trend in the sequence of extracted $\varepsilon'_{p,X}$, whereas the alternative hypothesis is that there is an increasing or decreasing trend. We repeated the above procedures by increasing α and when α failed to reject the null hypothesis, this value becomes α_c. The details and examples of the reverse arrangement test are provided in Bendat and Piersol (2011).

RESULTS AND DISCUSSION

Still Water Experiment

In still water, all velocity fields should be zero, and so measured residuals of signals represent the noises due to instrumental system and surroundings. **Figure 3** shows the relationships between the height of sampling volume (H_s) and the variances of fluctuating signals (σ_n^2) from each receiver in the various settings of velocity range (V_R). Here, σ_n^2 can be regarded as the magnitude of noises in the normal direction to the transmitter. **Figure 3A** shows that the noises decrease with increasing H_s in all velocity ranges for setup, since a larger sampling volume has more numbers of suspended particle and this intensifies backscattering signals and attenuates the noises. In a fixed sampling volume, the noises increase as the velocity range for setup increases, similar to the results obtained in previous studies (Nikora and Goring, 1998; Voulgaris and Trowbridge, 1998), in which experiments identical to the present cases were performed, but with three-receiver ADV.

Figure 3B presents the variances of the fluctuating signals collected from each receiver in the velocity range of ±0.03 m/s for setup. The paled colored lines indicate the noise variance of each velocity component in the Cartesian coordinate system (σ_u^2 , σ_v^2 , σ_{w1}^2 , and σ_{w2}^2), and the dark colored lines indicate the noises of the velocity component along each receiver axis (σ_{V1}^2 , σ_{V2}^2 , σ_{V3}^2 , and σ_{V4}^2). The noises of each receiver were calculated with Eq. 3 (e.g., $\sigma_{V1}^2 = \sigma_u^2 / \left(a_{11}^2 + a_{13}^2\right)$). As shown in **Figure 3B**, the noises along the receiver axis are almost same to each other regardless of H_s, although they were significantly amplified or attenuated during the coordinate transformation to the real velocity field. Considering **Table 1**, the elements of the transformation matrix increase the noises of each receiver by $7.86 = a_{11}^2 + a_{13}^2$, $8.10 = a_{22}^2 + a_{24}^2$, $0.53 = a_{31}^2 + a_{33}^2$, and $0.54 = a_{42}^2 + a_{44}^2$ for the u, v, w_1, and w_2 velocity components, respectively. As a result, the horizontal noises included in the streamwise and transverse normal stresses ($\overline{u'^2}$ and $\overline{v'^2}$) are approximately 15 times higher than the vertical ones included in the vertical normal stresses ($\overline{w_1'^2}$ and $\overline{w_2'^2}$). This tendency is analogous to that observed by Nikora and Goring (1998), who concluded that the horizontal velocity components include a significantly higher level of noise than the vertical component owing to the geometry of the three-receiver ADV system.

Although the noises in the measuring procedure cannot be eliminated, the noises in the vertical component can be reduced by using two vertical velocities measured with the

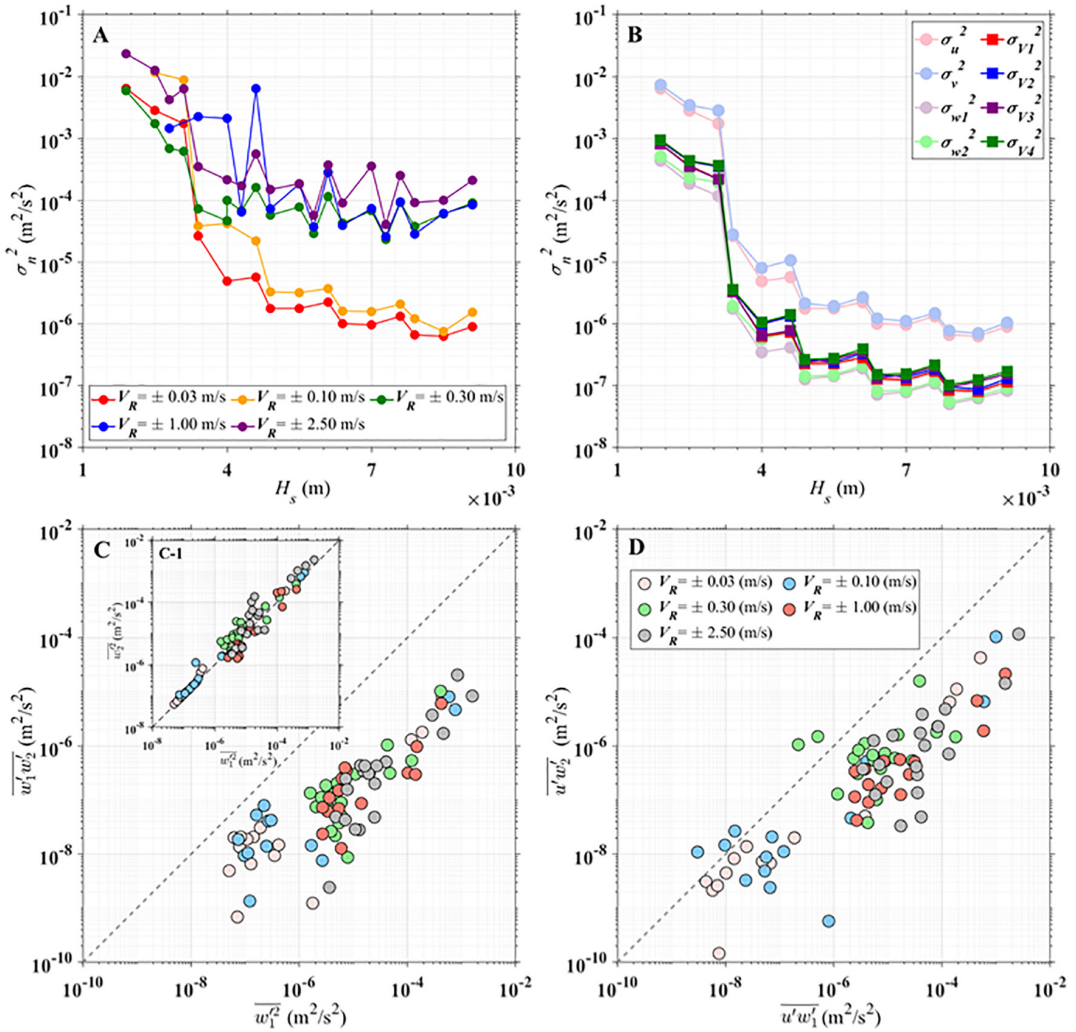

FIGURE 3 | (A) Relation between the noise variance of stream-wise velocity component and the height of sampling volume in the different velocity ranges for setup. **(B)** The relation between the noise and the height of sampling volume for V_R = ±0.03 m/s. Relationship between **(C)** $\overline{w_1'^2}$ and $\overline{w_1'w_2'}$ and between **(D)** $\overline{u'w_1'}$ and $\overline{u'w_2'}$ in different velocity ranges: the dotted lines mean that $y = x$.

orthogonally deployed receivers. In the present ADV, there are several ways to determine the variances of the vertical velocities. Two vertical velocities can be measured and compute the vertical normal stresses, $\overline{w_1'^2}$ and $\overline{w_2'^2}$ and another way is to use both two vertical velocities simultaneously measured from the orthogonally deployed receivers and compute $\overline{w_1'w_2'}$. **Figure 3C** compares the magnitudes of noise in the vertical normal stresses estimated using these methods. In all velocity ranges for setup, $\overline{w_1'^2}$ and $\overline{w_2'^2}$ have a strong linear correlation with each other (**Figure 3C-1**), indicating that they contain similar magnitudes of noise. In contrast, $\overline{w_1'w_2'}$ is $O(10^{-1}$–$10^{-2})$ times less than $\overline{w_1'^2}$ because the random noises from the orthogonally deployed receivers are statistically and theoretically uncorrelated, which leads to a noise covariance close to zero (Blanckaert and Lemmin, 2006).

Such a trend can also be found in **Figure 3D**, which presents the noise of the turbulent shear stresses estimated from the same pair of receivers ($\overline{u'w_1'}$) and orthogonally deployed receivers ($\overline{u'w_2'}$). The results for $\overline{u'w_2'}$ are generally less than those for $\overline{u'w_1'}$, which also supports the argument that the orthogonality in the deployment of receivers helps to reduce the noise when turbulent stress is estimated. Besides, the correlation coefficients u' and w_1' and between u' and w_2' were computed to be 0.25 and 0.01, respectively. These findings indicate that the noise signals measured from orthogonally positioned receivers are independent of each other and thus would be canceled out during the turbulent shear stress calculation process.

In addition to the system noises, when the flow velocity exceeds instantaneously the measurable range of the instrument or when an obstacle blocks the sound path between the transmitter and receiver, spurious spiking signals occur, and

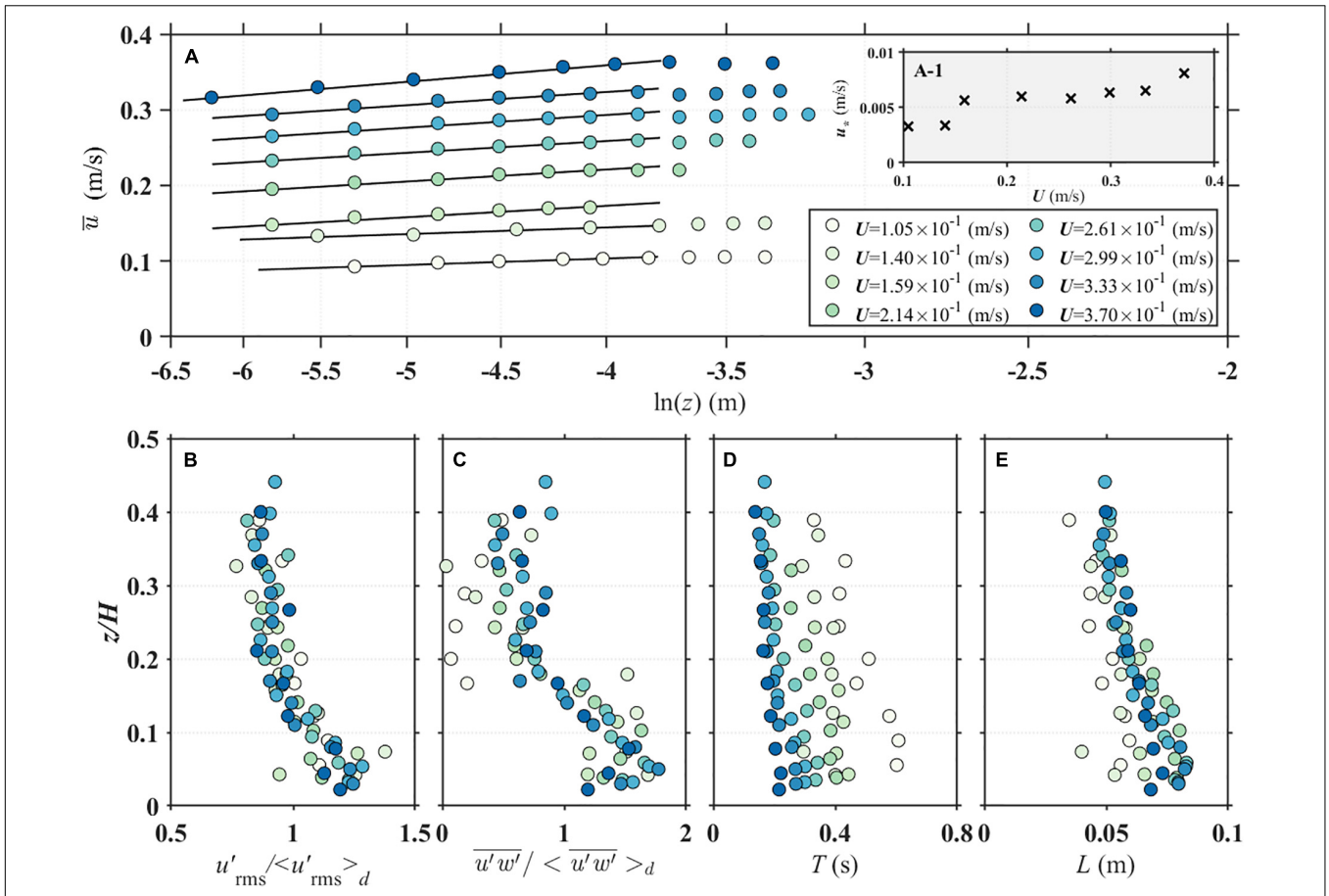

FIGURE 4 | Vertical profiles of the **(A)** temporal averaged stream-wise velocity, **(B)** stream-wise turbulence intensity, **(C)** Reynolds shear stress, **(D)** integral time scale, and **(E)** integral length scale.

they constitute one of the main sources of error influencing the turbulent stresses (Doroudian et al., 2010). Interestingly, in the case of the four-receiver ADV system, spikes are detected simultaneously in the same pair of receivers (**Supplementary Figure A.2**), leading to significant overestimation of the turbulent stresses. However, utilizing the velocities measured from the orthogonally positioned receivers enables this error to be corrected, yielding a relatively error-free turbulent stress.

Experiments in Channel Flows

In open channel flows, the sampling period or time may be strongly influenced by the flow characteristics and the measurement conditions. Before determining the optimal sampling time, we computed several hydrodynamic parameters representing the turbulent characteristics of flows. A total of six parameters, namely, the temporally averaged streamwise velocity ($\bar{u}$), streamwise turbulent intensity (u'_{RMS}), Reynolds shear stress ($\overline{u'w'}$), integral time scale (T), integral length scale (L), and shear velocity (^{u_*}) were considered. Here, u'_{RMS} was computed as $\sqrt{\overline{u'^2}}$ and the Reynolds shear stress ($\overline{u'w'}$) is calculated as $\overline{u'w'_2}$ based on the result of still water experiment. The overbar denotes the temporal average, and the prime indicates the velocity fluctuations computed by subtracting the temporally averaged velocity from the instantaneous velocities, e.g., $u' = u - \bar{u}$. The integral time scale was calculated from Eq. 4 and the integral length scale was determined by multiplying the temporal-averaged velocity ($\bar{u}$) times the integral time scale at each measurement point ($L = \bar{u} \cdot T$).

The shear velocity was computed with the law of the wall applicable to a near-wall region of the turbulent boundary layer (Nezu and Rodi, 1986):

$$u^+ = \frac{1}{\kappa} \ln\left(z^+\right) + C, \tag{10}$$

where κ is the von Karman constant ($\approx$0.41); u^+ and z^+ are defined as $\bar{u}/u_*$ and zu_*/ν , respectively; z is the distance of the measurement point from the bottom; ν is the kinematic viscosity of water; and C is a constant. Rearranging Eq. 10, the relationship between ln (z) and $\bar{u}$ becomes linear as follows:

$$\bar{u} = \frac{u_*}{\kappa} \ln(z) + \frac{u_*}{\kappa} \ln\left(\frac{u_*}{\nu}\right) + u_* C, \tag{11}$$

Because the above equation is applicable only to the logarithmic layer within the boundary layer, the measurement data satisfying

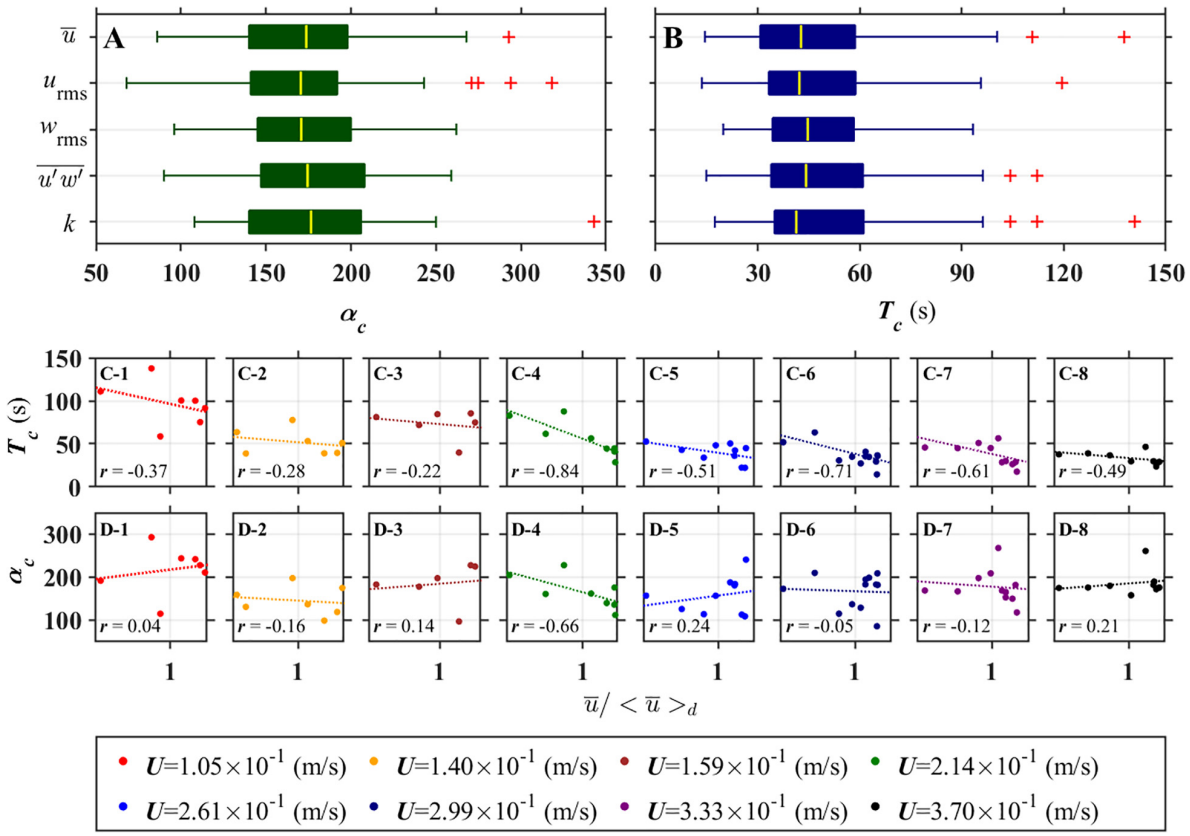

FIGURE 5 | Optimal sampling time of hydraulic parameters represented by **(A)** α_c and **(B)** real-time scale (T_c). The red plus signs indicate outliers. The relation between the non-dimensional stream-wise velocity and **(C)** T_c, and **(D)** α_c: r is the correlation coefficient.

the linear relationship were selected in this study and the shear velocity was computed from the slope of the trend line (solid line in **Figure 4A**) of the selected data.

According to **Figure 4A**, the shear velocity (u_*) increases linearly from 0.003 to 0.008 m/s as the inlet flow velocity (U) increases and this trend is similar to that obtained by Carvalho et al. (2010), who measured the shear velocity over the Perspex plate under flow conditions similar to those considered in this study. **Figures 4B,C** present the vertical distributions of the non-dimensional streamwise turbulence intensity (u'_{RMS}) and the Reynolds shear stress ($\overline{u'w'}$), respectively. Those parameters are non-dimensionalized with the depth-averaged values, $\langle u'_{\mathrm{RMS}} \rangle_d$ and $\left\langle \overline{u'w'} \right\rangle_d$, respectively. In all flow conditions, the turbulent intensity and Reynolds shear stress increase toward the bed and both reach maxima at $z/H \approx 0.05$. Near the bed region ($z/H < 0.05$), the viscous effect dominates the turbulent fluctuations, decreasing the turbulence quantities as expected.

Figures 4D,E, respectively, depict the computed integral time (T) and length (L) scales and their vertical profiles. The integral time scale increases with the decrease of U at the same locations. In the same flow conditions, differently from the length scale, the length scale is spatially larger in the near bed, where the mean flow is relatively slower than that in the outer region, as similarly observed by Köse (2011). In most of the experiments, integral length scales range from 0.04 to 0.08 m and the scales increase toward the bed since the bottom friction generates a strong shear near the bottom boundary layer than in the upper region and this shear produces larger turbulent eddies. Much closer to the bottom ($z/H < 0.05$), the integral length scale decreases, similar to the turbulent intensity and Reynolds shear stress, because the viscous effect suppresses the formation of turbulent eddies. While the integral time scale varies with the flow condition (**Figure 4D**), the integral length scales are almost similar to each other in each depth of all flow conditions (**Figure 4E**) since they are constructed with the integral time scale and the mean velocity which seems to be very close to time scale and velocity scale of the largest eddies.

Figure 5 shows the optimal sampling period for the turbulence statistics determined by using the reverse arrangement test. Considering the results from the still water experiments, the vertical turbulent intensity (w'_{rms}) and the turbulent kinetic energy (k) were computed as $\sqrt{\overline{w'_1 w'_2}}$ and $\left(\overline{u'^2} + \overline{v'^2} + \overline{w'_1 w'_2}\right)/2$, respectively. According to **Figure 5A**, the optimal sampling period ranges between 150 and 200 times the integral time scale for all turbulence statistics, indicating that for the turbulence statistics to reach a stationary state, at least 150 numbers or more of the integral scales of the largest eddies should be included

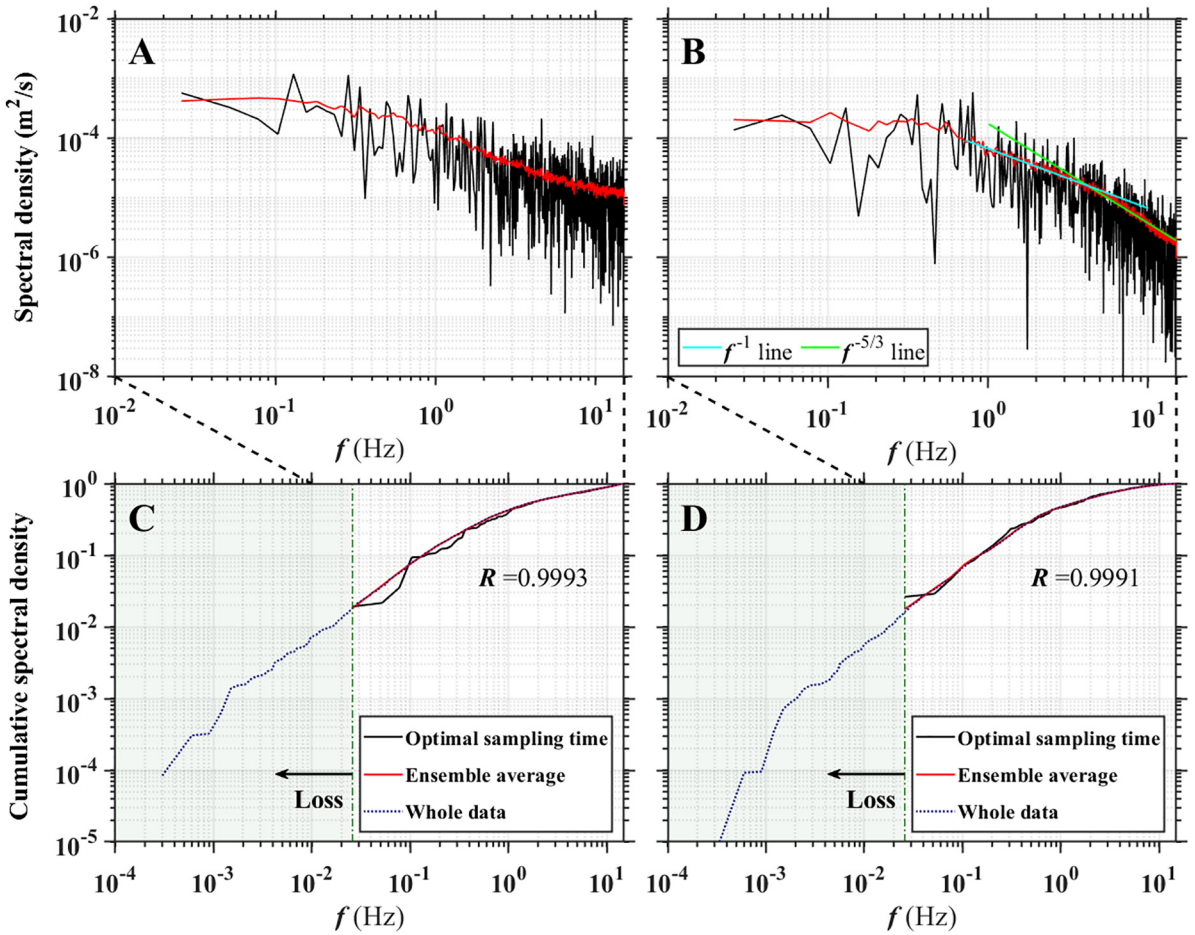

FIGURE 6 | Power spectral densities of **(A)** *u*' and **(B)** *w*' and cumulative spectral densities of **(C)** *u*' and **(D)** *w*'; The black line means the spectrum of a randomly chosen data having a length of optimal sampling time and the maximum frequency of power spectral densities is half of the sampling frequency.

during the measurement period. If we convert those critical number α_c into a recognizable real-time length by multiplying it times the integral time scale at each measurement as $T_c = \alpha_c.T$, the optimal sampling duration falls in the range of 40–60 s for all turbulence statistics (**Figure 5B**), which is similar to Buffin-Bélanger and Roy (2005).

Figures 5C,D present the variations of the optimal sampling period with the changes of the mean velocity when the sampling period is determined with the real-time duration (T_c) and the multiple of integral time scale (α_c). As shown in **Figure 5C**, T_c decreases with increasing U, which indicates that a longer sampling time is not required for the faster flows since it takes less time to capture turbulent eddies than in the slower flows if the sizes of the eddies are same in both flows. Such inverse relations can also be found in each flow condition, where the average correlation coefficient between $\bar{u}$ and T_c is evaluated to be approximately −0.51. At a fixed inlet velocity, a longer measurement time is required for a near-wall region since flow is much slower but turbulent eddy is larger than the upper region (**Figure 4E**). This finally causes a negative correlation coefficient between $\bar{u}$ and T_c.

Contrary to T_c, α_c is independent and uncorrelated with flow characteristics, thus, there is no specific trend (**Figure 5D**) and so the average correlation coefficients between α_c and mean velocities are around −0.05. In other words, the sampling period based on α_c is more independent of the flow characteristics and conditions than that based on T_c. This result can also be found clearly in **Supplementary Figure A.3**, which shows the relationship between $\bar{u}$ and T_c, and α_c for all cases. In this regard, when we establish a criterion for the optimal sampling period, it is more appropriate to use multiple of integral time scales as the basic unit rather than using real-time, which has high variability depending on the flow conditions.

To verify that the proposed optimal sampling period is long enough to describe the physical characteristics of turbulent flow, we spectrally analyzed the assumed true value (velocity data measured for approximately 1 h) and the data sampled during the optimal sampling period. The assumed true values were separated into several sets by dividing by a proposed optimal sampling time and the spectral densities of each set are were constructed and then those spectra were ensemble-averaged for presenting smooth spectral functions.

Figures 6A,B present the power spectral densities of streamwise and vertical turbulence intensities, respectively. The red and black lines represent the spectra of the assumed true values and optimal sampling period, respectively. Although the variance of the spectrum for data with an optimal sampling period is much larger than that of the assumed true value, they follow a similar trend. In the case of stream-wise velocity (**Figure 6A**), the inertial subrange having a −5/3 slope of power is hardly detected in either spectrum, and they become white noises in the range with higher frequencies owing to the instrumental or system limitations. In the case of vertical velocity (**Figure 6B**), the spectra follow a −5/3 slope well from 4 Hz to the Nyquist frequency without a white noise spectrum. Such results indicate that the streamwise velocity contains more noises than the vertical velocity, as discussed in the results of the still water experiment related to the elements of the transformation matrix, which amplify the noise variances by a factor of 15 in the streamwise velocity compared to the vertical velocity.

Figures 6C,D depict the cumulative power spectra. The y axis represents the ratio of the energy of motion with a frequency less than f to the whole energy. When the spectrum is obtained from data with an optimal sampling period, a shorter sampling period limits the length or period of the flow motion that can be captured, and thus, the spectral density starts from 0.02 Hz. In the frequency range of $0.02 < f < 0.1$ Hz, the energies occupy about 10% of the entire turbulence energy and the assumed true values and data having optimal sampling time show less than 2% disparity with each other, whereas they become identical at higher frequencies ($f > 0.1$ Hz), which is responsible for the remaining 90% of energy. Besides, the correlation coefficient between them for u' and w' is larger than 0.99, indicating that the data collected during the optimal sampling period are sufficient to describe the flow characteristics of the assumed true values.

Because it is impossible to capture flow motions with frequencies less than 0.02 Hz for the optimal sampling period, the corresponding flow motions and energies are lost. To investigate the amount of energy lost due to sampling time truncation, we also calculated the cumulative spectral density of the entire velocity data without an ensemble average (navy dotted lines in **Figures 6C,D**). According to the green-colored areas in **Figures 6C,D**, the energy losses at low frequencies are negligibly small as 1.6 and 1.1% for u' and w', respectively, signifying that there is little energy loss due to the sampling time truncation.

CONCLUSION

The present work proposed an appropriate operating method for a four-receiver ADV that can yield reliable turbulence quantities. Laboratory experiments were performed using this instrument and the proposed method under two flow conditions, and the principal findings of each experiment can be summarized as follows.

(a) The orthogonality in the deployment of four-receivers of the ADV has a great advantage in measuring the shear stresses. Transforming the received signals to the coordinates for each velocity modifies the electrical noises of the signals. Before transforming the signals to the velocity component, this original signals at each receiver are in a similar range of electrical noises, but after the signals were transformed to the velocity directions, the noise variances are amplified by approximately eight times in the stream-wise and lateral directions and they are reduced by half in the vertical direction. However, the Reynolds stresses were computed with the velocities obtained by the orthogonally deployed receivers and this orthogonality erases the uncorrelated random noises from each receiver in the Reynolds stress calculation.

(b) The integral time scale of turbulence is proposed as a base for an optimal sampling period. 150–200 times of the integral time scale seems to be almost invariant regardless of the measurement conditions. The conventionally proposed method based on a fixed real scale sampling period (e.g., 1,000 s) asks the various sampling periods depending on the vertical and horizontal locations even in a flow. For example, a near-wall region, where the mean flow velocity is relatively low and turbulent eddies are larger than other areas, requires a longer measurement time compared to a region far from the wall, where the mean flow is much higher and turbulent eddies are relatively small. In this regard, the integral time scale which reflects the information of the size of large eddies is a more suitable base than real-time scales for a sampling time criterion.

Although our approaches help to overcome the ambiguities faced by the previous researches using ADV, several limitations still remain with requiring future work. For example, since our framework was established through laboratory experiments with the assumption of stationary flow, it should be extended to the non-stationary flows with various scales of turbulent motion and also studied more for the application to the field experiments. Nevertheless, we expect that our framework will enable researchers to measure the Reynolds stress and other turbulence quantities effectively and obtain reliable data for fluid dynamics analysis.

DATA AVAILABILITY STATEMENT

The original contributions presented in the study are included in the article/**Supplementary Material**, further inquiries can be directed to the corresponding author.

AUTHOR CONTRIBUTIONS

HP performed laboratory experiments, analyzed the results, and wrote the original manuscript. JH conceptualized this research, reviewed the manuscript, and focused on revising the section "Results and Discussion." Overall, both authors contributed significantly and shared a lot of work and approved the submitted version.

FUNDING

This research was supported by Basic Science Research Program through the National Research Foundation of Korea (NRF) funded by the Korean Government Ministry of Science, ICT and Future Planning (No. 2020R1A2B5B01002249), Korean Ministry of Environment (MOE) as "Chemical Accident Response R&D program" (No. ARG201901179001), and administratively supported by the Institute of Engineering Research at Seoul National University.

SUPPLEMENTARY MATERIAL

The Supplementary Material for this article can be found online at: https://www.frontiersin.org/articles/10.3389/fmars.2021.681265/full#supplementary-material

REFERENCES

Beck, T. W., Housh, T. J., Weir, J. P., Cramer, J. T., Vardaxis, V., Johnson, G. O., et al. (2006). An examination of the runs test, reverse arrangements test, and modified reverse arrangements test for assessing surface EMG signal stationarity. *J. Neurosci. Methods* 156, 242–248. doi: 10.1016/j.jneumeth.2006.03.011

Bendat, J. S., and Piersol, A. G. (2011). *Random Data: Analysis and Measurement Procedures*, Vol. 729. Hoboken, NJ: John Wiley & Sons.

Blanckaert, K., and Lemmin, U. (2006). Means of noise reduction in acoustic turbulence measurements. *J. Hydraulic Res.* 44, 3–17. doi: 10.1080/00221686.2006.9521657

Buffin-Bélanger, T., and Roy, A. G. (2005). 1 min in the life of a river: selecting the optimal record length for the measurement of turbulence in fluvial boundary layers. *Geomorphology* 68, 77–94. doi: 10.1016/j.geomorph.2004.09.032

Carvalho, E., Maia, R., and Proença, M. F. (2010). Shear stress measurements over smooth and rough channel beds. *River Flow* 2010, 367–376.

Chanson, H. (2008). "Acoustic Doppler velocimetry (ADV) in the field and in laboratory: practical experiences," in *Proceeding of International Meeting on Measurements and Hydraulics of Sewers IMMHS'08, Summer School GEMCEA/LCPC, 19–21 August 2008*, (Bouguenais).

Chanson, H., Trevethan, M., and Koch, C. (2007). Discussion of "turbulence measurements with acoustic doppler velocimeters" by Carlos M. García, Mariano I. Cantero, Yarko Niño, and Marcelo H. García. *J. Hydraulic Eng.* 133, 1283–1286.

Doroudian, B., Bagherimiyab, F., and Lemmin, U. (2010). Improving the accuracy of four-receiver acoustic Doppler velocimeter (ADV) measurements in turbulent boundary layer flows. *Limnol. Oceanogr.: Methods* 8, 575–591. doi: 10.4319/lom.2010.8.0575

Goring, D. G., and Nikora, V. I. (2002). Despiking acoustic Doppler velocimeter data. *J. Hydraulic Eng.* 128, 117–126. doi: 10.1061/(asce)0733-9429(2002)128:1(117)

Kim, S. C., Friedrichs, C. T., Maa, J. Y., and Wright, L. D. (2000). Estimating bottom stress in tidal boundary layer from acoustic Doppler velocimeter data. *J. Hydraulic Eng.* 126, 399–406. doi: 10.1061/(asce)0733-9429(2000)126:6(399)

Köse, Ö (2011). Distribution of turbulence statistics in open-channel flow. *Int. J. Phys. Sci.* 6, 3426–3436.

Lane, S. N., Biron, P. M., Bradbrook, K. F., Butler, J. B., Chandler, J. H., Crowell, M. D., et al. (1998). Three-dimensional measurement of river channel flow processes using acoustic Doppler velocimetry. *Earth Surface Processes Landforms: J. British Geomorphol. Group* 23, 1247–1267. doi: 10.1002/(sici)1096-9837(199812)23:13<1247::aid-esp930>3.0.co;2-d

Lesht, B. M. (1980). Benthic boundary-layer velocity profiles: dependence on averaging period. *J. Phys. Oceanogr.* 10, 985–991. doi: 10.1175/1520-0485(1980)010<0985:bblvpd>2.0.co;2

McLelland, S. J., and Nicholas, A. P. (2000). A new method for evaluating errors in high-frequency ADV measurements. *Hydrol. Processes* 14, 351–366. doi: 10.1002/(sici)1099-1085(20000215)14:2<351::aid-hyp963>3.0.co;2-k

Nezu, I., and Rodi, W. (1986). Open-channel flow measurements with a laser Doppler anemometer. *J. Hydraulic Eng.* 112, 335–355. doi: 10.1061/(asce)0733-9429(1986)112:5(335)

Nikora, V. I., and Goring, D. G. (1998). ADV measurements of turbulence: can we improve their interpretation? *J. Hydraulic Eng.* 124, 630–634. doi: 10.1061/(asce)0733-9429(1998)124:6(630)

Nystrom, E. A., Rehmann, C. R., and Oberg, K. A. (2007). Evaluation of mean velocity and turbulence measurements with ADCPs. *J. Hydraulic Eng.* 133, 1310–1318. doi: 10.1061/(asce)0733-9429(2007)133:12(1310)

O'Neill, P. L., Nicolaides, D., Honnery, D., and Soria, J. (2004). "Autocorrelation functions and the determination of integral length with reference to experimental and numerical data," in *Proceeding of the 15th Australasian Fluid Mechanics Conference*, Vol. 1, (Sydney: University of Sydney), 1–4.

Park, H., and Hwang, J. H. (2019). Quantification of vegetation arrangement and its effects on longitudinal dispersion in a channel. *Water Resour. Res.* 55, 4488–4498. doi: 10.1029/2019wr024807

Petrie, J., Diplas, P., Gutierrez, M., and Nam, S. (2013). Data evaluation for acoustic Doppler current profiler measurements obtained at fixed locations in a natural river. *Water Resour. Res.* 49, 1003–1016. doi: 10.1002/wrcr.20112

Reidenbach, M. A., Monismith, S. G., Koseff, J. R., Yahel, G., and Genin, A. (2006). Boundary layer turbulence and flow structure over a fringing coral reef. *Limnol. Oceanogr.* 51, 1956–1968. doi: 10.4319/lo.2006.51.5.1956

Salim, S., Pattiaratchi, C., Tinoco, R., Coco, G., Hetzel, Y., Wijeratne, S., et al. (2017). The influence of turbulent bursting on sediment resuspension under unidirectional currents. *Earth Surface Dynamics* 5, 399–415. doi: 10.5194/esurf-5-399-2017

Soulsby, R. L. (1980). Selecting record length and digitization rate for near-bed turbulence measurements. *J. Phys. Oceanogr.* 10, 208–219. doi: 10.1175/1520-0485(1980)010<0208:srladr>2.0.co;2

Sukhodolov, A. N., and Rhoads, B. L. (2001). Field investigation of three-dimensional flow structure at stream confluences: 2. Turbulence. *Water Resour. Res.* 37, 2411–2424. doi: 10.1029/2001wr000317

Voulgaris, G., and Trowbridge, J. H. (1998). Evaluation of the acoustic Doppler velocimeter (ADV) for turbulence measurements. *J. Atmospheric Oceanic Technol.* 15, 272–289. doi: 10.1175/1520-0426(1998)015<0272:eotadv>2.0.co;2

Wang, X. Y., Yang, Q. Y., Lu, W. Z., and Wang, X. K. (2012). Experimental study of near-wall turbulent characteristics in an open-channel with gravel bed using an acoustic Doppler velocimeter. *Experiments Fluids* 52, 85–94. doi: 10.1007/s00348-011-1202-3

Conflict of Interest: The authors declare that the research was conducted in the absence of any commercial or financial relationships that could be construed as a potential conflict of interest.

Publisher's Note: All claims expressed in this article are solely those of the authors and do not necessarily represent those of their affiliated organizations, or those of the publisher, the editors and the reviewers. Any product that may be evaluated in this article, or claim that may be made by its manufacturer, is not guaranteed or endorsed by the publisher.

frontiers in Marine Science

METHODS
published: 20 August 2021
doi: 10.3389/fmars.2021.668673

Intelligent Buoy System (INBUS): Automatic Lifting Observation System for Macrotidal Coastal Waters

Jae-Youll Jin[1], Jong Dae Do[1], Jin-Soon Park[2], Jun Seok Park[2], Byunggil Lee[1], Sung-Doo Hong[3], Sung-Ju Moon[3], Keun Choon Hwang[2] and Yeon S. Chang[4]**

[1] East Sea Environment Research Center, Korea Institute of Ocean Science and Technology, Busan, South Korea, [2] Coastal Development and Ocean Energy Research Center, Korea Institute of Ocean Science and Technology, Busan, South Korea, [3] OCEANTECH Co., Ltd., Goyang-si, South Korea, [4] Maritime ICT R&D Center, Korea Institute of Ocean Science and Technology, Busan, South Korea

OPEN ACCESS

Edited by:
Ole Mikkelsen,
Sequoia Scientific, Inc., United States

Reviewed by:
Shaowei Zhang,
Institute of Deep-Sea Science and Engineering (CAS), China
Jun Choi,
Pukyong National University, South Korea

***Correspondence:**
Yeon S. Chang
yeonschang@kiost.ac.kr
Jong Dae Do
jddo@kiost.ac.kr

Specialty section:
This article was submitted to Ocean Observation, a section of the journal Frontiers in Marine Science

Received: 16 February 2021
Accepted: 04 August 2021
Published: 20 August 2021

Citation:
Jin J-Y, Dae Do J, Park J-S, Park JS, Lee B, Hong S-D, Moon S-J, Hwang KC and Chang YS (2021) Intelligent Buoy System (INBUS): Automatic Lifting Observation System for Macrotidal Coastal Waters. Front. Mar. Sci. 8:668673. doi: 10.3389/fmars.2021.668673

The west coast of South Korea is characterized by a wide macrotidal area with a maximum tidal range of ∼10 m. The sea surface elevation varies with the tidal phase, which leads to significant changes in the vertical structure of the physical, chemical, and biological properties of the water column, especially when the interaction by waves and/or the freshwater and sediment input from the river increases. Under such conditions, it is difficult to carry out continuous and consistent measurements of the vertical structures of the water qualities using a conventional observation system that is fixed to the seabed or sea surface because the thickness of the water column constantly changes. Based on the demand for long-term observations of the vertical structures of the water properties in macrotidal environments, the Intelligent Buoy System (INBUS) was developed by the Korea Institute of Ocean Science and Technology (KIOST). INBUS is a buoy equipped with an instrument frame, which is similar to other buoys that are fixed to the sea surface. During every measurement, INBUS detects the water depth and sends the frame down to the seabed to measure the water quality at every vertical level set up in the system. For example, if *N* levels are set in INBUS, the water depth of each measurement is divided by *N* layers and the instruments in the lifting frame measure the water properties of each of the *N* layers while they are descending to the bottom. Based on this procedure, the vertical structure of the water column is consistently measured in *N* layers regardless of changes of the water depth due to tides and waves. The lifting and measuring process is automatically controlled by INBUS once it is set up in the system. In addition, because INBUS allows bidirectional communication through code division multiple access (CDMA), the system can be controlled by stations on land. If the CDMA communication becomes inoperable owing to extreme wave conditions or the buoy is lost because of incidents such as a collision with a ship, the location of INBUS can be tracked by low-earth-orbit satellites.

Keywords: observation system, automatic lifting, buoy, macrotidal, acoustic instrument

INTRODUCTION

Coastal waters are interfaces between land and ocean and thus are important for human life because of their geographical proximity as well as their function as food, transportation, and recreation sources. The environment of coastal waters varies because of the continuous interaction between water and land. For example, the waves shoal and break when they propagate into shallower water, which releases a large amount of energy in the coastal zone, leading to various processes, such as beach erosion, which can cause environmental and economic damage (Alexandrakis et al., 2015). In addition, the tidal range increases in the coastal zone with the propagation of the water into shallow areas, which can result in differences on the scale of meters in the water level between low and high tides.

Various systems have been utilized to observe coastal waters. Because of the relatively shallow water depth compared with the open ocean, instruments are generally mounted on a frame that is fixed to the seabed. One example of a bottom-fixed instrument is a wave gauge that measures the pressure of the water column and converts it into surface elevation based on linear wave theory. Similarly, acoustic sensors, such as the Nortek Acoustic Wave and Current Profiler (AWAC; Pedersen et al., 2007), are mounted on a bottom-fixed frame facing upward to measure waves and currents (Jeong et al., 2020). In addition to wave and current measurements, the instruments fixed to the seabed can be used to measure the near-bed properties such as the sediment concentration and seabed morphology (Do et al., 2019). Other examples of observation systems that are commonly applied in coastal waters include surface buoys that measure near-surface properties and atmospheric data. Two types of surface buoys are available: surface-following buoys and mooring buoys. Surface-following buoys are based on the global positioning system (GPS) and are widely used for ocean wave measurements (Herbers et al., 2012). Mooring buoys are surface buoys that are moored in coastal waters to measure physical, meteorological, and biogeochemical data (Dorman and Winant, 1995; Bailey et al., 2019). They are connected to the seabed by mooring lines and facilitate observation of the subsurface water column *via* instruments attached to the mooring lines.

The west coast of South Korea has a wide tidal range, with a maximum value of ∼10 m because of the well-developed amphidromic point and strong tidal currents in the Yellow Sea (Kang, 1984; Yanagi and Inoue, 1995; Hwang et al., 2014). The large difference in the water level during the tidal cycle including waves and currents leads to spatiotemporal changes in the physical, chemical, and biological characteristics of the water throughout the water column (Cadier et al., 2017). However, the timely measurement of these properties is constrained because of the rapid change in the sea surface elevation. Neither of the observation systems discussed above, that is, instruments fixed to the seabed or mounted on a surface buoy, can detect the vertical structures of water properties in macrotidal regions because the water depth significantly changes. Therefore, to measure the variations of the properties within the water column on a timely basis, the vertical locations of the measuring points should be adjusted based on the changes in the surface elevation, which requires the development of an instrumentation system that is specifically suited for macrotidal environments.

In this paper, a suitable buoy system developed by Korea Institute of Ocean Science and Technology (KIOST)—called the Intelligent Buoy System (INBUS)—is described. INBUS is an automatic lifting-buoy system that sends the frame including instruments down to the seabed, and can measure the water quality at every vertical level delineated beforehand in the system. Furthermore, it differs from mooring buoys. In mooring buoys, the subsurface instruments attached to the mooring lines change their vertical positions with the surface elevation changes in the macrotidal environment and thus cannot measure the water properties in a fixed vertical coordinate system. Moreover, in macrotidal areas such as the Yellow Sea, which is a shallow (average depth of 44 m) marginal sea bounded by China and the Korean Peninsula (Hwang et al., 2014), the subsurface instruments connected to a mooring line may touch the seabed during low tides, which can lead to the contamination of the obtained data and even damage to the sensors. In contrast, by sending the instrument frame to the seabed INBUS can monitor the time variation of the vertical structure of various water properties. It can measure the properties at fixed positions in the normalized vertical coordinate system (i.e., INBUS can measure the data in a sigma coordinate in which the vertical grids follow the terrain such that the same number of vertical grid points are present regardless of water depth).

Various observation systems similar to INBUS currently exist, however, they all lack some of its key functionalities. The Marel Seine Bay Network (MSBN) developed by Ifremer, France is a real-time unmanned monitoring system for coastal environments (Woerther and Grouhel, 1998). MSBN consists of multiple buoys that measure data at different vertical levels and uses internet protocol and satellite communication for data transfer. However, MSBN does not have the automatic elevation system used by INBUS. Monitoring Your Sound (MYSound) is a real-time monitoring project for water environments, specifically in the areas near Long Island Sound, controlled by the U.S. Environmental Protection Agency (Tedesco et al., 2003). MYSound also consists of multiple stations located onshore and offshore, with observational buoys deployed to measure water qualities. The data are available in real time through the internet. Similar to MSBN, MYSound also does not have the automatic elevation system used by INBUS; it measures data at fixed vertical levels. Monitoring buoys that use an automatic elevation system similar to INBUS also exist (Fowler et al., 1997; Tercier-Waeber et al., 1999). However, the lowest water depths that the sensors can reach are fixed in these buoys so that they are not optimized for macrotidal environment. One of the advantages of INBUS is that it is optimized in macrotidal areas because it can detect the water depth using an altimeter and thus the lowest water depth and the vertical measuring levels can be determined in real time.

The remainder of this paper is organized as follows. Section "Development of INBUS" presents the motivation and development history of the various versions of INBUS. Section "Methods" describes in detail the structure and functions of INBUS. Sections "Results" and "Discussion" provide examples

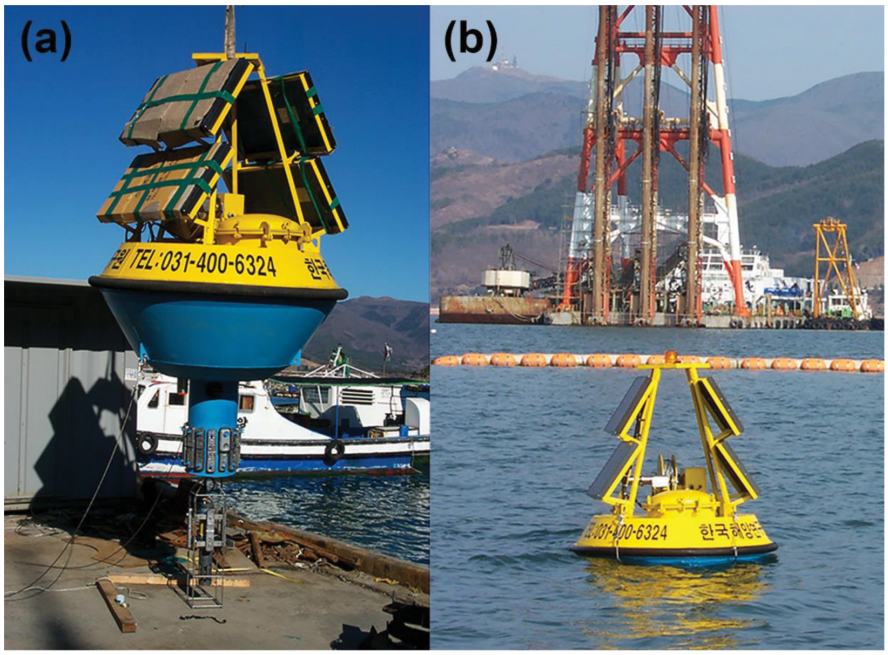

FIGURE 1 | (a) Photograph of Intelligent Buoy System (INBUS)-1 before mooring, **(b)** photograph of INBUS-1 after mooring.

of application to coastal observations in macrotidal areas and discussions on the current INBUS, respectively.

DEVELOPMENT OF INBUS

Intelligent Buoy System is an automatic lifting-buoy system developed by Korea Institute of Ocean Science and Technology (KIOST), 2004 that is designed specifically to monitor the marine environment in macrotidal regions with wide tidal ranges. Typical mooring observation buoys cannot effectively monitor the vertical structure of the water column in such regions. On the one hand, if the mooring buoy system is designed for water depths typical for high tides, the sensors attached to their communication cables can touch the seabed. On the other hand, if the system is designed for water depths typical of low tides, the sensors cannot measure data in the deeper part of the water column under high tides. Therefore, INBUS was specifically developed for macrotidal environments as it automatically detects the water depth and sends the sensors downward using an automatic winch system.

The data obtained by INBUS are used as the input for numerical models and for the verification of the model results. These data include the wave height, period, direction, water depth, current velocity, water temperature, salinity, dissolved oxygen (DO) content, conductivity, chlorophyll (Chl) -a content, and turbidity. In addition, meteorological data, such as the air pressure, temperature, and wind speed and direction, are measured by sensors mounted on top of the buoy. These data are transferred to a ground station in real time using code division multiple access (CDMA) communication. INBUS is also equipped with solar panels and thus has self-power capabilities. If there is an emergency, for example, the mooring line of INBUS is disconnected and the system drifts out of CDMA range, the communication system will connect to low-earth-orbit (LEO) satellites to locate INBUS, using Iridium satellite communications—which offer global voice and data connectivity through 66 LEO satellites. Since the first generation (INBUS-1) was developed in 2003, its functions have been upgraded and INBUS-2 has been introduced (2009). **Figures 1**, **2** present photographs of INBUS-1 and 2 before and after mooring, respectively. The figures show that the basic structure of INBUS-1 remains unchanged and both systems have similar shapes. Solar panels and antennas are mounted on top of the buoy and a long pipe, which is designed to protect the sensor frame, is attached to the bottom.

The first version of INBUS was initially developed to monitor the water quality only. Atmospheric data and physical parameters, such as wave and current data, were not measured, which limited its application to the analysis of the hydrodynamics and sediment dynamics of the water column depending on the weather conditions. Subsequently, wind and wave gauges and current meters were added to INBUS-2. Because the sensors are automatically sent down to the seabed on a regular basis, they can be damaged during lifting under harsh wave conditions. Because of the real-time monitoring of the wave conditions by INBUS-2, the lifting system of the buoy will not operate during extreme weather and thus the sensors are protected based on the detection of the wave heights. However, data must also be obtained under such harsh conditions because the water quality significantly changes. To continue underwater measurements of the water column even during the gap periods under harsh

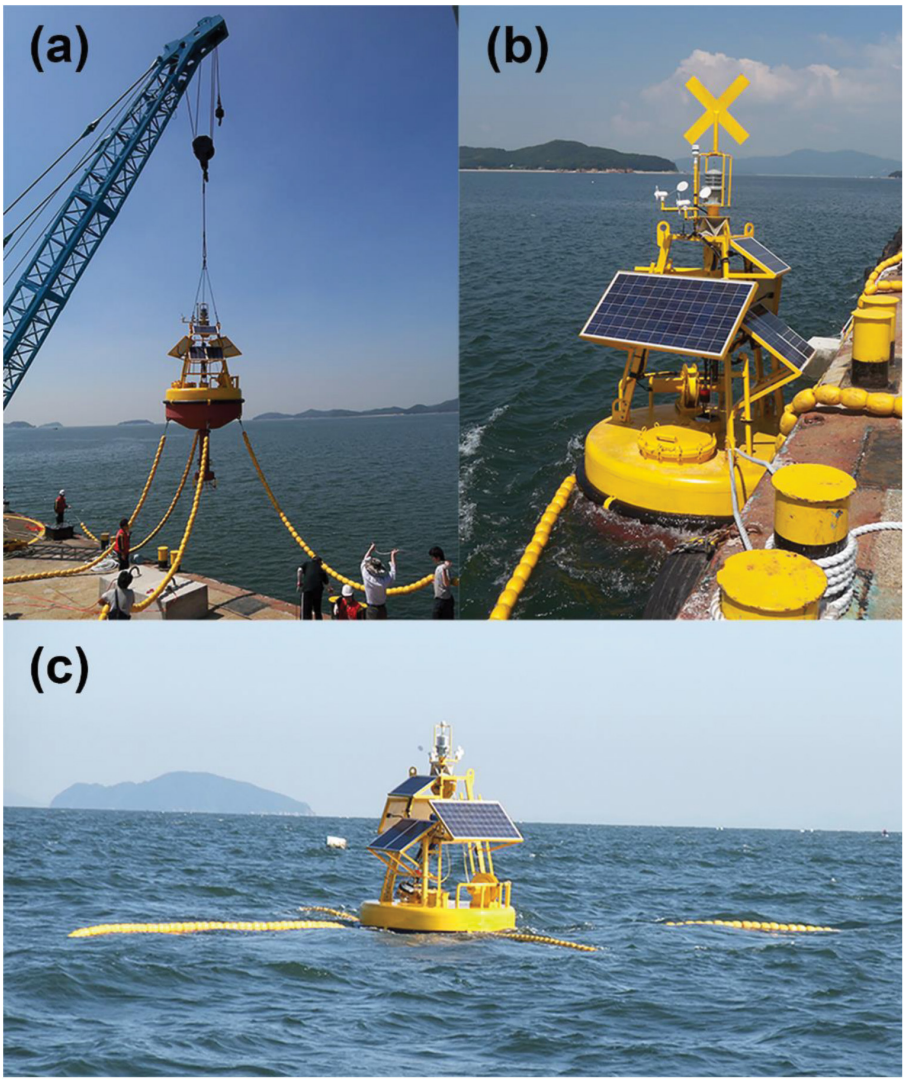

FIGURE 2 | (a,b) Photographs of INBUS-2 before mooring and **(c)** after mooring.

wave conditions, INBUS-2 is equipped with an acoustic Doppler current profiler (ADCP), which measures the vertical profiles of the currents and indirectly estimates the suspended sediment concentration (SSC) of the water column.

Currently, a third version of INBUS (INBUS-3) is being developed. INBUS-3 will be equipped with a laser *in situ* scattering and transmissometery (LISST) sensor that can directly measure the SSC for data calibration. In addition, a line of optical backscatter sensors (OBSs) will be installed in the bottom of the sensor frame of INBUS-3 to measure the near-bed SSC because there is a gap in the vertical detection range of INBUS-2 of ∼1 m near the seabed, although the frame is sent down close to the bottom. Therefore, it is expected that INBUS-3 will be able to accurately measure the SSC close to the seabed, which is particularly important to understand the near-bed sediment dynamics. In the following sections, the structure, functions, and sensors of the latest version of INBUS are described in detail.

METHODS

Intelligent Buoy System Structure

Figure 3 shows schematic drawings of INBUS-2 (which is currently operated in the field), including upgraded sensors and functions. The new functions of INBUS-3 are not introduced in this section because its development has not been completed yet. INBUS-2 has a hull shape with a long pipe. The height, width, and weight of INBUS-2 are 4.8 m (2.8 m underwater and 2.0 m in the air), 2.5 m, and ∼2,170 kg, respectively. A weight is added to the bottom of the pipe to stabilize the buoy by lowering the center of gravity. At the top of the buoy, wind sensors and antennas are mounted on a trapezoid frame. Two symmetrical frames are designed for the self-powered solar panels to achieve stability. The main console, including the main and underwater sensor controllers, is inside the battery hull. A winch is installed below the solar frames to automatically control the lifting system of

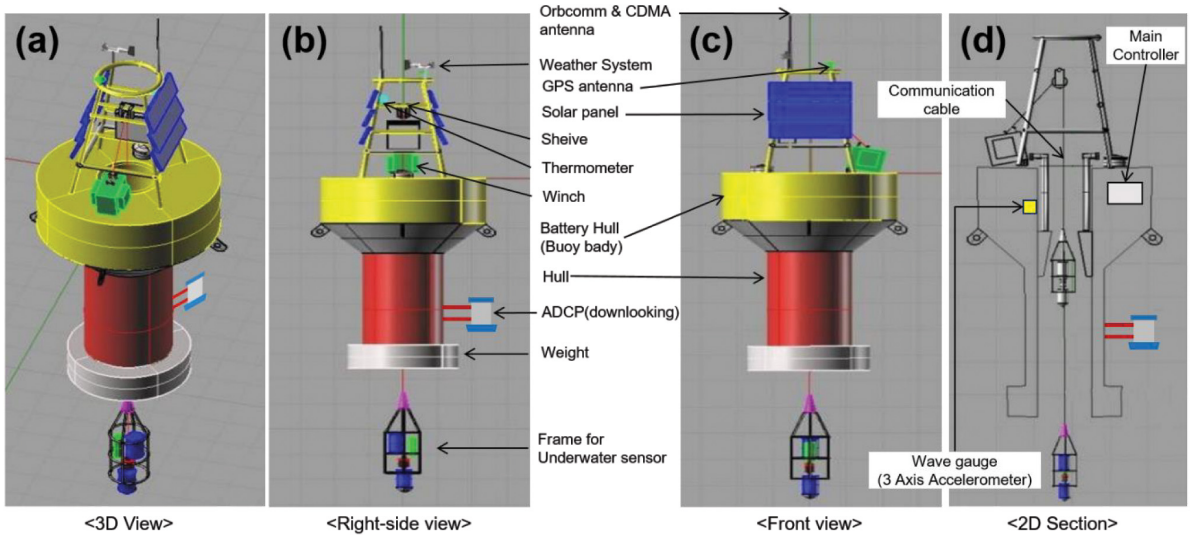

FIGURE 3 | (a) Schematic of INBUS-2 (the current INBUS generation operated in the field). **(b)** Right-side and **(c)** front views including the description of the equipment and sensors. **(d)** Two dimensional section view showing the inner part of INBUS.

TABLE 1 | Power supply configuration of INBUS-2.

Operating part	Battery		Solar panel	
	Applied voltage	Configuration	Applied voltage	Configuration
Winch	24 V 300 Ah	12 V 2S3P* (12 V 100 Ah 6ea)	24 V 190 W	24 V 3P (24 V 190 W 2ea)
Main controller	12 V 600 Ah	12 V 6P (12 V 100 Ah 6ea)	12 V 50 W	12 V 3P (12 V 50 W 3ea)

**S, series connection; P, parallel connection*

the underwater sensors. Two batteries are installed in the battery hull on the opposite side of the winch to stabilize the buoy as they support the power for the main controller and winch, respectively. The configuration for the batteries and solar panels are listed in **Table 1**. In the lower part of INBUS-2, a hull with a pipe shape is attached to the buoy. The center of the hull is empty such that the underwater sensors can move through it when they are lowered/lifted by the winch. The frame with underwater sensors is connected to the winch through the hull and weight. When the sensors are not in operation, they are inside the hull and thus protected from damage by suspended materials or waves. The positions of the equipment and sensors of INBUS-2 are shown in **Figure 3**.

Intelligent Buoy System Sensors

As mentioned above, INBUS-2 is self-powered based on the installation of solar panels. In addition, a 12 V battery is used to support the power system. The INBUS-2 sensors can be divided into five classes: (1) GPS and weather sensors that are mounted on top of the buoy; (2) altimeter and wave gauge, which are used to determine whether the lifting frame should be lowered based on the wave data and to measure the water depth to identify the vertical measuring distance; (3) water quality sensors and current meter, which are installed on the lifting frame to measure the water quality and flow velocity at each vertical level; (4) ADCP, which is used to measure the vertical current and SSC profiles, under harsh wave conditions when the lifting frame is not operated; and (5) CDMA system, which is used to transfer the real-time data to the ground station and to control INBUS from the ground station. If the buoy is disconnected from the mooring location and drifts away from the CDMA range, INBUS-2 can be located based on the connection to LEO satellites. The locations of the sensors are marked in **Figures 3**, **4**, and the specifications of the sensors of the five classes are presented in **Table 2**.

Operation

The operation procedure of INBUS-2 is as follows:

(1) Wake-up mode: the INBUS is switched from standby to wake-up mode 5 min prior to the observation to check the settings.
(2) Operation mode test: the main controller checks for command changes (e.g., sensing mode change, forced termination, ADCP reset) from the ground control station.
(3) Application of the changed command: resetting of INBUS according to the changed command (if any) in Step (2).
(4) INBUS status test: checking of the location of INBUS, communication cable loosening, encoder starting point, and emergency stop, INBUS voltage, and CDMA sensitivity.

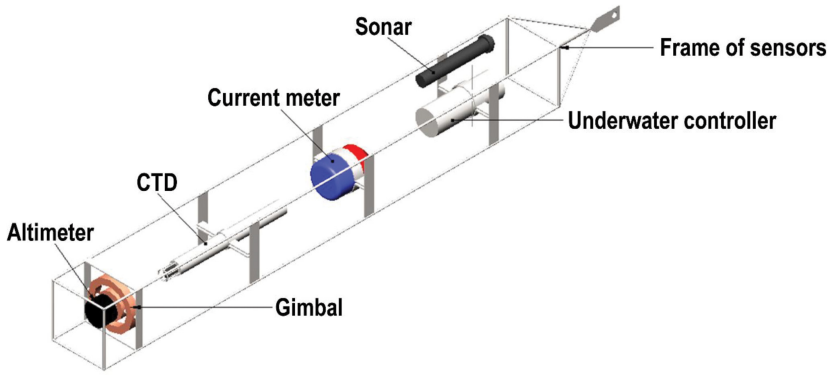

FIGURE 4 | Schematic of the frame marked in **Figure 3** and the underwater sensors mounted in the frame.

(5) Warning: if a problem is detected in Step (4), the current status is transmitted to the control station (or user) using the CDMA system. If the INBUS location deviates from the initial location, its current location is transmitted using the CDMA system or a LEO satellite if it is out of the CDMA range.
(6) Positioning of the lifting sensor frame: before the observation begins, the lifting sensor frame is moved to the home position (1 m below the water surface) inside the hull.
(7) Measuring of the weather and wave conditions.
(8) Decision-making for observation: based on the wave conditions measured in Step (7), a decision is made as to whether the lifting sensor frame should be lowered to start the observation.
(9) ADCP observation: the ADCP is set to start the measurement when the frame sensors are lifted. If the frame should not operate owing to harsh wave conditions, the ADCP starts the observation alone.
(10) Measurement of the water depth: if the system works under normal conditions after completing Step (8), the communication cable is lowered to move the lifting sensor frame 2.8 m below the water surface (first observation layer) outside the hull. The altimeter measures the water depth and divides it into N layers to determine the water depth of layer N for profiling.
(11) Profiling (observations using lifting frame sensors)
  (A) 1st to N – 1th layer:
  (A1) When the frame reaches the layer calculated by the altimeter, the water depth is measured again to check if the frame has reached the intended water depth. If it has not, the position of the frame is adjusted.
  (A2) Wait time of 1 min to allow the frame to stabilize; subsequently, the sensor measurements start (1 min).
  (A3) The data are saved in a data logger and a secure digital (SD) memory card for backup.
  (A4) INBUS status check: same procedure as Step (4). If the INBUS is operating under normal conditions, the communication cable is lowered to move to the next level.
  (B) Nth layer:
  (B1) The frame is 1 m above the seabed (to secure the safety of the sensor).
  (B2) Same procedures as described in Steps A2–A4.
(12) Returning to the home position: the winch is operated to move the frame back to the home position (1 m below the water surface) inside the hull.
(13) Data transfer: the data stored on the data logger are transferred to the ground station using the CDMA system.
(14) Standby: the INBUS is switched into standby mode.

The operation procedure of INBUS-2 is summarized by the flowchart in **Figure 5**.

When errors are detected during the operation of INBUS, an error message is sent to the users to notify them. The users can then fix the problems according to the error message received. The error messages and status updates are listed in **Table 3**.

Mooring, Automatic Lifting, and Data Transfer System

For the mooring of INBUS, a two-point mooring line is used considering the strong flow velocity in areas with a high tidal range (**Figure 6**). Two rows of anchor chains connected to the two weights are used to fix INBUS and minimize buoy movement. Several pressure buoys are attached to the mooring lines made of nylon ropes to prevent collisions and twists between the sensor unit and lines, which might occur when the lines loosen during low tides. The weights are placed onto the seabed perpendicular to the tidal current direction to increase the stability. In addition to the weights, four anchors are installed on both sides of the weights. The mooring system of INBUS-2 is illustrated in **Figure 6**. The lengths of the anchor chains and mooring lines marked in **Figure 6** are the distances between the sinkers and buoy used to prevent collisions and twists when the water depth is 15 m with a maximum tidal range of 9 m.

The automatic lifting system (ALS) consists of the winch and main controller, with the main controller deciding when and the length of communication cable to be lowered for reaching the destination levels from the winch. The winch consists of a motor, drum, reducer, SlipRing, communication

cable holder, waterproof housing, and supporter (**Figure 7**). The motor and reducer rewind the communication cables on the drum. The SlipRing protects the data transferred through the communication cables when they are rewound on the drum. The communication cable holder keeps the communication cables on the drum during rewinding. The motor, reducer, and SlipRing are waterproof and protected by a housing. The specifications of the winch system are presented in **Table 4**.

The efficiency of the reducer [(power of output shaft)/(power of input shaft) × 100] of INBUS-2 is increased by 30% compared to that of INBUS-1 by directly connecting it to the motor, that is, removing the chains used for the connection to the reducer. The motor is equipped with an electronic break to control the winch and save power when it is not in operation. In winter, the lubricants are often frozen, which reduces the efficiency and lifetime of the system. In INBUS-2, the lubricants are replaced with low-temperature grease and additional oils. In addition, the drum is equipped with bearings on both sides to prevent distortion due to the tension of the communication cables.

TABLE 2 | Specifications of the sensors mounted on INBUS-2.

Sensor		
Classification (sensor/manufacturer)	**Measuring data**	**Description**
Weather sensor (PB200/Airmar)	Wind speed	Measuring range: 0–41 m/s Resolution: 0.05 m/s Accuracy: ±0.5 m/s
	Wind direction	Measuring range: 0°–360° Resolution: 0.1° Accuracy: ±0.5°
	Air temperature	Measuring range: −25–55°C Resolution: 0.1°C Accuracy: ±0.1°C
	Air pressure	Measuring range: 850–1150 hPa Resolution: 0.1 hPa Accuracy: ±2 hPa
Altimeter (SS510/Airmar) and wave gauge (TinyWave/OTRONIX)	Water depth	Measuring range: 0.5–100 m Resolution: 0.03 m Frequency: 235 kHz Beamwidth: 6°
	Wave parameter	Measuring range: 0–20 m (wave height) 0–25 s (wave period) Resolution: 0.1 m/0.1 s
Water quality sensor (YSI6600/YSI; DCS 4100R/Aanderaa)	Current velocity, sensor depth, conductivity, water temperature, salinity, pH, DO, Chl, turbidity	Measuring range: 0–3.0 m/s (current speed); 0°–360° (current direction); −5–45°C (temperature); 0–100 mS/cm (conductivity); 0–1,000 NTU (turbidity); 0–400 μg/L (chlorophyl); 0–500 μM (DO). Accuracy: ±0.15 cm/s (current speed); ±5° (current direction); ±0.15°C (temperature); ±0.5% (conductivity); ±2 NTU (turbidity); 0.1 μg/L (chlorophyl); 8 μM (DO).
Current and SSC (ADCP600kHz/RDI)	Water profiling	**Vertical Resolution / Range / Std. Dev** 0.5 m / 38 m / 14.0 cm/s 1.0 m / 42 m / 7.0 cm/s 2.0 m / 46 m / 3.6 cm/s 4.0 m / 51 m / 1.8 cm/s
	Profile parameters	Velocity accuracy: 0.3% of water velocity relative to ADCP ± 0.3 cm/s Velocity resolution: 0.1 cm/s Velocity range: ±5 m/s default, ±20 m/s max Number of depth cells: 1–255 Ping rate: typical 2 Hz, Max. 10 Hz
	Echo intensity profile	Vertical resolution: depth cell size, user configurable Dynamic range: 80 dB Precision: ±1.5 dB

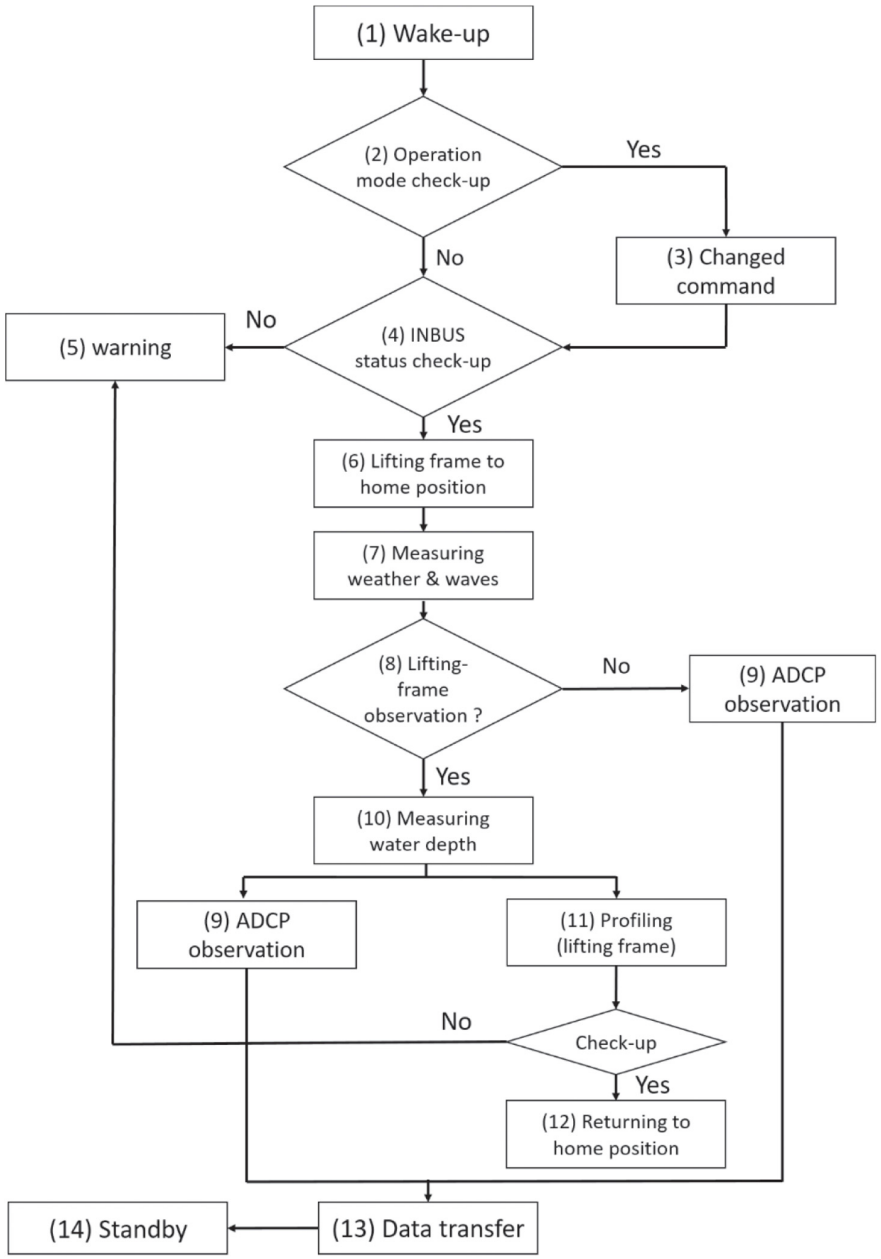

FIGURE 5 | Flowchart of INBUS-2 operation procedure.

The data measured by INBUS are transferred to the ground station using the CDMA network, which works well even in sea areas in which electronic signals are weak. The data are transferred using a CDMA-to-CDMA system and relay stations such that they can be safely received by the ground station (**Figure 8A**). The real-time data transferred by the CDMA network can be downloaded from a website. The users can remotely control INBUS by changing the number of observations and water depth of the lifting system. The users can make commands for sampling, emergency stop, or winch recovery. When an error occurs in INBUS, an error message is sent to the smartphone of the user without interference from the firewall. If INBUS is disconnected from the mooring system and drifts away from the CDMA area, the communication system connects to the Iridium satellites. **Figure 8B** shows the Iridium system. The users directly receive information from the Iridium station and can track the location of INBUS in real time.

RESULTS

In this section, examples of INBUS data are presented and analyzed to discuss the efficiency of the INBUS system in

TABLE 3 | Error messages and status updates sent from INBUS-2.

Error message	Status
AWS error	GPS information is not received or weather data are missing.
Buoy location error	The buoy is out of range of the permissible radius with respect to the initial position.
Encoder error	The length of the communication cable cannot be measured owing to mechanical problems.
Limit switch error	The limit switch that checks the position of the lifting sensor frame is not in operation.
Motor driver error	Electric current exceeds the threshold. This can occur when the water flow velocity is too strong or the buoy is disturbed by fishing gear (e.g., fishing net).
Home recovery error	The lifting sensor frame did not return to the home position, which is likely due to mechanical problems or disturbance by fishing gear.
UC data error	The data measured by the lifting frame sensors are not received by the main controller.
Profiling error	Lifting frame sensors cannot be operated owing to high waves.
Altimeter error	The altimeter cannot determine the vertical layers.

measuring the water properties in macrotidal environments. First, the time variation of the INBUS data measured in the air and water over a period of 1 month was plotted. Data on this scale are useful to analyze the variations in the water properties during the spring and neap tides with maximum and minimum tides, respectively. Second, the properties measured during the spring and neap tides were plotted for a shorter period of ∼2 days. Based on this scale, the detailed variation in the water column from high to low tide can be visualized and data obtained during the spring and neap tides can be compared, highlighting the performance of INBUS.

Time Variation

In this study, INBUS data were measured off the west coast of Korea near Incheon Airport (**Figure 9**). In this region, the semidiurnal tidal cycle can be clearly observed and the spring and neap tides significantly differ. The INBUS-2 system was installed at P1, which has a mean water depth of ∼18 m. The maximum tidal range during spring tide is ∼11 m, that is, >60% of the mean water depth. The maximum water depth during high tide is >20 m, whereas the minimum depth during low tide is ∼10 m, leading to difficulties measuring the water properties at fixed points in the water column owing to the significant change in the water level. The area is connected to a water channel north of Yeongjong-do Island (airport location), which produces strong tidal currents. Therefore, long-term observations of the water properties are required to monitor the marine environment near the airport. For this purpose, the INBUS-2 system was installed in October 2010 and the air and water properties at P1 were measured until August 2012.

Figures 10, **11** show examples of the data measured by INBUS-2 over 24 days from June 1 to 24. In this period, both the spring and neap tides were observed for comparison. During this experiment, a total of 15 properties were measured by INBUS-2 in the air (**Figure 10**) and water (**Figure 11**). The weather sensor measured the wind speed, direction (**Figures 10a,b**),

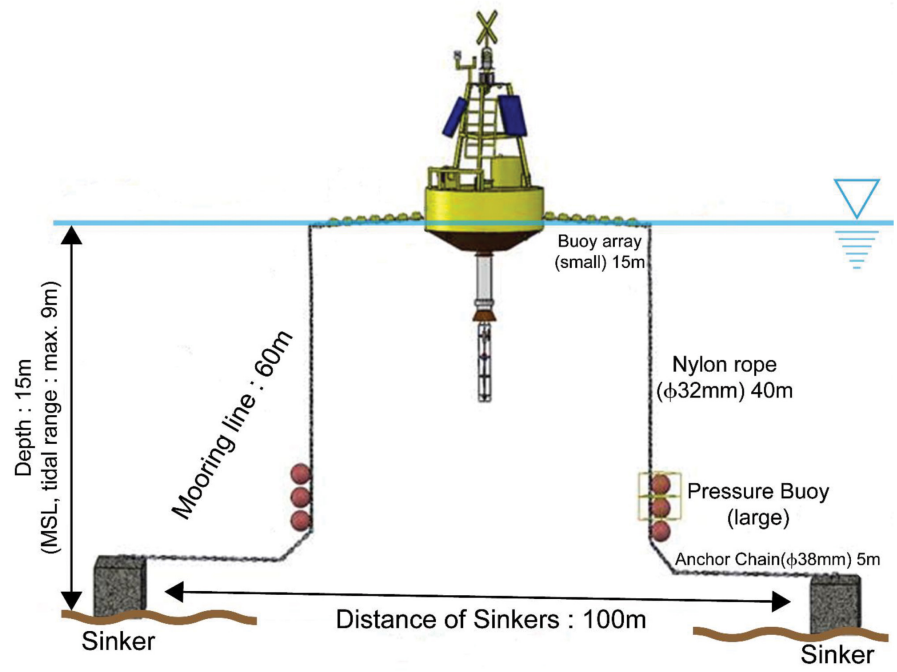

FIGURE 6 | Intelligent Buoy System (INBUS)-2 mooring system.

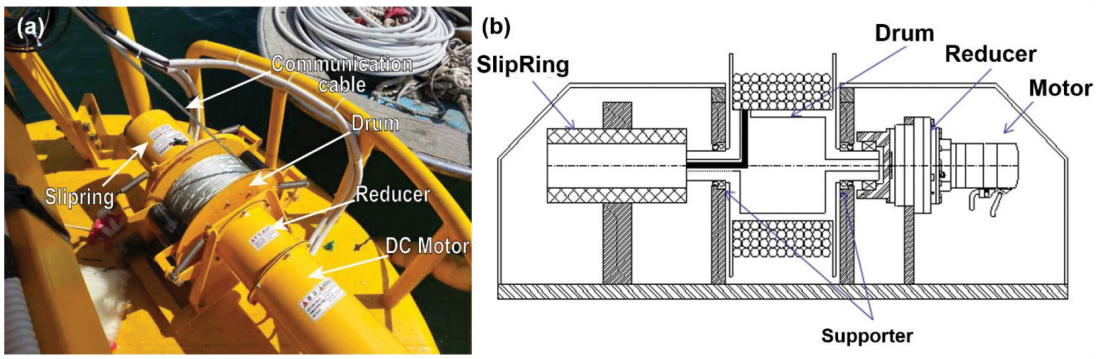

FIGURE 7 | (a) Picture of winch, **(b)** schematic of winch, which is controlled by the automatic lifting system (ALS).

TABLE 4 | Specifications of the winch mounted on INBUS-2.

Manufacturer	**OCEANTECH Co., Ltd.**
Model No.	ALE-2460-7DM
Material	SUS 316
Specifications	• Cable
	– 24 AWG × 7c
	– Size: approx. ϕ10 mm
	– weight: approx.0.161 kg/m
	– length: 60 m
	•Winding length: 60 m
	•Winding speed: 5 m/min
	•Winding torque: 15 kg.m
	•Power source: 24 VDC, ϕ1, 60 Hz
	•SlipRing: 2A × 7P
	•Total weight: approx.100 kg
	•Motor
	– 24 VDC, ϕ1, 60 Hz
	– 300 W, 3000 rpm, 1/600
	•Brake
	– 24 VDC

and air temperature and pressure (**Figures 10d,e**). The surface elevation was measured using an altimeter (**Figure 11a**) and the wave height was measured with TinyWave (**Figure 10c**). INBUS-2 sent down the lifting frame every 0.5 h to measure the water properties. Four internal levels were set up for this experiment such that the distance from the lifting frame to the seabed was divided by four during each observation (**Figure 11b**) and the water quality sensor measured the properties in four internal levels. In this experiment, the current speed and direction (**Figures 11c,d**), water temperature (**Figure 11e**), DO content (**Figure 11f**), Chl concentration (**Figure 11g**), turbidity (**Figure 11h**), salinity (**Figure 11i**), and conductivity (**Figure 11j**) were measured. In this experiment, the ADCP was not operated and thus current and SSC data are not available.

Based on the total water depth (**Figure 11A**), the spring tides occurred on June 7 and 21, with a maximum value of ∼11 m (June 7). The neap tide developed on June 14 with a tidal range of ∼4 m. During this period, the wind conditions were mild because the wind speed was less than 10 m/s (**Figure 10a**). Accordingly, the wave conditions were mild with wave heights below 0.3 m. Therefore, the main driving forces of the water properties were the tides. **Figure 11b** shows that the mean water depths of the four internal levels were ∼2, 7, 11, and 15 m, respectively. With the decrease in the tidal range from the spring tide (June 7) to the neap tide (June 14), the current speed of the first internal layer decreased from the maximum of ∼1.4 m/s to ∼0.6 m/s (**Figure 11c**). However, the current direction, which was 180° out of phase between the high and low tides, did not change (**Figure 11e**). During one tidal cycle, the water temperature fluctuates, with a mean difference of ∼2°C, which will be discussed in detail in the next section. The daily mean temperature during the experimental period gradually increased from ∼15 to ∼18°C with the start of the summer season. The water properties, such as the DO content, Chl concentration, and turbidity, differ in the spring and neap tides. Higher values were obtained during the spring tides under stronger mixing of the surface water due to stronger currents (**Figures 11f–h**). However, note that the DO and Chl contents were higher during the latter spring tide on June 21 than on June 7, whereas the tidal range was higher on June 7. This is likely related to the higher water temperature in the latter spring tide, which increased the primary production. In contrast, the turbidity was greater during the former spring tide because the sediment suspension increased under the stronger tidal current. The salinity and conductivity show similar patterns because the differences between the spring and neap tides were smaller than those of other properties. In contrast, the differences between the high and low tides were significant because higher values were obtained during the low tides (**Figures 11i,j**), which is likely due to the impact of freshwater inflow from the land (**Figure 11**).

Difference Between Internal Layers

In this section, the water properties are compared on a shorter time scale. **Figures 12a–g** show seven properties (total depth, depths of internal layers, current speed, water temperature, Chl, turbidity, and salinity) that were measured over 2 days starting on June 7 when the first spring tide occurred. Different colors are used to represent the data measured in the four different internal layers. The figures indicate clear

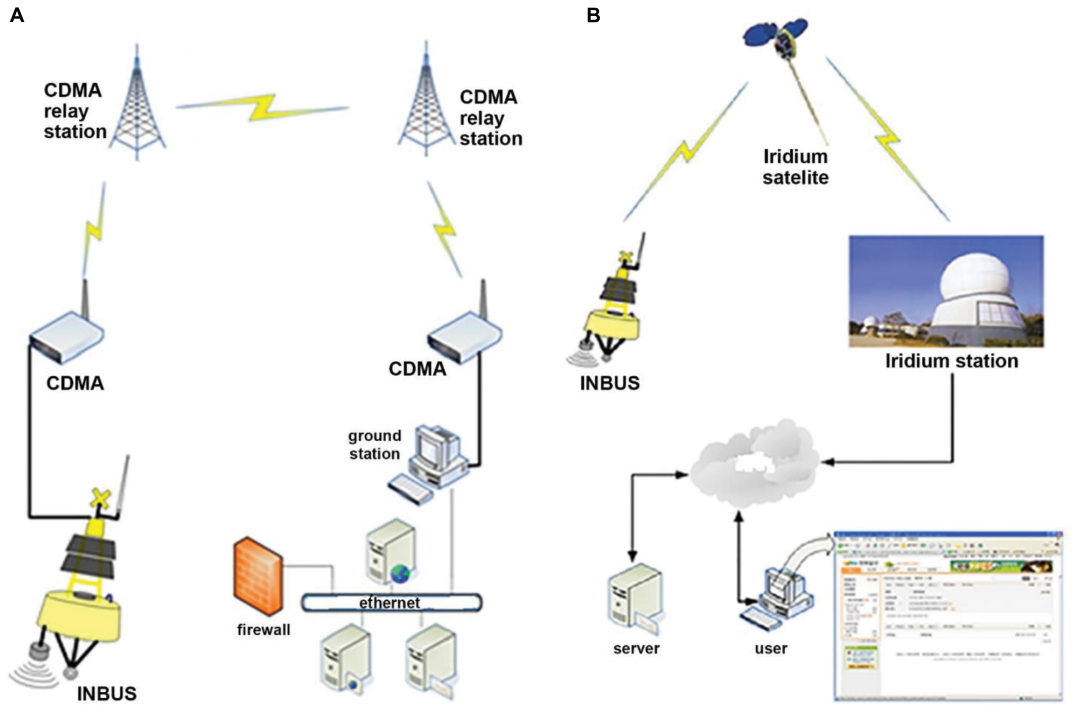

FIGURE 8 | (A) Data transmission system of INBUS-2. **(B)** Iridium satellite system for the tracking of the location of INBUS after disconnection from the mooring system.

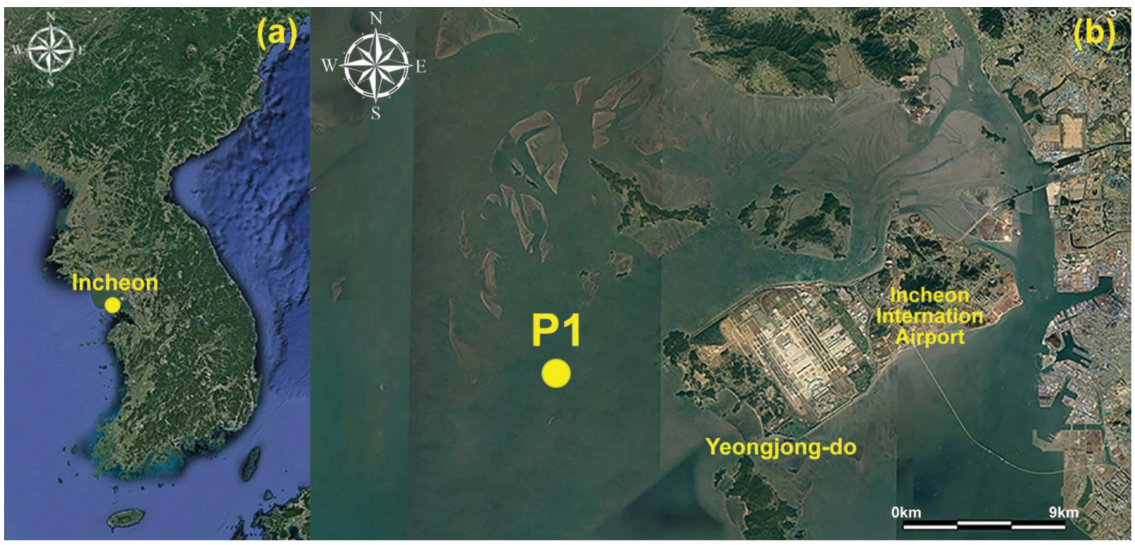

FIGURE 9 | (a,b) Map of the area near Yeongjong-do Island showing location P1 at which INBUS-2 data were measured.

differences between the first (top) and fourth (bottom) layers during the spring tide. The current speed of the top layer ($z < 5$ m) reached ∼1.4 m/s in the ebb and flood phases during the spring tide (**Figures 12b,c**). However, the maximum current speed of the bottom layer was only ∼0.8 m/s at z ∼15 m, which indicates the stratification of water during the spring tide.

Note that the water temperature is higher and lower during low and high tides, respectively (**Figure 12d**). The water temperature increased during the high tide in the shallower area in which mud flats developed (**Figure 8**) and flowed out to the deeper area (close to location P1) with the ebb tide. During the flood phase, the water temperature of the top layer was 1.0–1.5°C higher than that of the bottom layer. When the heavier cold water

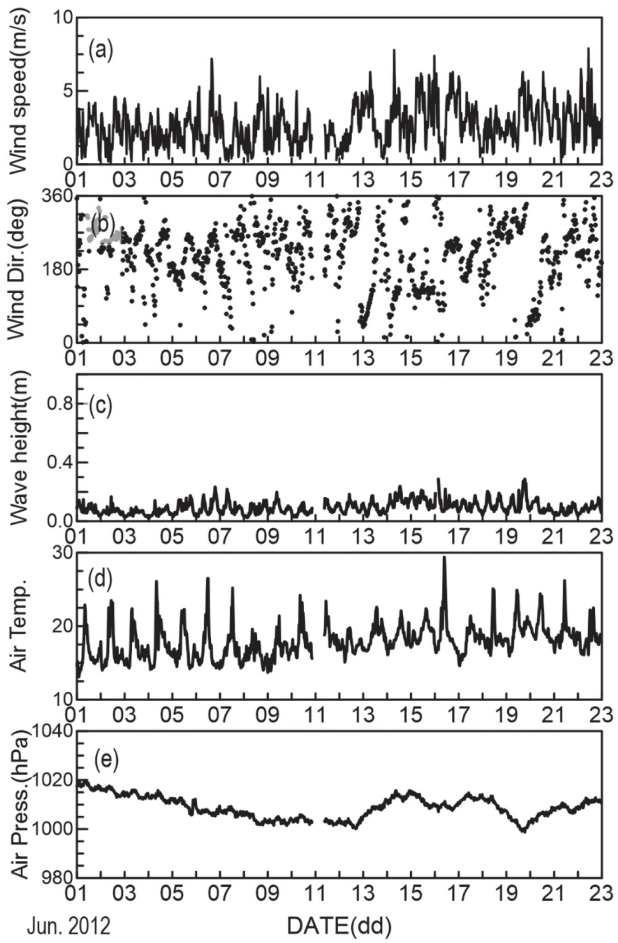

FIGURE 10 | Time variation of air properties measured by INBUS-2 at location P1 from June 1 to 23, 2012: **(a)** wind speed, **(b)** wind direction, **(c)** wave height, **(d)** air temperature, **(e)** air pressure.

in the deeper area reached the location with the flooding tide, it occupied the lower layers first owing to its weight, while the water in the top layer remained warm, leading to stratification.

The stratification during the flood phase is also reflected in the salinity data (**Figure 12g**). In contrast to the temperature, the salinity is higher during high tides and lower during low tides because the warmer but fresher water flows from shallower areas with ebbing tides to the area close to location P1. However, when the colder water with higher salinity flows from the deeper area to the location with the flooding tides, heavier salty water occupies the lower layers first and thus the salinity in the lower layers exceeds that of the top layer. The time-dependent patterns of the Chl content and turbidity are similar because the corresponding values are higher in the lower layers and lower in the top layer (**Figures 12e,f**), which is reasonable because a larger quantity of sediments is expected below the surface layer based on their weight. In addition, the maximum Chl content is generally measured below the surface layer (Loisel et al., 2001). Note that the differences in the Chl and turbidity values between the top and bottom layers increase in the flood tidal phases. This increase corresponds to the variation in the salinity (**Figure 12g**), which is due to the intrusion of heavy water from the deeper area during the flooding phase.

In **Figures 12h–n**, the same properties measured over 2 days starting on June 14 (neap tide) are compared. Compared with the spring tide, the difference between the top and bottom layers is smaller. The maximum current speed of the top layer is ∼0.7 m/s, that is, only half of that in the spring tidal period (**Figure 12j**). The maximum current speed of the bottom layer is ∼0.5 m/s. The water temperature and salinity differences between the high and low tides are also smaller during the neap tide (**Figures 12k,n**). Note that stratifications of the temperature and salinity were also observed, similar to those of the spring tide. However, the maximum stratification occurred during the low tides, indicating that the warmer and fresher water in the shallower areas during the high tides flowed out to the area close to location P1 and remained in this area during the low tides instead of flowing out further because the distance of the tidal current movement is shorter during the neap tide. Note also that the turbidity during the neap tide is only ∼10–15% of that in the spring tide (**Figure 12m**) because the suspension of sediments from the seabed weakened owing to the weaker current. This analysis demonstrates the advantages of the INBUS system. First, the time variation of the water properties can be continuously measured along the sigma layers during both the high and low tides, although the difference in the water surface elevation increases to ∼11 m during the spring tide. In addition, the differences between the water properties of the internal layers can be clearly detected by the INBUS system and, thus, the characteristics of the stratification depending on the tidal phase can be observed and analyzed.

The current buoy system (INBUS-2) is an upgraded version of the original system (INBUS-1), as described in the previous sections. However, the results of field experiments using INBUS-2 indicated weaknesses and thus a further upgrade is required. Therefore, a new version of the buoy, INBUS-3, is being designed. The upgrades planned for INBUS-3 are introduced in the following section.

DISCUSSION

One of the weaknesses of INBUS-2 is that the SSC indirectly measured by the YSI and the ADCP has a low accuracy, which limits the estimation of the sediment distribution under strong tidal current conditions. However, the accurate measurement of the sediment distribution in the water column is important to understand the coastal processes in macrotidal areas. The measured SSC can be used to validate the results of numerical models and thus the data accuracy is important. Other water quality properties, such as the DO or Chl contents, cannot be used to validate the model because the model requires accurate lateral boundary and initial conditions, which cannot be provided. In INBUS-3, this problem will be solved by mounting a LISST sensor (manufactured by Sequoia, United States) on the lifting sensor frame. The LISST sensor is a submersible laser diffraction-based particle size analyzer designed to measure the particle size

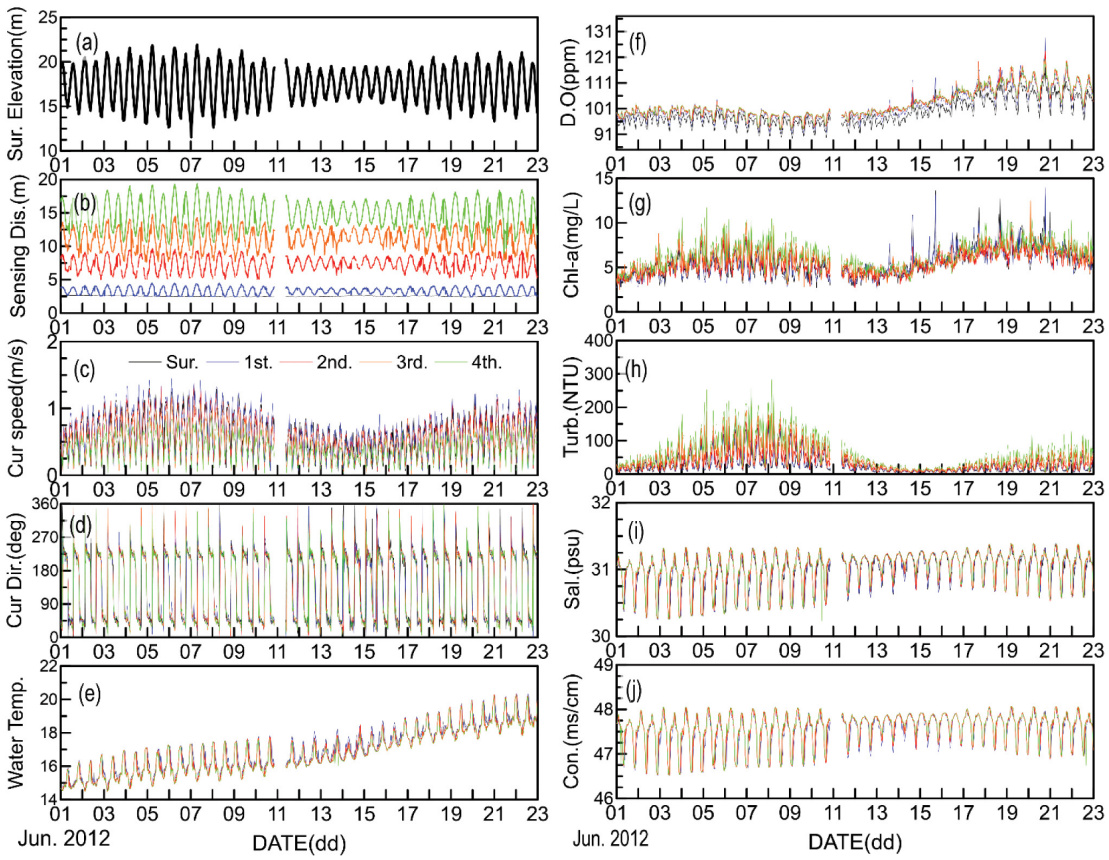

FIGURE 11 | Time variation of water properties measured by INBUS-2 at location P1 from June 1 to 23, 2012: **(a)** surface elevation, **(b)** distances from the four internal layers to the seabed, **(c)** current speed, **(d)** current direction, **(e)** water temperature, **(f)** dissolved oxygen (DO), **(g)** chlorophyll (Chl), **(h)** turbidity, **(i)** salinity, **(j)** conductivity. Black solid lines, measured at the water surface; blue lines, measured in the first internal layer; red lines, measured in the second internal layer; orange lines, measured in the third internal layer; green lines, measured in the fourth internal layer.

and concentration, which can be used in coastal waters. Because the LISST sensor can measure the SSC with high accuracy, the data can be used for numerical models and to calibrate the YSI and the ADCP data.

Although the LISST can measure the SSC in different layers in the water column based on the vertically moving lifting frame, it cannot detect the SSC close to the seabed, which is important for the determination of the near-bed sediment dynamics. To protect the lifting frame, the maximum water depth to which the lifting frame of INBUS-2 can be lowered is set to 1.0 m above the seabed. In INBUS-3, the structure of the lifting frame will be modified to allow it to be lowered to 0.3 m above the seabed for the $N + 1$th layer. As described, the conceptual design of INBUS-3 has been completed. However, because of the increasing cost, its development has been delayed and it is not yet complete. In addition, INBUS-2 has been successfully applied in the areas where its weakness does not pose a serious problem (i.e., where the accuracy of sediment concentration measurement is not necessarily required), which further causes the development of INBUS-3 to be viewed as not very urgent.

Intelligent Buoy System can be effectively applied in macrotidal environments in which the sea surface height significantly changes. The water column can be divided into N layers regardless of changes in the water depth such that the time-dependent water qualities and flow velocities can be measured after the layers are set in a manner similar to the sigma coordinates of numerical models, which benefits the validation of the model results based on that grid system. INBUS was initially designed to monitor marine environments close to tidal power plants (TPPs), which generate power using fast-flowing tidal currents. Marine environments can be significantly changed by the construction of TPPs. INBUS has been successfully applied for the long-term monitoring of the water qualities in areas close to TPPs in which the tidal range is high. The distribution of sediments suspended by strong tidal currents can be effectively determined and thus their effects on the marine environment close to fishing grounds and aquaculture farms can be analyzed.

In addition to macrotidal areas, INBUS is useful for monitoring the water quality near ports, especially those undergoing construction. During the construction of facilities and structures at ports, strong sediment suspension occurs and the sediments flow into nearby fishing grounds and farms, which might have a negative environmental impact. Such sediments may spread horizontally and vertically when they combine with

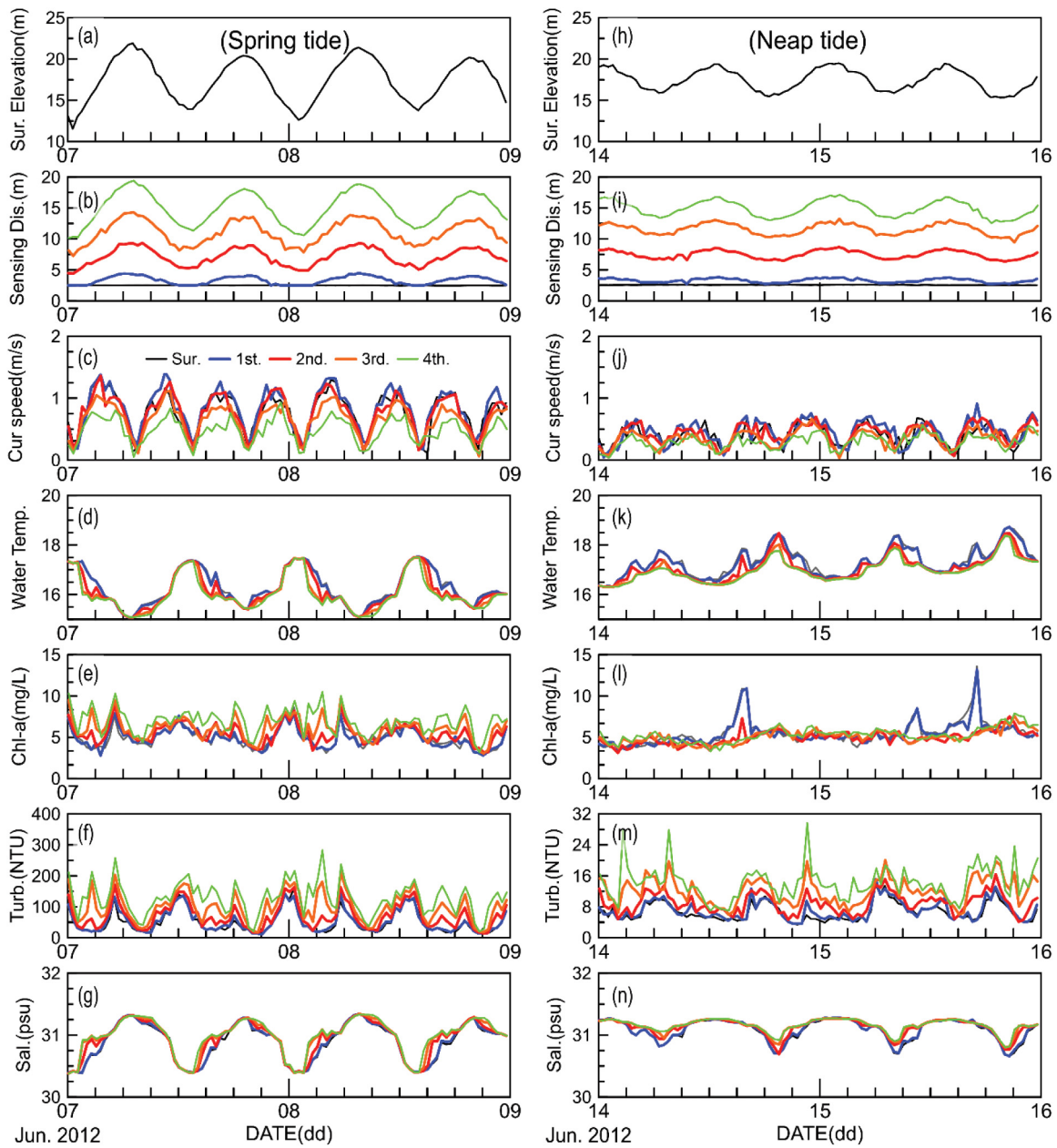

FIGURE 12 | Time variation of the **(a)** surface elevation, **(b)** distances from the four internal layers to the seabed, **(c)** current speed, **(d)** water temperature, **(e)** Chl content, **(f)** turbidity, and **(g)** salinity over 2 days (June 7–9, 2012) during the spring tide and the time variation of the **(h)** surface elevation, **(i)** distances from the four internal layers to the seabed, **(j)** current speed, **(k)** water temperature, **(l)** Chl content, **(m)** turbidity, and **(n)** salinity over 2 days (June 14–16, 2012) during the neap tide. Black solid lines, water surface; blue lines, first internal layer; red lines, second internal layer; orange lines, third internal layer; and green lines, fourth internal layer.

tides and/or coastal currents. INBUS has been effectively applied for the monitoring of the water quality variation under such conditions and the results used to establish plans to protect the environment.

Although not planned for the construction of INBUS-3, additional upgrades are recommended for future INBUS generations. One of the major purposes of INBUS is the long-term monitoring of the water quality in tide-dominated areas. This requires the sustainable maintenance of the system and sensors. Some of the turbidity, DO, and Chl data collected by INBUS are abnormal, especially during summer, which is due to the contamination of the instruments by the fouling of periphyton adhering to the underwater sensors. In addition to the sensors, fouling could occur on the frame and disturb the motion of the lifting system, which may result in the reduction of the INBUS lifetime. Therefore, it is important to remove the periphyton from the sensor and/or to prevent fouling to increase the maintainability of INBUS; for example, hydro-wipers can

be used to remove periphyton and prevent biofouling (Cotter et al., 2017). In addition, underwater systems that can be used to prevent the fouling on the bottom of ships have recently been proposed for the reduction of the toxicity of the antifouling paint (Amara et al., 2018; Lagerström et al., 2020). To optimize the buoy system, it may also be necessary to reduce the size of the winch while keeping or even enhancing its efficiency, which requires consideration in future upgrades of INBUS to make it suitable for long-term monitoring in tide-dominated coastal environments.

DATA AVAILABILITY STATEMENT

The raw data supporting the conclusions of this article will be made available by the authors, without undue reservation.

AUTHOR CONTRIBUTIONS

J-SP and J-YJ contributed to the conception and design of the study and wrote sections of the manuscript. JD, S-DH, S-JM, KH, and JP organized the database. JD and BL performed the statistical analysis. JD, J-YJ, and YC wrote the first draft of the manuscript. All authors contributed to the manuscript revision and read and approved the submitted version.

FUNDING

This work was supported by the Korea Institute of Ocean Science and Technology (Grant Number PE99932) and the Ministry of Oceans and Fisheries (Grant Number PM62220).

REFERENCES

Alexandrakis, G., Manasakis, C., and Kampanis, N. A. (2015). Valuating the effects of beach erosion to tourism revenue. A management perspective. *Ocean Coast. Manag.* 111, 1–11. doi: 10.1016/j.ocecoaman.2015.04.001

Amara, I., Miled, W., Slama, R. B., and Ladhari, N. (2018). Antifouling processes and toxicity effects of antifouling paints on marine environment. A review. *Environ. Toxicol. Pharmacol.* 57, 115–130. doi: 10.1016/j.etap.2017.12.001

Bailey, K., Steinberg, C., Davies, C., Galibert, G., Hidas, M., Mcmanus, M. A., et al. (2019). Coastal mooring observing networks and their data products: recommendations for the next decade. *Front. Mar. Sci.* 6:180. doi: 10.3389/fmars.2019.00180

Cadier, M., Gorgues, T., LHelguen, S., Sourisseau, M., and Memery, L. (2017). Tidal cycle control of biogeochemical and ecological properties of a macrotidal system. *Geophys. Res. Lett.* 44, 8453–8462. doi: 10.1002/2017gl074173

Cotter, E., Murphy, P., and Polagye, B. (2017). Benchmarking sensor fusion capabilities of an integrated instrumentation package. *Int. J. Mar. Energy* 20, 64–79. doi: 10.1016/j.ijome.2017.09.003

Do, J. D., Jin, J. Y., Jeong, W. M., and Chang, Y. S. (2019). Observation of rapid seabed erosion near closure depth during a storm period at Hujeong Beach, South Korea. *Geophys. Res. Lett.* 46, 9804–9812. doi: 10.1029/2019gl083910

Dorman, C. E., and Winant, C. D. (1995). Buoy observations of the atmosphere along the west coast of the United States, 1981–1990. *J. Geophys. Res. Oceans* 100, 16029–16044. doi: 10.1029/95jc00964

Fowler, G. A., Hamilton, J. M., Beanlands, B. D., Belliveau, D. J., and Furlong, A. R. (1997). "A wave powered profiler for long term monitoring," in *Proceedings of the Oceans'97. MTS/IEEE Conference*, Halifax, NS, 225–228.

Herbers, T., Jessen, P., Janssen, T., Colbert, D., and Macmahan, J. (2012). Observing ocean surface waves with GPS-tracked buoys. *J. Atmos. Ocean. Technol.* 29, 944–959. doi: 10.1175/jtech-d-11-00128.1

Hwang, J. H., Van, S. P., Choi, B.-J., Chang, Y. S., and Kim, Y. H. (2014). The physical processes in the Yellow Sea. *Ocean Coast. Manag.* 102, 449–457. doi: 10.1016/j.ocecoaman.2014.03.026

Jeong, W. M., Chang, Y. S., Oh, S.-H., and Baek, W. D. (2020). A study on calibration of underestimated wave heights measured by Wave and Tide Gauge (WTG). *J. Korean Soc. Coast. Ocean Eng.* 32, 296–306. doi: 10.9765/kscoe.2020.32.5.296

Kang, Y. Q. (1984). An analytic model of tidal waves in the Yellow Sea. *J. Mar. Res.* 42, 473–485. doi: 10.1357/002224084788506004

Korea Institute of Ocean Science and Technology (KIOST) (2004). *Studies on Improving Basic Observation Techniques for Marine Environment (Marine Remote Observation Techniques Development).* Techical Rep. BSPE83000-1498-1 (In Korean). Busan: Korea Institute of Ocean Science and Technology.

Lagerström, M., Ytreberg, E., Wiklund, A.-K. E., and Granhag, L. (2020). Antifouling paints leach copper in excess–study of metal release rates and efficacy along a salinity gradient. *Water Res.* 186:116383. doi: 10.1016/j.watres.2020.116383

Loisel, H., Stramski, D., Mitchell, B. G., Fell, F., Fournier-Sicre, V., Lemasle, B., et al. (2001). Comparison of the ocean inherent optical properties obtained from measurements and inverse modeling. *Appl. Opt.* 40, 2384–2397. doi: 10.1364/ao.40.002384

Pedersen, T., Siegel, E., and Wood, J. (2007). "Directional wave measurements from a subsurface buoy with an acoustic wave and current profiler (AWAC)," in *Proceedings of the OCEANS 2007, Vancouver, BC*, (Piscataway, NJ: IEEE), 1–10.

Tedesco, M., Bohlen, W. F., Howard-Strobel, M., Cohen, D., and Tebeau, P. (2003). "The Mysound project: building an estuary-wide monitoring network for Long Island Sound, U.S.A," in *Coastal Monitoring Partnerships*, eds B. D. Melzian, V. Engle, M. McAlister, S. Sandhu, and L. K. Eads (Dordrecht: Springer), 35–42. doi: 10.1007/978-94-017-0299-7_4

Tercier-Waeber, M. L., Buffle, J., Graziottin, F., and Koudelka-Hep, M. (1999). Novel voltametric probe in-situ trace element monitoring. *Sea Technol.* 40, 74–79.

Woerther, P., and Grouhel, A. (1998). "MAREL: automated measurement network for the coastal environment," in *Proceedings of the IEEE Oceanic Engineering Society, OCEANS'98 Conference*, Nice, Vol. 2, 1149–1154.

Yanagi, T., and Inoue, K. (1995). Tide and tidal current in the Yellow/East China Seas. *Oceanogr. Lit. Rev.* 6:425.

Conflict of Interest: S-DH and S-JM were employed by company OCEANTECH Co., Ltd.

The remaining authors declare that the research was conducted in the absence of any commercial or financial relationships that could be construed as a potential conflict of interest.

Publisher's Note: All claims expressed in this article are solely those of the authors and do not necessarily represent those of their affiliated organizations, or those of the publisher, the editors and the reviewers. Any product that may be evaluated in this article, or claim that may be made by its manufacturer, is not guaranteed or endorsed by the publisher.

frontiers in Marine Science

METHODS
published: 23 August 2021
doi: 10.3389/fmars.2021.675456

Novel Method for the Estimation of Vertical Temperature Profiles Using a Coastal Acoustic Tomography System

Yeongbin Park[1,2], Chanhyung Jeon[3], Hajin Song[1], Youngseok Choi[1,4], Jeong-Yeob Chae[1], Eun-Joo Lee[1], Jin Sung Kim[5] and Jae-Hun Park[1]**

[1] Department of Ocean Sciences, Inha University, Incheon, South Korea, [2] Underwater Survey Technology 21, Incheon, South Korea, [3] Department of Oceanography, Pusan National University, Busan, South Korea, [4] Department of Ocean Information Analysis, Geosystem Research Corporation, Gunpo, South Korea, [5] Gwangju Institute of Science and Technology, Gwangju, South Korea

Systems based on remote sensing technology, which use reciprocal acoustic signals to continuously monitor changes in the coastal oceanic environment, are referred to as coastal acoustic tomography (CAT) systems. These systems have been applied in regions in which heavy ship traffics, fishing and marine aquaculture activities make it difficult to establish *in situ* oceanic sensor moorings. Conventionally, CAT measurements were used to successfully produce horizontal maps of the depth-averaged current velocity and temperature in these coastal regions without attempting to produce a vertical temperature profile. This prompted us to propose a new method for vertical temperature profile estimation (VTPE) from CAT data using the available sea surface temperature (SST), near-bottom temperature (NBT), and water depth. The VTPE method was validated using data-assimilated and tide-included high-resolution ocean model outputs, including tide data, by comparing the estimated and simulated temperatures. Measurements were performed in the southern coastal region of Korea, where two CAT stations were moored to establish a continuous coastal ocean monitoring system. The validation results revealed that the algorithm performed well across all seasons. Sensitivity tests of the VTPE method with reasonable realistic random errors in the SST, NBT, and acoustic travel time measurements demonstrate that the method is applicable to CAT observation data because the monthly mean root-mean-squared difference (RMSD) for the vertical profiles for February, May, August, and November were 0.23, 0.30, 0.50, and 0.24°C, respectively. The VTPE method was applied to the CAT observation datasets acquired in February and August. The transceivers at the CAT stations were at depths 11 and 6 m on average. The RMSD between the estimated and observed temperatures in the middle layer (∼3 m depth) between two stations in February and August were 0.08 and 0.60°C, respectively, the accuracy of which is sufficient in largely time-varying coastal environments. We provide a novel method for continuous coastal subsurface environmental monitoring without interrupting maritime traffic, fishing, and marine aquaculture activities.

Keywords: coastal acoustic tomography, vertical temperature profile estimation, tide-considered algorithm, verification of VTPE, application of VTPE, coastal environmental monitoring

OPEN ACCESS

Edited by:
Ole Mikkelsen, Sequoia Scientific, United States

Reviewed by:
Peter Francis Worcester, University of California, San Diego, United States
John Wells, Ritsumeikan University, Japan

***Correspondence:**
Chanhyung Jeon
jeonc@pusan.ac.kr
Jae-Hun Park
jaehunpark@inha.ac.kr

Specialty section:
This article was submitted to Ocean Observation, a section of the journal Frontiers in Marine Science

Received: *03 March 2021*
Accepted: *28 July 2021*
Published: *23 August 2021*

Citation:
Park Y, Jeon C, Song H, Choi Y, Chae J-Y, Lee E-J, Kim JS and Park J-H (2021) Novel Method for the Estimation of Vertical Temperature Profiles Using a Coastal Acoustic Tomography System. Front. Mar. Sci. 8:675456. doi: 10.3389/fmars.2021.675456

INTRODUCTION

Sudden temperature changes in coastal marine environments have an unexpected adverse impact on coastal fisheries and the aquaculture industry (Lee et al., 2007; Choi et al., 2009; Kim and Kim, 2010). Recent progress in sea state monitoring systems has enabled us to obtain continuous high-resolution sea surface temperature (SST) fields from satellite remote sensing (Donlon et al., 2012; JPL Our Ocean Project, 2013). However, it is difficult to obtain continuous subsurface temperature measurements without *in situ* measuring equipment, and it is also challenging to maintain such equipment owing to extensive movements of maritime traffic, the high cost involved, and/or fishing and marine aquaculture activities in coastal seas. Therefore, a remote sensing measurement system that uses acoustic signals and is known as coastal acoustic tomography (CAT) has been suggested (e.g., Kaneko et al., 2020).

The CAT system is an innovative oceanographic technology that can continuously monitor changes in the coastal oceanic environment using reciprocal acoustic signals, regardless of the amount of maritime traffic, and fishing activities. The CAT system was developed on the basis of ocean acoustic tomography, introduced by Munk and Wunsch (1979). Both acoustic tomography systems measure one-way or reciprocally transmitted travel times between sites. In particular, CAT has demonstrated its ability to monitor coastal environmental changes in regions where direct *in situ* measurements are difficult (Zheng et al., 1997; Park and Kaneko, 2000, 2001; Yamaoka et al., 2002; Taniguchi et al., 2013; Zhu et al., 2013; Zhang et al., 2015; Syamsudin et al., 2017). Acoustic instruments measure sound speed structures in three dimensions between acoustic stations and can produce current and temperature fields. Nevertheless, the outputs of CAT measurements are mainly depth-averaged horizontal temperature and current velocity fields, which are difficult to obtain with traditional estimation methods.

In this study, we introduce a novel method for vertical temperature profile estimation (VTPE) based on the acoustic travel time (ATT) between CAT stations and use additionally available *in situ* measurements of SST, near-bottom temperature (NBT), and water depth. Using the output of the high-resolution tide-included ocean model, we first validated the performance of the VTPE method using data collected during all four seasons. This entailed comparing the simulated and estimated temperatures for the southern coastal region of Korea, where two CAT experimental points were set up to establish a continuous coastal ocean monitoring system (**Figure 1**). Then, the VTPE method was applied to the data recorded *in situ* by the CAT observation system, and the accuracy of the method was verified against independent temperature measurements collected in the middle layer between the CAT stations.

VTPE PROCEDURE

The VTPE method uses the ATT, water depth, SST, and NBT as its inputs. A schematic flowchart of the VTPE method is presented in **Figure 2**. The method aims to select a plausible vertical temperature profile among the intended vertical temperature profiles based on the fixed water depth, SST, NBT, and measured ATT. The details of the VTPE procedure are as follows.

The first step is to create plausible temperature profiles based on the water depth, SST, and NBT. The temperature profiles were set by modifying the thickness and depth of the seasonal thermocline with the fixed water depth, SST, and NBT from the measurements. The thickness and depth of the thermocline were varied in the range of 20, 40, 60, and 80% of the total depth; thus, a pair of SST and NBT values consists of 12 profiles (**Figure 2A**). The number of profiles is 12 instead of 16 because the thermocline can extend beyond the sea surface or sea bottom when the thickness of thermocline is 60 or 80% and the depth of thermocline is 20 or 80%. Note that all profiles are identical when the SST and NBT are the same.

The second step is to calculate the ATT using each predicted temperature profile. The temperature profiles were converted to sound speed profiles using the equation of Mackenzie (1981) with a fixed salinity of 33 psu, which is the annual mean in the study area. The Bellhop ray-tracing model (Hovem and Dong, 2019), designed to perform two-dimensional acoustic ray-tracing for a given sound speed profile in ocean waveguides with range-dependent bathymetry, is used to estimate the eigenrays associated with ATTs (**Figure 2B**).

The third step is to determine an optimal temperature profile by comparing the observed ATT with the ATTs calculated using the ray-tracing simulations (**Figure 2C**). If only the first-arrival acoustic travel time (ATT_{1st}) is detected in the observation, the algorithm finds the optimal profile with the least difference between the estimated and observed values of ATT_{1st} (**Figure 2D**). When the optimal ATT_{1st} with the least difference is not unique, an optimal vertical profile is produced by averaging the two closest predicted profiles. If both the ATT_{1st} and second-arrival acoustic travel time (ATT_{2nd}) are detected during an observation, preferentially, we select the second-arrival acoustic ray among multiple rays in ray-tracing simulations with each plausible profile based on the difference between the measured ATT_{1st} and ATT_{2nd}. Then, the optimal temperature profile is determined among profiles when the sum of the differences between the observed and estimated values of ATT_{1st} and ATT_{2nd} reaches a minimum.

VALIDATION OF VTPE METHOD

Numerical Ocean Model

The VTPE method was verified by utilizing data from four individual months (February, May, August, and November) in 2016 from data-assimilated three-dimensional fine-resolution numerical ocean model outputs. These outputs were used for the real-time ocean forecast system covering East Asian marginal seas[1]. The real-time forecast system has a horizontal resolution of 1/12° in longitude and 1/15° in latitude (Hirose et al., 2013) and is based on the RIAM Ocean Model (RIAMOM), a free-surface primitive general circulation model developed by the Research

[1]http://dreams-c1.riam.kyushu-u.ac.jp/vwp/

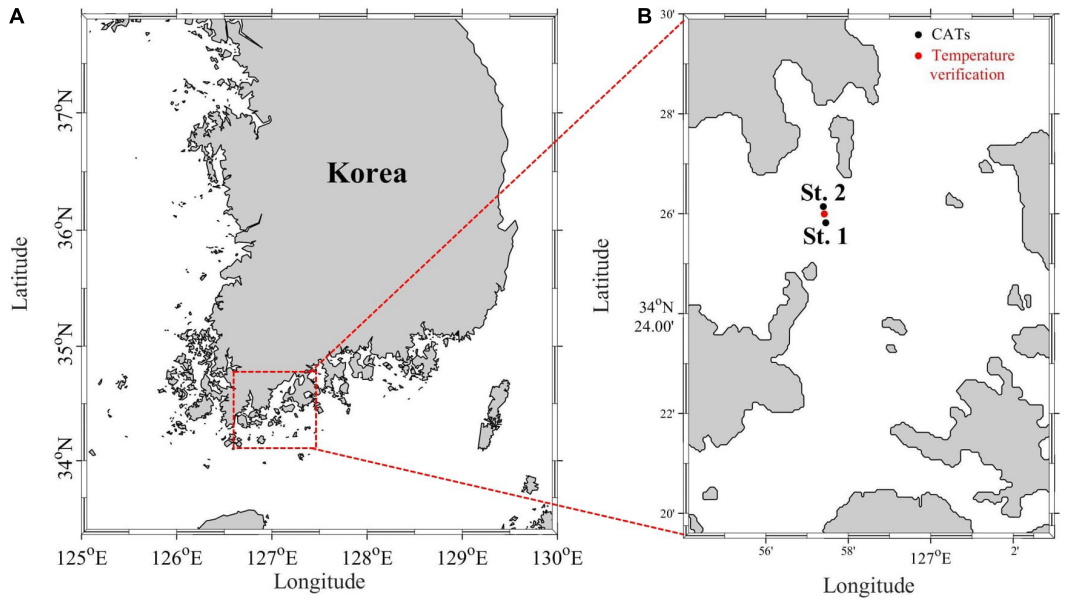

FIGURE 1 | (A) Locations of the two stations used in the CAT field experiment. Station 1 is deeper than Station 2. Temperatures between the estimated and the observed were compared at the location marked by the red dot in **(B)**.

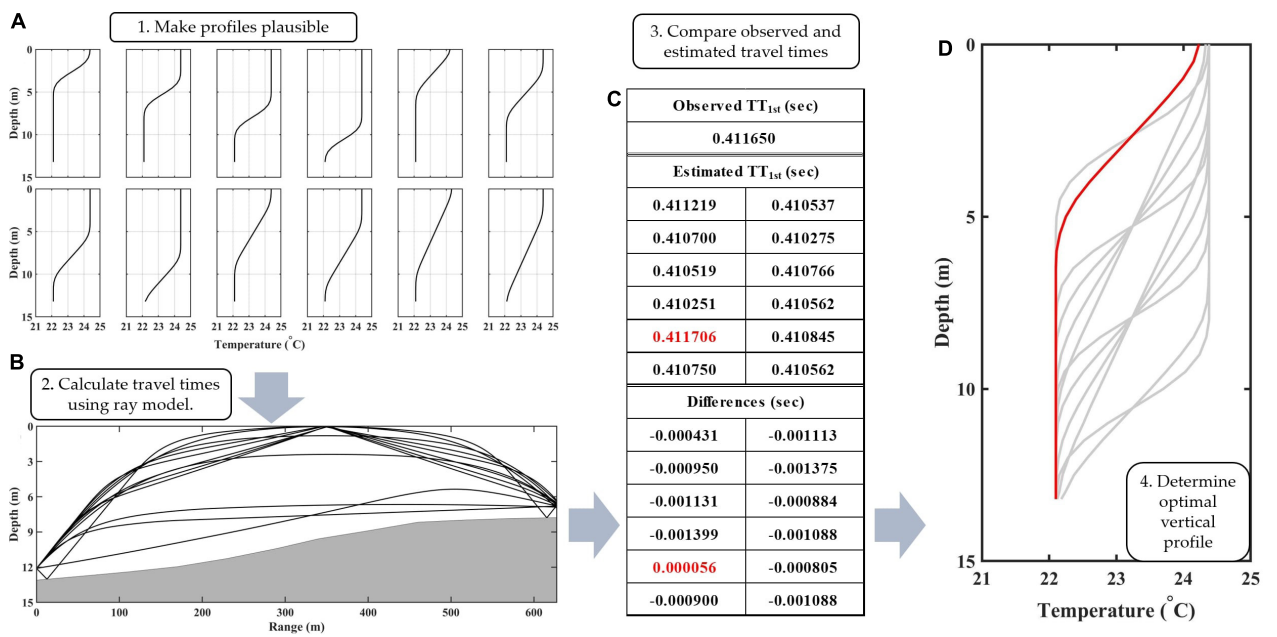

FIGURE 2 | (A) Temperature profiles created using water depth, SST, and NBT. **(B)** Eigenrays of the ATT_{1st} in each of the temperature profiles. **(C)** Example of comparison between observed ATT_{1st} and calculated ATT_{1st}. The value of ATT_{1st} closest to the observed value is displayed in red. **(D)** The determined optimal profile is plotted as the red line. SST, Sea surface temperature; NBT, Near-bottom temperature; and ATT, Acoustic travel time.

Institute for Applied Mechanics (RIAM) of Kyushu University (Lee, 1996; Lee et al., 2003). RIAMOM is a three-dimensional z-coordinate model that assumes hydrostatic balance and the Boussinesq approximation. The model uses 40 vertical levels of which the thickness increases with depth, from 1 m at the surface to 880 m near the bottom. The upper six layers are defined at depths of 1, 3, 5, 6.5, 10, 15, and 22 m; thus, the model can represent successive vertical temperature changes in shallow coastal regions. The model includes tides and ocean general circulation and is forced by 6-hourly atmospheric forcings. The gridded SST data (MGDSST) of the Japan Meteorological Agency were used for surface relaxation with a time scale of 3 days. The

along-track sea surface height of AVISO was assimilated into the model using a reduced-order Kalman filter. More details about the model configurations appear in the paper by Hirose et al. (2013).

Evaluation of VTPE

The temperature profiles estimated with the use of the VTPE method were compared with those generated by the model for February, May, August, and November to investigate the performance of the method in all four seasons. **Figure 3** compares the timeseries of the temperature profiles obtained with the model with those estimated using the VTPE method. For February, the temperature profile was vertically homogeneous. The results obtained with the VTPE method were in good agreement with the output of the model (**Figures 3A–C**). The monthly mean root-mean-squared difference (RMSD) for the vertical temperature profiles is less than 0.01°C. During May, the seasonal thermocline gradually develops and becomes warmer over time (**Figure 3D**). The results of the VTPE method were in good agreement with the temperature profiles from the ocean model (**Figures 3D,E**). The absolute errors in **Figure 3F** are less than 0.5°C overall, and the monthly mean RMSD for the vertical profiles is approximately 0.05°C. In August, a seasonal thermocline developed, and diurnal and semidiurnal internal fluctuations were evident in early- and mid-August (**Figure 3G**). These patterns are well reflected in the VTPE-estimated temperature timeseries (**Figure 3H**). The absolute errors were the largest in August, and most of the errors were distributed in the middle layer, when the seasonal thermocline well developed during the first half of the month (**Figure 3I**). The monthly mean RMSD for the vertical profiles is 0.18°C. In November, the stratification almost disappeared, similar to February (**Figure 3J**). The VTPE results corresponded well with the temperature profiles produced as model outputs (**Figure 3K**). The absolute errors are relatively small; hence, the monthly mean RMSD for the vertical profiles is ∼0.01°C (**Figure 3L**). The vertical distribution of mean-squared difference (MSD) in the water column at 1-m intervals [$(°C)^2$] was described in histograms on the right of **Figures 3C,F,I,L**. Overall, the MSD was relatively small at or near the sea surface and sea bottom but increased in the middle layer, particularly when the stratification developed.

Effects of Tides and Seasonal Thermocline on Ray-Tracing

In general, the tide can significantly impact the sea-level modulations in coastal regions. At our CAT stations, the tidal range had a maximum of ∼4 m, which is sufficiently large compared to the average depth of ∼9 m between the two CAT stations. We conducted ray-tracing simulations using the same temperature profiles (same SST, NBT, and thermocline structure), except for the water depth during the highest and lowest tides, to estimate the influence of tide-induced sea level changes on the propagation of acoustic signals. The 2 months of August and November were selected to investigate the impacts of the tide and seasonal thermocline on the propagation of acoustic signals and ATTs.

Ray-tracing simulations of the propagation of acoustic signals using temperature profiles on August 1, when the difference in SST and NBT was the largest, showed that the acoustic rays differed significantly between the highest and lowest tides in terms of their propagation distance, refraction, and reflection (**Figures 4A,B**). The simultaneous effects of the tidal elevation and seasonal thermocline complicate the behavior of the acoustic rays, which becomes nonlinear. For example, the first-arrival acoustic rays represented by the red line have different reflection times from the sea surface or sea floor between the highest (three times) and lowest (five times) tides. In November, because the seasonal thermocline almost disappears, only the effect of tidal elevation is predominant (**Figures 4C,D**); thus, all acoustic rays calculated using temperature profiles recorded on November 23, when the difference between SST and NBT was the smallest, became simpler and more straightforward. The propagation distance of the first-arrival acoustic rays is obviously longer during the highest tides but it is linear. Quantitatively, tidal elevation results in significant differences in ATT_{1st} with a range of RMSD of 0.53 and 0.12 ms in August and November, respectively, which is sufficiently large to miscalculate the temperature profiles. Hence, the seasonal thermocline and tides in the coastal regions would need to be considered to accurately estimate the temperature profiles from CAT data.

Sensitivity Test of VTPE Method

Application of the VTPE method to real ocean measurements could be affected by various measurement errors in SST, NBT, and ATT (first and second ATT measurements in the case of our CAT observation). Sensitivity tests of the VTPE method were carried out by conducting ray-tracing simulations including reasonable observational errors. Four experiments were conducted, one in each of the four seasons: Cases 1 and 2 adopted random errors within ±0.5°C for SST and NBT, respectively. Case 3 added errors of ±0.5% to the ATT, the error of which includes time-varying location of transducers as it is floated in the water, and Case 4 includes all the random errors of Cases 1–3.

The monthly mean RMSD for the vertical profiles was calculated by comparing the temperature that was estimated with the error-included pseudo-observations and those obtained as an output of the numerical model (**Table 1**). Among the four cases, the RMSDs were similar in Cases 1 and 2 for each of the 4 months: a decrease in the homogenous period (February and November) and an increase in the well-stratified period (May and August). In Case 3, the RMSD differed distinctly between the two periods; the RMSD reached 0.4°C in August, but 0.01°C in February and November. The behavior of the acoustic rays during homogenous months is straightforward compared with that in August and May; hence, ATT errors can have significant impacts on VTPE in well-stratified time.

The results of Case 4 demonstrate an obvious increase in noisy deviation owing to the random errors added (**Figure 5**). Overall, the differences are smaller at the surface and in layers near the bottom than in the middle layer. For February, the effect of the errors was smaller than in the other months. The

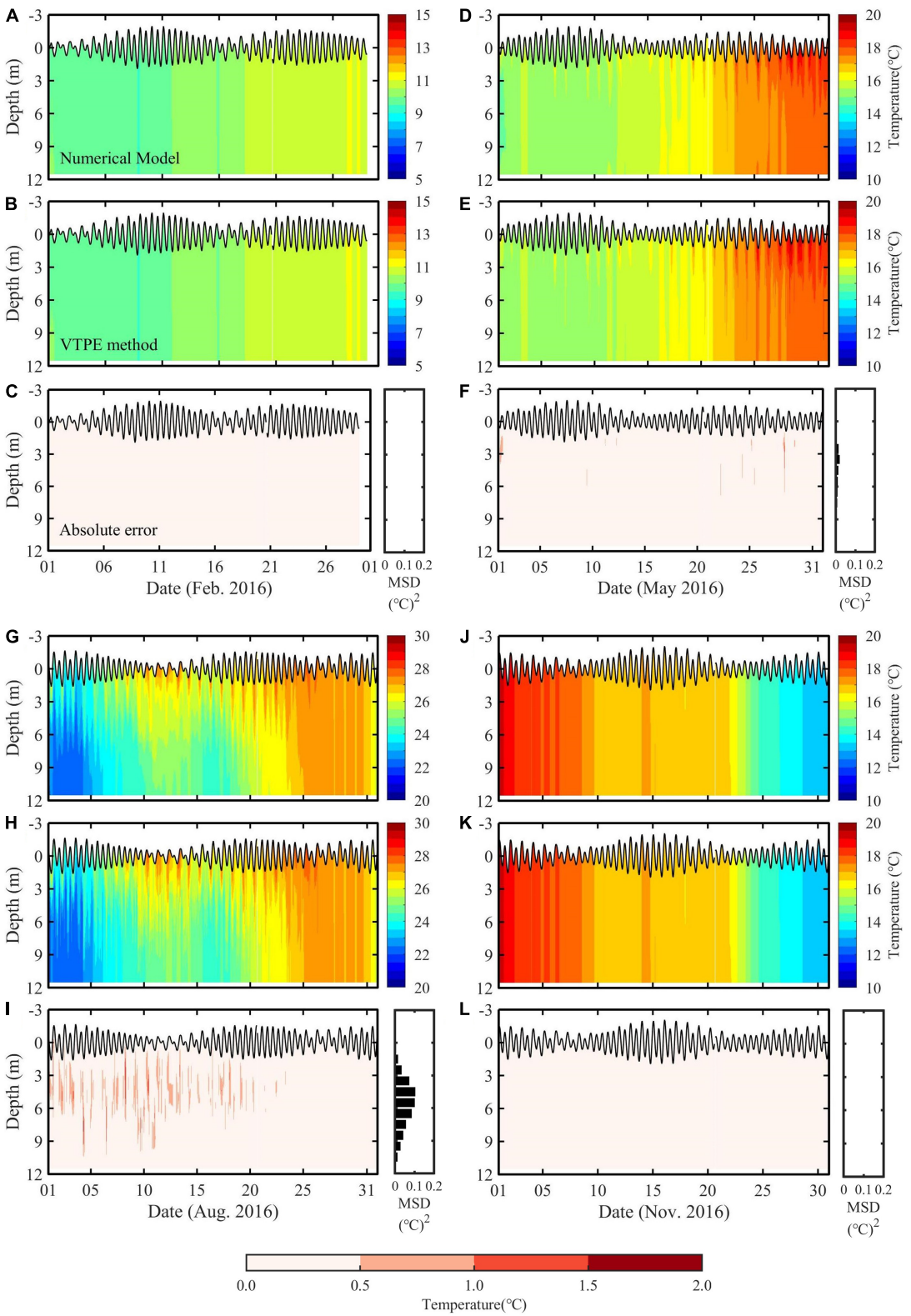

FIGURE 3 | (A,D,G,J) Timeseries of temperature profiles obtained as output of the numerical model for February, May, August, and November 2016 together with the sea level modulations. **(B,E,H,K)** Timeseries of temperature profile estimated from the VTPE method. **(C,F,I,L)** Absolute errors in temperature between the output of the numerical model and VTPE results. The colorbar for absolute errors is shown at the bottom. Histograms on the right of **(C,F,I,L)** represent the vertical distribution of MSD [$(°C)^2$] in the water column at 1-m intervals.

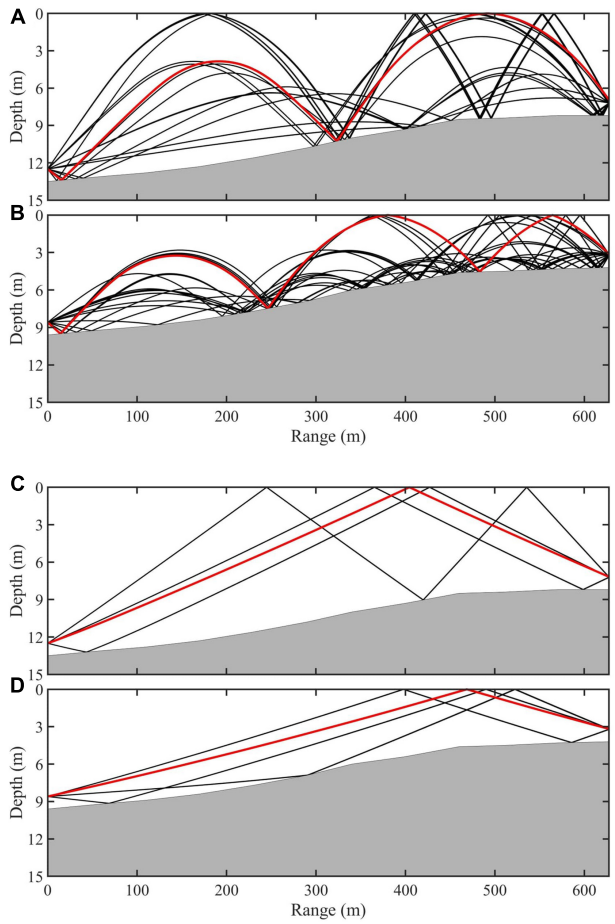

FIGURE 4 | Eigenrays for the **(A,C)** highest and **(B,D)** lowest tides in **(A,B)** August and **(C,D)** November. The red and black curves indicate the first acoustic ray and those that subsequently arrived, respectively.

TABLE 1 | Sensitivity tests with reasonable random errors in each case.

Method	February	May	August	November	Avg.
Case 1 (SST)	0.11	0.13	0.23	0.11	0.15
Case 2 (NBT)	0.12	0.16	0.24	0.12	0.16
Case 3 (ATT)	0.01	0.17	0.40	0.01	0.13
Case 4 (All)	0.23	0.30	0.50	0.24	0.32

Values are the average RMSD over the vertical profiles between the temperature estimated with the VTPE method and that obtained with the numerical model. The unit is °C.

estimated temperature profiles appeared noisy but were in good agreement with the model outputs with a monthly mean RMSD for the vertical temperature profiles of 0.23°C. For May, the timeseries of the temperature profiles present more noise than for February, especially after the 25th when the seasonal thermocline developed; hence, the monthly mean RMSD increases to 0.30°C. For August, the absolute errors were the largest among the 4 months with a monthly mean RMSD of 0.50°C. For November, the temperature profiles correspond well with the model outputs with an RMSD of 0.24°C (**Table 1**).

The vertical distribution of MSD [(°C)^2] in the water column at 1-m intervals in case of all random errors included was described in histograms on the right of 5B, 5D, 5F, and 5H. The MSD was relatively small at or near the sea surface and sea bottom but increased in the middle layer, particularly in May and August when the stratification developed.

APPLICATION OF VTPE METHOD FOR *IN SITU* OBSERVATION

In situ Observations and Distance Correction

For sustainable real-time coastal ocean monitoring, a pilot CAT experiment was carried out near Noryeok Island on the southern coast of Korea in February and August 2019 for 14 and 9 days, respectively (see **Figure 1**). The transceiver (SonoTube 008/D13) at each of the two stations, separated by ∼630 m, was located ∼1 m above the sea floor, approximate average depths were 11 and 6 m at station 1 and 2, respectively. The transceiver transmitted 10 kHz acoustic signals reciprocally. Their phases were modulated by one period [(2^8–1) digits] of an eigth-order M-sequence, and the ATT_{1st} and ATT_{2nd} were recorded in 1-min intervals. The resolution of ATT measurement is 0.025 ms (=0.000025 s) which is sufficient to differentiate plausible sound-speed and temperature profiles. The pressure at the bottom of the ocean was measured with OMNI instruments (PTM/N/RS485), and temperature sensors (RBRduet^3 T.D) were moored at the sea surface, middle layer, and sea floor at three sites: station 1, station 2, and between the two stations (**Figure 1B**). All data were transmitted instantly to the onshore storage server at the Gwangju Institute of Science and Technology. The VTPE calculations were conducted by using the *in situ* SST, NBT, and bottom pressure measurements recorded at station 1 (deeper station) and the ATTs. The middle layer (∼3 m depth) temperature was separately measured between stations 1 and 2 to validate the VTPE results.

Temperature estimation using acoustic tomography is very sensitive to the distance between acoustic transceivers (Munk et al., 1995). In our field experiment, the transceiver is moored near the sea floor and connected to a surface barge with a global positioning system (GPS) sensor via a slack mooring cable. Because it was difficult to obtain accurate GPS coordinates of the transceiver from the GPS sensor, we used the following procedure to reduce the distance error. We calculated the mean distance (S), $S = C\bar{\tau}$, where C is the sound speed computed using NBT, and $\bar{\tau}$ is the bidirectionally averaged ATT_{1st}. The distance was then corrected in the acoustic ray-tracing simulations in the second step of the VTPE method.

Application of the VTPE Method to *in situ* Observations

The temperature profiles for February and August were successfully constructed using the VTPE method. The estimated vertical temperature profile during February 12–26 (with 15 h missing on February 20) is shown in **Figure 6**. The temperature

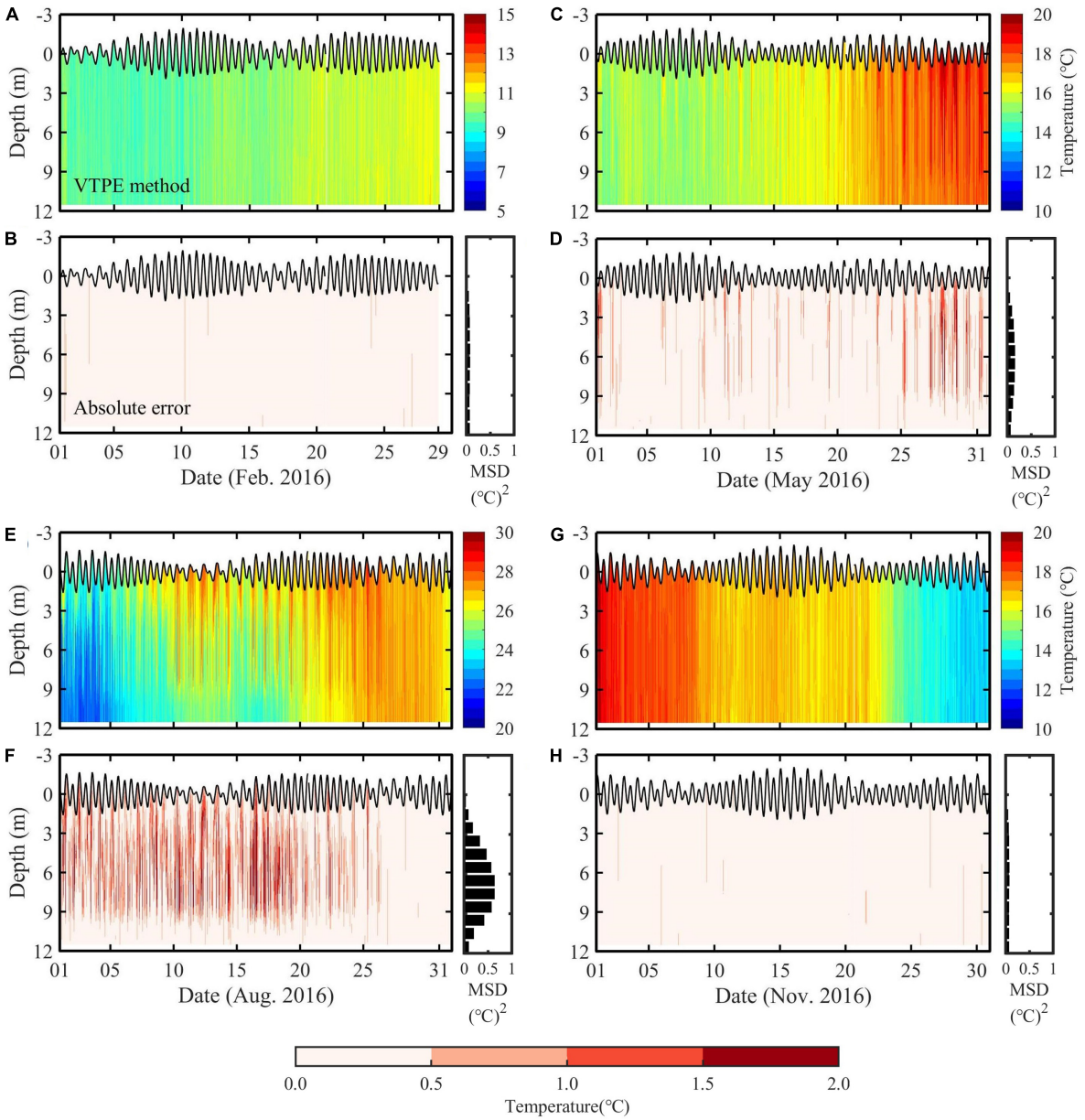

FIGURE 5 | (A,C,E,G) Timeseries of temperature profile estimated with the VTPE method by including the random-error data and **(B,D,F,H)** absolute errors of the temperature between the output of the numerical model and the VTPE results in **(A,B)** February, **(C,D)** May, **(E,F)** August, and **(G,H)** November 2016. The colorbar for absolute errors is shown at the bottom. Histograms on the right of **(B,D,F,H)** represent the vertical distribution of the MSD [(°C)^2] in the water column at 1-m intervals.

fluctuates within a range of ±1.5°C from the mean temperature of ∼8°C and represents the typical pattern of a vertically homogeneous temperature change in February. The semidiurnal and diurnal fluctuations in temperature seem to be caused by tidal variability. To verify the VTPE result, the middle-layer temperature was compared to the *in situ* temperature measured at the site between the two CAT stations (**Figure 6B**). The timeseries of the *in situ* measured and the estimated temperatures were in good agreement, and the average RMSD in the middle layer (∼3 m depth) was 0.08°C (**Figure 6C**).

The timeseries of the estimated vertical temperature profile for the period August 1–9 is shown in **Figure 7A**. The temperature profile describes a stratified water column, a typical structure that is observed in August, and the development of a seasonal thermocline on August 8–9. The overall temporal variability in the temperature seems to be associated with semidiurnal and diurnal tides, although surface tides of semidiurnal frequency are weak. The estimated middle-layer temperature was compared with that measured *in situ* at the site between the two CAT stations (**Figure 7B**). The temperature estimated using the VTPE

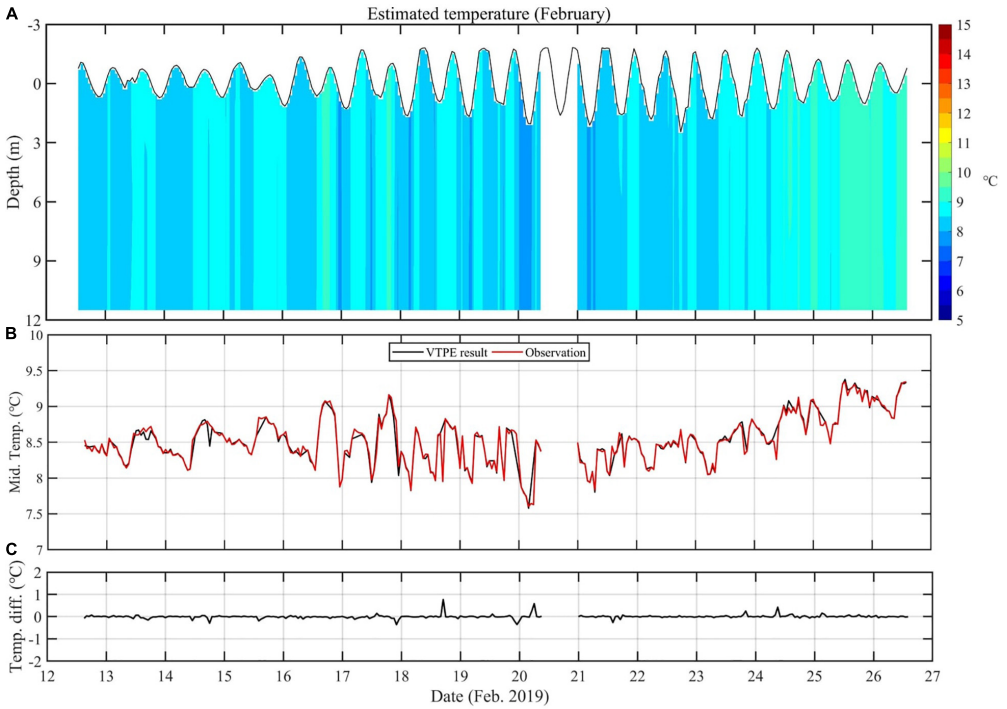

FIGURE 6 | (A) Timeseries of temperature profiles estimated with the VTPE method using the field observation data of February 2019. Note that the SST observation failed for 15 h on February 20. **(B)** Comparison of the middle-layer temperatures that were estimated and measured *in situ* at the site between the two CAT stations. **(C)** Difference between the two timeseries of temperatures shown in **(B)**.

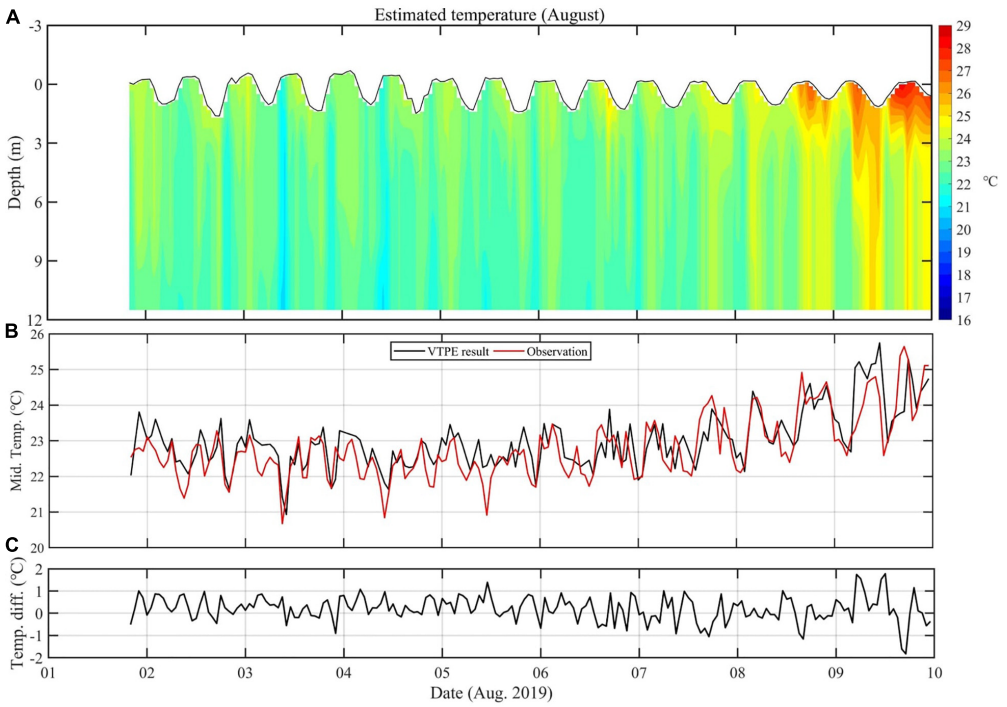

FIGURE 7 | (A) Timeseries of temperature profiles estimated from the VTPE method using the field observation data gathered in August 2019. **(B)** Comparison of middle-layer temperatures between the estimated and the *in situ* measurement at a site between the two CAT stations. **(C)** Difference of the two timeseries of temperatures shown in **(B)**.

method is in good correspondence with that measured *in situ*, including the increasing tendency on August 7–9. The average RMSD between the estimated and measured temperatures in the middle layer is 0.60°C, which is satisfactory considering the highly fluctuating conditions in coastal regions (**Figure 7C**).

In addition, we compared the performance of the VTPE method with existing widely used regularized inverse method (Zhu et al., 2013; Zhang et al., 2015; Syamsudin et al., 2017) with and without the distance correction, though the inverse method has not been used to produce vertical temperature profile in previous studies. The middle-layer temperature RMSD of 6.21, 0.96, and 0.60°C was obtained from the inverse method without and with the distance correction, and from the VTPE method with the distance correction, respectively (see **Supplementary Material**), indicating that the VTPE method and the distance correction suggested here should be valid and practical for the CAT data obtained from non-fixed transceivers.

SUMMARY AND CONCLUSION

We propose a novel method for VTPE from CAT systems using additional available data, such as SST, NBT, and water depth. The proposed VTPE method is validated using data-assimilated and tide-included high-resolution ocean model outputs by comparing the estimated and model-simulated temperatures in the southern coastal region of Korea, where the CAT stations have been moored to establish a continuous coastal ocean monitoring system. Our novel VTPE method was then applied to the *in situ* observation data.

The validation of the VTPE method using the numerical ocean model outputs reveals that the algorithm delivers good performance for all seasons, with monthly mean RMSD for the vertical profiles of 0.01, 0.05, 0.18, and 0.01°C in February, May, August, and November, respectively. Sensitivity tests with reasonable random errors added to SST, NBT, and ATT demonstrate that the method can reproduce accurate temperature profiles with somewhat increased monthly mean RMSD for the vertical profiles of 0.23, 0.30, 0.50, and 0.24°C in February, May, August, and November, respectively. The VTPE method was applied to *in situ* observation data for 15 days in February and 9 days in August. The VTPE results realistically reproduce the seasonality and high-frequency variabilities of temperature. Comparisons of middle-layer temperature between the VTPE-estimated and the observed temperature in February and August revealed mean RMSDs of 0.08 and 0.60°C, respectively, which is satisfactory for coastal ocean monitoring.

Although the data from the two CAT stations enabled the estimation of a one-dimensional temperature profile, the VTPE method proposed in this study can pave the way for continuous monitoring of two- and three-dimensional temperature fields by combining multiple CAT stations. The VTPE method, monitoring subsurface temperature profile, will help crisis managements in coastal fisheries and the aquaculture industries due to impacts of warming climate and marine heat wave (Caputi et al., 2016; Rogers et al., 2021).

The estimated temperature profile using two CAT stations produces spatially averaged range-independent temperature profiles between two stations. Estimation of the range-dependent vertical profiles considering spatial scales of oceanic phenomena would be important for high-resolution coastal monitoring. Also, the effect of salinity on the VTPE method was not considered in this study; however, it could have an impact on ATTs when events such as fresh water discharge or intrusion and heavy precipitation occur. Lastly, the VTPE method might have a limitation in regions where the stratification is very complicated due to such as significant temperature inversion. Therefore, these problems would need to be addressed in future to improve the VTPE method.

DATA AVAILABILITY STATEMENT

The raw data supporting the conclusions of this article will be made available by the authors, without undue reservation.

AUTHOR CONTRIBUTIONS

YP: primary writing and calculation. CJ: writing and discussion. HS, YC, J-YC, and E-JL: data collection and discussion. JSK: *in situ* observation and data management. J-HP: overall coordination and discussion. All authors modify the manuscript.

FUNDING

This research was supported by the "Development of Ocean Acoustic Echo Sounders and Hydro-Physical Properties Monitoring System" project and "Development of 3-D Ocean Current Observation Technology for Efficient Response to Maritime Distress" project (20210642), funded by the Ministry of Ocean and Fisheries, South Korea.

SUPPLEMENTARY MATERIAL

The Supplementary Material for this article can be found online at: https://www.frontiersin.org/articles/10.3389/fmars.2021.675456/full#supplementary-material

REFERENCES

Caputi, N., Kangas, M., Denham, A., Feng, M., Pearce, A., Hetzel, Y., et al. (2016). Management adaptation of invertebrate fisheries to an extreme marine heat wave event at a global warming hot spot. *Ecol. Evol.* 6, 3583–3593. doi: 10.1002/ece3.2137

Choi, H.-S., Myoung, J.-I., Park, M.-A., and Cho, M.-Y. (2009). A study on the summer mortality of Korean rockfish *Sebastes schlegeli* in Korea. *J. Fish Pathol.* 22, 155–162.

Donlon, C. J., Martin, M., Stark, J., Roberts-Jones, J., Fiedler, E., and Wimmer, W. (2012). The operational sea surface temperature and sea ice analysis (OSTIA) system. *Remote Sens. Environ.* 116, 140–158. doi: 10.1016/j.rse.2010.10.017

Hirose, N., Takayama, K., Moon, J.-H., Watanabe, T., and Nishida, Y. (2013). Regional data assimilation system extended to the East Asian marginal seas. *Sea Sky* 89, 43–51.

Hovem, J. M., and Dong, H. (2019). Understanding ocean acoustics by eigenray analysis. *J. Mar. Sci. Eng.* 7:118. doi: 10.3390/jmse7040118

JPL Our Ocean Project (2013). GHRSST Level 4 G1SST Global Foundation Sea Surface Temperature Analysis. Pasadena, CA: PO.DAAC. doi: 10.5067/GHG1S-4FP01

Kaneko, A., Zhu, X.-H., and Lin, J. (2020). *Coastal Acoustic Tomography*. Amsterdam: Elsevier, 347.

Kim, S.-H., and Kim, D.-S. (2010). Effect of temperature on catches of anchovy and sea mustard (Undaria pinnatifida) in southern part of east sea of Korea. *J. Korean Soc. Mar. Environ. Saf.* 16, 153–159.

Lee, H. C. (1996). *A Numerical Simulation for the Water Masses and Circulations of the Yellow Sea and the East China Sea,* Ph.D. thesis. Fukuoka: Kyushu University.

Lee, H.-J., Yoon, J.-H., Kawamura, H., and Kang, H.-W. (2003). Comparison of RIAMOM and MOM in modeling the East Sea/Japan Sea circulation. *Ocean Polar Res.* 25, 287–302. doi: 10.4217/OPR.2003.25.3.287

Lee, Y.-H., Shim, J.-M., Kim, Y.-S., Hwang, J.-D., Yoon, S.-H., Lee, C., et al. (2007). The variation of water temperature and the mass mortalities of sea squirt, Halocynthia roretzi along Gyeongbuk coasts of the east sea in summer, 2006. *J. Korean Soc. Mar. Environ. Saf.* 13, 15–19.

Mackenzie, K. V. (1981). Nine-term equation for sound speed in the oceans. *J. Acoust. Soc. Am.* 70, 807–812. doi: 10.1121/1.386920

Munk, W., Worcester, P., and Wunsch, C. (1995). *Ocean Acoustic Tomography*. Cambridge, MA: Cambridge University Press, 212.

Munk, W., and Wunsch, C. (1979). Ocean acoustic tomography: a scheme for large scale monitoring. *Deep Sea Res. A Oceanogr. Res. Pap.* 26, 123–161. doi: 10.1016/0198-0149(79)90073-6

Park, J.-H., and Kaneko, A. (2000). Assimilation of coastal acoustic tomography data into a barotropic ocean model. *Geophys. Res. Lett.* 27, 3373–3376.

Park, J.-H., and Kaneko, A. (2001). Computer simulation of coastal acoustic tomography by a two-dimensional vortex model. *J. Oceanogr.* 57, 593–602.

Rogers, L. A., Wilson, M. T., Duffy-Anderson, J. T., Kimmel, D. G., and Lamb, J. F. (2021). Pollock and "the Blob": impacts of a marine heatwave on walleye pollock early life stages. *Fish. Oceanogr.* 30, 142–158. doi: 10.1111/fog.12508

Syamsudin, F., Chen, M., Kaneko, A., Adityawarman, Y., Zheng, H., Mutsuda, H., et al. (2017). Profiling measurement of internal tides in Bali Strait by reciprocal sound transmission. *Acoust. Sci. Technol.* 38, 246–253. doi: 10.1250/ast.38.246

Taniguchi, N., Huang, C.-F., Kaneko, A., Liu, C.-T., Howe, B. M., Wang, Y.-H., et al. (2013). Measuring the Kuroshio current with ocean acoustic tomography. *J. Acoust. Soc. Am.* 134, 3272–3281. doi: 10.1121/1.4818842

Yamaoka, H., Kaneko, A., Park, J.-H., Zheng, H., Gohda, N., Takano, T., et al. (2002). Coastal acoustic tomography system and its field application. *IEEE J. Ocean. Eng.* 27, 283–295.

Zhang, C., Kaneko, A., Zhu, X., and Gohda, N. (2015). Tomographic mapping of a coastal upwelling and the associated diurnal internal tides in Hiroshima Bay, Japan. *J. Geophys. Res. Oceans* 120, 4288–4305. doi: 10.1002/2014JC010676

Zheng, H., Gohda, N., Noguchi, H., Ito, T., Yamaoka, H., Tamura, T., et al. (1997). Reciprocal sound transmission experiment for current measurement in the Seto Inland Sea, Japan. *J. Oceanogr.* 53, 117–127.

Zhu, X.-H., Kaneko, A., Wu, Q., Zhang, C., Taniguchi, N., and Gohda, N. (2013). Mapping tidal current structures in Zhitouyang Bay, China, using coastal acoustic tomography. *IEEE J. Ocean. Eng.* 38, 285–296. doi: 10.1109/JOE.2012.2223911

Conflict of Interest: YP and YC were employed by the companies Underwater Survey Technology 21 and the Geosystem Research Corporation, respectively.

The remaining authors declare that the research was conducted in the absence of any commercial or financial relationships that could be construed as a potential conflict of interest.

Publisher's Note: All claims expressed in this article are solely those of the authors and do not necessarily represent those of their affiliated organizations, or those of the publisher, the editors and the reviewers. Any product that may be evaluated in this article, or claim that may be made by its manufacturer, is not guaranteed or endorsed by the publisher.

frontiers in Marine Science

PERSPECTIVE
published: 24 August 2021
doi: 10.3389/fmars.2021.669413

Clearing a Path to Commercialization of Marine Renewable Energy Technologies Through Public–Private Collaboration

Grace Chang[1], Genevra Harker-Klimeš[2], Kaustubha Raghukumar[1], Brian Polagye[2,3], Joseph Haxel[2], James Joslin[4], Frank Spada[1] and Garrett Staines[2]*

[1] Integral Consulting Inc., Santa Cruz, CA, United States, [2] Pacific Northwest National Laboratory, Sequim, WA, United States, [3] Department of Mechanical Engineering, University of Washington, Seattle, WA, United States, [4] MarineSitu Inc., Seattle, WA, United States

Governments are increasingly turning toward public–private partnerships to bring industry support to improving public assets or services. Here, we describe a unique public–private collaboration where a government entity has developed mechanisms to support public and private sector advancement and commercialization of monitoring technologies for marine renewable energy. These support mechanisms include access to a range of skilled personnel and test facilities that promote rapid innovation, prove reliability, and inspire creativity in technology development as innovations move from concept to practice. The ability to iteratively test hardware and software components, sensors, and systems can accelerate adoption of new methods and instrumentation designs. As a case study, we present the development of passive acoustic monitoring technologies customized for operation in energetic waves and currents. We discuss the value of testing different systems together, under the same conditions, as well as the progression through different test locations. The outcome is multiple, complementary monitoring technologies that are well suited to addressing an area of high environmental uncertainty and reducing barriers to responsible deployment of low-carbon energy conversion systems, creating solutions for the future.

Keywords: marine renewable energy, acoustics, underwater sound, public–private, commercialization, environmental monitoring, technology

OPEN ACCESS

Edited by:
Wayne Homer Slade, Sequoia Scientific, Inc., United States

Reviewed by:
Ann Clarke, University of Southern Denmark, Denmark
Andrew Barnard, Sea-Bird Scientific, United States

****Correspondence:***
Grace Chang
gchang@integral-corp.com

Specialty section:
This article was submitted to Ocean Observation, a section of the journal Frontiers in Marine Science

Received: *18 February 2021*
Accepted: *30 July 2021*
Published: *24 August 2021*

Citation:
Chang G, Harker-Klimeš G, Raghukumar K, Polagye B, Haxel J, Joslin J, Spada F and Staines G (2021) Clearing a Path to Commercialization of Marine Renewable Energy Technologies Through Public–Private Collaboration. Front. Mar. Sci. 8:669413. doi: 10.3389/fmars.2021.669413

INTRODUCTION

Public–private partnerships (PPPs) are efficient mechanisms that bring industry needs and knowledge into public services. They are widely used to ensure quality at an optimal price, particularly for public infrastructure and services (Roehrich et al., 2014). This framework for quality and public responsibility also applies to research and development (e.g., Wilczak et al., 2015; Shaw et al., 2019 for wind energy forecasting).

The United States Department of Energy (DOE) Water Power Technologies Office (WPTO) is employing multiple approaches to research and development (R&D) that advance the marine renewable energy (MRE) industry. These include PPPs to develop monitoring technologies that can help to identify and mitigate impacts from MRE generation systems (Copping and Hemery, 2020). Providing academia and commercial entities access to testing sites,

development facilities, and expertise enhances all stages of R&D across multiple scales, while bringing in new ideas and perspectives. Finding innovative ways to enable these partnerships is critical to their success, and WPTO has achieved this with the Triton Initiative, a PPP.

This perspective article discusses the Triton PPP, with a focus on distinct and complementary acoustic monitoring technologies. We highlight the value and effectiveness of the Triton program to accelerate deployment of MRE monitoring systems through collaborative, multi-scale testing procedures over a range of environmental conditions.

TRITON INITIATIVE

The Triton PPP supports R&D and advancement of technologies for MRE applications, including environmental monitoring capabilities necessary to progress the industry in a sustainable manner. Triton is spearheaded by the Pacific Northwest National Laboratory's Marine and Coastal Research Laboratory (PNNL's MCRL), which provides facilities and technical support for Triton projects focused on underwater noise, electromagnetic fields, marine organism interaction, benthic habitat mapping, and integrated sensor packages.

A key element of Triton is access to vessels and skilled personnel at marine testing locations that are permitted for a range of environmental monitoring system deployments. Testing locations include a quiescent site, tidally energetic area, deeper water site, and a site with consistent waves – all accessed from a single shore facility. This facilitates technology readiness level (TRL) advancement from proof-of-concept to commercialization by enabling baseline field-testing, design comparisons to existing technologies, benchmark improvements, and field demonstrations.

ACOUSTIC MONITORING CASE STUDY

In 2016, WPTO released a Triton funding opportunity announcement to develop and/or advance environmental monitoring systems that could overcome limitations with existing technologies in energetic environments. This included electromagnetic field measurements, benthic habitat surveys, acoustic target detection, optical imaging, and passive acoustic monitoring of radiated noise from marine energy converters. For the latter, two technologies were selected – one from commercial business (Integral Consulting Inc.) and one from academia (University of Washington). Both project teams leveraged MCRL support and expertise, and benefited from broader collaboration that emerged under the PPP.

Many industrial activities associated with MRE installation, operation, and decommissioning generate anthropogenic sounds that overlap spatially, temporally, and in bandwidths pertinent to marine fauna (Copping and Hemery, 2020). Monitoring potential disturbances and the correlated vocal reactions by marine fauna will inform mitigation efforts of regulatory and stakeholder relevance. Radiated noise from MRE devices must also not exceed regulatory thresholds for acoustic harassment [National Marine Fisheries Service (NMFS), 2018]. While passive acoustic monitoring in the marine environment is common (Sousa-Lima et al., 2013), MRE monitoring requires accurate measurements in energetic currents (>1 m/s speed) and waves (>2 m height). Further, given the limited understanding of noise radiated by MRE systems, passive acoustic monitoring must be able to differentiate between MRE noise and other natural or anthropogenic sources, as well as comply with international standards [International Electrotechnical Commission (IEC), 2019] to increase transferability of data across sites and systems.

The Triton PPP facilitated collaborative testing that was conducted at several locations near MCRL, which is located at the mouth of Sequim Bay in Washington State, United States. The bay is a sheltered body adjacent to the Strait of Juan de Fuca and is roughly 3.2 km long and 1.6 km wide at the mouth. The maximum water depth in the bay is 35 m, with the bottom consisting primarily of mud. Sequim Bay is tidally influenced, with tidal ranges from 1.5 m (neap tide) to 2.5 m (spring tide) [National Oceanic and Atmospheric Administration (NOAA), 2021]. Acoustic testing was conducted in four areas: a relatively shallow, quiescent site near the middle of Sequim Bay (SB2; ∼25 m); the mouth of the Bay in the energetic tidal channel (MSL; ∼10 m); in deeper-water in Dungeness Bay (>50 m); and in Clallam Bay, an energetic location in the Strait that is subject to stronger waves (**Figure 1**).

Acoustic Technologies

NoiseSpotter®

NoiseSpotter® is a passive acoustic monitoring device developed by Integral Consulting Inc. (Integral) to characterize, classify, and provide accurate location information, in near real-time, for underwater anthropogenic and natural sounds (Raghukumar et al., 2020). It consists of a compact array of particle motion sensors that measure acoustic pressure and three-dimensional particle velocities associated with the propagation of an acoustic wave, enabling triangulation of individual bearings and sound source localization with a single unit (Raghukumar et al., 2020). These sensors (GeoSpectrum Technologies Inc.) measure tri-axial particle motion and omnidirectional pressure at a frequency range of 50 Hz – 3 kHz, at a sample rate of 20 kHz, as well as earth-referenced orientation with an integrated inertial measurement unit (IMU).

At the beginning of the project, NoiseSpotter® was at TRL 4 (bench-scale prototype). Four advancements were required to achieve TRL 8 (field-tested commercial prototype):

- Develop continuous and synchronous data logging and real-time transmission
- Improve data quality, detection sensitivity, and location estimation by minimizing electronic, system, and flow-noise interferences
- Increase the power budget to achieve autonomous operation for at least 7 days
- Create a portable system with modular configuration capabilities to facilitate field operations for a wide range of environments.

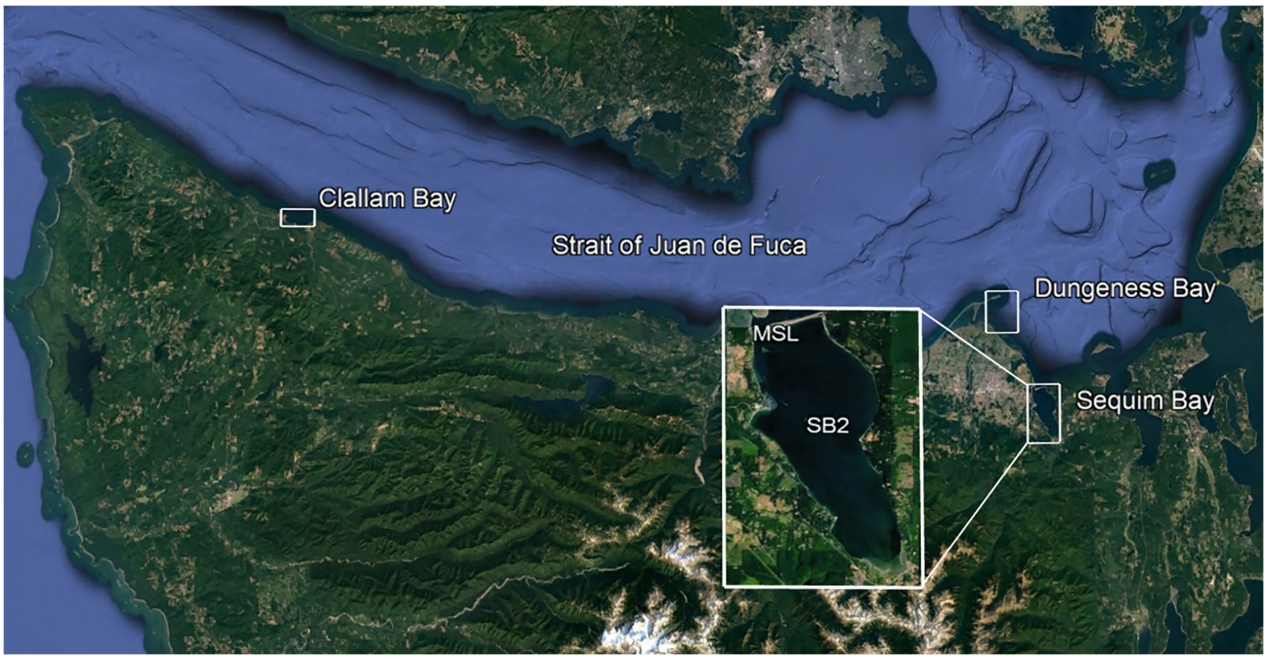

FIGURE 1 | Triton Initiative test sites: SB2, MSL, Dungeness Bay, and Clallam Bay, located along Washington State's (United States) northern coast.

These advancements were facilitated through a series of five field-tests, supported by the Triton PPP, conducted at SB2, MSL, and Dungeness Bay (**Figure 1**). Field-tests involved moored deployments of the NoiseSpotter® V1–V4 and controlled acoustic source-signal transmissions over a range of source-receiver separation distances. The original NoiseSpotter® V1 design was a linear particle motion sensor array on a mid-water column mooring with each sensor cabled to an off-the-shelf data logger and battery pack, housed in a surface buoy (**Figure 2A**). Testing at SB2 helped identify several issues, primarily stemming from the mid-water column design. Issues included system instability and acoustic contamination, cable-induced signal losses of 8 dB, and difficulties with field operations due to unwieldy cables. Data logger self-noise was observed at multiple frequencies, as well as high-amplitude sound at low frequencies (<200 Hz), indicative of flow-noise (Strasberg, 1979; Bassett et al., 2014).

These issues were mitigated by redesigning NoiseSpotter® such that the sensors, data logger, and batteries were mounted on a stable bottom platform (**Figures 2B–D**), thereby reducing cable lengths from 15 m to <1 m. Further improvements were made by incorporating a custom, low-power, low-noise, high-capacity data logger, and custom flow-noise shields (Raghukumar et al., 2019). Particle motion sensors with flow-noise shields were vertically and horizontally separated on the bottom platform (**Figures 2C,D**) to facilitate accurate geolocation estimation. The data logger pressure housing was designed and fabricated with the support of MCRL under the Triton PPP.

Field-tests of the NoiseSpotter® V2–3 (TRL 5–6) at SB2, MSL, and Dungeness Bay demonstrated simplified deployment, zero cable-induced signal losses, no platform instability, little to no data logger self-noise, reduced power requirements (by ∼1 A), increased data storage (by ∼2 TB), and flow-noise reduction of ∼10 dB. The remaining issues for the NoiseSpotter® V3 design included mitigating potential acoustic reflectance from aluminum, time-consuming system mobilization, and insufficient power. NoiseSpotter® V4a,b (TRL 7, 8) was thus redesigned with modular, high-density polyethylene frames (**Figure 2D**; Raghukumar et al., 2020) to reduce acoustic reflectance potential and custom 258 Ahr rechargeable battery packs. NoiseSpotter® V4b includes onboard real-time data processing and telemetry of acoustic data metrics to a cloud server.

The Triton PPP undoubtedly accelerated development for the NoiseSpotter®. Three different, permitted test locations, and the collaborative environment facilitated by the PPP helped overcome design challenges ranging from data and power budgets, electronic and environmental acoustic interference, to difficulties with field operations. Integral is currently transitioning NoiseSpotter® from research-grade to a commercial acoustic monitoring device (United States Utility Patent No. 16/879,434; approved) and is a product available for lease with contracted services for operation and data analysis.

DAISY

The Drifting Acoustic Instrumentation SYstem (DAISY) was developed by the University of Washington (UW). The DAISY's primary sensor is a hydrophone sensitive to acoustic pressure. Unlike NoiseSpotter®, source localization requires multiple time-synchronized DAISYs to be deployed around an MRE device, but the resolvable frequency range is wider (1 Hz–200 kHz). As previously mentioned, relative motion between a hydrophone

FIGURE 2 | (A–D) Photographs of Integral Consulting Inc.'s NoiseSpotter® design iterations from V1 through V4, respectively. **(E,F)** Schematic diagram of University of Washington's DAISY design. **(G)** Schematic diagram of Oregon State University's spar buoy drifting hydrophone. **(H)** Concurrent benchmarking of DAISYs and SBDH at SB2.

and surrounding water produces high-amplitude, low-frequency pressure and velocity fluctuations (advected and shed turbulence) that are indistinguishable from propagating sound (Strasberg, 1979; Bassett et al., 2014) and can mask radiated noise from MRE devices. Because of this, the DAISY is designed to drift with the prevailing metocean forcing, a suspension system decouples the hydrophone and logger from the surface expression with GPS tracking, and, when drifting in currents, a flow shield (inspired by Wilson et al., 2014) is employed to create a quiescent pocket around the hydrophone.

The DAISY V1 (TRL 5) was a modified version of a SWIFT buoy used to measure wave dissipation (Thomson, 2012). A rigid hull coupled a hydrophone (Loggerhead Instruments DSG) at 1 m depth to a surface expression for tracking. This approach was effective at minimizing flow-noise in unidirectional river currents (Polagye and Murphy, 2015), but resulted in significant flow-noise and self-noise in wavy environments. Further, the hydrophones could not be synchronized for source localization. The DAISY V1.5 (TRL 6), initially tested at the MSL and SB2 sites, replaced the rigid spar with a 2.5 m rubber cord, incorporated a flow shield, and changed the hydrophone to an OceanSonics icListen HF to allow multi-DAISY synchronization.

Ideally, technology development proceeds linearly through TRLs, but for DAISY development, it was necessary to take a few steps back to move forward. The OceanSonics hydrophone constituted >80% of the total system cost and, because it was designed for stand-alone deployment, the batteries, clock, and onboard processors were redundant with the DAISY's. For these reasons, UW developed a custom data acquisition board for an HTI-99-UHF built around a low-cost microcontroller (BeagleBone Black). This required several iterations to minimize electrical self-noise, particularly at frequencies about 10 kHz, such that the DAISY regressed to TRL 4/5, before advancing to TRL 7 (**Figure 2E**) in recent testing at MSL and SB2. Similar iterations were also required to design and manufacture a flow shield with sufficient durability.

To support commercialization, UW partnered with MarineSitu Inc. to provide a commercial version of DAISY for purchase or lease, as well as contracted monitoring services and data processing. The primary goal of this partnership is to ensure that DAISY technology is made available to the greater marine industry, rather than remaining an academic research tool. As a UW spin-off company, MarineSitu's technology translation is supported by CoMotion, UW's commercialization office. MarineSitu is working with CoMotion to license the underlying technology and develop marketing materials for the DAISY.

Spar Buoy Drifting Hydrophone

One of the Triton PPP objectives was benchmarking performance of new systems against existing technologies. A spar buoy drifting hydrophone (SBDH), developed by Oregon State University (OSU), served as the benchmark system for acoustic measurements and characterization of MRE devices and background sound levels. The SBDH has been operated at several open ocean project sites off the Oregon coast (e.g., PacWave, Camp Rilea, and Charleston) and consists of a broadband hydrophone (10 Hz–20 kHz) mounted on a 3 m long, 10.15 cm diameter PVC spar buoy with lead ballast near the bottom for increased inertial moment (**Figure 2G**). A shock cord is soft-tethered to the spar buoy, followed by a static line of variable length depending on the project site. The static line is connected to a motion damping disc or heave plate, followed by the suspended hydrophone instrument. Unlike the NoiseSpotter® and DAISY, the SBDH does not support synchronized timing and cannot be used for source localization.

DISCUSSION AND CONCLUSION

In addition to individual support offered to NoiseSpotter® and DAISY technology R&D, the Triton PPP facilitated co-located field-testing of the NoiseSpotter®, DAISY, and SBDH systems for unique benchmark comparisons in quiescent and high-energy environments (**Figure 2H**). Benchmark comparison testing consisted of three objectives:

1. Compare acoustic recordings in quiescent conditions in Sequim Bay with light currents and no wave action for system noise floor evaluations. The SBDH and three DAISYs were deployed in close proximity (<5 m) for these tests. The NoiseSpotter® was deployed on the seabed and DAISYs and SBDH drifted over it.
2. Compare acoustic recordings in more energetic current conditions at the MSL site (**Figure 1**). The NoiseSpotter® was deployed on the seabed and DAISYs drifted over it.
3. Compare acoustic recordings in more energetic wave conditions at the Clallam Bay site (**Figure 1**). The SBDH and three DAISYs were deployed in close proximity and at similar depths (12 m) for an evaluation of measured noise levels during higher energy conditions. In Clallam Bay tests, the DAISY suspension system consisted of a rubber cord and heave plate and did not include a flow shield (**Figure 2F**).

Results from these tests were encouraging. Benchmark comparisons between the DAISY and SBDH resulted in nearly identical response in the frequency bands of highest interest for MRE radiated noise (10 Hz–3 kHz) in waves and the quiescent environment. Quiescent testing also identified high frequency, broadband electrical noise in the prototype DAISY. Similarly, a comparison with a shielded broadband hydrophone on the NoiseSpotter® platform demonstrated that the drifting, shielded DAISY had a noise floor roughly 20 dB lower than a fixed, shielded hydrophone at frequencies <100 Hz. Beyond the technical outcomes from this testing, the experience of shared field operations with academic and industrial colleagues allowed all parties to pass on best practices and better understand the strengths and weaknesses of each system.

Under the Triton PPP, MRCL supported the project teams in multiple ways. All field-testing involving NoiseSpotter® and DAISY were conducted aboard MCRL vessels and their staff participated in deployment and recovery operations. MCRL consolidated all necessary permits and environmental reviews for field testing, reducing the administrative load on the technology teams and the compliance burden for federal and state resource managers. Acoustic sources employed during field-testing, and ancillary environmental data (e.g., conductivity-temperature-depth and current velocity) were collected by MCRL. NoiseSpotter® and DAISY development further benefited from technical expertise and capabilities at MCRL, with electrical engineering staff providing input on the design and fabrication of the custom data logger

for the NoiseSpotter® as well as initial design of the custom hydrophone acquisition board for the prototype DAISYs.

The NoiseSpotter® and DAISY each started at different TRLs but benefited equally from government-supported facilities and expertise, while also gaining the opportunity to collaborate and improve their systems. Multiscale acoustic testing facilitated by the Triton PPP allowed for comparison of various technological approaches (e.g., moored versus drifting, near-surface versus near-bottom, and sound pressure versus pressure/particle motion) that have been developed to assess sound from MRE installations. Having technology-agnostic facilities enabled systematic testing of different technologies throughout the R&D process, with rapid turnarounds from in-water testing, to bench improvements, and back to in-water testing. Each of the technological solutions advanced under the Triton PPP have unique capabilities, while simultaneously accommodating specific engineering tradeoffs that include flow-noise suppression, deployment duration, sensitivity, frequency range, and cost. Testing of systems at a common facility allows for objective evaluation of each system's capabilities and tradeoffs regarding their use in acoustic characterization of MRE installations. These tests served to build confidence in the technology design and approach used for measuring and characterizing MRE radiated noise.

Several factors contributed to the success of Triton; these practices are recommended for other technology development PPPs. First, MCRL played an independent, convening role for all project teams, allowing lessons learned from one test to transfer seamlessly to another. National laboratories are well positioned for this function, particularly when they are technology-agnostic. Second, WPTO encouraged teams to collaborate transparently and emphasized the overall success of the Triton PPP, rather than individual outcomes. This provided a strong incentive for teams to share knowledge and expertise. Similarly, as teams identified additional opportunities to work together outside of the original workplan, WPTO provided additional resources to MCRL to support these efforts – the combined benchmarking system test of the NoiseSpotter®, DAISY, and SBDH systems was one such activity. Third, while team members for the acoustic measurement projects had not worked extensively together before Triton, all were professionally acquainted and came into the project from a position of mutual respect. This demonstrates the benefits of informal, collaborative research communities.

The ability to access publicly funded facilities that employ consistent methods and testing procedures, enables sharing of knowledge and rapid innovation, benefiting all aspects of R&D. It is hoped that the success of Triton and related PPPs such as the European Marine Energy Centre Ltd., and DOE Testing Expertise and Access for Marine Energy Research (TEAMER™) program provide blueprints for additional PPPs that advance technology development spanning the MRE and oceanographic industries. A critical factor is the availability of a range of testing sites with different conditions that are suitable for technologies at different stages of development, coupled with the opportunity to work with other researchers who are developing related technologies.

DATA AVAILABILITY STATEMENT

The original contributions presented in the study are included in the article; further inquiries can be directed to the corresponding author/s.

AUTHOR CONTRIBUTIONS

GH-K and GC conceived the idea of this Perspective article. GC, KR, BP, JH, JJ, GS, and FS designed and participated in the multi-scale and co-testing case study. All authors wrote sections of the manuscript and contributed to manuscript revision, read, and approved the submitted version.

FUNDING

This material was based on work supported by the United States Department of Energy's Office of Energy Efficiency and Renewable Energy (EERE) under the Water Power Technologies Office Award Numbers DE-EE0007822 (KR and GC) and DE-EE0007823 (BP). PNNL is managed by Battelle Memorial Institute under Contract No. DE-AC05-76RL01830 with the United States Department of Energy.

ACKNOWLEDGMENTS

GC, KR, and FS wish to acknowledge Sean Griffin and Jesse Spence for their assistance with NoiseSpotter® technology development and testing; and Craig Jones, Sharon Kramer, and Jesse Roberts for project support. GH-K, GS, and JH wish to acknowledge the key contribution of the field team at the Marine and Coastal Research Laboratory, and Andrea Copping for working through ideas that led to this article. BP wishes to acknowledge the contributions of Corey Crisp, Jessica Noe, Paul Murphy, and Christopher Bassett of the University of Washington to the development of DAISY technology.

REFERENCES

Bassett, C., Thomson, J., Dahl, P. H., and Polagye, B. (2014). Flow-noise and turbulence in two tidal channels. *J. Acoust. Soc. Am.* 135, 1764–1774. doi: 10.1121/1.4867360

Copping, A. E., and Hemery, L. G. (2020). *OES-Environmental 2020.* State of the Science Report (No. PNNL-29976). Richland, WA: Pacific Northwest National Laboratory (PNNL).

International Electrotechnical Commission (IEC) (2019). *Technical Specification 62600-40: Marine energy-Wave, Tidal and Other Water Current Converters-Part 40: Acoustic characterization of marine energy converters.* Geneva: International Electrotechnical Commission.

National Marine Fisheries Service (NMFS) (2018). *2018 Revisions to: Technical Guidance for Assessing the Effects of Anthropogenic Sound on Marine Mammal Hearing (Version 2.0): Underwater Thresholds for Onset of Permanent and Temporary Threshold Shifts.* Silver

Spring, MD: NOAA Technical Memorandum NMFS-OPR-59, 167.

National Oceanic and Atmospheric Administration (NOAA) (2021). https://tidesandcurrents.noaa.gov/stationhome.html?id=9444555 [accessed February 16, 2021].

Polagye, B., and Murphy, P. (2015). "Acoustic characterization of a hydrokinetic turbine," in *Proceedings of the 11th European Wave and Tidal Energy Conference, September 6–11, 2015, Nantes, France*. Seattle, WA: University of Washington.

Raghukumar, K., Chang, G., Spada, F., and Jones, C. (2020). A vector sensor-based acoustic characterization system for marine renewable energy. *J. Mar. Sci. Eng.* 8:187. doi: 10.3390/jmse8030187

Raghukumar, K., Chang, G., Spada, F., Jones, C., Spence, J., Griffin, S., et al. (2019). "Performance characteristics of a vector sensor array in an energetic tidal channel," in *Proceedings of the Fifth Underwater Acoustics Conference and Exhibition*, ed. J. S. Papadakis (Crete, Greece), 653–658.

Roehrich, J. K., Lewis, M. A., and George, G. (2014). Are public–private partnerships a healthy option? A systematic literature review. *Soc. Sci. Med.* 113, 110–119. doi: 10.1016/j.socscimed.2014.03.037

Shaw, W. J., Berg, L. K., Cline, J., Draxl, C., Djalalova, I., Grimit, E. P., et al. (2019). The second wind forecast improvement project (wfip2): general overview. *Bull. Am. Meteorol. Soc.* 100, 1687–1699. doi: 10.1175/BAMS-D-18-0036.1

Sousa-Lima, R. S., Norris, T. F., Oswald, J. N., and Fernandes, D. P. (2013). A review and inventory of fixed autonomous recorders for passive acoustic monitoring of marine mammals. *Aquat. Mamm.* 39, 205–210. doi: 10.1578/am.39.2.2013.205

Strasberg, M. (1979). Nonacoustic noise interference in measurements of infrasonic ambient noise. *J. Acoust. Soc. Am.* 66, 1487–1493. doi: 10.1121/1.383543

Thomson, J. (2012). Wave breaking dissipation observed with "SWIFT" drifters. *J. Atmos. Ocean. Technol.* 29, 1866–1882. doi: 10.1175/jtech-d-12-00018.1

Wilczak, J., Finley, C., Freedman, J., Cline, J., Bianco, L., Olson, J., et al. (2015). The wind forecast improvement project (WFIP): a public–private partnership addressing wind energy forecast needs. *Bull. Am. Meteorol. Soc.* 96, 1699–1718. doi: 10.1175/BAMS-D-14-00107.1

Wilson, B., Lepper, P. A., Carter, C., and Robinson, S. P. (2014). "Rethinking underwater sound-recording methods to work at tidal-stream and wave-energy sites," in *Marine Renewable Energy Technology and Environmental Interactions*, eds M. A. Shields, and A. I. L. Payne (Dordrecht: Springer), 111–126. doi: 10.1007/978-94-017-8002-5_9

Author Disclaimer: This material was prepared as an account of work sponsored by an agency of the United States Government. Neither the United States Government nor any agency thereof, nor any of their employees, makes any warranty, express or implied, or assumes any legal liability or responsibility for the accuracy, completeness, or usefulness of any information, apparatus, product, or process disclosed, or represents that its use would not infringe privately owned rights. Reference herein to any specific commercial product, process, or service by trade name, trademark, manufacturer, or otherwise does not necessarily constitute or imply its endorsement, recommendation, or favoring by the United States Government or any agency thereof. The views and opinions of authors expressed herein do not necessarily state or reflect those of the United States Government or any agency thereof.

Conflict of Interest: GC, KR, and FS are employed by Integral Consulting Inc., and JJ is employed by MarineSitu Inc.

The remaining authors declare that the research was conducted in the absence of any commercial or financial relationships that could be construed as a potential conflict of interest.

Publisher's Note: All claims expressed in this article are solely those of the authors and do not necessarily represent those of their affiliated organizations, or those of the publisher, the editors and the reviewers. Any product that may be evaluated in this article, or claim that may be made by its manufacturer, is not guaranteed or endorsed by the publisher.

frontiers in Marine Science

PERSPECTIVE
published: 26 August 2021
doi: 10.3389/fmars.2021.695938

Promoting Instrument Development for New Research Avenues in Ocean Science: Opening the Black Box of Grazing

Susanne Menden-Deuer[1], Wayne Homer Slade[2] and Heidi Dierssen[3]*

[1] Graduate School of Oceanography, University of Rhode Island, Narragansett, RI, United States, [2] Sequoia Scientific, Inc., Bellevue, WA, United States, [3] Department of Marine Sciences, University of Connecticut, Groton, CT, United States

While recent research has provided increasing insight into ocean ecosystem functions and rapidly improving predictive ability, it has become clear that for some key processes, including grazing by zooplankton, there simply is no currently available instrumentation to quantify relevant stocks and rates, remotely or *in situ*. When measurement capacity is lacking, collaborative research between instrument manufacturers and researchers can bring us closer to addressing key knowledge gaps. By necessity, this high risk, high rewards research will require iterative steps from best case scenarios under highly controlled and often artificial laboratory conditions to empirical verification in complex *in situ* conditions with diverse biota. To illustrate our point, we highlight the example of zooplankton grazing in marine planktonic food webs. Grazing by single-celled zooplankton accounts for the majority of organic carbon loss from marine primary production but is still measured with logistically demanding, point-sample incubation methods that result in reproducible results but at insufficient resolution to adequately describe temporal and spatial dynamics of grazer induced impacts on primary production, export production and the annual cycle of marine plankton. We advance a collaborative research and development agenda to eliminate this knowledge gap. Resolving primary production losses through grazing is fundamental to a predictive understanding of the transfer of matter and energy through marine ecosystems, major reservoirs of the global carbon cycle.

Keywords: grazing, ocean optics, remote sensing, phytoplankton, zooplankton, inherent optical properties, primary production

OPEN ACCESS

Edited by:
Oscar Schofield, Rutgers, The State University of New Jersey, United States

Reviewed by:
Christoph Waldmann, University of Bremen, Germany
John Conroy, Virginia Institute of Marine Science, William & Mary, United States

****Correspondence:***
Susanne Menden-Deuer
smenden@uri.edu

Specialty section:
This article was submitted to Ocean Observation, a section of the journal Frontiers in Marine Science

Received: *15 April 2021*
Accepted: *20 July 2021*
Published: *26 August 2021*

Citation:
Menden-Deuer S, Slade WH and Dierssen H (2021) Promoting Instrument Development for New Research Avenues in Ocean Science: Opening the Black Box of Grazing. Front. Mar. Sci. 8:695938. doi: 10.3389/fmars.2021.695938

INTRODUCTION

Grazing remains one of the key unknowns in global predictive models of carbon flux, food web structure and ecosystem characteristics, because empirical grazing measurements are sparse, resulting in poor parameterization of grazing functions (e.g., Stock and Dunne, 2010; Bisson et al., 2020). To overcome this critical knowledge gap, we suggest focused effort be placed on the development of instrumentation that can link changes in phytoplankton biomass or optical properties with grazing. We contend that to gain a mechanistic understanding of ocean production and carbon fluxes, targeted, empirically validated instrument design, and model development is needed on how grazing influences the optical properties of the water column directly. The ultimate goal is to leverage linkages between grazing and optical properties to predict grazing using remote and autonomous sensors on a global scale.

Grazing is a central, rate-setting process in ocean ecosystems and a driver of marine biogeochemical cycling (Worden et al., 2015). In all ocean ecosystems, grazing by heterotrophic protists constitutes the single largest loss factor of marine primary production and alters particle size distributions (PSD; Steinberg and Landry, 2017). Grazing affects all pathways of export production, rendering grazing important both for surface and deep carbon processes (Mariani et al., 2013). Predicting central paradigms of ocean ecosystem function, including responses to environmental change requires accurate representation of grazing in global biogeochemical, ecosystem and cross-biome-comparison models (e.g., Stock and Dunne, 2010). Several large-scale analyses have concluded that phytoplankton losses, which are dominated by grazing are the putative explanation for annual cycles in phytoplankton biomass, accumulation rates and export production (Behrenfeld, 2010; Mignot et al., 2018; Bisson et al., 2020). While these analyses were based on *in situ* or remote observations, none quantified grazing empirically.

We hypothesize that grazing influences the absorption coefficients and scattering functions of seawater due to changes in the relative amounts and spectral slopes of detrital, colored dissolved and particulate materials through grazer release of dissolved matter, size-selective removal of phytoplankton, fractionation of cells and breakdown of cellular constituents during grazing **(Figure 1)**. Hence, different amounts of cellular materials will be released into the water, changing the PSD and vertical structure of phytoplankton, as well as detrital and dissolved materials. Developing proxies of grazing from changes in optical properties can enable approximating grazing over large spatial and temporal scales using *in situ* or remote observational technology. To date, there are no approaches that support direct retrieval of grazing related signals from space or autonomous *in situ* instrumentation (Brewin et al., 2021). To alleviate this important limitation, we outline a suggested empirical approach that demonstrates how iterative laboratory experiments, field testing and modeling can provide grazing proxies for existing *in situ* and remote sensing applications. A case for collaboration between the research community and industrial partners is interwoven within this approach, wherein the industrial partners are closely involved with the basic research and experimental design to better inform instrument development to expand observational capabilities to achieve the research goals. Such industry-research partnerships are essential for research where the applicability of currently available instrumentation is unknown. We conclude by highlighting some of the benefits and challenges of these collaborative relationships.

GRAZING

Background

Grazing is the term used to describe the consumption of phytoplankton by zooplankton, although a broader application of the term is common. This removal of phytoplankton can be measured in terms of abundance (i.e., cells), biomass [e.g., Carbon (C)] or biomass proxies (e.g., Chl *a*). Zooplankton are diverse including single celled protozoans such as flagellates and ciliates, as well as multi-cellular crustaceans such as copepods and krill and gelatinous forms, including salps and ctenophores. While single celled protozoans typically number in the 100 to 1,000 per mL, abundance of multi-cellular types is typically orders of magnitude lower, although aggregations can result in high density patches and swarms. Each zooplankton group differs in fundamental aspects, such as sexual or asexual reproduction, which can yield exponential population increases for single-celled types. The single-celled zooplankton, protists, have garnered particular attention because through exponential growth they can rapidly match increases in phytoplankton abundance, such as during the development of a bloom. We will refer to these here as "herbivorous protists" and identify them as particularly important in understanding particle concentrations in the ocean. Not only do these single celled organisms reproduce asexually and exponentially, they also modify the abundance, size and species composition of their phytoplankton prey (Menden-Deuer and Kiørboe, 2016). Grazing involves a great deal of selectivity and feeding strategies differ broadly, including filter feeding of large volumes of water or uptake of individual particles in a raptorial fashion. While most zooplankton eat prey that is 10-fold smaller in body size, some dinoflagellates can eat phytoplankton, especially large diatoms that are 10-fold larger than their body size (Menden-Deuer et al., 2005), which means that the largest phytoplankton particles can still be grazed by herbivorous protists. Thus, grazing alters PSD (Morison et al., 2020), which is of key importance to optical backscattering properties and remote sensing (Dall'Olmo et al., 2009; Buonassissi and Dierssen, 2010; Slade et al., 2015).

Our focus on herbivorous protist grazing is motivated by their vastly greater impact on primary production. Grazing by herbivorous protists is known to be the largest loss factor of primary production, removing on average ∼66% of global primary production (Calbet and Landry, 2004) compared to <10% removal of primary production contributed by multicellular zooplankton (Calbet, 2001). Of course these estimates have high variance and exceptions occurr in time and space. Model analyses suggest that the majority of C export due to grazing may be due to microzooplankton (Bisson et al., 2020). This may be rooted in the fact that over 25% of the biomass ingested by microzooplankton can be re-excreted (Strom et al., 1997). Protists are important conduits in transferring organic matter across trophic levels (Steinberg and Landry, 2017) and grazing persists in removing organic matter in the ocean's twilight zone (McNair and Menden-Deuer, 2020). Predation by herbivorous protists has a significant impact on both dissolved and particulate phases of seawater constituents (Verity, 1986; Strom, 2007; Mariani et al., 2013). Effects on PSD and the nature of protistan fecal material are poorly constrained, but is likely to have substantive effects on the optical properties of the dissolved and particulate phase of seawater (**Figure 2**).

Herbivorous protists have become a prime target for grazing studies, based on their high abundance, capacity for exponential growth and ability to feed on the full spectrum of planktonic particles. These features have implications for grazing effects on the abundance and composition of phytoplankton communities

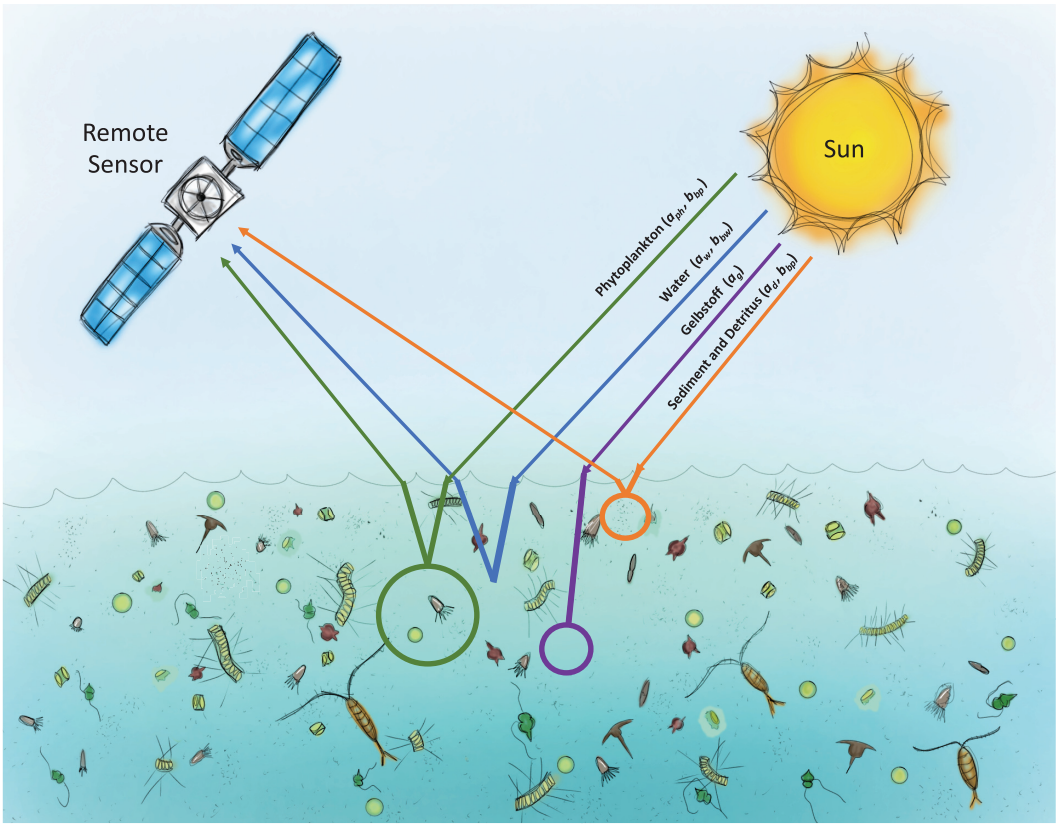

FIGURE 1 | Schematic of how common seawater constituents, including particulate and dissolved components, could both be generated and altered through the process of herbivorous grazing.

and the PSD, as well as effects on the optical properties of the dissolved phase.

Grazing Rate Measurement

Despite ample evidence of the importance of herbivorous predation on phytoplankton, we lack a mechanistic understanding and predictive ability of the quantitative effects of predation on primary production, due to the lack of adequate measurement technology. Although grazing in diverse zooplankton has been studied for decades, measurements rely on incubation based methods that have been refined but fundamentally did not change over time (Frost, 1972; Landry and Hassett, 1982). The currently most widely used method to study grazing in herbivorous protists is the dilution method, which involves contrasting phytoplankton growth and mortality in bottle incubations at manipulated grazer concentrations (Landry and Hassett, 1982; Morison and Menden-Deuer, 2017). Although the dilution method has yielded remarkable insights into the environmental drivers and quantitative importance of grazing in ocean ecosystems (e.g., Landry et al., 2009; Morison et al., 2019) and generated intriguing hypotheses (e.g., Behrenfeld, 2010), incubation based methods pose logistical challenges that result in limited sampling on a global scale (Schmoker et al., 2013). These methods all rely on capturing and handling organisms and incubating them under controlled and defined conditions. These characteristics imply that grazing estimates could well be affected by experimentally induced biases, although Lagrangian grazing studies, comparing *in situ* and incubation based plankton population dynamics typically show good agreement and reliability of the bottle incubation approach (Landry et al., 2009; Morison et al., 2019; McNair et al., 2021). Although reliable, due to logistical constraints and the need for incubation, grazing measurements are limited in their spatial and temporal resolution. Clearly, measuring grazing one bottle at a time is no means to understanding fundamental ecosystem process in a global context across seasons and habitats. Autonomous *in situ* and remote sensing capabilities provide a unique opportunity to increase the quantity and resolution of grazing rate measurements. To do so, there is an urgent need to examine the effects of grazing on optical properties of seawater and to leverage optical and ultimately remote sensing approaches to quantify grazing on the global scale.

OPTICAL PROPERTIES

Although planktonic grazers affect both the dissolved and particulate constituents of seawater, little is known about grazing influences on seawater optical properties. Although sequential

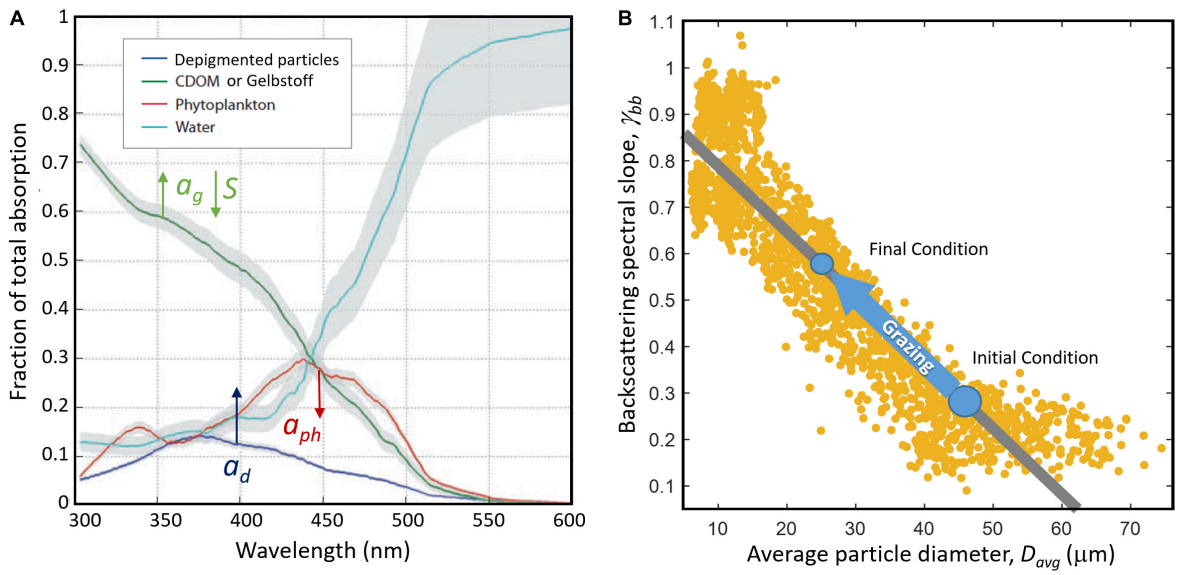

FIGURE 2 | Grazing is hypothesized to change spectral absorption and backscattering across UV and visible wavelengths. **(A)** As particles are grazed, absorption by gelbstoff (a_g) may increase and the spectral slope (S) may flatten compared to background gelbstoff subject to photobleaching. The contribution of depigmented particle absorption (a_d) may increase and phytoplankton absorption (a_{ph}) may decrease as particles are grazed. The relative changes in these components result in spectral dips and troughs that may be observed in the remote sensing reflectance, particularly in sensors that can detect spectral changes in the UV like PACE. Modified from Nelson and Siegel (2013). **(B)** Backscattering is expected to increase with increased detrital matter produced by grazing. In addition, we hypothesize that the spectral slope of backscattering g_γ, will increase as the average particle size decreases with decreasing phytoplankton and increasing detrital particles. Modified from Slade et al. (2015) showing trends in these parameters from field measurements.

time series approaches are possible, and increasing resolution by satellites will increase the opportunities for this approach, we still lack the ability to remotely retrieve direct signals of grazing (Brewin et al., 2021). Two inherent optical properties (IOPs) commonly related to remote sensing include spectral absorption $a(\lambda)$ and scattering $b(\lambda)$ coefficients (λ is the wavelength), describing the amount of a light beam absorbed or scattered per unit distance within the medium (units m^{-1}; see Mobley, 1994; Dierssen and Randolph, 2013). Oceanic constituents that are primarily responsible for absorption of photons include water molecules, phytoplankton pigments, particulate detritus, minerogenic material, and colored dissolved organic material. Scattering processes occur at the boundary of a particle with a different index of refraction from the surrounding water. Both absorption and scattering processes create targets for satellite retrieval of ocean color in terms of the magnitude and spectral shape of reflected light. Here we suggest that grazing will affect absorption and scattering properties and have the potential to be detected with ocean color remote sensing techniques (**Figure 1**).

Absorption

There is an urgent need and great opportunity to identify changes in absorption over time associated with grazing and to explore potential optical proxies for grazing rates that can be applied to remote sensing imagery. The total absorption coefficient of seawater is often represented in terms of the sum of the pure water component $a_w(\lambda)$, a particulate component $a_p(\lambda)$, and a dissolved or "gelbstoff" component $a_g(\lambda)$ that is operationally defined as anything that passes through a 0.2-µm filter. Dissolved matter can include pigment-like components, amino acid or protein-like components and small colloids that pass through the filter.

The particulate absorption coefficient can be further partitioned into a phytoplankton component $a_{ph}(\lambda)$ and a component related to depigmented particles $a_d(\lambda)$ that has traditionally been referred to as non-algal or detrital particles, which include depigmented algal particles, detritus generated through feeding, as well as minerals and suspended sediment. The spectral shapes of both $a_g(\lambda)$ and $a_d(\lambda)$ are smooth monotonically decreasing functions. Because of the similarity in spectral shape, it is often challenging to separate these components optically with multi-channel sensors, and the two are often combined in remote sensing approaches like the Generalized Inherent Optical Properties algorithm (GIOP; Werdell et al., 2013) or quasi-analytical algorithm (QAA; Lee et al., 2002) models. The sources and sinks of these two constituents are quite different and the combination is challenging to interpret from a biogeochemical perspective.

With the advent of hyperspectral sensors like those in development for future NASA missions (e.g., geosynchronous littoral imaging and monitoring radiometer (GLIMR), and surface biology and geology (SBG) missions (Dierssen et al., 2021), models are being proposed to separate the relative contributions of $a_d(\lambda)$ and $a_g(\lambda)$ in the surface ocean from the remote sensing signal globally. An important component will be to investigate the influence of grazing on IOPs in a controlled setting to identify applications to the suite of new measurement technology in the pipeline for these new missions.

For example, new methods have been proposed to improve partitioning of total absorption into the three components, $a_{ph}(\lambda)$, $a_d(\lambda)$ and $a_g(\lambda)$ with an inversion scheme (Zheng et al., 2015; Stramski et al., 2019). The ability to partition absorption into its components may provide information on primary production and associated grazing.

Scattering

As with absorption, changes in scattering provides another opportunity to link grazing, optical properties, and remote sensing. Scattering is inherently an angle-dependent process, described by the volume scattering function [VSF, $\beta(\psi, \lambda)$, units m^{-1} sr^{-1}], where ψ is the scattering angle relative to the incident light. The magnitude, angular shape, and polarization properties of scattering by particles in seawater are dependent on particle size, shape, and composition. Associations between particle properties and optical scattering properties allow for proxy models to estimate a wide range of particle properties and dynamics *in situ* (e.g., Sullivan et al., 2005).

Measurement of the particulate backscattering coefficient $b_{bp}(\lambda)$ (essentially the integral of the VSF over the backward hemisphere) is of particular importance since it is a critical element of understanding ocean color remote sensing signals (Werdell et al., 2018, references therein), which are being used to describe global-scale biogeochemical processes and changes therein due to climate change (e.g., Siegel et al., 2016; Dutkiewicz et al., 2019). Backscattering measurements are also becoming common on autonomous platforms where they have recently been used to constrain biogeochemical processes (e.g., Mignot et al., 2018; Uchida et al., 2019). Fluctuations in the optical properties can also be used to estimate particle size (Briggs et al., 2013). This concept was expanded by leveraging fluctuations in the backscattering signal during a flux event to partition the stock into multiple size fractions to examine the effect of fragmentation of settling aggregates on carbon flux (Briggs et al., 2020).

Theoretical work has suggested that the scattering or backscattering spectral shape depends on the PSD (e.g., Morel, 1973; Boss et al., 2001, references therein). Limited indirect measurements of backscattering using *in situ* radiometric or ocean color (Loisel et al., 2006; Gordon et al., 2009) and direct measurements of spectral backscattering and PSD (Slade et al., 2015) support the possibility of spectral backscattering as a proxy for particle size. The shape of the VSF measured at multiple angles can also be used to invert for PSD and composition (e.g., organic vs. mineral) using a variety of approaches (e.g., Agrawal and Pottsmith, 2000; Zhang et al., 2011).

Polarization of scattering by particles in the ocean is also expected to depend on PSD and composition, however, only limited measurements have been made *in situ* or of ocean samples (Voss and Fry, 1984; Koestner et al., 2018). The most detailed examinations of angular dependence of polarized scattering have been of phytoplankton cultures (Volten et al., 1998; Svensen et al., 2011), where significant differences were found between measurements and theoretical predictions for a wide range of cell sizes, shapes, and structures. Thus, there remains need and opportunity to unify theoretical expectations with empirical observations of phytoplankton scattering functions, both under controlled laboratory conditions and those representative of the heterogeneous and dynamic ocean.

DISCUSSION

Linking Grazing and Optics: A Possible Path Forward

To explore the utility of optical properties for the quantitative analysis of grazing pressure in marine planktonic food webs, we envision a collaborative effort that closely ties the research needs with instrument development. These could leverage existing instrumentation and methods (**Table 1**) to measure grazing impacts on particle fields (Menden-Deuer et al., 2020), scattering and PSD relationships (Slade et al., 2015), dissolved and detrital absorption, as well as changes in phytoplankton absorption and pigments (**Figure 2**). The overall concept is to measure removal of algal prey by zooplankton first in laboratory grazing experiments. These experiments consist of bottle incubations that pair a grazer and a phytoplankton prey species and a control of the phytoplankton species incubated by itself (Frost, 1972; Jeong, 2007). The predator-free control allows to estimate the effects of other sources of mortality and the magnitude of growth in the absence of grazing. Experiments with targeted single predator prey pairs provide a best-case scenario approach to maximize the signal to noise ratio and examine the sensitivity of existing instruments to these idealized conditions.

Since this is exploratory research with well-founded hypotheses, but without prior empirical support, a broad net needs to be cast to determine grazer induced changes in optical properties both in the particulate and dissolved phases. Measuring abundance, PSD, angular and polarized scattering, and absorption of the dissolved and particulate (algal and non-algal) components, can aid in delivering diagnostic data linking optical properties to grazing pressure, qualitatively (presence or absence of grazing) and quantitatively (across a prey concentration gradient; **Figure 2**). Finally, to examine the utility of these idealized measurements for remote sensing applications, the absorption and scattering measurements can be examined in terms of their individual and combined effects on ocean color signals using a radiative transfer model such as HydroLight (Hedley and Mobley, 2019).

Once promising targets for optical grazing signatures are identified, field experiments can commence to probe grazing measurements that utilize incubations (e.g., Morison and Menden-Deuer, 2017) for correlations between optical proxies and concurrent measurements of grazing rates. The final testing goal would then be to characterize the optical properties *in situ* and probe for grazing signatures at high resolution over large spatial and temporal scales. Such measurements would open the door to test ocean color remote sensing algorithms for retrieving IOPs under different grazing conditions. Obviously, this would require *in situ* validation and inter-comparison efforts and could benefit from leveraging existing data sets with concurrent optical measurements and grazing incubations for retrospective analysis, as available.

TABLE 1 | Examples of measurement approaches that can aid in quantifying grazing impacts on the optical properties of seawater, their methodologies, applicability to lab and/or field studies, and estimated uncertainties.

Measurement	Quantities (units)	Instrument/Method	Lab/Field	Uncertainty
Predator/prey concentration	Abundance (cells mL^{-1})	Microscopy/Image analysis (provides cell characteristics)	Lab, Field *In situ*	±10% (Menden-Deuer et al., 2020)
		Coulter Counter (CC) (rapid processing but no cell characteristics)	Lab, Field Discrete	±1% (Menden-Deuer et al., 2020)
Predator/prey biomass	Biomass ($\mu gC\ L^{-1}$)	Microscopy/Image Analysis	Lab, Field *In situ*	±30% (Menden-Deuer and Lessard, 2000)
Grazing rate	Change in Abundance (cells $predator^{-1}\ day^{-1}$) and Biomass ($\mu gC\ predator^{-1}\ day^{-1}$)	Microscopy/Image analysis	Lab, Field *In situ*	±10% of algal counts (Menden-Deuer et al., 2018)
		Coulter Counter	Lab, Field Discrete	
Particle size	PSD, $N(D)$ (#/mL)	Coulter Counter	Lab, Field Discrete	±1% (Menden-Deuer et al., 2020)
	PSD, $V(D)$ ($\mu L/L$)	LISST-200X	Lab, Field *In situ*	Approx. 3% D50 repeatability (ISO, 2020)
	D_{avg} (μm)	Optical signal fluctuations in c_p and b_{bp}	Lab, Field *In situ*	10%–24% (Briggs et al., 2013)
Particulate absorption	$a_p(\lambda)$ (m^{-1})	QFT-ICAM	Lab, Field Discrete	±1.5% (Röttgers et al., 2016)
		ac-9/ac-s	Lab, Field, *In situ*	$\pm 0.006\ m^{-1}$[a] (Twardowski et al., 2018)
Particulate absorption (constituents)	$a_d(\lambda)$ (m^{-1}) $a_{ph}(\lambda)$ (m^{-1})	Models for partitioning particulate absorption into $a_d(\lambda)$ and $a_{ph}(\lambda)$	Model	Stramski et al., 2019
Phytoplankton community composition		Imaging methods FlowCytometry	Lab, Field *In situ*	(see Lombard et al., 2019)
		Diagnostic Pigment Analysis	Lab, Field Discrete	Chase et al., 2020
Dissolved absorption	$a_g(\lambda)$ (m^{-1})	Spectrometry	Lab, Field Discrete	∼10% wavelength-dependent (IOCCG, 2018)
		ac-9/ac-s	Lab, Field, *In situ*	$\pm 0.001\ m^{-1}$[a] (Twardowski et al., 2018)
Particulate attenuation	$c_p(\lambda)$ (m^{-1})	ac-9/ac-s	Lab, Field, *In situ*	$<0.004\ m^{-1}$[a,b] (IOCCG Protocol Series, 2019)
	$c_p(520)$ (m^{-1})	LISST optics	Lab, Field, *In situ*	$<0.01\ m^{-1}$
Volume scattering function (VSF)	$\beta_p(\psi, 520)$ ($m^{-1}\ sr^{-1}$)	LISST-Horizon[(2)] LISST-VSF	Lab, Field, *In situ*	Typ. 3–10% uncertainty (Zhang et al., 2011)
Backscattering	$b_{bp}(700)$ (m^{-1})	ECO-VSF	Lab, Field *In situ*	±5–10% relative (Sullivan et al., 2013)
	$b_{bp}(520)$ (m^{-1})	Extrapolation and integration of measured VSF (LISST-VSF)	Lab, Field *In situ*	To be determined
Turbidity	TSS (NTU)	Turbidimeter	Lab, Field *In situ*	∼55% (Boss et al., 2009)
Particulate scattering	$b_p(\lambda)$ (m^{-1})	ac-9/ac-s	Lab, Field *In situ*	$\pm 0.007^{a,b}\ m^{-1}$ (Sullivan et al., 2013)
	$b_p(520)$ (m^{-1})	Extrapolation and integration of measured VSF	Lab, Field *In situ*	To be determined
Polarized scattering	DoLP	LISST-Horizon LISST-VSF	Lab, Field *In situ*	To be determined

[a] *approximately double this for short blue and long red wavelengths.*
[b] *plus ∼5–10% underestimation from scattered light <0.8 not detected.*
Absorption, attenuation and scattering instrumentation will require additional innovation to tailor measurements for the proposed grazing studies.

While laboratory experiments will provide a linkage between IOPs and grazing under idealized conditions, field experiments will also be required to assess grazing under realistic environmental conditions. This approach will provide an understanding of grazing with changing predator and prey compositions and physical conditions including turbulence and mixing. Under such conditions, particle imaging techniques will be useful to assess the distribution, sizes and types of particles (Lombard et al., 2019) potentially impacted by grazing. Techniques like holography can provide particle imaging in a large undisturbed sample volume without disturbance of the particle orientation (Nayak et al., 2018). Several different commercially available holographic imaging instruments are now being offered (Walcutt et al., 2020).

The Case for Science-Industry Partnerships

Research scientists, often in government or academic settings, typically do not have the facilities, expertise, and leeway to pursue de-novo instrument development. Instrument vendors, on the other hand, typically need to rely on broad application of their existing instrumentation and do not have the economic incentive to develop instruments for a novel application. Through a partnership, instrument developments can be tailored

to urgent measurement gaps. However, these partnerships can be difficult to frame as collaborative proposals, where the risk of instrumentation development often does not fit into panel review criteria. Neither do these efforts fit into technology development funding calls such as through the US SBIR/STTR program, since there may not be a clear commercialization potential.

Specifically, a commercial-academic partnership is needed when, as in our case, there are many unknowns associated with a particular research endeavor. Although the question is important and developing remote sensing approaches for grazing would be transformative, there are two major obstacles. First, there is no current technology to measure grazing other than through incubation methods; and second, although we have half a dozen or more possible targets, there has been no specific target identified. This situation is utterly unattractive to instrument developers. The cost to generate a new instrument is approximately 10-fold greater than modification of an existing one. To incentivize the development, we propose that much of the research effort of identifying a target should be done by academic partners at the cutting edge of the field. Bringing instrument developers on board right away provides opportunities to possibly modify existing technology in support of novel science applications.

In the case we have outlined here, there are clear opportunities for science-industry collaboration. For the laboratory effort, a variety of angular, spectral, and polarized scattering measurements are made to address the hypothesis that grazing changes the IOP of seawater in characteristic ways. It is unrealistic for the project to absorb the costs associated with acquiring, maintaining, and developing expertise around a full suite of instrumentation to examine possible scattering-based biogeochemical proxies. Providing the ability to lease instruments with associated consulting services may enhance science and industry partnerships that provide high quality data at more cost-effective rates than purchasing new instrumentation and training personnel. Close involvement of the industrial partner in the experimental design helps to ensure that instrument modifications, method development, and/or prototype development is focused on the needs of the science partners and is technically feasible and potentially comercializable. This arrangement provides the additional benefit for the industrial partner to test new instruments and methodologies in the field, often a costly and logistically difficult proposition, especially for a small company.

When new technology developments are successful and commercially viable, science and industry partnerships thrive. In this manner, a high-risk, high-reward project of identifying novel optical proxies can hold immense value in breaking new scientific grounds as well as stimulating adoption of existing technology to novel applications and development of new technology. Here, we have outlined how the pressing scientific question of assessing global grazing rates requires a host of new optical measurements that could be used to enhance science and industry partnerships and lead to much needed scientific capacities to understand ocean ecosystems and carbon flux.

DATA AVAILABILITY STATEMENT

The datasets presented in the study are included in the article, further inquiries can be directed to the corresponding author/s.

AUTHOR CONTRIBUTIONS

All authors listed have made a substantial, direct and intellectual contribution to the work, and approved it for publication.

FUNDING

Support for SM-D was provided by the National Aeronautics and Space Administration (80NSSC17K0716) and the National Science Foundation (OCE-1736635). Support for HD was provided by NASA (80NSSC20M0206).

ACKNOWLEDGMENTS

We thank Ivona Cetinic for facilitating initial discussion of this work and Sara Shapiro for creating the drawing for **Figure 1**. We appreciate careful review and comments from two reviewers who have improved this manuscript.

REFERENCES

Agrawal, Y. C., and Pottsmith, H. C. H. (2000). Instruments for particle size and settling velocity observations in sediment transport. *Mar. Geol.* 168, 89–114. doi: 10.1016/S0025-3227(00)00044-X

Behrenfeld, M. J. (2010). Abandoning Sverdrup's critical depth hypothesis on phytoplankton blooms. *Ecology* 91, 977–989. doi: 10.1890/09-1207.1

Bisson, K., Siegel, D. A., and DeVries, T. (2020). Diagnosing mechanisms of ocean carbon export in a satellite-based food web model. *Front. Mar. Sci.* 7:505. doi: 10.3389/fmars.2020.00505

Boss, E., Taylor, L., Gilbert, S., Gundersen, K., Hawley, N., Janzen, C., et al. (2009). Comparison of inherent optical properties as a surrogate for particulate matter concentration in coastal waters. *Limnol. Oceanogr. Methods* 7, 803–810. doi: 10.4319/lom.2009.7.803

Boss, E., Twardowski, M. S., and Herring, S. (2001). Shape of the particulate beam attenuation spectrum and its inversion to obtain the shape of the particulate size distribution. *Appl. Opt.* 40:4885. doi: 10.1364/AO.40.004885

Brewin, R. J. W., Sathyendranath, S., Platt, T., Bouman, H., Ciavatta, S., Dall'Olmo, G., et al. (2021). Sensing the ocean biological carbon pump from space: a review of capabilities, concepts, research gaps and future developments. *Earth Sci. Rev.* 217:103604. doi: 10.1016/j.earscirev.2021.103604

Briggs, N., Dall'Olmo, G., and Claustre, H. (2020). Major role of particle fragmentation in regulating biological sequestration of CO2 by the oceans. *Science* 793, 791–793. doi: 10.1126/science.aay1790

Briggs, N. T., Slade, W. H., Boss, E. S., and Perry, M. J. (2013). Method for estimating mean particle size from high-frequency fluctuations in beam attenuation or scattering measurements. *Appl. Opt.* 52, 6710–6725. doi: 10.1364/AO.52.006710

Buonassissi, C. J., and Dierssen, H. M. (2010). A regional comparison of particle size distributions and the power law approximation in oceanic and estuarine surface waters. *J. Geophys. Res.* 115, 1–12. doi: 10.1029/2010JC006256

Calbet, A. (2001). Mesozooplankton grazing effect on primary production: a global comparative analysis in marine ecosystems. *Limnol. Oceanogr.* 46, 1824–1830. doi: 10.4319/lo.2001.46.7.1824

Calbet, A., and Landry, M. R. (2004). Phytoplankton growth, microzooplankton grazing, and carbon cycling in marine systems. *Limnol. Oceanogr.* 49, 51–57. doi: 10.4319/lo.2004.49.1.0051

Chase, A. P., Kramer, S. J., Haëntjens, N., Boss, E. S., Karp-Boss, L., Edmondson, M., et al. (2020). Evaluation of diagnostic pigments to estimate phytoplankton size classes. *Limnol. Oceanogr. Methods* 18, 570–584. doi: 10.1002/lom3.10385

Dall'Olmo, G., Westberry, T. K., Behrenfeld, M. J., Slade, W. H., Boss, E. S., and Slade, W. H. (2009). Significant contribution of large particles to optical backscattering in the open ocean. *Biogeosciences* 6, 947–967. doi: 10.5194/bg-6-947-2009

Dierssen, H. M., Ackleson, S., Joyce, K., Hestir, E., Castagna, A., Lavender, S., et al. (2021). Living up to the hype of hyperspectral aquatic remote sensing: science, resources and outlook. *Front. Environ. Sci.* 9:134. doi: 10.3389/fenvs.2021.649528

Dierssen, H. M., and Randolph, K. (2013). "Remote sensing of ocean color," in *Earth System Monitoring*, ed. J. Orcutt (New York, NY: Springer New York), 439–472. doi: 10.1007/978-1-4614-5684-1_18

Dutkiewicz, S., Hickman, A. E., Jahn, O., Henson, S., Beaulieu, C., and Monier, E. (2019). Ocean colour signature of climate change. *Nat. Commun.* 10:578. doi: 10.1038/s41467-019-08457-x

Frost, B. W. (1972). Effects of size and concentration of food particles on the feeding behavior of the marine planktonic copepod Calanus pacificus. *Limnol. Oceanogr.* 17, 805–815. doi: 10.4319/lo.1972.17.6.0805

Gordon, H. R., Lewis, M. R., McLean, S. D., Twardowski, M. S., Freeman, S. A., Voss, K. J., et al. (2009). Spectra of particulate backscattering in natural waters. *Opt. Express* 17, 16192–16208. doi: 10.1364/OE.17.016192

Hedley, J. D., and Mobley, C. D. (2019). *HydroLight 6.0 Users' Guide*. Tiverton: Numerical Optics Ltd.

IOCCG (2018). *IOCCG Ocean Optics and Biogeochemistry Protocols for Satellite Ocean Colour Sensor Validation. Inherent Optical Property Measurements and Protocols: Absorption Coefficient*, Vol. 1.0, eds. A. R. Neeley and A. Mannino [Dartmouth, NS: International Ocean-Colour Coordinating Group (IOCCG)], 78. doi: 10.25607/OBP-119

IOCCG Protocol Series (2019). *Beam Transmission and Attenuation Coefficients: Instruments, Characterization, Field Measurements and Data Analysis Protocols*. Available online at: http://dx.doi.org/10.25607/OBP-458

ISO (2020). *Particle Size Analysis – Laser Diffraction Methods*. Geneva. Available online at: https://www.iso.org/standard/69111.html

Jeong, H. J. (2007). The ecological roles of heterotrophic dinoflagellates in marine planktonic community. *J. Eukaryot. Microbiol.* 46, 390–396. doi: 10.1111/j.1550-7408.1999.tb04618.x

Koestner, D., Stramski, D., and Reynolds, R. A. (2018). Measurements of the volume scattering function and the degree of linear polarization of light scattered by contrasting natural assemblages of marine particles. *Appl. Sci.* 8, 1–32. doi: 10.3390/app8122690

Landry, M. R., and Hassett, R. (1982). Estimating the grazing impact of marine micro-zooplankton. *Mar. Biol.* 67, 283–288. doi: 10.1007/bf00397668

Landry, M. R., Ohman, M. D., Goericke, R., Stukel, M. R., and Tsyrklevich, K. (2009). Lagrangian studies of phytoplankton growth and grazing relationships in a coastal upwelling ecosystem off Southern California. *Prog. Oceanogr.* 83, 208–216. doi: 10.1016/j.pocean.2009.07.026

Lee, Z., Carder, K. L., and Arnone, R. A. (2002). Deriving inherent optical properties from water color: a multiband quasi-analytical algorithm for optically deep waters. *Appl. Opt.* 41:5755. doi: 10.1364/AO.41.005755

Loisel, H., Nicolas, J.-M., Sciandra, A., Stramski, D., and Poteau, A. (2006). Spectral dependency of optical backscattering by marine particles from satellite remote sensing of the global ocean. *J. Geophys. Res.* 111, 1–14. doi: 10.1029/2005JC003367

Lombard, F., Boss, E. S., Waite, A. M., Uitz, J., Stemmann, L., Sosik, H. M., et al. (2019). Globally consistent quantitative observations of planktonic ecosystems. *Front. Mar. Sci.* 6:196. doi: 10.3389/fmars.2019.00196

Mariani, P., Andersen, K. H., Visser, A. W., Barton, A. D., and Kiørboe, T. (2013). Control of plankton seasonal succession by adaptive grazing. *Limnol. Oceanogr.* 58, 173–184. doi: 10.4319/lo.2013.58.1.0173

McNair, H., Morison, F., Graff, J., Rynerason, T., and Menden-Deuer, S. (2021). Microzooplankton grazing constrains pathways of carbon export in the subarctic North Pacific. *Limnol. Oceanogr.* 66, 2697–2711. doi: 10.1002/lno.11783

McNair, H. M., and Menden-Deuer, S. (2020). Protist grazing contributes to microbial food web at the upper boundary of the twilight zone in the subarctic Pacific. *Mar. Ecol. Prog. Ser.* 636, 235–241. doi: 10.3354/meps13246

Menden-Deuer, S., and Kiørboe, T. (2016). Small bugs with a big impact: linking plankton ecology with ecosystem processes. *J. Plankton Res.* 38, 1036–1043. doi: 10.1093/plankt/fbw049

Menden-Deuer, S., Lawrence, C., and Franzé, G. (2018). Herbivorous protist growth and grazing rates at in situ and artificially elevated temperatures during an Arctic phytoplankton spring bloom. *PeerJ* 6:e5264. doi: 10.7717/peerj.5264

Menden-Deuer, S., and Lessard, E. J. (2000). Carbon to volume relationships for dinoflagellates, diatoms, and other protist plankton. *Limnol. Oceanogr.* 45, 569–579. doi: 10.4319/lo.2000.45.3.0569

Menden-Deuer, S., Lessard, E., Satterberg, J., and Grünbaum, D. (2005). Growth rates and starvation survival of three species of the pallium-feeding, thecate dinoflagellate genus *Protoperidinium*. *Aquat. Microb. Ecol.* 41, 145–152. doi: 10.3354/ame041145

Menden-Deuer, S., Morison, F., Montalbano, A. L., Franzè, G., Strock, J., Rubin, E., et al. (2020). Multi-instrument assessment of phytoplankton abundance and cell sizes in mono-specific laboratory cultures and whole plankton community composition in the North Atlantic. *Front. Mar. Sci.* 7:254. doi: 10.3389/fmars.2020.00254

Mignot, A., Ferrari, R., and Claustre, H. (2018). Floats with bio-optical sensors reveal what processes trigger the North Atlantic bloom. *Nat. Commun.* 9:190. doi: 10.1038/s41467-017-02143-6

Mobley, C. D. (1994). *Light and Water: Radiative Transfer in Natural Waters*. San Diego, CA: Academic Press.

Morel, A. (1973). "Diffusion de la lumi'ere par les eaux de mer. R'esultats exp'erimentaux et approche th'eorique," in *Optics of the Sea, AGARD Lect. Ser.* 61, 3.1.1–76, Neuilly-sur-Seine: NATO. Available online at: https://apps.dtic.mil/sti/pdfs/AD0767474.pdf

Morison, F., Harvey, E., Franzè, G., and Menden-Deuer, S. (2019). Storm-induced predator-prey decoupling promotes springtime accumulation of north atlantic phytoplankton. *Front. Mar. Sci.* 6:608. doi: 10.3389/fmars.2019.00608

Morison, F., and Menden-Deuer, S. (2017). Doing more with less? Balancing sampling resolution and effort in measurements of protistan growth and grazing-rates. *Limnol. Oceanogr. Methods* 15, 794–809. doi: 10.1002/lom3.10200

Morison, F., Pierson, J., Oikonomou, A., and Menden-Deuer, S. (2020). Mesozooplankton grazing minimally impacts phytoplankton abundance during spring in the Western North Atlantic. *PeerJ* 8:e9430. doi: 10.7717/peerj.9430

Nayak, A. R., McFarland, M. N., Sullivan, J. M., and Twardowski, M. S. (2018). Evidence for ubiquitous preferential particle orientation in representative oceanic shear flows. *Limnol. Oceanogr.* 63, 122–143. doi: 10.1002/lno.10618

Nelson, N. B., and Siegel, D. A. (2013). The global distribution and dynamics of chromophoric dissolved organic matter. *Ann. Rev. Mar. Sci.* 5, 447–476. doi: 10.1146/annurev-marine-120710-100751

Röttgers, R., Doxaran, D., and Dupouy, C. (2016). Quantitative filter technique measurements of spectral light absorption by aquatic particles using a portable integrating cavity absorption meter (QFT-ICAM). *Opt. Express* 24:A1. doi: 10.1364/OE.24.0000A1

Schmoker, C., Hernández-León, S., and Calbet, A. (2013). Microzooplankton grazing in the oceans: impacts, data variability, knowledge gaps and future directions. *J. Plankton Res.* 35, 691–706. doi: 10.1093/plankt/fbt023

Siegel, D. A., Buesseler, K. O., Behrenfeld, M. J., Benitez-Nelson, C. R., Boss, E. S., Brzezinski, M. A., et al. (2016). Prediction of the export and fate of global ocean net primary production: The EXPORTS science plan. *Front. Mar. Sci.* 3:22. doi: 10.3389/fmars.2016.00022

Slade, W. H., and Boss, E. S. (2015). Spectral attenuation and backscattering as indicators of average particle size. *Appl. Opt.* 54, 7264–7277. doi: 10.1364/AO.54.007264

Steinberg, D. K., and Landry, M. R. (2017). Zooplankton and the ocean carbon cycle. *Ann. Rev. Mar. Sci.* 9, 413–444. doi: 10.1146/annurev-marine-010814-015924

Stock, C., and Dunne, J. (2010). Controls on the ratio of mesozooplankton production to primary production in marine ecosystems. *Deep Sea Res. Part I Oceanogr. Res. Pap.* 57, 95–112. doi: 10.1016/j.dsr.2009.10.006

Stramski, D., Li, L., and Reynolds, R. A. (2019). Model for separating the contributions of non-algal particles and colored dissolved organic matter to light absorption by seawater. *Appl. Opt.* 58:3790. doi: 10.1364/AO.58.003790

Strom, S. L. (2007). Microbial ecology of ocean biogeochemistry: a community perspective. *Science* 320:1043. doi: 10.1126/science.1153527

Strom, S. L., Benner, R., Ziegler, S., and Dagg, M. J. (1997). Planktonic grazers are a potentially important source of marine dissolved organic carbon. *Limnol. Oceanogr.* 42, 1364–1374. doi: 10.4319/lo.1997.42.6.1364

Sullivan, J., Twardowski, M., Zaneveld, J. R. V., and Moore, C. (2013). "Measuring optical backscattering in water," in *Light Scattering Reviews 7: Radiative Transfer and Optical Properties of Atmosphere and Underlying Surface, Springer Praxis Books*, ed. A. Kokhanovsky (Berlin: Springer), 189–224. doi: 10.1007/978-3-642-21907-8_6

Sullivan, J. M., Twardowski, M. S., Donaghay, P. L., and Freeman, S. A. (2005). Use of optical scattering to discriminate particle types in coastal waters. *Appl. Opt.* 44, 1667–1680. doi: 10.1364/AO.44.001667

Svensen, Ø, Stamnes, J. J., Kildemo, M., Aas, L. M. S., Erga, S. R., and Frette, Ø (2011). Mueller matrix measurements of algae with different shape and size distributions. *Appl. Opt.* 50, 5149–5157. doi: 10.1364/AO.50.005149

Twardowski, M., Freeman, S., Pegau, S., Zaneveld, J. R. V., Mueller, J., and Boss, E. (2018). "Chapter 2: reflective tube absorption meters," in *IOCCG Absorption Protocol Protocols, Inherent Optical Property Measurements and Protocols*, Vol. I, ed. A. Neely, 37–51.

Uchida, T., Balwada, D., Abernathey, R., Prend, C. J., Boss, E. S., and Gille, S. T. (2019). Southern Ocean phytoplankton blooms observed by biogeochemical floats. *J. Geophys. Res. Ocean* 124, 1–16. doi: 10.1029/2019JC015355

Verity, P. G. (1986). Grazing of phototrophic nanoplankton by microzooplankton in narragansett bay. *Mar. Ecol. Prog. Ser.* 29, 105–115. doi: 10.3354/meps029105

Volten, H., de Haan, J. F., Hovenier, J. W., Schreurs, R., Vassen, W., Dekker, A. G., et al. (1998). Laboratory measurements of angular distributions of light scattered by phytoplankton and silt. *Limnol. Oceanogr.* 43, 1180–1197. doi: 10.4319/lo.1998.43.6.1180

Voss, K. J., and Fry, E. S. (1984). Measurement of the Mueller matrix for ocean water. *Appl. Opt.* 23:4427. doi: 10.1364/AO.23.004427

Walcutt, N. L., Knörlein, B., Cetinić, I., Ljubesic, Z., Bosak, S., Sgouros, T., et al. (2020). Assessment of holographic microscopy for quantifying marine particle size and concentration. *Limnol. Oceanogr. Methods* 18, 516–530. doi: 10.1002/lom3.10379

Werdell, P. J., Franz, B. A., Bailey, S. W., Feldman, G. C., Boss, E. S., Brando, V. E., et al. (2013). Generalized ocean color inversion model for retrieving marine inherent optical properties. *Appl. Opt.* 52, 2019–2037. doi: 10.1364/AO.52.002019

Werdell, P. J., McKinna, L. I. W., Boss, E., Ackleson, S. G., Craig, S. E., Gregg, W. W., et al. (2018). An overview of approaches and challenges for retrieving marine inherent optical properties from ocean color remote sensing. *Prog. Oceanogr.* 160, 186–212. doi: 10.1016/j.pocean.2018.01.001

Worden, A. Z., Follows, M. J., Giovannoni, S. J., Wilken, S., Zimmerman, A. E., and Keeling, P. J. (2015). Rethinking the marine carbon cycle: factoring in the multifarious lifestyles of microbes. *Science.* 347:1257594. doi: 10.1126/science.1257594

Zhang, X., Twardowski, M., and Lewis, M. (2011). Retrieving composition and sizes of oceanic particle subpopulations from the volume scattering function. *Appl. Opt.* 50:1240. doi: 10.1364/AO.50.001240

Zheng, G., Stramski, D., and DiGiacomo, P. M. (2015). A model for partitioning the light absorption coefficient of natural waters into phytoplankton, nonalgal particulate, and colored dissolved organic components: a case study for the Chesapeake Bay. *J. Geophys. Res. Ocean.* 120, 2601–2621. doi: 10.1002/2014JC010604

Conflict of Interest: WS is Vice President for Science & Technology at Sequoia Scientific, Inc.

The remaining authors declare that the development of this perspective was conducted in the absence of any commercial or financial relationships that could be construed as a potential conflict of interest.

Publisher's Note: All claims expressed in this article are solely those of the authors and do not necessarily represent those of their affiliated organizations, or those of the publisher, the editors and the reviewers. Any product that may be evaluated in this article, or claim that may be made by its manufacturer, is not guaranteed or endorsed by the publisher.

frontiers in Marine Science

ORIGINAL RESEARCH
published: 20 October 2021
doi: 10.3389/fmars.2021.697611

Industry Partnership: Lab on Chip Chemical Sensor Technology for Ocean Observing

Matt Mowlem[1,2], Alexander Beaton[1,2], Robin Pascal[1,2], Allison Schaap[1], Socratis Loucaides[1], Sam Monk[2], Andrew Morris[1], Christopher L. Cardwell[1,2], Sara E. Fowell[1], Matthew D. Patey[1] and Patricia López-García[1]*

[1] Ocean Technology and Engineering Group, National Oceanography Centre, Southampton, United Kingdom, [2] ClearWater Sensors Ltd., Westbourne, United Kingdom

OPEN ACCESS

Edited by:
Ole Mikkelsen,
Sequoia Scientific, United States

Reviewed by:
Feng Pan,
Xiamen University, China
Joseph Needoba,
Oregon Health and Science University, United States

***Correspondence:**
Matt Mowlem
matm@noc.ac.uk;
matt.mowlem@clearwatersensors.com

Specialty section:
This article was submitted to Ocean Observation, a section of the journal Frontiers in Marine Science

Received: 19 April 2021
Accepted: 08 September 2021
Published: 20 October 2021

Citation:
Mowlem M, Beaton A, Pascal R, Schaap A, Loucaides S, Monk S, Morris A, Cardwell CL, Fowell SE, Patey MD and López-García P (2021) Industry Partnership: Lab on Chip Chemical Sensor Technology for Ocean Observing. Front. Mar. Sci. 8:697611. doi: 10.3389/fmars.2021.697611

We introduce for the first time a new product line able to make high accuracy measurements of a number of water chemistry parameters *in situ*: i.e., submerged in the environment including in the deep sea (to 6,000 m). This product is based on the developments of *in situ* lab on chip technology at the National Oceanography Centre (NOC), and the University of Southampton and is produced under license by Clearwater Sensors Ltd., a start-up and industrial partner in bringing this technology to global availability and further developing its potential. The technology has already been deployed by the NOC, and with their partners worldwide over 200 times including to depths of ∼4,800 m, in turbid estuaries and rivers, and for up to a year in seasonally ice-covered regions of the arctic. The technology is capable of making accurate determinations of chemical and biological parameters that require reagents and which produce an electrical, absorbance, fluorescence, or luminescence signal. As such it is suitable for a wide range of environmental measurements. Whilst further parameters are in development across this partnership, Nitrate, Nitrite, Phosphate, Silicate, Iron, and pH sensors are currently available commercially. Theses sensors use microfluidics and optics combined in an optofluidic chip with electromechanical valves and pumps mounted upon it to mix water samples with reagents and measure the optical response. An overview of the sensors and the underlying components and technologies is given together with examples of deployments and integrations with observing platforms such as gliders, autonomous underwater vehicles and moorings.

Keywords: submersible, autonomous, *in situ*, lab on chip, microfluidics, analytical chemistry, chemical sensors

INTRODUCTION

The oceans cover over 70% of our planet and directly contribute $2.5Trillion/yr in economic benefit, which is equivalent to the world's 7th largest economy (2016) (Hoegh-Guldberg, 2015). They provide $25Trillion in ecosystem services such as production of food. Whilst 90% of their value depends on healthy ecosystems, 30–35% of critical marine habitats are overused or have been

destroyed, ocean acidity is up 26%, and oxygen is depleting in key areas (G7 Science and Technology Ministers, 2016).

Oceanic chemistry plays a central role in ecosystems through biogeochemical processes. State of the art operational Earth System/lower trophic level ecosystem models (such as Butenschoen et al., 2016) include the carbonate system and macro nutrient variables in both pelagic (water) and benthic (sediment) representations as well as iron (Fe) in the pelagic and CO_2 flux between the ocean and atmosphere. Hence their measurement in both process studies and operationally are critical in the development and calibration of these models and therefore our understanding and operational awareness of ocean health. Further the outputs from such lower trophic levels can be used to force models predicting higher trophic levels from "primary producers to top predators" (Coll et al., 2020) under a range of climate and hence ocean chemistry change scenarios. Therefore, the measurement of ocean chemistry is critical to understanding the health and productivity (including fisheries and bioresources) of our oceans in a changing climate and in mitigating negative effects.

Ocean chemistry also has an impact on the marine environment's capacity to absorb CO_2 and act as a climate mitigating carbon sink (DeVries et al., 2019). Whilst the flux of CO_2 at the ocean surface is a physicochemical process (Woolf et al., 2019) this is modulated by the difference in ocean and atmospheric CO_2 concentration. This difference is affected by biogeochemical processes which are influenced by variations in nutrient, iron and other carbonate system chemical variables (Macovei et al., 2020) and is likewise modeled with ecosystem models (see above).

Elevated atmospheric, and therefore oceanic, CO_2 concentrations also cause ocean acidification (Doney et al., 2009). This reduction of pH, currently at a global average of about 0.002 pH units per year (Bates et al., 2014; Iida et al., 2021), occurs as CO_2 dissolves in the oceans to form carbonic acid (H_2CO_3), which readily dissociates to bicarbonate (HCO_3^-), carbonate (CO_3^{2-}), and H^+. "Impacts of unmitigated ocean acidification are estimated to represent a loss to the world economy of more than US $1 trillion annually by 2100" (Secretariat of the Convention on Biological Diversity, 2014). This includes for example reductions due to damage and critical endangerment of corals and calcifying invertebrates. Decreased pH also decreases the ability of the oceans to absorb more CO_2 and hence will accelerate climate change.

Harmful Algal Blooms (HABs) can have devastating impacts on both fisheries and aquaculture with single events resulting in export losses of $800M (Trainer et al., 2020) as well as significant effects on tourism and public health (Grattan et al., 2016). Whilst their prevalence is increasing with climate change, the role of ocean chemistry is complex. In many settings ocean stratification suppresses nutrient and micronutrient supply creating conditions where HABs can outcompete other phytoplankton. But also, when dominant HAB species do encounter elevated nutrients, for example due to coastal pollution, a population explosion or bloom can then lead to widespread negative impacts (Trainer et al., 2020). Regardless of these differing mechanisms, monitoring of nutrients is a useful tool for predicting and observing HAB occurrence and mitigating their impact.

Given the importance of ocean nutrient and carbonate system variables in multiple processes with large environmental, economic and societal impact, it is perhaps not surprising that the requirement for their measurement has been highlighted by the international ocean observing community. For example, the Framework for Ocean Observing (Tanhua et al., 2019) adopted by the Global Ocean Observing System (GOOS) lists macronutrients and carbonate system variables in the top three biogeochemical measurements in terms of impact and importance to this global effort. Beyond ocean environments there are also numerous applications for example in water industries and agriculture.

Despite the value of measurement of nutrient and carbonate system variables, their routine measurement is still dominated by sample collection and laboratory analysis with concomitant high cost, low spatial and temporal resolution, and risk of systematic error from contamination or degradation of samples. There has been considerable effort in both the academic community and in industry to develop nutrient and carbonate system sensors.

Optical (direct spectrophotometry of seawater) sensors (Finch et al., 1998; Johnson and Coletti, 2002) offer reagent free, high frequency and low energy per measurement data, are commercially available (e.g., SUNA v2, Seabird Scientific, United States), robust and deployable on the small platforms such as profiling floats (Johnson et al., 2010). Whilst they currently only measure nitrate operationally, they could also access nitrite (Wang et al., 2021) using spectral chemometrics and with the addition of acid titration can also measure [CO_3^{2-}] (Martz et al., 2009). However, they are prone to interference from overlapping absorption spectra of other natural water constituents, biofouling and calibration drift (Sakamoto et al., 2009; Wang et al., 2021) and are less accurate/precise (2 μM/0.3 μM; Suna V2, Seabird Scientific, United States) than traditional nutrient analysis (0.1/0.1 μM; Hydes et al., 2010; Becker et al., 2020).

Optode based *in situ* pH sensors have been developed by the Technical University Graz and PyroScience GmbH (Aachen, Germany) and these devices are now commercially available (PyroScience GmbH, Germany). They have accuracy in the order of 0.02 pH (Staudinger et al., 2018) and worst case drift 0.003 pH/day at 24 or 25°C, but undetectable at 10°C (Staudinger et al., 2018, 2019). The optodes consist of two essential components: a pH sensing material and the read-out module. The pH sensing material utilizes the pH-dependent fluorescence of an aza-BODIPY indicator dye (Klimant et al., 2001; Staudinger et al., 2018, 2019). The optodes have a low power consumption (∼1 mW at acquisition rate of one measurement point in 10 s) and have been demonstrated with a 2-month deployment (Fritzsche et al., 2018).

Electrochemical sensors for oceanic nutrients are not currently used for operational nutrient sensing because of metrology and robustness challenges (Wei et al., 2021). However, low limits of detection (6.1 nM) have been demonstrated in the lab for phosphate with plastic electrodes decorated with an alkyl Mo-polyoxometalate (Figueredo et al., 2021). Devices for silicate (Legrand et al., 2021) with limit of detection 0.32 μM have been deployed in shallow demonstrations and similar

devices for phosphate characterized in laboratory conditions (Barus et al., 2016).

Electrochemical sensors for pH (Shitashima et al., 2002; Martz et al., 2010; Easley and Byrne, 2012; Johnson et al., 2016; Briggs et al., 2017; McLaughlin et al., 2017; Gonski et al., 2018; Miller et al., 2018; Takeshita et al., 2018; Saba et al., 2019) are the most mature and widely used in operational oceanography. This is motivated by small size and robustness (Johnson et al., 2016), low power (e.g., 340–400 mW, SeaFET v2, Seabird Scientific, United States), fast response (<5 s, MSFET 3330, Microsens Switzerland) (Flohr et al., 2021), and good metrology performance (precision 0.004 pH, accuracy ± 0.05 pH, SeaFET v2, Seabird Scientific, United States). This has resulted in use on gliders (Saba et al., 2019; Takeshita et al., 2021) and profiling floats (Takeshita et al., 2018). However, a conditioning period when immersed in a new ionic concentration (4–5 days to settle to within 0.005 of spectrophotometric reference measurements; Saba et al., 2019), biofouling (in shallow warm waters on a glider offsets of < 0.2 pH were observed Saba et al., 2019), and sensor drift (0.003 pH/month, SeaFET v2) all affect performance. Solutions to these challenges include operation downstream of antifouling chemistry used in conductivity sensors (Takeshita et al., 2021), the presentation of *in situ* standards to the sensor (requiring fluidics) (Bresnahan et al., 2021) or calibration in stable waters, such as in the deep-sea (Johnson et al., 2017; Takeshita et al., 2018) the latter can achieve uncertainties of 0.005 ± 0.007 but adds additional operational constraints.

Electrochemical sensors for oceanic carbonate ion (Choi et al., 2002) and Total Alkalinity (Briggs et al., 2017) have also been developed but are yet to be demonstrated for *in situ* deployment.

Despite these advances there remains a requirement to improve nutrient and carbonate system metrology in sensors. Because of the superior metrology performance of reagent based analytical methods (Waterbury et al., 1996; Patey et al., 2008, 2010; Ma et al., 2014a; Nagul et al., 2015; Birchill et al., 2019; Takeshita et al., 2020), numerous sensors and analytical systems have been developed employing these techniques. This includes *in situ* deployed systems for Nitrate (Jannasch et al., 1994; David et al., 1998; Steimle et al., 2002; Adornato et al., 2007; Vuillemin et al., 2009; Yaqoob et al., 2012; Bodini et al., 2015), Phosphate (Adornato et al., 2007; Barnard et al., 2009; Moscetta et al., 2009; Ma et al., 2014b; Bodini et al., 2015; Yang et al., 2020), Iron (Chapin et al., 2002; Johnson et al., 2007; Huang et al., 2012; Meyer et al., 2012), and pH (Waterbury et al., 1996; Bellerby et al., 2002; Martz et al., 2003; Liu et al., 2006; Nakano et al., 2006; Wang et al., 2007, 2015; Seidel et al., 2008; Assmann et al., 2011; Spaulding et al., 2011; Lai et al., 2018). Some of these systems are commercially available (Hanson, 2000; Barnard et al., 2009; Spaulding et al., 2011; Bodini et al., 2015; Lai et al., 2018). However, previously there has not been widespread uptake of these technologies for operational oceanography because of perceived and actual barriers presented by: reliability (many moving parts); fragility; complexity of operation (such as reagent preparation and pre/post deployment protocols); device size, weight and power; and significant volumes of reagent consumption and waste production.

Microfluidics technologies (Nightingale et al., 2015; Mowlem et al., 2019) have been proposed as a solution to some of these barriers and there are examples in the literature of *in situ* systems targeting nutrients and carbonate. These include systems for nitrate (Beaton et al., 2012; Cogan et al., 2015; Nightingale et al., 2018, 2019), phosphate (Cleary et al., 2007; McGraw et al., 2007; Slater et al., 2010; Legiret et al., 2013; Clinton-Bailey et al., 2017; Grand et al., 2017), silicate (Cao et al., 2017), iron (Milani et al., 2015; Geißler et al., 2017), and pH (Rerolle et al., 2012, 2013; Pinto et al., 2019).

The advantages of microfluidics include integrated fluidic manifolds that reduce fluidic and electrical connectors (improving reliability and robustness) as well as complexity of operation: mixers, fluidic junctions and optical cells can be included in a continuous channel within the manifold. Similarly, this integration can reduce device size, weight and power. Whilst dispersion (Aris and Taylor, 1956) increases flushing volumes beyond the internal volume of the device, reagent consumption and waste production are dramatically reduced vs. macrofluidics [e.g., from 50 mL/sample (Barnard et al., 2009) to 0.3 mL/sample (Beaton et al., 2012) total waste]. Because volumes of reagents and waste are minimized, reagent cartridges (e.g., see also Barnard et al., 2009) can be extended to include capture of all waste from extended deployments.

It is the low sample consumption enjoyed by microfluidics, that enables use of relatively small inlet filters [e.g., 0.45-μm pore size Millex HP inline filter (Millipore, United States) (Beaton et al., 2012)]. In our experience, whilst the sensors may experience biofouling externally, the filters maintain operation without blocking. This enables superior biofouling resistance/robustness compared to other technologies. Filter blocking is only seen in very high turbidity settings (e.g., in the Maumee River Johengen et al., 2016) and then only rarely, and can be dealt with using larger or multiple filters, or more frequent changes.

Small fluidic consumption also enables regular measurement of onboard fluid standards and blanks which enables improved accuracy. In addition, microfluidics also enable inclusion of multiple sensing cells (e.g., colorimetric absorption channels of differing lengths) in a single device (Beaton et al., 2012; Clinton-Bailey et al., 2017; Geißler et al., 2017; Grand et al., 2017) which can be used to extend dynamic range and optimize limits of detection. Microfluidics also enable stable laminar/low Reynolds number flows with advantages in repeatable dosing and accelerated diffusive mixing over shorter diffusion length scales. Furthermore, dispersion (Aris and Taylor, 1956) can also be used to create time or length dependent titrations (e.g., Rerolle et al., 2013) and can smooth out the effects of flow rate variations in matched pumps that would otherwise couple directly into analytical signals.

However, the use of microfluidics does not, without additional engineering measures, fully address the barriers of complexity of operation and fragility/lack of robustness common to reagent-based systems. Key challenges remain in the production of reliable and matched microfluidic flow (rates) into analytical devices to avoid variable dilution of sample with reagents or incorrect assay dosing. This requires robust

and precision pump and fluidic manifold design together with well controlled valve backlash/elasticity (if valves are used). Similarly addressing complexity of operation also requires robust automation of setup, calibration, deployment, and post deployment calibration procedures.

An example of the use of microfluidics, coupled with the engineering measures to address use barriers (as above) is the *in situ* lab on chip (LOC) technology developed at the National Oceanography Centre (NOC), and the University of Southampton (Beaton et al., 2012; Rerolle et al., 2013; Clinton-Bailey et al., 2017; Geißler et al., 2017; Grand et al., 2017; Mowlem et al., 2018, 2019) and now produced under license by Clearwater Sensors Ltd.[1] a startup and industrial partner in bringing this technology to worldwide availability and further developing its potential.

The technology is capable of making accurate determinations of chemical and biological parameters that require reagents and that produce an electrical, absorbance, fluorescence is a subset of luminescence signal. As such it is suitable for a wide range of environmental measurements. Whilst further parameters are in development across this partnership, Nitrate, Nitrite, Phosphate, Silicate, Iron and pH sensors are currently available commercially.

Theses sensors use microfluidics (Mowlem et al., 2019) and optics (Mowlem et al., 2018) combined in an optofluidic chip with electromechanical valves and pumps mounted upon it to mix water samples with reagents and measure the optical response. Each type uses a different analytical chemistry method/assay to access a different variable, but these are all based upon certified or trusted existing gold standard laboratory methods. This enables intercomparison with existing data sets and speeds transition from sample-based measurements. All of the nutrient sensors as well as the iron sensor carry with them small volumes of standards and blanks allowing *in situ* calibration. The pH sensor instead uses a stable and laboratory characterized indicating dye obviating the need for *in situ* calibration. In all of the sensors, drift is virtually eliminated and service intervals extended to just short of the lifetime of the reagents used which can be many months, or years in cold climates or in the case of pH.

The hardware differences between the sensors are minimized as all of the assays for nutrients, iron and pH use colorimetry. The only differences between the variants are the fluidic layout of the chip, the optics (e.g., LED wavelength and absorption cell pathlengths) and minor electronics differences. The latter are minimized by using multiple Printed Circuit Boards (PCBs) with the main PCB containing the microprocessor and most of the functionality common to all systems. Only smaller daughter PCBs are specific to each variant. These accommodate small differences in components, layouts and functions. This use of common components enables improved robustness and reliability (through more extensive testing and focused design effort) in addition to economies of scale. An example of the robustness enabled is the depth rating of this technology: 6,000 m for all variants offered commercially.

[1] www.clearwatersensors.com

The technology has already been deployed by the NOC, and with their partners worldwide over 200 times including to depths of ∼4,800 m, in turbid estuaries and rivers, and for up to a year in seasonally ice-covered regions of the arctic. We briefly review some of those deployments as well as presenting new data and deployment information.

The public-private sector collaboration between the National Oceanography Centre, the University of Southampton, and the startup Clearwater Sensors Ltd. has been critical for making this technology available to the ocean observing, and wider water chemistry measurement customers/stakeholders. Without commercialization, this technology could only be produced in limited numbers and could only be deployed in collaboration. Because of the legal status of the public sector institutions, without commercialization the sensors could not be offered easily for commercial sale nor with indemnity or warranty. In addition, repetitive production of a consistent product is also at odds with research institutions remit for novelty and invention and there is a risk because of constant innovation, that the technologies developed would never be used at scale for the purpose they were developed.

In contrast commercial partnership enables: investment in productization and production, a focus on quality, engineering and testing to ensure compliance with regulations and standards (e.g., CE and ISO), customer support and documentation, warranties and services including calibration, servicing, reagent supply, installation support, communication, and data solutions. Investment can come from private funds, recycled sales income, or in limited circumstances grant funding. In the latter case some funds are only accessible if led by a company, and therefore would be inaccessible to public sector institutions without a commercial partnership.

Clearwater Sensors Ltd. has been founded by members of the Ocean Technology and Engineering Group at the National Oceanography Centre. The principal reasons for this arrangement were to ease knowledge transfer and upskilling of a commercial partner, and to reward/incentivize academic staff who could otherwise see this activity as a distraction from their core role. This has the effect of reducing the knowledge transfer burden on the public sector partners as well as shortening the time to market. It also enables the company to continue to improve the product and make innovations from a high knowledge base. To maximize the benefits for the overall partnership improvements made by the company can flow back to the public sector partners which benefits further research, and also minimizes divergence in the technology between the partners and duplication of effort. In addition, the public sector partners benefit from commercial success through license payments and other incentives for innovation (e.g., UKRI Research Excellence Framework). The public sector institutions now also have access to off the shelf products to include in research work that focuses on applications, whilst reserving their technology research and development effort for innovations and research rather tie it up with repetitive manufacture.

MATERIALS AND METHODS

In this section we give details of the technology and example deployments.

Technology

A photograph of sensor (in this case the silicate variant) with cable attached is shown in **Figure 1**. And with reagent cartridge disassembled in **Figure 2**. Fully assembled the sensor is 56 cm in height. The advantage of a reagent cartridge is that the operator does not need have the analytical chemistry experience or skills required to make up reagents, standards, or blanks. The reagent cartridge can be supplied as a unit to the user and spent cartridges can be returned to Clearwater Sensors Ltd. for safe disposal of waste and refilled for subsequent deployments. The use of wet mating fluidic connectors enables cartridges to be easily swapped in the field: simplifying and shortening field servicing. For some deployments (see below) a cartridge may not be suitable because of limited space in a vehicle for example, in which case individual flexible tube linked storage bags can be used and packed into available space.

The lower gray sensor's housing has the microfluidic chip as one of its endcaps. This arrangement minimizes the fluid connections and shortens the connection to the environment. This is advantageous for minimizing fluid consumption (because of a reduction in the flushing requirement which increases with long pipes due to dispersion) and also greatly reduces risks of failure and leaks. The outer surface of the microfluidic chip has fluidic connections for the input filter (typically 0.4 μm pore size), the corresponding wet mating fluidic ports used with the reagent cartridge, and connections for off chip components (for example the reduction column for the nitrate variant). It also hosts the wet mating electrical connector (SubConn MCBH8M, MacArtney UK Ltd.).

The chip itself is formed from three layers of stray, scattered and ambient light suppressing "tinted" polymethyl methacrylate (PMMA) with tint optimized to each assay and location of each layer (Floquet et al., 2011). Channels (typically 150 μm width) and features, including pockets for Light Emitting Diodes (LEDs), photodiodes, thermistors, waveguides, encapsulated fixing nuts, and seats for pumps valves and PCBs, hydraulic pressure compensation channels and mounting holes for electrical and fluidic connectors are formed in the PMMA by micro-milling prior to solvent mediated polishing and bonding (Ogilvie et al., 2010). An advantage of this arrangement is that including multiple absorption cells of differing lengths has little impact on chip cost or production times, and this greatly improves both the limits of detection (long cells, typically 25–80 mm long) and range of linearity (short cells, typically $<$ 1 mm long). Thus, a single chip can offer excellent metrology across wide concentration ranges with very simple and hence robust optical cells (LEDs and photodiode pairs). For example, the nitrate sensor variant has a limit of detection of 20 nM (0.28 mg/L as Nitrate) and a linear range to 1 μM (14 mg/L as Nitrate): a ratio of 1–50,000.

The sensor housing is formed from PVC, is watertight, oil filled and includes an elastomeric membrane/bellows to compensate for volume changes due to temperature and pressure variation. In this way the internals of the sensor are also at ambient (submerged) pressure and there is no differential pressure on the end cap. This cost-effective setup enables the polymer housing and chip/endcap to survive extreme ambient pressures of the deep sea (tested to 6,000 m). Polymers are also resistant to corrosion (including in high salt brines), are stable over environmental temperature and pH ranges. In addition, the inclusion of a compensating oil and bladder system enables mitigation of combined effects of pressure and temperature in both cold high-pressure deep-sea and warm low-pressure surface ocean environments. Prior to previous deployments (which are summarized in section "Applications and Deployments") this concept was tested within the temperature controlled hyperbaric facility at NOC (−10°C to +35°C, 0–70 MPa) and optimized.

On the inner surface of the chip are mounted valves (LFNA1250125H, Lee Co., United States) and bespoke syringe pumps with multiple pump barrels driven by a single sliding plate via a stepper motor. This arrangement ensures that the ratios of reagent to fluid analyzed (sample, standard, blank) remain fixed and with very low variability: otherwise for the nutrient and iron sensors any relative variation in pump flow rates couples directly into noise in the measurement by analyte dilution with reagent. The pump is controlled with position feedback.

Also mounted on the inside of the chip are the microprocessor and daughter PCBs. The microprocessor PCB is based on the low-power Microchip (previously Atmel) SAM4L utilizing an ARM Cortex-M4 chipset (Microchip, United States) and performs all logging and control scheduling functions. It controls the pumps and valves and interfaces with the daughter boards which have variant specific combinations of LED drivers, analog electronics (for photodiodes and thermistors for on chip temperature measurement) and analog to digital conversion (16 bit). The electronics store all raw data (flash memory card) and can stream processed data when deployed over RS232 via the electrical connector (SubConn MCBH8M, MacArtney UK Ltd.). The latter enables connection to ocean vehicle/observing platforms or communication systems for near real time data relay. Clearwater Sensors Ltd also offer GSM and other communication solutions/hardware. A key feature of the electronics is their specification to work in oil at ambient pressure (tested to 6,000 m) and hence they do not need protecting in a pressure case. This has cost, weight and robustness advantages.

The sensors do not have an internal battery other than a small reserve to preserve the operation of the real time clock. The external power required is 12 v (10–16 v) and a typical power consumption of 1.8 W. Each measurement typically consumes ∼500 J and hence a deployment with 2,000 measurements of samples and/or calibration materials requires 1,000 kJ (∼23 Ah) battery capacity at operation temperature. Such batteries are widely available including in deep-sea rated versions.

The sensors are setup and programmed via a Microsoft Windows Graphical User Interface application that enables the user to pick and adjust a range or predefined schedules or to specify when the sensor is quiescent, sampling, flushing or making standard and blank measurements. These "states" can also be triggered via the RS232 interface and the GUI enables

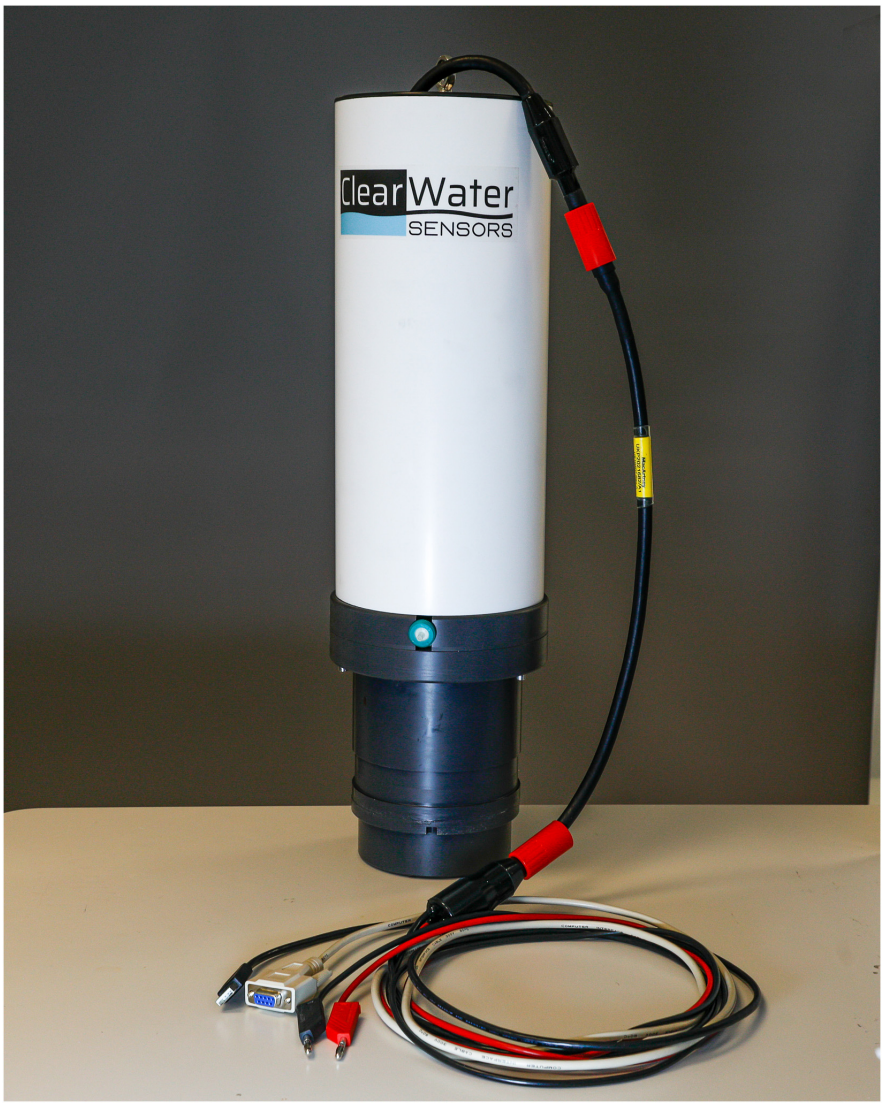

FIGURE 1 | Photograph of a silicate sensor (Clearwater Sensors Ltd., total height 56 cm) connected to a deployment cable which is then connected to a lab cable for connection to a bench power supply and PC for testing/calibration. The USB connection is used for setup and download of raw data, while RS232 can provide real time processed data in the field. The upper part including a larger gray collar and white tube is a reagent cartridge containing standards, blanks, reagents and waste storage capacity (all waste is captured). The lower gray cylindrical part houses the microfluidics, optics, pumps, valves and electronics (the sensor itself).

this to be setup, e.g., to respond to environmental conditions or external communications. In this way the sensors can form part of a smart sensing network.

Variants and Assays Used

Table 1 summarizes the assays used, power requirements and performance for each currently commercially available variant. In all cases the commercial versions of the instruments are developed from the research devices in the published literature and from the public sector partners know how. Changes include reduced diameter of the chip to match stock tube internal diameter of 4" (101.6 mm, from 119 mm) to aid manufacture and reduce waste (swarf) in housing production, a rework of the electronics to replace legacy/obsolete components, improved positioning and conformal coating of the electronics to enhance robustness, new valve component ported for better response to dynamic pressure changes and oil filling, new valve electrical connection.

The nitrate and nitrite sensor developed from Beaton et al. (2012, 2017b), Yuecel et al. (2015), and Vincent et al. (2018) uses the Greiss assay which detects nitrite by diazotization with sulphanilamide and subsequent coupling with N-(1-naphthyl)-ethylenediamine dihydrochloride (NED) to form an intensely colored azo dye. Nitrate is reduced to nitrite using a copperised cadmium column in the presence of an imidazole buffer. To aid safety and recyclability this is formed from a solid cadmium/copper tube that is processed to reduce internal volume and encapsulated in epoxy resin. It is attached to the chip

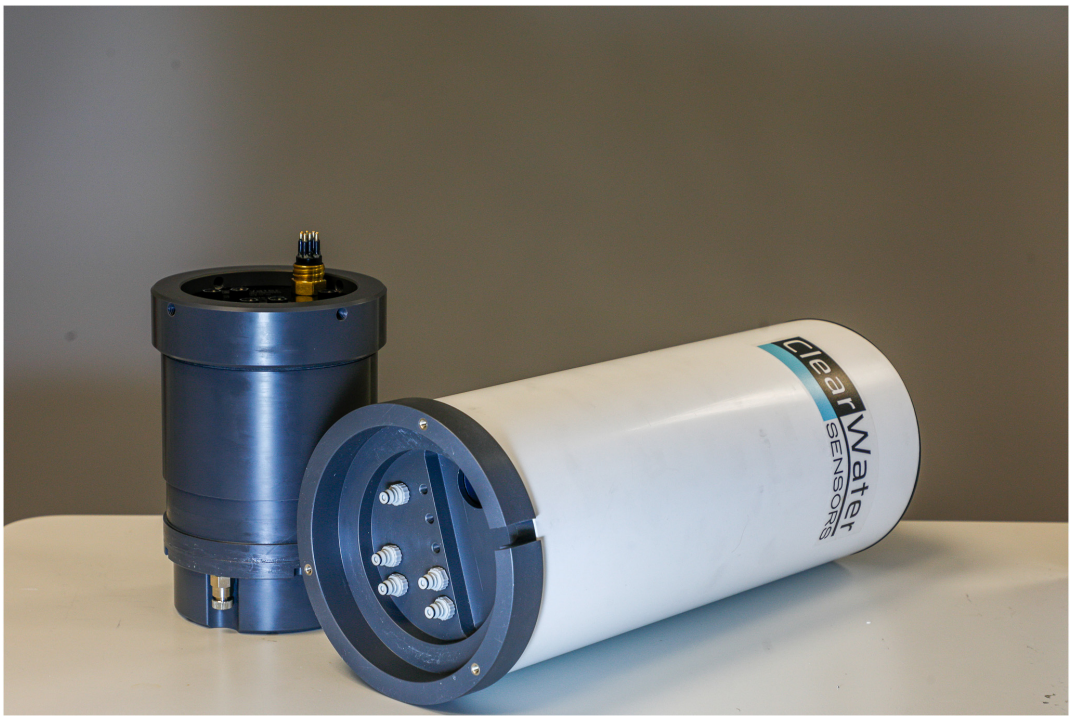

FIGURE 2 | Photograph of a silicate sensor (Clearwater Sensors Ltd.) shown with reagent cartridge (white) separated from the sensor (gray).

via connecting tubes on the outside face and can therefore be removed for recycling (e.g., returned to Clearwater Sensors Ltd.). The encapsulation ensures users do not come into contact with the cadmium and concentrations of this metal in the waste are low, and all of the waste is retained and is returned together with the depleted cartridge.

The phosphate sensor, developed from Clinton-Bailey et al. (2017); Grand et al. (2017), and Birchill et al., 2019) utilizes a modified molybdenum blue assay which in its standard form (Nagul et al., 2015) is used widely to determine an operationally defined Soluble Reactive Phosphorus (SRP) frequently referred to in the literature as PO_4^{3-} by convention. Key adaptations for *in situ* use include proprietary catalyst and surfactants able to work over the full operational temperature and salinity ranges. In contrast to the previous published literature, this improved assay enables accurate determinations below 5°C.

TABLE 1 | Summary of LOC sensor variants assays used and performance.

LOC sensor variant	Analytical method/assay	LOD/precision*	Max power/energy per measurement
Nitrate + nitrite	Griess assay (with Cd reduction)	20 nM	1.8 W, 500 J
Phosphate	Molybdenum blue (modified)	40 nM	1.8 W, 500 J
Iron (II), Iron (III)	Ferrozine [with ascorbic acid reduction for Fe (III)]	<20 nM	1.8 W, 500 J
Silicate	Silicomolybdic acid	0.75 μM	1.8 W, 500 J
pH	Spectrophotometry using purified *meta*-Cresol Purple	*0.001 pH	3 W, 1300 J

**denotes precision (rather than limit of detection).*

The silicate sensor uses a novel proprietary formulation based on the standard assay (see segmented flow analyser method in Birchill et al., 2019) which is based on the formation of silicomolybdic acid by reaction with ammonium molybdate tetrahydrate in an acidic solution including sulphuric and oxalic acids as well as surfactants and stabilizing agents. Optimisation of the assay has focused on performance over a wide range of environmental conditions including minimizing interference from phosphate.

The iron sensor developed from Geißler et al. (2017) uses an assay with a buffered ferrozine solution and a ferrozine/ascorbic acid mixture for Fe(II) and labile Fe(III) analyses, respectively. The commercial version of this sensor employs both an acidification step and a longer assay development (wait) time in the protocol as suggested in Milani et al. (2015); Geißler et al. (2017) which as anticipated resolves the low and variable recovery of DFe [Fe(II)+Fe(III)] they encountered without these modifications.

The pH sensor developed from Rerolle et al. (2013, 2018) has been fully implemented in the common lab on chip platform, including the use of on chip mounted LEDs and the 6,000 m rated infrastructure. The device uses a spectrophotometric assay using purified *meta*-Cresol Purple. Unlike all the other assays above, pH determination does not use *in situ* calibration using standards

and blanks, nor does it use stopped flow analysis to allow time for reaction in an axially homogenous sample contained in an absorption cell. Instead pH is determined in continuous flow where a range of indicator dye concentrations are produced as a function of time through dispersion of an injected slug of dye upstream of the optical cell. The dye response at a range of concentrations is measured at two wavelengths corresponding approximately to the absorbance maxima of the protonated and unprotonated forms of the dye. The pH is a function of the ratio of these absorbances, but to achieve high accuracy the measured ratio of a purified and standardized dye is corrected for (a) the effects of perturbation in pH by the presence of the dye; and (b) the mismatch of the optics (ideal 578 nm vs. 590 nm in the device). The former is achieved by regressing *in situ* data at a range of dye concentrations back to the y intercept (zero dye) whilst the latter is corrected by laboratory calibration at a range of temperatures using high accuracy TRIS/HCl buffers. A correction is also required if the detection in the optical cell is at a different temperature to ambient. The effect of these corrections is to improve accuracy to better than 0.006 pH units at pH 8.5 with no temperature difference ($\leq$0.009 pH units with typical temperature differences) for example. This compares to a stated accuracy of 0.050 pH units for best in class commercial ISFET based pH sensors. In addition, the drift of the spectrophotometric method is negligible.

Deployments

The sensors have been deployed over 200 times by the NOC. This has enabled the sensors to reach Technology Readiness Level 7 (TRL 7, see ISO 16290:2013) *prior* to commercialization through real world fault finding and robust engineering response over many years.

Because of strong user demand as well as excellent metrology performance with certified or widely accepted assays, robustness, depth capability, low power, small size, low reagent consumption, low (and fully captured) waste, long duration, ease of integration and ease of use; the sensors have also been deployed widely in applications delivering data for science and stakeholders. Examples are given in section "Results."

Integration is enabled either by simple mechanical integration (e.g., with brackets) and connection to a battery/power source or by utilizing the power and communications (RS 232) interface provided. For the latter a command set enables external control and triggering of pre-programmed states as well as either platform driven (polled) or sensor-initiated transfer of data.

For the first of the deployments detailed in this paper, the nitrate analyser was deployed at an Environment Agency gauging station on the River Avon (Hampshire, United Kingdom), between 15th October 2014 and 15th October 2015. It collected hourly nitrate data (subject to some short gaps) for the entire year. Data was telemetered in real time via a YSI Storm logger. The sensor was visited every 3 months in order that the reagents and onboard standard could be changed, the waste bag emptied, and the inlet filter changed. The analyser and the cadmium reduction tube were not changed for the entire year.

The accuracy of the nitrate analyser is dependent on the stability of the onboard calibration standard. In this case, the onboard standard (300 μM) was preserved using 0.1% chloroform. Subsamples of the standard were analyzed before and after each deployment, and no evidence of degradation was found over the duration of the deployment. Co-samples were collected by the Environment Agency, and as part of the Macronutrient Cycles program (Panton et al., 2020).

For the second example data set a nitrate and phosphate sensor were deployed at approximately 1 m depth off a pontoon in Empress Dock, Southampton United Kingdom in December 2016. No manual sampling or reference measurement were made: the sensors were simply deployed following analysis of the onboard standards and blanks which provide *in situ* calibration.

For both deployments A YSI EXO2 sonde was deployed alongside nutrient sensors to collect temperature and salinity data.

RESULTS

Applications and Deployments

We summarize here some of the over two hundred deployments undertaken with the *in situ* chemical sensor technology described above.

Thirty-three LOC sensors were deployed in total measuring Dissolved Inorganic Carbon (DIC), Total Alkalinity (TA), pH, nitrate and phosphate on a variety of platforms/vehicles throughout the STEMM-CCS experiment (Research expedition JC180 in particular) (Flohr et al., 2021). This ambitious but successful experiment demonstrated the ability to monitor and quantify the integrity of offshore Carbon Capture and Storage (CCS) reservoirs through detecting and measuring the chemical signature of a simulated (but in operation extremely unlikely) leak. A leak was simulated by injecting a known volume of CO_2 into the sediments at a depth of $\sim$3 m in the region of the proposed Goldeneye CCS reservoir (Dean and Tucker, 2017), a depleted field offshore from Scotland in the Outer Moray Firth (North Sea). LOC sensors made measurements at various locations around the site of CO_2 release to both determine the spatial extent of the releases impact and quantify the release. Sensors were fully integrated with the ROV Isis (German et al., 2003) and benthic landers. These were deployed to measure baseline chemical characteristics and also to quantify the volume of CO_2 released. For example, the pH sensors were used to quantify vertical gradients in pH upstream and downstream of the benthic release and in combination with hydrodynamic measurements to calculate CO_2 flux (Schaap et al., 2021). The ability to detect a leak at very low release rates was demonstrated (14 kg/day) well below the suggested 0.01%/year of stored gas proposed in the literature (Hepple and Benson, 2005) which would equate to 274–5,480 kg/day in year 1 and after 20 years of injection, respectively, for this site (Flohr et al., 2021).

The sensors have been deployed on some of the smallest and lowest power platforms used in oceanography including on profiling floats as part of the SenseOcean project (614141, FP7, EU) where profiles of nutrients were obtained in the Mediterranean. They have also been deployed on ocean gliders numerous times including nitrate sensing on a Kongsberg

Seaglider (Vincent et al., 2018) where the sensor was fully integrated with the glider electronics allowing command and data transfer and enabling nitrate data to be transmitted to shore via the glider's communication capability. There was "excellent agreement between the LOC and shipboard nitrate + nitrite measurements (r^2 = 0.98, n = 11)" and the sensor data revealed nitrate uptake due to phytoplankton spring bloom. The combination of sensor and glider enabled accurate data at high resolution, on both spatial and temporal scales. A phosphate sensor has been integrated with a Seaglider as part of the AlterEco project (NE/P013899/1, NERC, United Kingdom) completing a 120 km transect in North Sea in 44 days observing reduction in surface concentrations and variations in the bottom mixed layer (Birchill et al., 2021). A pH sensor was also integrated into a Seaglider (iRobot/Kongsberg, part of the UEA fleet, United Kingdom) and used in the North Sea for 10 days together with O_2 and salinity data to derive CO_2 content air sea fluxes of oxygen and CO_2 demonstrating high spatial and temporal resolution (Possenti et al., 2021). The sensor platform has also been integrated with a Slocum glider (Teledyne Webb, United States) and demonstrated (with a nitrate sensor) as part of the project AutoNuts (NE/P020798/1, NERC, United Kingdom).

The sensors have also been deployed by scientists external to the Ocean Technology and Engineering Group at NOC who developed them. For example, a silicate and nitrate sensor were deployed for a year on a mooring at the site of the US NSF funded Ocean Observatories Initiative (OOI) Southern Ocean Array for over a year and returned excellent data funded by the CUSTARD project (NE/P021247/2, NERC, United Kingdom). In another deployment, a nitrate + nitrite and a separate nitrite sensor were deployed in the Mauritanian oxygen minimum zone, offshore Western Africa (Yuecel et al., 2015). Here sensor data augmented with oxygen and physical data enable observation of cross-shelf transport contributing to the understanding of the benthic biogeochemical dynamics.

Sensors have also been deployed at physical and geographical extremes including: to depths of ∼4,800 m [nitrate (Stinchcombe, 2017), phosphate (Ruhl, 2018), Total Alkalinity and pH (Hartman, 2019)] at the Porcupine Abyssal Plain Sustained Observatory (PAP-SO, 49N 16.5W) in the north-west Atlantic Ocean, in ice littered and sediment laden pro-glacial melt waters (Beaton et al., 2017b) as well as in rivers and estuaries (see example data).

A promising recent development is the integration of large numbers of sensors in medium sized autonomous underwater vehicles and their use in autonomous surface vehicles. For example, the OCEANIDS project (Industrial Strategy Challenge Fund, BEIS, United Kingdom) and the allied sensors projects AutoNuts (NE/P020798/1, NERC, United Kingdom) and CarCASS (NE/P02081X/1, NERC, United Kingdom) have enabled the integration of 9 different lab on chip sensors [DIC, TA, pH, nitrate, nitrite, phosphate, silicate, iron (Ferrozine method), trace iron (luminol method)] into the Autosub Long Range (ALR) platform (Furlong et al., 2012; Roper et al., 2017; Salavasidis et al., 2019) as well as up to two sensors at a time (including a new ammonia LOC sensor) into a Waveglider SV3 (Liquid Robotics, United States). Such capability opens the possibility of measuring all the major inorganic chemical variables in biogeochemical models over wide spatial and temporal scales from the surface to the deep ocean at a fraction of the cost and carbon expenditure of traditional ship-based sampling and laboratory analysis-based monitoring.

Example Data

A subset of the nitrate data returned from the LOC nitrate sensor deployed at the Environment Agency gauging station on the Hampshire Avon in 2014/15 is shown in **Figure 3**. The nitrate sensor data (top panel, blue line) shows excellent correlation with traditional manual and laboratory analyzed samples (red discs). The differing frequency of these two data sets demonstrates the advantage of a sensor in returning high temporal resolution data with reduced logistical effort (∼3 monthly site visits). The consistency of the sensor data also shows there is no loss in accuracy before or after replenishment of reagents (approximately at the same time as manual samples in end December, end February and early June). Operation in water at 500 μS/cm conductivity underlines the ability of the sensor and assay to work across a wide salinity range. Whilst there are common features and timing of dilution events in both the nitrate and conductivity data, there is not a direct correlation across the data set. For example, nitrate levels are supressed more than conductivity in the months at the beginning and the end of the dataset. There are also periods of a pronounced diurnal signal (in April particularly) in the nitrate data which are not present in the conductivity data. This difference is not simply explained by discharge/river flow emphasizing the utility of chemical sensors in greater understanding of biogeochemical fluxes, processes and concentrations within a river catchment.

Example data from nitrate and phosphate sensors deployed in Empress Dock in 2016 is show in **Figure 4**. The top panel with blue line shows the nitrate concentration recorded by a LOC sensor whilst the middle and bottom panels show LOC phosphate and EXO2 derived salinity, respectively. There is no manual seawater sampling in this data set, the sensors were simply deployed following analysis of the onboard standards and blanks which provide *in situ* calibration. Best practice is to measure sensor performance against a nutrient reference material or measure sample(s) of the standard solutions analyzed against reference materials in accordance with recommendations by SCOR working group 147.[2] Data from previous deployments (e.g., above) has underlined confidence that analysis of the standards and blanks is sufficient to assure the accuracy of the data produced. The data show an approximate inverse relationship between salinity and both nitrate and phosphate which illustrates dilution of high concentration freshwater inputs with lower concentration sea water in the estuarine setting. However, there are significant deviations from a direct correlation between nutrients and salinity, with nitrate and phosphate showing different features. Sources of these differences will include differing benthic fluxes, temporal variation in both

[2]https://scor-int.org/group/147/

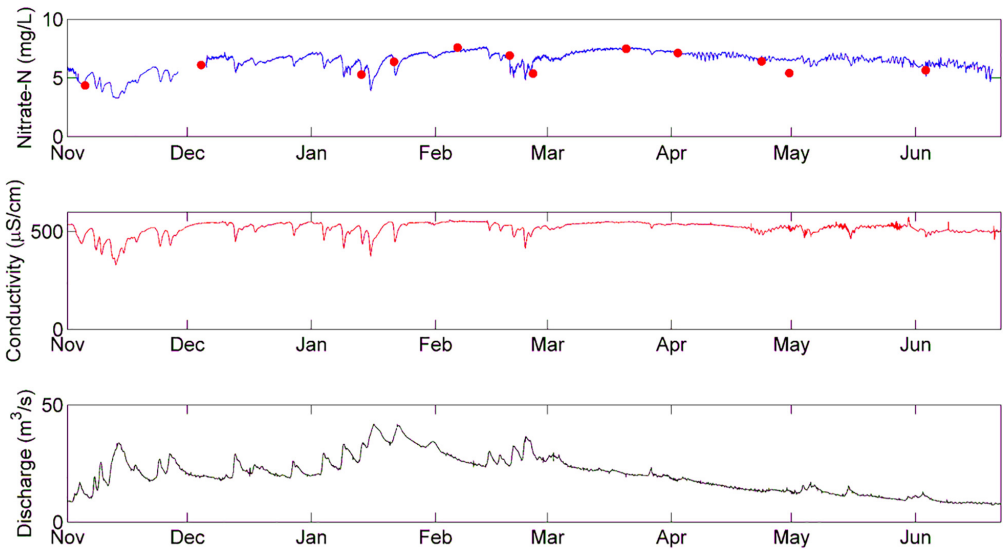

FIGURE 3 | A ∼7.5 month subset of a year-long data series (Nov 2014–late June 215) from the deployment of a Lab On Chip nitrate sensor, and reference physical sensors at an Environment Agency gauging station on the Hampshire Avon. Data sourced from BODC archive (Beaton et al., 2017a). Top panel shows sensor nitrate timeseries (blue line) and discrete spot samples (red discs). The middle and bottom panels show conductivity and river discharge timeseries, respectively.

river and seawater inputs and local inputs of nutrients, e.g., from direct rainwater/waste water inputs in the region as well as directly into Empress Dock.

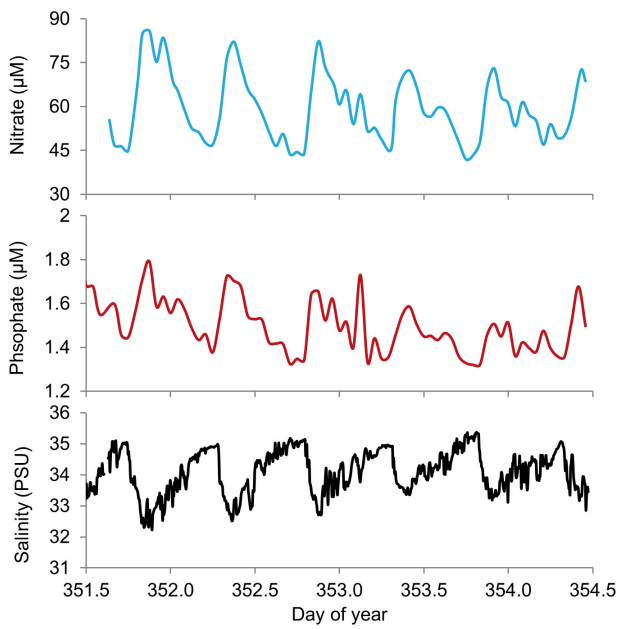

FIGURE 4 | A 3 day timeseries of sensor nitrate and phosphate together with salinity (EXO2, YSI, United States) from deployment in Empress Dock, Southampton, United Kingdom in December 2016. The top panel with blue line shows the nitrate concentration recorded by a LOC sensor whilst the middle and bottom panels show LOC phosphate and EXO2 derived salinity, respectively.

DISCUSSION

The principal findings from this work are that with sufficient attention to robustness, and extensive testing and feedback into design, reagent-based sensors can progress the Technology Readiness Level scale to proven commercial products (TRL 9) and can deliver unique high spatial and temporal resolution data sets from our oceans and seas. This is also possible in the deep-sea and in inhospitable environments such as high turbidity and low (icing) temperatures. Further the use of microfluidics allows processing of low (hundreds of microliters to 2 mL) of sample, and smaller volumes of reagent per sample enabling all waste to be captured even for deployments of months to years. Despite the narrow channels used in the sensors (typically 150 mm × 300 mm) biofouling has not been seen to impact the quality of the data produced. If this were encountered in the future, the inlet filter is the vulnerable element, with clogging and a change in the chemical environment (e.g., nutrient uptake, respiration/photosynthesis and change of $[CO_2]$/pH) possible. However, because of the ability to automate variations to the fluid flow within the chip it is possible to backflush and even clean the filter *in situ* should this be an issue. In many settings the sensor is regularly (e.g., ∼3 months in the example data from the Hampshire Avon, **Figure 3**.) retrieved and reagents replaced and a conservative approach is to replace the inlet filter at this time. However, it should be noted that operations producing long datasets where this measure is not possible (e.g., the CUSTARD mooring deployment of nutrient sensors for > 12 months as reported in section "Results" above) have not shown vulnerability to fouling.

For many oceanographic applications the combination of a small, low power sensor and an autonomous vehicle presents a cost effective method for large spatial and temporal scale

data collection. This approach can enable high spatial and temporal biogeochemical data acquisition, alongside existing physical sensing on the host vehicle. A promising approach, for minimizing both the cost of deployment and also carbon emissions from operations, is to remove the requirement of a research ship to make sensor deployments by hosting the sensors on a shore or small/coastal boat launched vehicle. As has been reviewed above, the LOC chemical sensors have been successfully integrated into various ocean gliders, surface vehicles and even a profiling float. A powerful capability is generated by the use of multiple sensors in a shore launched autonomous vehicle, such as Autosub Long Range (see above) where it is possible to include sensors for all of the chemical variables represented in biogeochemical models. As has been demonstrated in the STEMM-CCS project such chemical sensing can also be used for verification of offshore CCS reservoir integrity. The ability to do surveys for this purpose with shore launched autonomy is a powerful tool in reducing the cost and carbon footprint of reservoir monitoring which would otherwise reduce the carbon storage and cost efficiency of this approach.

An advantage of the deployment of chemical sensors, and the upscaling in spatial and temporal resolution of the data is that events, patches and transitions in biogeochemistry can be observed at greater detail. Without high frequency data, features such as diurnal and tidal signals in estuarine environments (e.g., **Figure 4**) would be missed entirely by daily or weekly sampling. Events such as pollution events, storm water runoff, or progression of planktonic blooms can also be captured and observed in near real time (e.g., using communication systems such as the in the Hampshire Avon and Seaglider deployments above) enabling redirection of monitoring effort or management response (e.g., harvesting in aquaculture).

Reagent based sensors, particularly those with *in situ* calibration, offer superior performance (particularly accuracy and limits of detection) when compared to existing optical (e.g., nitrate sensors based on reagent-less UV spectrophotometry; Finch et al., 1998; Johnson and Coletti, 2002) and electrochemical sensors (e.g., Johnson et al., 2016; Briggs et al., 2017; McLaughlin et al., 2017; Gonski et al., 2018; Takeshita et al., 2018). However, the *in situ* calibration of electrochemical sensors is a promising advancement for improved accuracy (Bresnahan et al., 2021) if somewhat at the expense of complexity. A key advantage of reagent-based sensors remains the ability to use certified, or widely accepted assays, and to access the majority of chemical variables required by users and stakeholders.

Research currently underway to continue to extend the capability of the LOC technology includes: further reductions in power and reagent/sample consumption, modifications to enable faster measurements. The current sensors report a value in 3–10 min depending on the assay. Simple multiplexing (Ogilvie et al., 2011) has been demonstrated as a possible solution and is being developed for *in situ* deployment. An alternative is to combine the accuracy of the reagent-based sensors with faster, but less accurate (e.g., electrochemical pH) sensors and using data fusion produce both a high resolution and accurate dataset. This approach is in active development as part of the CarCASS project for example.

The ability to manipulate fluids and observe electrical and optical responses can also be used for biological detection such as cytometry (Benazzi et al., 2007; Barat et al., 2012) of phytoplankton or molecular analysis of organisms or biomolecules (Loukas et al., 2017; Walker et al., 2017). Whilst each new assay presents its own challenges (such as the lifetime of molecular assay reagents Loukas et al., 2017) the use of microfluidics is attractive for enabling higher spatial and temporal resolution data for these variables also.

Partnership with a company enables the capability of this technology to reach a wider audience/user group and ensures its continued improvement and progression to high Technology Readiness Levels. In addition, partnership unloads research teams from the burden of routine manufacture, enables additional investment and innovation funding, and provides mechanisms to incentivise and reward further exploitation and innovation. By including the inventing team in commercial partnerships the benefits include improved knowledge transfer and reduced time to market. However, this requires careful navigation of conflicts of interest but this is possible if given due time and attention.

DATA AVAILABILITY STATEMENT

Data are from Beaton et al. (2017a).

AUTHOR CONTRIBUTIONS

MM and AB wrote the first draft of the manuscript. AS and AB produced **Figures 4**, **3**, respectively. RP provided photographs used in **Figures 1**, **2**. SL provided expertise and edited sections on carbonate variables. SM, AB, CC, and RP produced the commercial version of the sensors shown in **Figures 1**, **2**. AM provided advise and edited sections on commercial partnership. All authors contributed to editing and writing of the manuscript.

FUNDING

The development, deployment and commercialization of this technology has been funded in part by: UK Natural Environmental Research through grants NE/P013902/1; NE/P020798/1; NE/P02081X/1; NE/P021247/2; NE/M021858/1; NE/J011975/1; NE/J007129/1; NE/I012974/1; NE/H001328/1; 4D Biogeochemical Sensors, NERC, Oceans2025, theme 8.1. EPSCR through grant EP/E016774/1. Industrial Strategy Challenge Fund, BEIS, UK through the OCEANIDS project. Funding from the European Union's Horizon 2020 Research and Innovation Programme under grant agreement no. 101000858 (TechOceanS). Funding provided by the European Union's Horizon 2020 Research and Innovation Programme under the grant agreement no. 654462 (STEMM-CCS). Funding provided by the European Union's Horizon 2020 Research and Innovation Programme under the

grant agreement no. 635359 (BRIDGES). Funding provided by the European Union's Horizon 2020 Research and Innovation Programme under the grant agreement no. 633211 (AtlantOS). Funding from the European Union Seventh Framework Program (FP7/2007-2013) under grant agreement no. 614141 (SenseOCEAN). Funding from the European Union Seventh Framework Program (FP7/2007-2013) under grant agreement no. 237868 (SENSEnet). Funding from innovate UK (UKRI) project 53925 "Assuring water quality : a new generation of miniaturised microfluidic chemical analysers".

ACKNOWLEDGMENTS

We would like to acknowledge the support of the Ocean Technology and Engineering Group and the Marine Autonomous and Robotic Systems group at the National Oceanography Centre as well as the wider teams at NOC, Clearwater Sensors Ltd. and associated project partners worldwide for their support in developing and deploying and applying the technology described in this paper.

REFERENCES

Adornato, L. R., Kaltenbacher, E. A., Greenhow, D. R., and Byrne, R. H. (2007). High-resolution *In situ* analysis of nitrate and phosphate in the oligotrophic ocean. *Environ. Sci. Technol.* 41, 4045–4052. doi: 10.1021/es0700855

Aris, R., and Taylor, G. I. (1956). On the dispersion of a solute in a fluid flowing through a tube. *Proc. R. Soc. Lond. A Math. Phys. Sci.* 235, 67–77. doi: 10.1098/rspa.1956.0065

Assmann, S., Frank, C., and Kortzinger, A. (2011). Spectrophotometric high-precision seawater pH determination for use in underway measuring systems. *Ocean Sci.* 7, 597–607. doi: 10.5194/os-7-597-2011

Barat, D., Spencer, D., Benazzi, G., Mowlem, M. C., and Morgan, H. (2012). Simultaneous high speed optical and impedance analysis of single particles with a microfluidic cytometer. *Lab Chip* 12, 118–126. doi: 10.1039/c1lc20785g

Barnard, A. H., Rhoades, B., Wetzel, C., Derr, A., Zaneveld, J. R. V., Moore, C., et al. (2009). "Real-time and long-term monitoring of phosphate using the *in-situ* CYCLE sensor," in *Proceedings of the Oceans 2009*, Vol. 1-3, (Biloxi, MS: IEEE), 1698–1703.

Barus, C., Romanytsia, I., Striebig, N., and Garcon, V. (2016). Toward an *In situ* phosphate sensor in seawater using Square Wave Voltammetry. *Talanta* 160, 417–424. doi: 10.1016/j.talanta.2016.07.057

Bates, N. R., Yrene, M. A., Kim, C., John, E. D., Melchor, G.-D., Laura, L., et al. (2014). A time-series view of changing ocean chemistry due to ocean uptake of anthropogenic CO_2 and ocean acidification. *Oceanography* 27, 126–141.

Beaton, A. D., Cardwell, C. L., Thomas, R. S., Sieben, V. J., Legiret, F.-E., Waugh, E. M., et al. (2012). Lab-on-chip measurement of nitrate and nitrite for *In situ* analysis of natural waters. *Environ. Sci. Technol.* 46, 9548–9556. doi: 10.1021/es300419u

Beaton, A. D., Mowlem, M., Purdie, D. A., Panton, A., and Owsianka, D. R. (2017a). *Nitrate and Nitrite Data from a National Oceanography Centre (NOC) Lab-on-Chip (LOC) Analyser at Knapp Mill.* Hampshire Avon: British Oceanographic Data Centre - Natural Environment Research Council U.K.

Beaton, A. D., Wadham, J. L., Hawkings, J., Bagshaw, E. A., Lamarche-Gagnon, G., Mowlem, M. C., et al. (2017b). High-resolution *In situ* measurement of nitrate in runoff from the Greenland ice sheet. *Environ. Sci. Technol.* 51, 12518–12527. doi: 10.1021/acs.est.7b03121

Becker, S., Aoyama, M., Woodward, E. M. S., Bakker, K., Coverly, S., Mahaffey, C., et al. (2020). GO-SHIP repeat hydrography nutrient manual: the precise and accurate determination of dissolved inorganic nutrients in seawater, using continuous flow analysis methods. *Front. Mar. Sci.* 7:581790. doi: 10.3389/fmars.2020.581790

Bellerby, R. G. J., Olsen, A., Johannessen, T., and Croot, P. (2002). A high precision spectrophotometric method for on-line shipboard seawater pH measurements: the automated marine pH sensor (AMpS). *Talanta* 56, 61–69. doi: 10.1016/s0039-9140(01)00541-0

Benazzi, G., Holmes, D., Sun, T., Mowlem, M. C., and Morgan, H. (2007). Discrimination and analysis of phytoplankton using a microfluidic cytometer. *IET Nanobiotechnol.* 1, 94–101. doi: 10.1049/iet-nbt:20070020

Birchill, A. J., Beaton, A. D., Hull, T., Kaiser, J., Mowlem, M., Pascal, R., et al. (2021). Exploring ocean biogeochemistry using a lab-on-chip phosphate analyser on an underwater glider. *Front. Mar. Sci.* 8:698102. doi: 10.3389/fmars.2021.698102

Birchill, A. J., Clinton-Bailey, G., Hanz, R., Mawji, E., Cariou, T., White, C., et al. (2019). Realistic measurement uncertainties for marine macronutrient measurements conducted using gas segmented flow and Lab-on-Chip techniques. *Talanta* 200, 228–235. doi: 10.1016/j.talanta.2019.03.032

Bodini, S., Sanfilippo, L., Savino, E., Moscetta, P., and IEEE. (2015). *Automated Micro Loop Flow Reactor Technology to Measure Nutrients in Coastal Water: State of the Art and Field Application*. New York, NY: IEEE.

Bresnahan, P. J., Takeshita, Y., Wirth, T., Martz, T. R., Cyronak, T., Albright, R., et al. (2021). Autonomous *In situ* calibration of ion-sensitive field effect transistor pH sensors. *Limnol. Oceanogr. Methods* 19, 132–144. doi: 10.1002/lom3.10410

Briggs, E. M., Sandoval, S., Erten, A., Takeshita, Y., Kummel, A. C., and Martz, T. R. (2017). Solid state sensor for simultaneous measurement of total alkalinity and pH of seawater. *ACS Sens.* 2, 1302–1309. doi: 10.1021/acssensors.7b00305

Butenschoen, M., Clark, J., Aldridge, J. N., Allen, J. I., Artioli, Y., Blackford, J., et al. (2016). ERSEM 15.06: a generic model for marine biogeochemistry and the ecosystem dynamics of the lower trophic levels. *Geosci. Model Dev.* 9, 1293–1339. doi: 10.5194/gmd-9-1293-2016

Cao, X., Zhang, S. W., Chu, D. Z., Wu, N., Ma, H. K., and Liu, Y. (2017). "A design of spectrophotometric microfluidic chip sensor for analyzing silicate in seawater," in *Proceedings of the 3rd International Conference on Water Resource and Environment*, ed. P. Li (Quingdao: IOP Publishing Ltd).

Chapin, T. P., Jannasch, H. W., and Johnson, K. S. (2002). *In situ* osmotic analyzer for the year-long continuous determination of Fe in hydrothermal systems. *Anal. Chim. Acta* 463, 265–274. doi: 10.1016/s0003-2670(02)00423-3

Choi, Y. S., Lvova, L., Shin, J. H., Oh, S. H., Lee, C. S., Kim, B. H., et al. (2002). Determination of oceanic carbon dioxide using a carbonate-selective electrode. *Anal. Chem.* 74, 2435–2440. doi: 10.1021/ac0108459

Cleary, J., Slater, C., Diamond, D., and IEEE. (2007). "Field-deployable microfluidic sensor for phosphate in natural waters," in *Proceedings of the 2007 IEEE Sensors*, Vol. 1-3, (New York, NY: IEEE), 1001–1004.

Clinton-Bailey, G. S., Grand, M. M., Beaton, A. D., Nightingale, A. M., Owsianka, D. R., Slavikt, G. J., et al. (2017). A lab-on-chip analyzer for *In situ* measurement of soluble reactive phosphate: improved phosphate blue assay and application to fluvial monitoring. *Environ. Sci. Technol.* 51, 9989–9995. doi: 10.1021/acs.est7b01581

Cogan, D., Fay, C., Boyle, D., Osborne, C., Kent, N., Cleary, J., et al. (2015). Development of a low cost microfluidic sensor for the direct determination of nitrate using chromotropic acid in natural waters. *Anal. Methods* 7, 5396–5405. doi: 10.1039/c5ay01357g

Coll, M., Steenbeek, J., Pennino, M. G., Buszowski, J., Kaschner, K., Lotze, H. K., et al. (2020). Advancing global ecological modeling capabilities to simulate future trajectories of change in marine ecosystems. *Front. Mar. Sci.* 7:567877. doi: 10.3389/fmars.2020.567877

David, A. R. J., McCormack, T., Morris, A. W., and Worsfold, P. J. (1998). A submersible flow injection-based sensor for the determination of total oxidised nitrogen in coastal waters. *Anal. Chim. Acta* 361, 63–72. doi: 10.1016/s0003-2670(98)00023-3

Dean, M., and Tucker, O. (2017). A risk-based framework for Measurement, Monitoring and Verification (MMV) of the Goldeneye storage complex for the Peterhead CCS project, UK. *Int. J. Greenhouse Gas Control* 61, 1–15. doi: 10.1016/j.ijggc.2017.03.014

DeVries, T., Le Quere, C., Andrews, O., Berthet, S., Hauck, J., Ilyina, T., et al. (2019). Decadal trends in the ocean carbon sink. *Proc. Natl. Acad. Sci. U.S.A.* 116, 11646–11651. doi: 10.1073/pnas.1900371116

Doney, S. C., Fabry, V. J., Feely, R. A., and Kleypas, J. A. (2009). Ocean acidification: the other CO2 problem. *Annu. Rev. Mar. Sci.* 1, 169–192. doi: 10.1146/annurev.marine.010908.163834

Easley, R. A., and Byrne, R. H. (2012). Spectrophotometric calibration of pH electrodes in seawater using purified m-cresol purple. *Environ. Sci. Technol.* 46, 5018–5024. doi: 10.1021/es300491s

Figueredo, F., Girolametti, F., Aneggi, E., Lekka, M., Annibaldi, A., and Susmel, S. (2021). Plastic electrode decorated with polyhedral anion tetrabutylammonium octamolybdate N(C4H9)(4) (4) Mo8O26 for nM phosphate electrochemical detection. *Anal. Chim. Acta* 1161:10. doi: 10.1016/j.aca.2021.338469

Finch, M. S., Hydes, D. J., Clayson, C. H., Weigl, B., Dakin, J., and Gwilliam, P. (1998). A low power ultra violet spectrophotometer for measurement of nitrate in seawater: introduction, calibration and initial sea trials. *Anal. Chim. Acta* 377, 167–177. doi: 10.1016/s0003-2670(98)00616-3

Flohr, A., Schaap, A., Achterberg, E. P., Alendal, G., Arundell, M., Berndt, C., et al. (2021). Towards improved monitoring of offshore carbon storage: a real-world field experiment detecting a controlled sub-seafloor CO2 release. *Int. J. Greenhouse Gas Control* 106:103237. doi: 10.1016/j.ijggc.2020.103237

Floquet, C. F. A., Sieben, V. J., Milani, A., Joly, E. P., Ogilvie, I. R. G., Morgan, H., et al. (2011). Nanomolar detection with high sensitivity microfluidic absorption cells manufactured in tinted PMMA for chemical analysis. *Talanta* 84, 235–239. doi: 10.1016/j.talanta.2010.12.026

Fritzsche, E., Staudinger, C., Fischer, J. P., Thar, R., Jannasch, H. W., Plant, J. N., et al. (2018). A validation and comparison study of new, compact, versatile optodes for oxygen, pH and carbon dioxide in marine environments. *Mar. Chem.* 207, 63–76. doi: 10.1016/j.marchem.2018.10.009

Furlong, M. E., Paxton, D., Stevenson, P., Pebody, M., McPhail, S. D., Perrett, J., et al. (2012). "Autosub long range: a long range deep diving AUV for ocean monitoring," in *Proceedings of the 2012 IEEE/Oes Autonomous Underwater Vehicles*, (Southampton: IEEE).

G7 Science and Technology Ministers (2016). *Attachment 2 to Tsukuba Communiqué*. Tsukuba: G7.

Geißler, F., Achterberg, E. P., Beaton, A. D., Hopwood, M. J., Clarke, J. S., Mutzberg, A., et al. (2017). Evaluation of a ferrozine based autonomous *In situ* lab-on-chip analyzer for dissolved iron species in coastal waters. *Front. Mar. Sci.* 4:322. doi: 10.3389/fmars.2017.00322

German, C., Tyler, P., and Griffiths, G. (2003). The maiden voyage of UK ROV Isis. *Ocean Chall.* 12, 16–18.

Gonski, S. F., Cai, W.-J., Ullman, W. J., Joesoef, A., Main, C. R., Pettay, D. T., et al. (2018). Assessment of the suitability of Durafet-based sensors for pH measurement in dynamic estuarine environments. *Estuar. Coast. Shelf Sci.* 200, 152–168. doi: 10.1016/j.ecss.2017.10.020

Grand, M. M., Clinton-Bailey, G. S., Beaton, A. D., Schaap, A. M., Johengen, T. H., Tamburri, M. N., et al. (2017). A lab-on-chip phosphate analyzer for long-term *In situ* monitoring at fixed observatories: optimization and performance evaluation in estuarine and oligotrophic coastal waters. *Front. Mar. Sci.* 4:255. doi: 10.3389/fmars.2017.00255

Grattan, L. M., Holobaugh, S., and Morris, J. G. (2016). Harmful algal blooms and public health. *Harmful Algae* 57, 2–8. doi: 10.1016/j.hal.2016.05.003

Hanson, A. K. (2000). "A new *In situ* chemical analyzer for mapping coastal nutrient distributions in real time," in *Proceedings of the OCEANS 2000 MTS/IEEE Conference and Exhibition*, (Providence, RI: IEEE).

Hartman, S. (2019). *RRS Discovery Cruise 103, 21 June-10 July 2019. Water Column and Seafloor Time-Series Studies at the Porcupine Abyssal Plain Sustained Observatory, in: 61*. Southampton: National Oceanography Centre.

Hepple, R. P., and Benson, S. M. (2005). Geologic storage of carbon dioxide as a climate change mitigation strategy: performance requirements and the implications of surface seepage. *Environ. Geol.* 47, 576–585. doi: 10.1007/s00254-004-1181-2

Hoegh-Guldberg, O. (2015). *Reviving the Ocean Economy: the Case for Action-2015*. Geneva: WWF International.

Huang, Y. M., Yuan, D. X., Dai, M. H., and Liu, Y. X. (2012). Reverse flow injection analysis method for catalytic spectrophotometric determination of iron in estuarine and coastal waters: a comparison with normal flow injection analysis. *Talanta* 93, 86–93. doi: 10.1016/j.talanta.2012.01.050

Hydes, D., Aoyama, M., Aminot, A., Bakker, K., Becker, S., Coverly, S., et al. (2010). *Determination of Dissolved Nutrients (N, P, Si) in Seawater with High Precision and Inter-Comparability Using Gas-Segmented Continuous Flow Analysers*. Paris: UNESCO.

Iida, Y., Takatani, Y., Kojima, A., and Ishii, M. (2021). Global trends of ocean CO2 sink and ocean acidification: an observation-based reconstruction of surface ocean inorganic carbon variables. *J. Oceanogr.* 77, 323–358. doi: 10.1007/s10872-020-00571-5

Jannasch, H. W., Johnson, K. S., and Sakamoto, C. M. (1994). Submersible, osmotically pumped analyzers for continuous determination of nitrate *in-situ*. *Anal. Chem.* 66, 3352–3361. doi: 10.1021/ac00092a011

Johengen, T., Purcell, H., Tamburri, M., Loewensteiner, D., Smith, G. J., Schar, D., et al. (2016). *Performance Verification Statement for Noc Nitrate Analyzer*. Solomons, MD: Alliance For Coastal Technologies, 47.

Johnson, K. S., and Coletti, L. J. (2002). *In situ* ultraviolet spectrophotometry for high resolution and long-term monitoring of nitrate, bromide and bisulfide in the ocean. *Deep Sea Res. Part I Oceanogr. Res. Papers* 49, 1291–1305. doi: 10.1016/s0967-0637(02)00020-1

Johnson, K. S., Jannasch, H. W., Coletti, L. J., Elrod, V. A., Martz, T. R., Takeshita, Y., et al. (2016). Deep-sea DuraFET: a pressure tolerant pH sensor designed for global sensor networks. *Anal. Chem.* 88, 3249–3256. doi: 10.1021/acs.analchem.5b04653

Johnson, K. S., Needoba, J. A., Riser, S. C., and Showers, W. J. (2007). Chemical sensor networks for the aquatic environment. *Chem. Rev.* 107, 623–640. doi: 10.1021/cr050354e

Johnson, K. S., Plant, J. N., Coletti, L. J., Jannasch, H. W., Sakamoto, C. M., Riser, S. C., et al. (2017). Biogeochemical sensor performance in the SOCCOM profiling float array. *J. Geophys. Res. Oceans* 122, 6416–6436. doi: 10.1002/2017JC012838

Johnson, K. S., Riser, S. C., and Karl, D. M. (2010). Nitrate supply from deep to near-surface waters of the North Pacific subtropical gyre. *Nature* 465, 1062–1065. doi: 10.1038/nature09170

Klimant, I., Huber, C., Liebsch, G., Neurauter, G., Stangelmayer, A., and Wolfbeis, O. S. (2001). "Dual lifetime referencing (DLR) — a new scheme for converting fluorescence intensity into a frequency-domain or time-domain information," in *New Trends in Fluorescence Spectroscopy: Applications to Chemical and Life Sciences*, eds B. Valeur and J.-C. Brochon (Berlin: Springer Berlin Heidelberg), 257–274.

Lai, C. Z., DeGrandpre, M. D., and Darlington, R. C. (2018). Autonomous optofluidic chemical analyzers for marine applications: insights from the submersible autonomous moored instruments (SAMI) for pH and pCO(2). *Front. Mar. Sci.* 4:438. doi: 10.3389/fmars.2017.00438

Legiret, F.-E., Sieben, V. J., Woodward, E. M. S., Bey, S. K. A. K., Mowlem, M. C., Connelly, D. P., et al. (2013). A high performance microfluidic analyser for phosphate measurements in marine waters using the vanadomolybdate method. *Talanta* 116, 382–387. doi: 10.1016/j.talanta.2013.05.004

Legrand, D. C., Mas, S., Jugeau, B., David, A., and Barus, C. (2021). Silicate marine electrochemical sensor. *Sens. Actuators B Chem.* 335:8. doi: 10.1016/j.snb.2021.129705

Liu, X. W., Wang, Z. H. A., Byrne, R. H., Kaltenbacher, E. A., and Bernstein, R. E. (2006). Spectrophotometric measurements of pH *in-situ*: laboratory and field evaluations of instrumental performance. *Environ. Sci. Technol.* 40, 5036–5044. doi: 10.1021/es0601843

Loukas, C. M., McQuillan, J. S., Laouenan, F., Tsaloglou, M. N., Ruano-Lopez, J. M., and Mowlem, M. C. (2017). Detection and quantification of the toxic microalgae *Karenia brevis* using lab on a chip mRNA sequence-based amplification. *J. Microbiol. Methods* 139, 189–195. doi: 10.1016/j.mimet.2017.06.008

Ma, J., Adornato, L., Byrne, R. H., and Yuan, D. X. (2014a). Determination of nanomolar levels of nutrients in seawater. *Trac Trends Anal. Chem.* 60, 1–15. doi: 10.1016/j.trac.2014.04.013

Ma, J., Li, Q. L., and Yuan, D. X. (2014b). Loop flow analysis of dissolved reactive phosphorus in aqueous samples. *Talanta* 123, 218–223. doi: 10.1016/j.talanta.2014.02.020

Macovei, V. A., Hartman, S. E., Schuster, U., Torres-Valdes, S., Moore, C. M., and Sanders, R. J. (2020). Impact of physical and biological processes on temporal variations of the ocean carbon sink in the mid-latitude North Atlantic (2002-2016). *Progr. Oceanogr.* 180:14. doi: 10.1016/j.pocean.2019.102223

Martz, T. R., Carr, J. J., French, C. R., and DeGrandpre, M. D. (2003). A submersible autonomous sensor for spectrophotometric pH measurements of natural waters. *Anal. Chem.* 75, 1844–1850. doi: 10.1021/ac020568l

Martz, T. R., Connery, J. G., and Johnson, K. S. (2010). Testing the Honeywell Durafet (R) for seawater pH applications. *Limnol. Oceanogr. Methods* 8, 172–184. doi: 10.4319/lom.2010.8.172

Martz, T. R., Jannasch, H. W., and Johnson, K. S. (2009). Determination of carbonate ion concentration and inner sphere carbonate ion pairs in seawater by ultraviolet spectrophotometric titration. *Mar. Chem.* 115, 145–154. doi: 10.1016/j.marchem.2009.07.002

McGraw, C. M., Stitzel, S. E., Cleary, J., Slater, C., and Diamond, D. (2007). Autonomous microfluidic system for phosphate detection. *Talanta* 71, 1180–1185. doi: 10.1016/j.talanta.2006.06.011

McLaughlin, K., Dickson, A., Weisberg, S. B., Coale, K., Elrod, V., Hunter, C., et al. (2017). An evaluation of ISFET sensors for coastal pH monitoring applications. *Reg. Stud. Mar. Sci.* 12, 11–18. doi: 10.1016/j.rsma.2017.02.008

Meyer, D., Prien, R. D., Dellwig, O., Connelly, D. P., and Schulz-Bull, D. E. (2012). *In situ* determination of iron(II) in the anoxic zone of the central Baltic Sea using ferene as spectrophotometric reagent. *Mar. Chem.* 130, 21–27. doi: 10.1016/j.marchem.2011.12.002

Milani, A., Statham, P. J., Mowlem, M. C., and Connelly, D. P. (2015). Development and application of a microfluidic *in-situ* analyzer for dissolved Fe and Mn in natural waters. *Talanta* 136, 15–22. doi: 10.1016/j.talanta.2014.12.045

Miller, C. A., Pocock, K., Evans, W., and Kelley, A. L. (2018). An evaluation of the performance of Sea-Bird Scientific's SeaFET (TM) autonomous pH sensor: considerations for the broader oceanographic community. *Ocean Sci.* 14, 751–768. doi: 10.5194/os-14-751-2018

Moscetta, P., Sanfilippo, L., Savino, E., Moscetta, P., Allabashi, R., Gunatilaka, A., et al. (2009). "Instrumentation for continuous monitoring in marine environments," in *Proceedings of the Oceans 2009*, Vol. 1-3, (New York, NY: IEEE), 737.

Mowlem, M., Beaton, A., and Slavik, G. (2018). *Oceanographic and Aquatic: Applications of Optic Sensing Technologies*. Boca Raton, FL: CRC Press-Taylor & Francis Group.

Mowlem, M., Schaap, A., and Beaton, A. (2019). *Microfluidics-Based Sensors: a Lab on a Chip*. Amsterdam: Elsevier Science.

Nagul, E. A., McKelvie, I. D., Worsfold, P., and Kolev, S. D. (2015). The molybdenum blue reaction for the determination of orthophosphate revisited: opening the black box. *Anal. Chim. Acta* 890, 60–82. doi: 10.1016/j.aca.2015.07.030

Nakano, Y., Kimoto, H., Watanabe, S., Harada, K., and Watanabe, Y. W. (2006). Simultaneous vertical measurements of *In situ* pH and CO2 in the sea using spectrophotometric profilers. *J. Oceanogr.* 62, 71–81. doi: 10.1007/s10872-006-0033-y

Nightingale, A. M., Beaton, A. D., and Mowlem, M. C. (2015). Trends in microfluidic systems for *In situ* chemical analysis of natural waters. *Sens. Actuators B Chem.* 221, 1398–1405. doi: 10.1016/j.snb.2015.07.091

Nightingale, A. M., Hassan, S. U., Warren, B. M., Makris, K., Evans, G. W. H., Papadopoulou, E., et al. (2019). A droplet microfluidic-based sensor for simultaneous *In situ* monitoring of nitrate and nitrite in natural waters. *Environ. Sci. Technol.* 53, 9677–9685. doi: 10.1021/acs.est.9b01032

Nightingale, A. M., Sammer-ul, H., Evans, G. W. H., Coleman, S. M., and Niu, X. Z. (2018). Nitrate measurement in droplet flow: gas-mediated crosstalk and correction. *Lab Chip* 18, 1903–1913. doi: 10.1039/c8lc00092a

Ogilvie, I. R. G., Sieben, V. J., Floquet, C. F. A., Zmijan, R., Mowlem, M. C., and Morgan, H. (2010). Reduction of surface roughness for optical quality microfluidic devices in PMMA and COC. *J. Micromech. Microeng.* 20:065016. doi: 10.1088/0960-1317/20/6/065016

Ogilvie, I. R. G., Sieben, V. J., Mowem, M. C., and Morgan, H. (2011). Temporal optimization of microfluidic colorimetric sensors by use of multiplexed stop-flow architecture. *Anal. Chem.* 83, 4814–4821. doi: 10.1021/ac200463y

Panton, A., Couceiro, F., Fones, G. R., and Purdie, D. A. (2020). The impact of rainfall events, catchment characteristics and estuarine processes on the export of dissolved organic matter from two lowland rivers and their shared estuary. *Sci. Total Environ.* 735:14. doi: 10.1016/j.scitotenv.2020.139481

Patey, M. D., Achterberg, E. P., Rijkenberg, M. J. A., Statham, P. J., and Mowlem, M. (2010). Interferences in the analysis of nanomolar concentrations of nitrate and phosphate in oceanic waters. *Anal. Chim. Acta* 673, 109–116. doi: 10.1016/j.aca.2010.05.029

Patey, M. D., Rijkenberg, M. J. A., Statham, P. J., Stinchcombe, M. C., Achterberg, E. P., and Mowlem, M. (2008). Determination of nitrate and phosphate in seawater at nanomolar concentrations. *Trac Trends Anal. Chem.* 27, 169–182. doi: 10.1016/j.trac.2007.12.006

Pinto, V. C., Araujo, C. F., Sousa, P. J., Goncalves, L. M., and Minas, G. (2019). A low-cost lab-on-a-chip device for marine pH quantification by colorimetry. *Sens. Actuators B Chem.* 290, 285–292. doi: 10.1016/j.snb.2019.03.098

Possenti, L., Humphreys, M. P., Bakker, D. C., Cobas-García, M., Fernand, L., Lee, G. A., et al. (2021). Air-sea gas fluxes and remineralisation from a novel combination of pH and O2 sensors on a glider. *Front. Mar. Sci.* 8. doi: 10.3389/fmars.2021.696772

Rerolle, V. M. C., Achterberg, E. P., Ribas-Ribas, M., Kitidis, V., Brown, I., Bakker, D. C. E., et al. (2018). High resolution pH measurements using a lab-on-chip sensor in surface waters of northwest European shelf seas. *Sensors* 18:2622. doi: 10.3390/s18082622

Rerolle, V. M. C., Floquet, C. F. A., Harris, A. J. K., Mowlem, M. C., Bellerby, R. R. G. J., and Achterberg, E. P. (2013). Development of a colorimetric microfluidic pH sensor for autonomous seawater measurements. *Anal. Chim. Acta* 786, 124–131. doi: 10.1016/j.aca.2013.05.008

Rerolle, V. M. C., Floquet, C. F. A., Mowlem, M. C., Bellerby, R., Connelly, D. P., and Achterberg, E. P. (2012). Seawater-pH measurements for ocean-acidification observations. *Trac Trends Anal. Chem.* 40, 146–157. doi: 10.1016/j.trac.2012.07.016

Roper, D. T., Phillips, A. B., Harris, C. A., Salavasidis, G., Pebody, M., Templeton, R., et al. (2017). "Autosub Long Range 1500: an ultra-endurance AUV with 6000 Km range," in *Proceedings of the Oceans 2017*, (Aberdeen: *IEEE*).

Ruhl, H. (2018). *RRS James Cook Cruise 165 19 May–12 Jun 2018. Water Column and Seafloor Time-Series Studies at the Porcupine Abyssal Plain Sustained Observatory, in (National Oceanography Centre Cruise Report, No. 57*. Southampton: National Oceanography Centre. .

Saba, G. K., Wright-Fairbanks, E., Chen, B. S., Cai, W. J., Barnard, A. H., Jones, C. P., et al. (2019). The development and validation of a profiling glider deep ISFET-based pH sensor for high resolution observations of coastal and ocean acidification. *Front. Mar. Sci.* 6:17. doi: 10.3389/fmars.2019.00664

Sakamoto, C. M., Johnson, K. S., and Coletti, L. J. (2009). Improved algorithm for the computation of nitrate concentrations in seawater using an *In situ* ultraviolet spectrophotometer. *Limnol. Oceanogr. Methods* 7, 132–143. doi: 10.4319/lom.2009.7.132

Salavasidis, G., Munafo, A., Harris, C. A., Prampart, T., Templeton, R., Smart, M., et al. (2019). Terrain-aided navigation for long-endurance and deep-rated autonomous underwater vehicles. *J. Field Robot.* 36, 447–474. doi: 10.1002/rob.21832

Schaap, A., Koopmans, D., Holtappels, M., Dewar, M., Arundell, M., Papadimitriou, S., et al. (2021). Quantification of a subsea CO2 release with lab-on-chip sensors measuring benthic gradients. *Int. J. Greenhouse Gas Control* 110:103427. doi: 10.1016/j.ijggc.2021.103427

Secretariat of the Convention on Biological Diversity. (2014). "An updated synthesis of the impacts of ocean acidification on marine biodiversity, technical series No. 75," in *Technical Series*, eds S. Hennige, J. M. Roberts, and P. Williamson (Montreal: Secretariat of the Convention on Biological Diversity), 99.

Seidel, M. P., DeGrandpre, M. D., and Dickson, A. G. (2008). A sensor for *In situ* indicator-based measurements of seawater pH. *Mar. Chem.* 109, 18–28. doi: 10.1016/j.marchem.2007.11.013

Shitashima, K., Kyo, M., Koike, Y., Henmi, H., and IEEE. (2002). *Development of In situ pH Sensor Using ISFET*. New York, NY: IEEE.

Slater, C., Cleary, J., Lau, K. T., Snakenborg, D., Corcoran, B., Kutter, J. P., et al. (2010). Validation of a fully autonomous phosphate analyser based on a microfluidic lab-on-a-chip. *Water Sci. Technol.* 61, 1811–1818. doi: 10.2166/wst.2010.069

Spaulding, R., DeGrandpre, M., and Harris, K. (2011). Autonomous pH and pCO(2) measurements in marine environments quantifying the inorganic carbon system with *In-Situ* SAMI technology. *Sea Technol.* 52:15.

Staudinger, C., Strobl, M., Breininger, J., Klimant, I., and Borisov, S. M. (2019). Fast and stable optical pH sensor materials for oceanographic

applications. *Sens. Actuators B Chem.* 282, 204–217. doi: 10.1016/j.snb.2018.11.048

Staudinger, C., Strobl, M., Fischer, J. P., Thar, R., Mayr, T., Aigner, D., et al. (2018). A versatile optode system for oxygen, carbon dioxide, and pH measurements in seawater with integrated battery and logger. *Limnol. Oceanogr. Methods* 16, 459–473. doi: 10.1002/lom3.10260

Steimle, E. T., Kaltenbacher, E. A., and Byrne, R. H. (2002). *In situ* nitrite measurements using a compact spectrophotometric analysis system. *Mar. Chem.* 77, 255–262. doi: 10.1016/s0304-4203(02)00003-8

Stinchcombe, M. (2017). "RRS discovery cruise DY050, 18 Apr - 08 May 2016. Cruise to the porcupine abyssal plain sustained observatory," in *National Oceanography Centre Cruise Report, 45*, (Southampton: National Oceanography Centre).

Takeshita, Y., Johnson, K. S., Coletti, L. J., Jannasch, H. W., Walz, P. M., and Warren, J. K. (2020). Assessment of pH dependent errors in spectrophotometric pH measurements of seawater. *Mar. Chem.* 223:7. doi: 10.1016/j.marchem.2020.103801

Takeshita, Y., Johnson, K. S., Martz, T. R., Plant, J. N., and Sarmiento, J. L. (2018). Assessment of autonomous pH measurements for determining surface seawater partial pressure of CO2. *J. Geophys. Res. Oceans* 123, 4003–4013. doi: 10.1029/2017jc013387

Takeshita, Y., Jones, B. D., Johnson, K. S., Chavez, F. P., Rudnick, D. L., Blum, M., et al. (2021). Accurate pH and O-2 measurements from spray underwater gliders. *J. Atmos. Ocean. Technol.* 38, 181–195. doi: 10.1175/jtech-d-20-0095.1

Tanhua, T., McCurdy, A., Fischer, A., Appeltans, W., Bax, N., Currie, K., et al. (2019). What we have learned from the framework for ocean observing: evolution of the global ocean observing system. *Front. Mar. Sci.* 6:471. doi: 10.3389/fmars.2019.00471

Trainer, V. L., Moore, S. K., Hallegraeff, G., Kudela, R. M., Clement, A., Mardones, J. I., et al. (2020). Pelagic harmful algal blooms and climate change: lessons from nature's experiments with extremes. *Harmful Algae* 91:14. doi: 10.1016/j.hal.2019.03.009

Vincent, A. G., Pascal, R. W., Beaton, A. D., Walk, J., Hopkins, J. E., Woodward, E. M. S., et al. (2018). Nitrate drawdown during a shelf sea spring bloom revealed using a novel microfluidic *In situ* chemical sensor deployed within an autonomous underwater glider. *Mar. Chem.* 205, 29–36. doi: 10.1016/j.marchem.2018.07.005

Vuillemin, R., Le Roux, D., Dorval, P., Bucas, K., Sudreau, J. P., Hamon, M., et al. (2009). CHEMINI: a new *In situ* CHEmical MINIaturized analyzer. *Deep Sea Res. Part I Oceanogr. Res. Papers* 56, 1391–1399. doi: 10.1016/j.dsr.2009.02.002

Walker, D. I., McQuillan, J., Taiwo, M., Parks, R., Stenton, C. A., Morgan, H., et al. (2017). A highly specific *Escherichia* coil qPCR and its comparison with existing methods for environmental waters. *Water Res.* 126, 101–110. doi: 10.1016/j.watres.2017.08.032

Wang, H., Ju, A. B., and Wang, L. Q. (2021). Ultraviolet spectroscopic detection of nitrate and nitrite in seawater simultaneously based on partial least squares. *Molecules* 26:12. doi: 10.3390/molecules26123685

Wang, Z. A., Sonnichsen, F. N., Bradley, A. M., Hoering, K. A., Lanagan, T. M., Chu, S. N., et al. (2015). *In situ* sensor technology for simultaneous spectrophotometric measurements of seawater total dissolved inorganic carbon and pH. *Environ. Sci. Technol.* 49, 4441–4449. doi: 10.1021/es504893n

Wang, Z. H. A., Liu, X. W., Byrne, R. H., Wanninkhof, R., Bernstein, R. E., Kaltenbacher, E. A., et al. (2007). Simultaneous spectrophotometric flow-through measurements of pH, carbon dioxide fugacity, and total inorganic carbon in seawater. *Anal. Chim. Acta* 596, 23–36. doi: 10.1016/j.aca.2007.05.048

Waterbury, R. D., Byrne, R. H., Kelly, J., Leader, B., McElligott, S., and Russell, R. (1996). *Development of an Underwater in-Situ Spectrophotometric Sensor for Seawater pH*. Bellingham, WAS: SPIE.

Wei, H., Pan, D. W., and Han, H. T. (2021). Electrochemical monitoring of marine nutrients: from principle to application. *Trac Trends Anal. Chem.* 138:14. doi: 10.1016/j.trac.2021.116242

Woolf, D. K., Shutler, J. D., Goddijn-Murphy, L., Watson, A. J., Chapron, B., Nightingale, P. D., et al. (2019). Key uncertainties in the recent air-sea flux of CO2. *Glob. Biogeochem. Cycles* 33, 1548–1563. doi: 10.1029/2018gb006041

Yang, Z. M., Li, C., Zhang, Z. Z., Lu, G. X., Cai, Z. F., and Cao, W. X. (2020). Development of an *In Situ* analyzer based on sequential injection analysis and liquid waveguide capillary flow cell for the determination of dissolved reactive phosphorus in natural waters. *Sensors* 20:12. doi: 10.3390/s20102967

Yaqoob, M., Biot, B. F., Nabi, A., and Worsfold, P. J. (2012). Determination of nitrate and nitrite in freshwaters using flow-injection with luminol chemiluminescence detection. *Luminescence* 27, 419–425. doi: 10.1002/bio.1366

Yuecel, M., Beaton, A. D., Dengler, M., Mowlem, M. C., Sohl, F., and Sommer, S. (2015). Nitrate and nitrite variability at the seafloor of an oxygen minimum zone revealed by a novel microfluidic *in-situ* chemical sensor. *PloS One* 10:e0132785. doi: 10.1371/journal.pone.0132785

Conflict of Interest: MM was a director, CTO, shareholder and employee of ClearWater Sensors Ltd. that manufacture and sell Lab on Chip chemical sensors utilizing intellectual property licensed from the University of Southampton and the National Oceanography Centre. This IP is used in the sensors described in this paper. Matt maintains employment in the NOC with interactions governed by a detailed conflict of interest policy. AB, RP, and CC were shareholders and employees of ClearWater Sensors Ltd. whilst maintaining employment in the NOC with interactions governed by a detailed conflict of interest policy. SM was a student and then postdoc at the University of Southampton and NOC during the development of sensors and the fieldwork described in the paper, but now is a visiting associate at the NOC and works as an employee exclusively for ClearWater Sensors Ltd.

The remaining authors declare that the research was conducted in the absence of any commercial or financial relationships that could be construed as a potential conflict of interest.

Publisher's Note: All claims expressed in this article are solely those of the authors and do not necessarily represent those of their affiliated organizations, or those of the publisher, the editors and the reviewers. Any product that may be evaluated in this article, or claim that may be made by its manufacturer, is not guaranteed or endorsed by the publisher.

frontiers in Marine Science

ORIGINAL RESEARCH
published: 04 November 2021
doi: 10.3389/fmars.2021.695845

Comparison of Methods for Determining Erosion Threshold of Cohesive Sediments Using a Microcosm System

*Hun Jun Ha and Ho Kyung Ha**

Department of Ocean Sciences, Inha University, Incheon, South Korea

Erosion of cohesive sediments is a ubiquitous phenomenon in estuarine and intertidal environments. Several methods have been proposed to determine the surface erosion threshold (τ_{c0}), which are still debatable because of the numerous and uncertain definitions. Based on erosion microcosm experiments, we have compared three different methods using (1) eroded mass (EM), (2) erosion rate (ER), and (3) suspended sediment concentration (SSC), and suggested a suitable method for revealing the variation of erodibility in intertidal sediments. Erosion experiments using a microcosm system were carried out in the Muuido tidal flat, west coast of South Korea. The mean values of τ_{c0} for three methods were: 0.20 ± 0.08 Pa (EM); 0.18 ± 0.07 Pa (ER); and (3) 0.17 ± 0.09 Pa (SSC). The SSC method yielded the lowest τ_{c0}, due to the outflow of suspended sediment from the erosion chamber of the microcosm. This was because SSC gradually decreased with time after depleting the erodible sediment at a given bed shear stress (τ_b). Therefore, the regression between SSC and applied τ_b might skew an *x*-intercept, resulting in the underestimation (or "not-determined") of τ_{c0}. The EM method yielded robust and accurate (within the range of τ_b step at which erosion begins) results. The EM method represents how the erodible depth thickens as τ_b increases and therefore seems better suited than the SSC and ER methods for representing depth-limited erosion of cohesive sediments. Furthermore, this study identified the spatiotemporal variations of τ_{c0} by EM method in an intertidal flat. The τ_{c0} in mud flat was about two times higher than that in mixed flat. Compared to the end of tidal emersion, the sediment was 10–40% more erodible at the beginning stage.

Keywords: erosion threshold, intertidal flat, cohesive sediment, methods, microcosm system

OPEN ACCESS

Edited by:
Joanna Staneva,
Institute of Coastal Systems
Helmholtz Centre Hereon, Germany

Reviewed by:
Courtney Harris,
College of William and Mary,
United States
Jun Choi,
Pukyong National University,
South Korea

***Correspondence:**
Ho Kyung Ha
hahk@inha.ac.kr;
hokyung.ha@gmail.com

Specialty section:
This article was submitted to Coastal Ocean Processes, a section of the journal Frontiers in Marine Science

Received: *15 April 2021*
Accepted: *15 October 2021*
Published: *04 November 2021*

Citation:
Ha HJ and Ha HK (2021) Comparison of Methods for Determining Erosion Threshold of Cohesive Sediments Using a Microcosm System. Front. Mar. Sci. 8:695845. doi: 10.3389/fmars.2021.695845

INTRODUCTION

The sediment erodibility plays a key role in the evaluation of resistance to erosion, and is quantified as the eroded mass (EM) and erosion rate (ER). Understanding the erodibility of cohesive sediments is important for many ecological (e.g., primary production, benthic-pelagic coupling, and toxicity problems) and engineering applications (e.g., siltation of harbors, dredging of navigation channels, and coastal protection). The erodibility of non-cohesive sediments is primarily determined by their physical properties (e.g., grain size and bulk density) (Roberts et al., 1998). As cohesive sediments have highly variable parameters in space

and time, however, it is difficult to directly measure or predict them. Furthermore, complex interactions occur between the physical, biological, and chemical parameters that impact the erodibility of cohesive sediment (Black et al., 2002; Grabowski et al., 2011). Thus, the site- and time-specific field experiments are often required to obtain the information on the erodibility of cohesive sediments.

The surface erosion threshold (τ_{c0}, also known as an initial critical shear stress for erosion) is largely used as one of parameters representing for sediment erodibility. It is defined as the bed shear stress (τ_b) at which the sediment erosion begins (Winterwerp and van Kesteren, 2004). Currently, several methods have been proposed to estimate a specific threshold. Amos et al. (2003), for instance, proposed three practical methods to define τ_{c0}: (1) the surface intercept of the failure-envelope on a plot of eroded depth vs. τ_b; the extrapolation to the ambient level through the regression of (2) ER and (3) suspended sediment concentration (SSC) vs. τ_b, respectively.

Despite such methodological efforts, the determination of τ_{c0} is still debatable because of the investigator's subjective definitions used to identify the initial sediment motion on the seabed (Sutherland et al., 1998). A portable and easy-to-use erosion microcosm system capable of deployment in the field has been developed. This type of device has been widely used in littoral environments, particularly intertidal flats, to quantify spatiotemporal variations of erodibility (Dickhudt et al., 2009; Wiberg et al., 2013; Ha H. J. et al., 2018). To date, many researchers have visually defined a τ_{c0} based on the abrupt increase in SSC (or ER) (e.g., Maa and Kim, 2002), however, this approach is quite subjective. For example, τ_{c0} was defined as the τ_b when an abrupt increase of SSC (>1.5 mg l^{-1}) was first observed (Ha H. K. et al., 2018). Thus, there is a need to develop an accurate and objective method for determining τ_{c0} using the extrapolation method (Widdows et al., 2007; Seo et al., 2020).

A series of erosion experiments were conducted on the intertidal flat, the west coast of South Korea to meet the aforementioned technical needs in the cohesive sediment community. The collected data were used as input in the three extrapolation methods using EM (the amount of erodible sediment at the bed), ER (the mass loss per unit time and area), and SSC, respectively. The main objectives of this study were (1) to compare methods for estimating τ_{c0}, and (2) to suggest a method suitable for revealing the spatiotemporal variation of erodibility in intertidal environments.

MATERIALS AND METHODS

Study Area

The study area is located in the Muuido tidal flat, the west coast of South Korea (**Figure 1**). In Gyeonggi Bay, extensive tidal flats comprising a total area of 873 km^2 have developed around the bedrock islands (Koh and Khim, 2014). The surface sediments consist of fine sand to silt with a mean grain size of 51.5 μm (Ha H. K. et al., 2018). Erosion experiments have been conducted at two sites: mud flat (GB01) and mixed flat (GB02) from September 11 to 17, 2020. Sediment cores were selectively collected at the neap (N1: September 11; and N2: September 13) and spring (S1: September 16; and S2: September 17) tides to examine the spring-neap tidal variation of erodibility (**Figure 2A**). The tides have a semi-diurnal regime, with mean tidal range of approximately 9 m (KMA, 2017), and tidal currents are ebb-dominated, reaching up to 1.5 m s^{-1} (Lee et al., 2013). Winds are dominated by the regional monsoon with mild south-southeasterly winds during summer and strong north-northwesterly winds during winter (KMA, 2017). The SSC was observed ranging from about 100–1,000 mg l^{-1} at nearby tidal channel (Park and Lee, 2016).

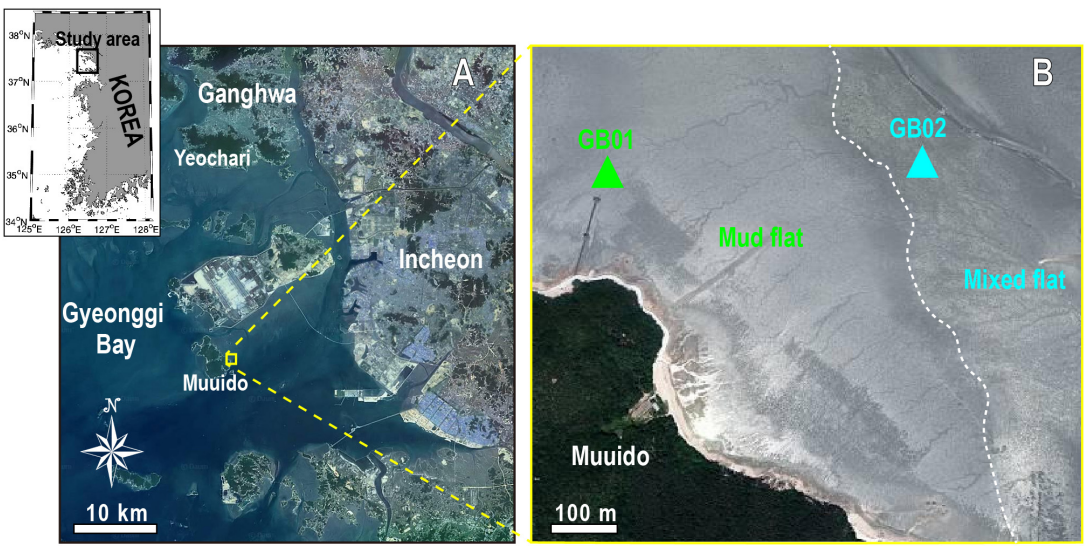

FIGURE 1 | (A) Satellite image of the Gyeonggi Bay. The upper left inset shows the coast of Korean Peninsula. **(B)** Study area on the Muuido tidal flat showing the two sampling sites (GB01 and GB02) for sediment cores. All satellite images were acquired from http://map.kakao.com.

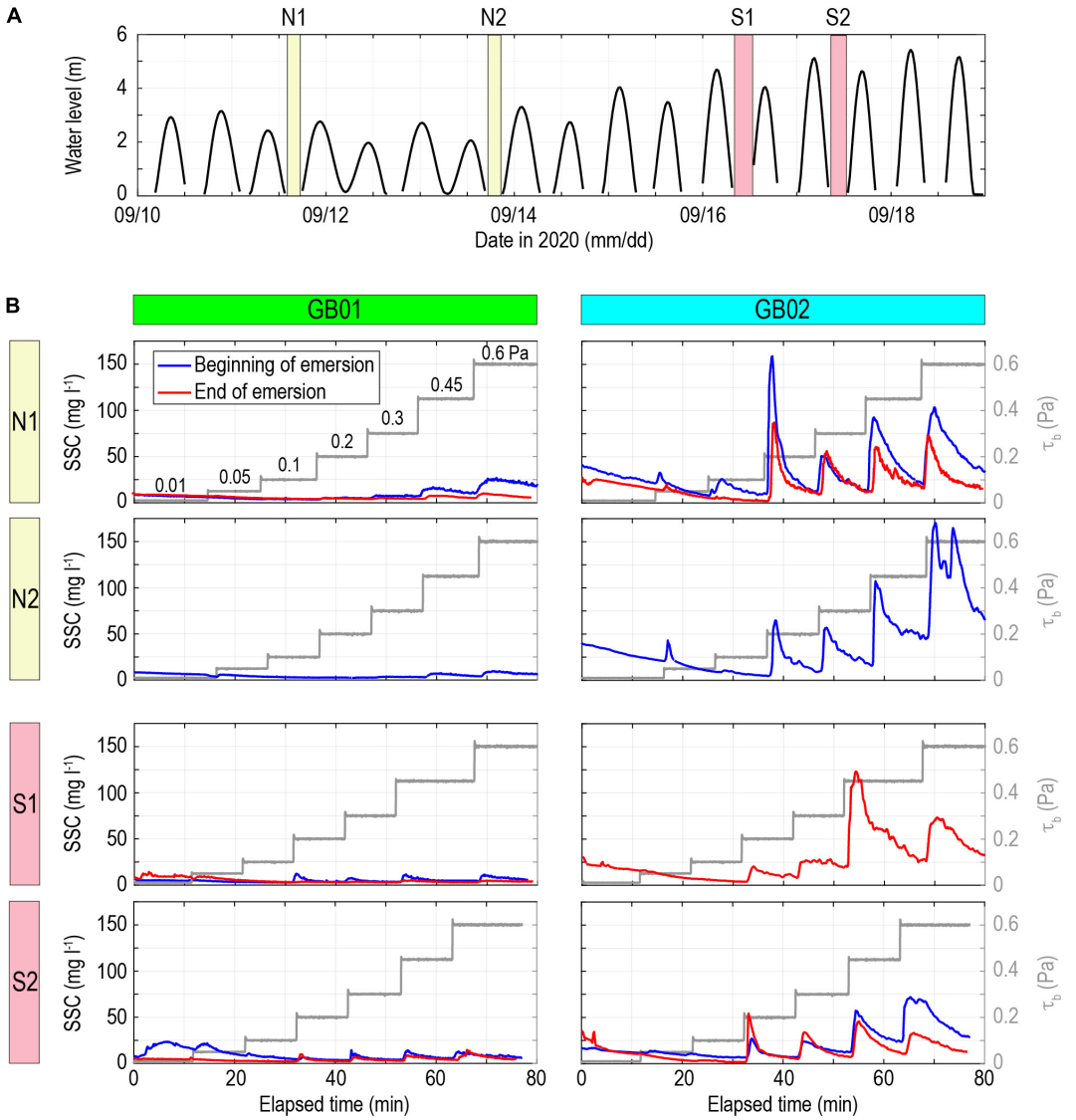

FIGURE 2 | (A) Time series of water level (m) at GB02. Pressure sensor (RBR SoloD) was deployed at 0.1 m above bed. Pressure data were converted to water level. The shaded areas indicate the sampling times at 09/11 (N1), 09/13 (N2), 09/16 (S1), and 09/17 (S2). **(B)** Results of GEMS experiments. Sediment cores were collected at the beginning (blue line) and the end (red line) of emersion. Seven steps of τ_b (0.01–0.6 Pa) were applied for approximately 10 min per each step.

Microcosm Experiments

Sediment erodibility was measured using a dual-core Gust Erosion Microcosm System (GEMS) designed by Gust and Müller (1997). A GEMS comprises an erosion chamber, electronic control box, turbidimeter (Hach, 2100AN), water pump, erosion motor, and rotating disk (**Supplementary Figure 1**). A series of increasing τ_b is applied to the surficial of the sediment core by controlling both the rotation rate of disk and the water pumping rate. A conceptual diagram and a photograph of the GEMS could be found in Ha H. K. et al. (2018) and Seo et al. (2020). Sediment cores for erosion microcosm experiments were collected using an acrylic cylinder at the beginning and end of tidal emersion. The emersion time, which indicates how long since the site emerged from tidal flooding, was determined by the pressure sensor (RBR SoloD) at GB02. This sensor was deployed at 0.1 m above bed. After the collection, sediment cores were carefully carried to the laboratory, and then installed in the GEMS. Measurement of erodibility was started within 2 h after collecting a sediment core, to minimize the effects of dewatering and self-weight consolidation. Prior to the beginning of the erosion experiment, the sediment surface within the core was positioned at 10 cm below the bottom unit of rotating disk. Seven stepwise sequences of τ_b (0.01, 0.05, 0.1, 0.2, 0.3, 0.45, and 0.6 Pa) were applied to the top surface of core for approximately 10 min at each step. During the first 10 min of the experiment, a minimum τ_b (i.e., 0.01 Pa) was applied to flush out pre-existing suspended sediments within the core and inlet/outlet tubes. While the rotating disk began applying a given

stress, the seawater obtained from the field site was pumped into the erosion chamber. The effluent water containing the eroded or resuspended sediments was passed through a turbidimeter, which was continuously recorded in turbidity [in nephelometric turbidity units (NTU)]. Throughout the erosion experiments, the τ_b and turbidity data were logged at 1 s interval. The effluent water from each stress step was sampled and then filtered through a 0.7 μm glass fiber filter (GF/F). The filters were oven dried at 105°C for 24 h and then weighed to estimate the ground-truth SSC (in mg l^{-1}). The turbidity was converted to SSC using a linear regression between recorded NTU and the SSC derived from filtering (R^2 = 0.92, not shown). This was then used to determine the EM at each τ_b. An erosion formulation developed by Sanford and Maa (2001) and Sanford (2006) was used as follows:

$$ER(m, t) = M(m)[\tau_b(t) - \tau_c(m)]e^{-\lambda t} \quad (1)$$

where m is the eroded mass (kg m^{-2}), t is the elapsed time (s), ER is the erosion rate (kg m^{-2} s^{-1}), M is the erosion rate parameter (kg m^{-2} s^{-1} Pa^{-1}), τ_c is the depth-varying erosion threshold (Pa), and λ is the rate of sediment depletion (s^{-1}).

Estimation of Surface Erosion Thresholds

In microcosm experiments, sediment erosion can be determined by the responses of SSC under increasing τ_b, which is expressed as the EM and ER. The τ_{c0}, a point of initial erosion of the bed, was estimated by three methods: (1) EM method: τ_{c0} was determined by an x-intercept of the regression of the eroded mass vs. τ_b; (2) ER method: τ_{c0} was determined, at background level of ER, through the linear regression of the time-averaged erosion rate vs. τ_b; and (3) SSC method: τ_{c0} was determined, at background level of SSC, through the linear regression of the time-averaged SSC vs. τ_b. All the three have been used to compare the τ_{c0} from various erosion devices (e.g., Neumeier et al., 2007; Widdows et al., 2007; Thompson et al., 2013; Seo et al., 2020) (**Supplementary Table 1**). In case of the ER and SSC methods, using time-averaged erosion rate and SSC from each τ_b, the linear regression was computed to remove the horizontal heterogeneity in τ_b and erosion parameters (Schoellhamer et al., 2017). Many researchers (e.g., Sanford, 2006; Jacobs et al., 2011) have interpreted the erosion rate for each applied τ_b as the average over the time interval. Detail explanations of each method are given in Widdows et al. (1998) and Amos et al. (2003).

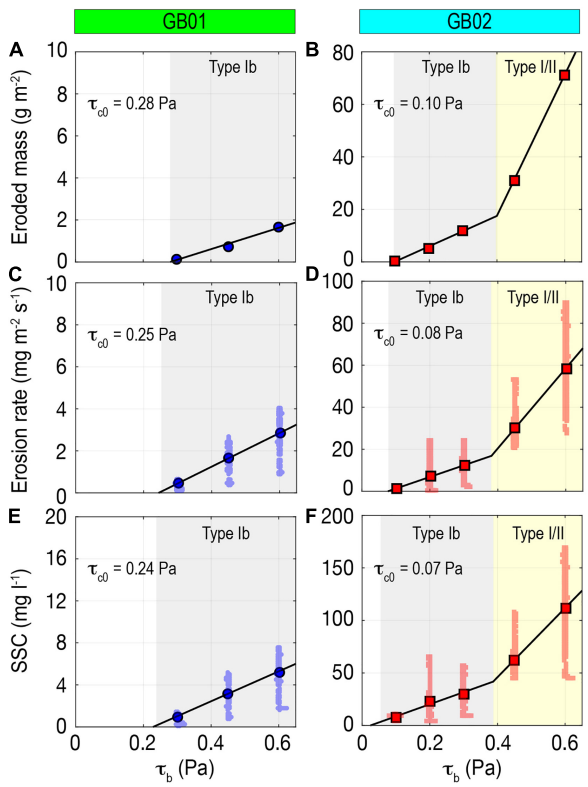

FIGURE 3 | Plots used in the determination of surface erosion threshold (τ_{c0}) in GB01 **(A,C,E)** and GB02 **(B,D,F)** at the beginning of emersion during N2 period (see **Figure 2A**): eroded mass **(A,B)**, erosion rate **(C,D)**, and SSC **(E,F)** as a function of applied bed shear stress (τ_b), respectively. Blue dots and red squares indicate mean values at each step of τ_b. Black solid lines indicate the fitting of regression line. Areas of light gray and yellow indicate the erosion of type Ib and type I/II, respectively.

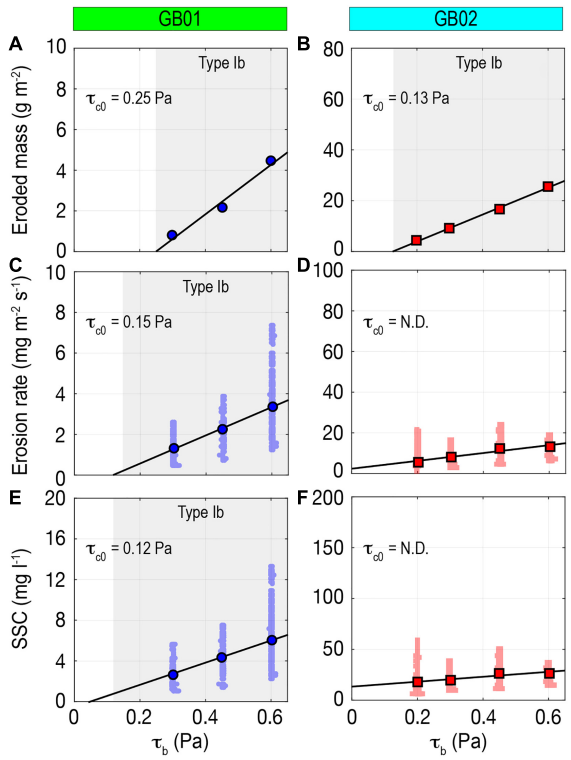

FIGURE 4 | Plots used in the determination of surface erosion threshold (τ_{c0}) in GB01 **(A,C,E)** and GB02 **(B,D,F)** at the end of emersion during S2 period (see **Figure 2A**): eroded mass **(A,B)**, erosion rate **(C,D)**, and SSC **(E,F)** as a function of applied bed shear stress (τ_b), respectively. Blue dots and red squares indicate mean values at each step of τ_b. Black solid lines indicate the fitting of regression line. Area of light gray indicates the erosion of type Ib. N.D., not determined.

TABLE 1 | Results of erosion microcosm experiments.

Sites	Date in 2020 (mm/dd)	Emersion time (h)	Eroded mass (g m^{-2})	Maximum erosion rate (mg m^{-2} s^{-1})	Maximum SSC (mg l^{-1})	τ_{c0} (Pa)		
						EM method	ER method	SSC method
GB01	09/11	1	13.06	17.16	24.45	0.28	0.28	0.23
		5	2.99	3.66	7.92	0.31	0.24	0.25
	09/13	1	3.38	4.08	7.54	0.28	0.25	0.24
	09/16	1	4.19	4.87	9.82	0.24	0.15	0.11
		6	1.23	1.72	3.36	0.32	0.27	0.35
	09/17	1	4.96	5.84	11.91	0.26	0.13	0.07
		6	4.43	7.38	13.43	0.25	0.15	0.12
GB02	09/11	1	61.92	73.08	158.78	0.07	0.08	N.D.
		5	32.33	39.47	86.96	0.11	N.D.	N.D.
	09/13	1	71.26	90.00	170.18	0.10	0.08	0.07
	09/16	1	56.29	62.52	123.06	0.16	0.14	0.13
	09/17	1	39.48	38.89	72.14	0.15	0.16	0.17
		5	25.55	24.38	57.89	0.13	N.D.	N.D.

N.D., not determined.

The type of erosion was determined from the trends in erosion rate through time (Amos et al., 1992). Depth-limited erosion (type I), which is characterized by an increase in bed resistance and a decrease in erodibility with depth, is identified by an erosion rate that peaks rapidly when τ_b is increased, but then declines exponentially with time. Steady-state erosion (type II) is identified as having a near-constant erosion rate for a given τ_b because the τ_c does not change with depth in the sediment bed. Erosion of type I/II is a transitional form between type I and type II. The process of type I began with entrainment of the organic-rich fluff layer (type Ia), which then gave way to erosion of surface bed materials (type Ib) (Amos et al., 2003). Type Ib is considered more significant threshold concerning bed erosion (Widdows et al., 2007). The erosion amount of the fluff layer was negligibly small because it was a thin layer; and its threshold for erosion was small because this material was newly deposited and did not have sufficient time to develop self-weight consolidation (Ha and Maa, 2009). In this study, therefore, τ_{c0} was determined by the onset of type Ib. If the linear regression between the erosion variables (EM, erosion rate, and SSC) and τ_b is divided into two parts by an inflection point, thereby transitioning from type Ib to type I/II (Seo et al., 2020). This partitioning of erosion type would be better suited for threshold estimation than no partitioning of this.

RESULTS AND DISCUSSION

Comparison of Different Surface Erosion Thresholds

Figure 2B shows the time series of SSC under the applied τ_b's. At GB01, SSC decreased with time until τ_b = 0.05 Pa, except the sediment core at the beginning of the emersion during S2 period. At GB02, SSC increased slightly in the transition period at which τ_b increased stepwise from 0.01–0.05 Pa, and then it quickly decreased. This small amount of erosion is representative of the removal of the fluff layer. The highest SSC generated among all the sediment cores was 24.45 mg l^{-1} at GB01, and it was 170.18 mg l^{-1} at GB02, indicating the presence of more erodible sediments at GB02. In GB01 and GB02, there was initial erosion of sediment at the τ_b of 0.3–0.45 Pa and 0.1–0.2 Pa, respectively.

τ_{c0} was derived using linear regression between the erosion variables and τ_b. Representative cases of the three methods for estimating τ_{c0} are shown in **Figures 3**, **4**. For example, the time series of SSC at each τ_b in GB02 during N2 period (see **Figure 2B**) was converted to the data in **Figure 3F** indicated by the light red squares. The regression of ER and SSC method was fit through the time-averaged ER and SSC at each τ_b, respectively. At GB01,

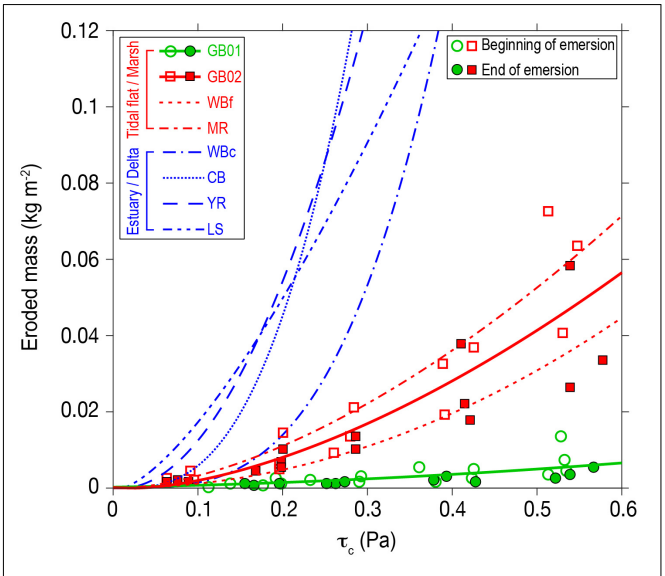

FIGURE 5 | Relationship between eroded mass and erosion threshold (τ_c) in GB01 (green circles) and GB02 (red squares). Data at other sites are from Sanford (2006); Dickhudt et al. (2009), Wiberg et al. (2013), and Xu et al. (2014, 2016). See **Table 2** for site information in legend.

the relationship between erosion variables and τ_b showed a linear regression without an inflection point corresponding to type Ib (**Figures 3A,C,E**). At GB02, the relationship between the EM and τ_b revealed two phases (except the sediment cores at the end of emersion during N1 and S2): the first was a region of steady increase in EM with increasing τ_b from 0.1–0.3 Pa; the second was a distinct inflection in the regression line at the τ_b between 0.3 and 0.45 Pa (**Figure 3B**). These phases might correspond to type Ib and type I/II, respectively. There was also an inflection in the regression line between the ER (and SSC) and τ_b (**Figures 3D,F**). At the end of emersion during N1 and S2 periods, a linear regression between the EM and τ_b reflected type Ib (i.e., a single regression line without inflection) in GB02 (**Figure 4B**).

A summary of τ_{c0} is provided in **Table 1**. At GB01, the mean values of τ_{c0} for three methods were: (1) 0.28 ± 0.03 Pa (EM); (2) 0.21 ± 0.06 Pa (ER); and (3) 0.20 ± 0.10 Pa (SSC). The τ_{c0} in ER and SSC methods were similar. The τ_{c0} by EM method was consistently higher than the results from ER and SSC methods, due to the steeper slope in the regression line (**Figures 4A,C,E**). At GB02, the τ_{c0} by ER and SSC methods partly yielded a negative *x*-intercept caused by the extremely low slope in regression (**Figures 4D,F**), resulting in the "not-determined (N.D.) τ_{c0}" (**Table 1**). During N2 and S1 periods, the τ_{c0} by EM method was about 25% higher than the results from ER and SSC methods. During S2 period, it was about 10% lower than the τ_{c0} by ER and SSC methods. Because the EM representing the erodible depth was accumulated with increasing τ_b, the EM method is suitable for reflecting the depth-limited erosion of cohesive sediments. After the erodible sediment was removed at each step of τ_b, SSC and ER gradually decreased with time. Thus, the regression of the SSC and ER vs. τ_b might skew an *x*-intercept. Especially, the SSC method yielded the lowest τ_{c0} due to the outflow water containing eroded sediments from the erosion chamber.

The data from the GEMS experiments could be represented as the plots of the EM vs. τ_c (**Figure 5**). Based on the data from all sediment cores at each site, the equation was obtained using a best-fit power law regression in the form of $m = a(\tau_c - \tau_{c0})^b$, where m is the eroded mass (kg m^{-2}) (Sanford and Maa, 2001; Dickhudt et al., 2009). This regression equation could be used in sediment transport models (Fall et al., 2014). The results of other published erodibility data in tidal flat/marsh environments

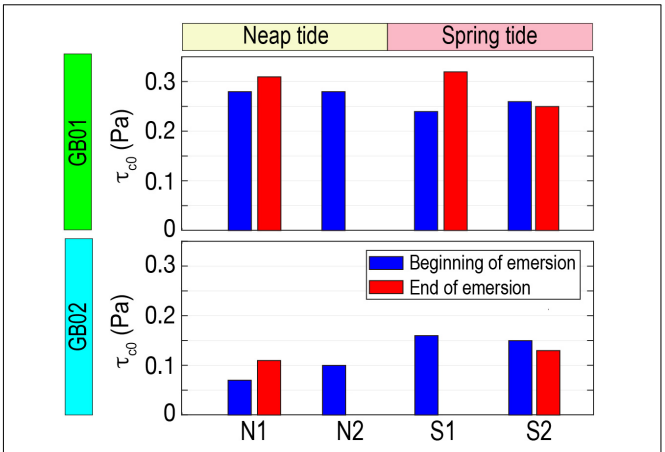

FIGURE 6 | The surface erosion threshold (τ_{c0}) at GB01 (upper panel) and GB02 (lower panel) sites during N1, N2, S1, and S2 periods (see **Figure 2A**).

measured by GEMS were similar to the results presented here from the Muuido tidal flat (**Figure 5**). Based on the best-fit curve, the τ_{c0} in GB02 was determined as 0.03 Pa, which corresponds to an erosion threshold of fluff layer (i.e., type Ia) (Jago et al., 2002; Ha and Maa, 2009). However, the τ_{c0} in GB01 could not be determined because of a negative *x*-intercept of the regression curve caused by low erodibility. In this case, the previous studies (see references in **Table 2**) suggested either 0.01 Pa (the minimum τ_b applied for GEMS) or 0 Pa for τ_{c0} to ensure that the fit produced reasonable data.

Spatiotemporal Variation in Erodibility

The erodibility of cohesive sediment has been quantified as the τ_{c0} and EM (Dickhudt et al., 2009; Ha H. K. et al., 2018). Our results indicated a spatial variation of erodibility between mud flat and mixed flat. The τ_{c0} by EM method in GB01 (mud flat, mean = 0.28 ± 0.03 Pa) was about two times higher than that in GB02 (mixed flat, mean = 0.12 ± 0.03 Pa). The EM in GB01 (mean = 4.89 ± 3.80 g m^{-2}) also was about one order lower than that in GB02 (mean = 47.81 ± 18.03 g m^{-2}). As seen in the erosion curves (**Figure 5**), the mixed flat was more erodible than the mud flat. Previous studies suggested that the spatial variations of erodibility of intertidal flats were caused by two main factors: (1) the sediment composition; and

TABLE 2 | Power law fit parameters relating erosion threshold to eroded mass.

Sites	Sedimentary environments	*a*	τ_{c0}	*b*	R^2	Number of samples	References
Gyeonggi Bay, South Korea (GB01)	Mud flat	0.02	0.01	1.62	0.46	7	This study
Gyeonggi Bay, South Korea (GB02)	Mixed flat	0.14	0.03	1.63	0.76	6	This study
Willapa Bay, United States (WBf)	Mud flat	0.13	0.00	2.03	0.89	27	Wiberg et al., 2013
Willapa Bay, United States (WBc)	Mesotidal channel	2.83	0.00	3.30	0.99	8	Wiberg et al., 2013
Chesapeake Bay estuary, United States (CB)	Estuarine channel	4.23	0.01	2.73	0.95	2	Sanford, 2006
York River estuary, United States (YR)	Estuarine channel	1.43	0.01	1.97	0.87	50	Dickhudt et al., 2009
Mississippi River delta, United States (MR)	Marsh	0.17	0.01	1.65	-	12	Xu et al., 2016
Louisiana shelf, United States (LS)	Shelf mud	0.52	0.01	1.42	-	106	Xu et al., 2014

(2) the extracellular polymeric substances (EPS) concentration (Panagiotopoulos et al., 1997; Andersen et al., 2010). Even small amounts of mud content can create the cohesive attachment when mixed in non-cohesive sediment. Proportions of clay greater than 10% is sufficient for sediment stabilization (van Ledden et al., 2004). Ha H. J. et al. (2018) found that the sediment erodibility in mud flat was about seven times lower than that in mixed flat due to increasing clay content on the Yeochari tidal flat, northern Gyeonggi Bay (for location, see **Figure 1A**). Therefore, the field-based measurements of spatial variability in erodibility and sediment composition are needed to understand the regional-scale sediment transport and morphology evolution. The EPS, which is secreted out of microphytobenthos (MPB), plays a key role in the "biostabilization" (Andersen et al., 2010). The EPS concentration and MPB biomass, which have a semi-annual to annual variability, are at their lowest levels from September to November (Park et al., 2014). In this study, it seems unlikely that the sediment erodibility was affected by EPS.

Temporal variation of sediment erodibility has been found on various timescales such as intra-tidal and spring-neap tidal cycles (Grabowski et al., 2011). As shown in **Figure 6**, the τ_{c0} at the beginning of tidal emersion was about 10–40% lower than that at the end, indicating that the subaerial emersion time might be a factor to determine the intra-tidal variation of τ_{c0} (Fagherazzi et al., 2017). In addition, the sediment in the spring tide was about 80% less erodible than in the neap tide at GB02 (**Figure 6**). As the spring tides have stronger currents compared to neap tides, more sediments are resuspended into the water column, and the consolidated (i.e., low erodibility) sediment beds are more exposed.

CONCLUSION

Three methods for determining the τ_{c0} of cohesive sediments in an intertidal flat were compared using an erosion microcosm system. The conclusions drawn from this study could be summarized as follows:

(1) The τ_{c0} by EM method was slightly higher than the results from the ER and SSC methods. The EM method is more robust and accurate (within the range of τ_b step at which erosion begins) than the ER and SSC methods. The τ_c of the consolidated sediment bed increased with sediment depth, and thus the eroded mass representing the erodible depth was accumulated with increasing τ_b. This suggested that the EM method is suitable for reflecting the depth-limited erosion of cohesive sediments.

(2) The SSC method produced the lowest τ_{c0}, owing to the outflow of suspended sediment from the erosion chamber. After depleting the erodible sediment at each step of τ_b, the SSC gradually decreased with time. Therefore, the regression between SSC and applied τ_b might skew an x-intercept, leading to a lower τ_{c0}.

(3) This study identified the spatiotemporal variations of sediment erodibility in an intertidal flat. The τ_{c0} in mud flat was about two times higher than that in mixed flat. Compared to the end of tidal emersion, the sediment was 10–40% more erodible at the beginning stage. The τ_{c0} during spring tide was about 80% higher than that during neap tide.

DATA AVAILABILITY STATEMENT

The datasets generated for this study are available on request to the corresponding author.

AUTHOR CONTRIBUTIONS

HJH designed the study, performed the experiments, and wrote the manuscript. HKH identified research goals, performed the analysis, and supervised the study. Both authors contributed to the article and approved the submitted version.

FUNDING

This study is supported by the National Research Foundation of Korea (NRF-2018R1D1A1A02085804). This study is also supported by the project entitled "Marine Ecosystem-Based Analysis and Decision-Making Support System Development for Marine Spatial Planning" (20170325), and "Development of Advanced Science and Technology for Marine Environmental Impact Assessment" (20210427), funded by the Ministry of Oceans and Fisheries of Korea (MOF).

SUPPLEMENTARY MATERIAL

The Supplementary Material for this article can be found online at: https://www.frontiersin.org/articles/10.3389/fmars.2021.695845/full#supplementary-material

REFERENCES

Amos, C. L., Daborn, G. R., Christian, H. A., Atkinson, A., and Robertson, A. (1992). In situ erosion measurements on fine-grained sediments from the Bay of Fundy. *Mar. Geol.* 108, 175–196. doi: 10.1016/0025-3227(92)90171-D

Amos, C. L., Droppo, I. G., Gomez, E. A., and Murrphy, T. P. (2003). The stability of a remediated bed in Hamilton Harbour, Lake Ontario, Canada. *Sedimentology* 50, 149–168. doi: 10.1046/j.1365-3091.2003.00542.x

Andersen, T. J., Lanuru, M., van Bernem, C., Pejrup, M., and Riethmueller, R. (2010). Erodibility of a mixed mudflat dominated by microphytobenthos and *Cerastoderma edule*, East Frisian Wadden Sea, Germany. *Estuar. Coast. Shelf Sci.* 87, 197–206. doi: 10.1016/j.ecss.2009.10.014

Black, K. S., Tolhurst, T. J., Paterson, D. M., and Hagerthey, S. E. (2002). Working with natural cohesive sediments. *J. Hydraul. Eng.* 128, 2–8. doi: 10.1061/(ASCE)0733-94292002128:1(2)

Dickhudt, P. J., Friedrichs, C. T., Schaffner, L. C., and Sanford, L. P. (2009). Spatial and temporal variation in cohesive sediment erodibility in the York

River estuary, eastern USA: a biologically influenced equilibrium modified by seasonal deposition. *Mar. Geol.* 267, 128–140. doi: 10.1016/j.margeo.2009.09.009

Fagherazzi, S., Viggato, T., Vieillard, A., Mariotti, G., and Fulweiler, R. W. (2017). The effect of evaporation on the erodibility of mudflats in a mesotidal estuary. *Estuar. Coast. Shelf Sci.* 194, 118–127. doi: 10.1016/j.ecss.2017.06.011

Fall, K. A., Harris, C. K., Friedrichs, C. T., Rinehimer, J. P., and Sherwood, C. R. (2014). Model behavior and sensitivity in an application of the cohesive bed component of the community sediment transport modeling system for the York River Estuary, VA, USA. *J. Mar. Sci. Eng.* 2, 413–436. doi: 10.3390/jmse2020413

Grabowski, R. C., Droppo, I. G., and Wharton, G. (2011). Erodibility of cohesive sediment: the importance of sediment properties. *Earth Sci. Rev*. 105, 101–120. doi: 10.1016/j.earscirev.2011.01.008

Gust, G., and Müller, V. (1997). "Interfacial hydrodynamics and entrainment functions of currently used erosion devices," in *Cohesive Sediments*, eds N. Burt, R. Parker, and J. Watts (Wallingford, CT: Wiley), 149–174.

Ha, H. J., Choi, S. M., Seo, J. Y., and Ha, H. K. (2018). Erodibility of sand-mud mixed sediment on the Yeochari tidal flat, Gyeonggi Bay, Korea. *J. Coast. Res.* 85, 416–420. doi: 10.2112/SI85-084.1

Ha, H. K., Ha, H. J., Seo, J. Y., and Choi, S. M. (2018). Effects of vegetation and fecal pellets on the erodibility of cohesive sediments: Ganghwa tidal flat, west coast of Korea. *Environ. Pollut.* 241, 468–474. doi: 10.1016/j.envpol.2018.05.067

Ha, H. K., and Maa, J. P.-Y. (2009). Evaluation of two conflicting paradigms for cohesive sediment deposition. *Mar. Geol.* 265, 120–129. doi: 10.1016/j.margeo.2009.07.001

Jacobs, W., Le Hir, P., van Kesteren, W., and Cann, P. (2011). Erosion threshold of sand-mud mixtures. *Cont. Shelf Res*. 31, S14–S25. doi: 10.1016/j.csr.2010.05.012

Jago, C. F., Jones, S. E., Latter, R. J., McCandliss, R. R., Hearn, M. R., and Howarth, M. J. (2002). Resuspension of benthic fluff by tidal currents in deep stratified waters, northern North Sea. *J. Sea Res*. 48, 259–269. doi: 10.1016/S1385-1101(02)00181-8

Koh, C.-H., and Khim, J. S. (2014). The Korean tidal flat of the Yellow sea: physical setting, ecosystem and management. *Ocean Coast. Manage.* 102, 398–414. doi: 10.1016/j.ocecoaman.2014.07.008

KMA (2017). *National Climate Data Service System*. Available online at: http://sts.kma.go.kr/. (accessed September 30, 2020).

Lee, H. J., Park, J. Y., Lee, S. H., Lee, J. M., and Kim, T. K. (2013). Suspended sediment transport in a rock-bound, macrotidal estuary: Han estuary, eastern Yellow sea. *J. Coast. Res.* 29, 358–371. doi: 10.2112/JCOASTRES-D-12-00066.1

Maa, J. P.-Y., and Kim, S. C. (2002). A constant erosion rate model for fine sediment in the York River, Virginia. *Environ. Fluid Mech.* 1, 343–360. doi: 10.1023/A:1015799926777

Neumeier, U., Friend, P. L., Gangelhof, U., Lunding, J., Lundkvist, M., Bergamasco, A., et al. (2007). The influence of fish feed pellets on the stability of seabed sediment: a laboratory flume investigation. *Estuar. Coast. Shelf Sci.* 75, 347–357. doi: 10.1016/j.ecss.2007.04.036

Panagiotopoulos, I., Voulgaris, G., and Collins, M. B. (1997). The influence of clay on the threshold of movement of fine sandy beds. *Coast. Eng.* 32, 19–43. doi: 10.1016/S0378-3839(97)00013-6

Park, H. B., and Lee, G. (2016). Evaluation of ADCP backscatter inversion to suspended sediment concentration in estuarine environments. *Ocean Sci. J.* 51, 109–125. doi: 10.1007/s12601-016-0010-3

Park, J., Kwon, B. O., Kim, M., Hong, S., Ryu, J., Song, S. J., et al. (2014). Microphytobenthos of Korean tidal flats: a review and analysis on floral distribution and tidal dynamics. *Ocean Coast. Manag.* 102, 471–482. doi: 10.1016/j.ocecoaman.2014.07.007

Roberts, J., Jepsen, R., Gotthard, D., and Lick, W. (1998). Effects of particle size and bulk density on erosion of quartz particles. *J. Hydraul. Eng.* 124, 1261–1267. doi: 10.1061/(ASCE)0733-94291998124:121261

Sanford, L. P. (2006). Uncertainties in sediment erodibility estimates due to a lack of standards for experimental protocols and data interpretation. *Integr. Environ. Assess. Manage.* 2, 29–34. doi: 10.1002/ieam.5630020106

Sanford, L. P., and Maa, J. P. Y. (2001). A unified erosion formulation for fine sediments. *Mar. Geol.* 179, 9–23. doi: 10.1016/S0025-3227(01)00201-8

Schoellhamer, D. H., Manning, A. J., and Work, P. A. (2017). Erosion characteristics and horizontal variability for small erosion depths in the Sacramento-San Joaquin River Delta, California, USA. *Ocean Dyn.* 67, 799–811. doi: 10.1007/s10236-017-1047-2

Seo, J. Y., Choi, S. M., Ha, H. K., and Lee, K. E. (2020). Enhanced erodibility of deep-sea sediments by presence of calcium carbonate particles. *Geo Mar. Lett.* 40, 559–571. doi: 10.1007/s00367-020-00651-x

Sutherland, T. F., Amos, C. L., and Grant, J. (1998). "The erosion threshold of biotic sediments: a comparison of methods," in *Sedimentary Processes in the Intertidal Zone*, eds K. S. Black, D. M. Paterson, and A. Cramp (London: Geological Society), 295–307.

Thompson, C. E. L., Couceiro, F., Fones, G. R., and Amos, C. L. (2013). Shipboard measurements of sediment stability using a small annular flume-Core Mini Flume (CMF). *Limnol. Oceanogr. Methods* 11, 604–615. doi: 10.4319/lom.2013.11.604

van Ledden, M., van Kesteren, W. G. M., and Winterwerp, J. C. (2004). A conceptual framework for the erosion behavior of sand-mud mixtures. *Cont. Shelf Res.* 24, 1–11. doi: 10.1016/j.csr.2003.09.002

Wiberg, P. L., Law, B. A., Wheatcroft, R. A., Milligan, T. G., and Hill, P. S. (2013). Seasonal variations in erodibility and sediment transport potential in a mesotidal channel-flat complex, Willapa Bay, WA. *Cont. Shelf Res.* 60S, S185–S197. doi: 10.1016/j.csr.2012.07.021

Widdows, J., Brinsley, M. D., Bowley, N., and Barrett, C. (1998). A benthic annular flume for in situ measurement of suspension feeding/biodeposition rates and erosion potential of intertidal cohesive sediments. *Estuar. Coast. Shelf Sci.* 46, 27–38. doi: 10.1006/ecss.1997.0259

Widdows, J., Friend, P. L., Bale, A. J., Brinsley, M. D., Pope, N. D., and Thompson, C. E. L. (2007). Inter-comparison between five devices for determining erodability of intertidal sediments. *Cont. Shelf Res.* 27, 1174–1189. doi: 10.1016/j.csr.2005.10.006

Winterwerp, J. C., and van Kesteren, W. G. M. (2004). *Introduction to the Physics of Cohesive Sediment Dynamics in the Marine Environment*. Oxford: Elsevier B.V.

Xu, K., Bentley, S. J., Robichaux, P., Sha, X., and Yang, H. (2016). Implications of texture and erodibility for sediment retention in receiving basins of coastal Louisiana diversions. *Water* 8:26. doi: 10.3390/w8010026

Xu, K., Corbett, D., Walsh, J., Young, D., Briggs, K., Cartwright, G. M., et al. (2014). Seabed erodibility variations on the Louisiana continental shelf before and after the 2011 Mississippi River flood. *Estuar. Coast. Shelf Sci.* 149, 283–293. doi: 10.1016/j.ecss.2014.09.002

Conflict of Interest: The authors declare that the research was conducted in the absence of any commercial or financial relationships that could be construed as a potential conflict of interest.

Publisher's Note: All claims expressed in this article are solely those of the authors and do not necessarily represent those of their affiliated organizations, or those of the publisher, the editors and the reviewers. Any product that may be evaluated in this article, or claim that may be made by its manufacturer, is not guaranteed or endorsed by the publisher.

frontiers in Marine Science

BRIEF RESEARCH REPORT
published: 15 November 2021
doi: 10.3389/fmars.2021.695780

Derivation and Evaluation of Satellite-Based Surface Current

*Jun Myoung Choi[1], Wonkook Kim[2], Tran Thy My Hong[1] and Young-Gyu Park[3]**

[1] Ocean Engineering, College of Environmental and Marine Sciences and Technology, Pukyong National University, Busan, South Korea, [2] Department of Civil and Environmental Engineering, Pusan National University, Busan, South Korea, [3] Ocean Circulation and Climate Research Center, Korea Institute of Ocean Science and Technology, Busan, South Korea

Observations of real-time ocean surface currents allow one to search and rescue at ocean disaster sites and investigate the surface transport and fate of ocean contaminants. Although real-time surface currents have been mapped by high-frequency (HF) radar, shipboard instruments, satellite altimetry, and surface drifters, geostationary satellites have proved their capability in satisfying both basin-scale coverage and high spatiotemporal resolutions not offered by other observational platforms. In this paper, we suggest a strategy for the production of operational surface currents using geostationary satellite data, the particle image velocimetry (PIV) method, and deep learning-based evaluation. We used the model scalar field and its gradient to calculate the corresponding surface current *via* PIV, and we estimated the error between the true velocity field and calculated velocity field by the combined magnitude and relevance index (CMRI) error. We used the model datasets to train a convolutional neural network, which can be used to filter out bad vectors in the surface current produced by arbitrary model scalar fields. We also applied the pretrained network to the surface current generated from real-time Himawari-8 skin sea surface temperature (SST) data. The results showed that the deep learning network successfully filtered out bad vectors in a surface current when it was applied to model SST and created stronger dynamic features when the network was applied to Himawari SST. This strategy can help to provide a quality flag in satellite data to inform data users about the reliability of PIV-derived surface currents.

Keywords: surface current, geostationary satellite, convolutional neural network, sea surface temperature, particle tracking velocimetry, submesoscale circulations

OPEN ACCESS

Edited by:
Ho Kyung Ha,
Inha University, South Korea

Reviewed by:
Dongmin Jang,
Korea Institute of Science and Technology Information (KISTI), South Korea
Byoung-Ju Choi,
Chonnam National University, South Korea

****Correspondence:***
Young-Gyu Park
ypark@kiost.ac.kr

Specialty section:
This article was submitted to Ocean Observation, a section of the journal Frontiers in Marine Science

Received: *15 April 2021*
Accepted: *13 October 2021*
Published: *15 November 2021*

Citation:
Choi JM, Kim W, Hong TTM and Park Y-G (2021) Derivation and Evaluation of Satellite-Based Surface Current. Front. Mar. Sci. 8:695780. doi: 10.3389/fmars.2021.695780

INTRODUCTION

Ocean surface currents are the most complex flows in the ocean, as non-homogeneous, non-isotropic, and non-stationary processes dominate the flows with temporal variability from hours to years. They are also the most interactive flows, as biological, geochemical, and physical processes coexist to create the unique phenomena between the ocean interior and the atmosphere. Although many observational platforms have been successfully introduced to monitor the complex surface currents, there is still a need to observe the broader surface area in more detail and even more frequently.

The information of surface currents is crucial in practical and scientific applications. Accurate real-time estimation of surface currents is required for conducting search and rescue activities at

maritime accidents and predicting the transport of contaminants in the ocean surface layer (Walker et al., 2005; Breivik and Allen, 2008; Rypina et al., 2014). Maritime accidents such as the Malaysian Airlines Flight 370 airplane crash in 2014 (Corrado et al., 2017) and the Stellar Daisy bulk carrier sinking in 2017 (Dalziel and Pelot, 2019) demonstrate the importance of surface currents, which can be used to backtrack paths to the initial accident locations (Dohan, 2017). Most ocean contaminants [e.g., crude oil (Laxague et al., 2018), radioactive substances (Buesseler et al., 2012), microplastic (Iwasaki et al., 2017), sargassum (Kwon et al., 2019), river plume of nutrient-rich agricultural runoff (Sklar and Browder, 1998)] are initially distributed in the surface layer and persist in the upper layer for a while. Consequently, the surface information provides a crucial clue to estimate the fate of the contaminants. The derivation of surface currents also enables scientific estimations of the spectral behavior of kinetic energy, local dispersion, biological productivity, energy transfer, frontal behavior, and air–sea interaction, which elucidate the roles they play in weather and climate (Boccaletti et al., 2007; LaCasce, 2008; Molemaker et al., 2010; Mahadevan, 2016; Choi et al., 2019).

A major breakthrough in generating surface currents was facilitated by the advancement of satellite remote sensing. Surface currents have been measured by not only *in situ* observations at moorings and ships (Rocha et al., 2016) but also remote observations such as floats, drifters, and high-frequency (HF) radar (Bracco et al., 2003; Lumpkin and Pazos, 2007; Rypina et al., 2014; Berta et al., 2015; Yoo et al., 2018). Starting from the geophysical-scale velocity field calculated by Leese et al. (1971), the products of a polar-orbiting satellite have been successfully exploited to generate surface currents (Emery et al., 1986; Zavialov et al., 2002; Osadchiev and Sedakov, 2019). The high-resolution surface roughness measurements from SAR have also shown great potential to create surface currents unaffected by cloud block (Dohan and Maximenko, 2010; Yanovsky et al., 2020).

Over the past decade, a geostationary satellite has been used to generate submesoscale currents using ocean color products (Yang et al., 2014; Kim et al., 2016; Sun et al., 2016; Park et al., 2018; Choi et al., 2019). Its unique "stationary" feature alleviates the chronic issue of low temporal resolution of the polar-orbiting satellite. Thanks to the capability of high temporal measurements, the Geostationary Ocean Color Imager has been used to not only generate high-resolution surface currents but also study submesoscale turbulence in the surface layer (Choi et al., 2019).

Although the geostationary satellite is capable of resolving submesoscale currents and the demand for data on surface currents has increased, no geostationary satellite-based operational surface currents have been used in practice. The AVISO global geostrophic currents have been operated by using data from satellite altimetry, and data-assimilated products such as the Ocean Surface Currents Analyses Real-time (OSCAR) are also being operated to produce mixed-layer surface currents combining AVISO geostrophic currents and Ekman and thermal wind components. However, those platforms have coarse resolutions (∼1 day, 25 km) unsuitable for narrowing the location of a surface target whose movement is affected by wind, tides, and small-scale circulations and understanding vertical transport associated with submesoscale phenomena.

In this paper, considering the geostationary satellite as an operational surface currents platform, we propose a preliminary strategy for generating the satellite-based surface currents by applying a deep learning convolutional neural network (CNN). Deep learning examines the relationship between input data and output data to prepare rules for estimating or evaluating output associated with new input data. As a subset of deep learning, CNNs are commonly applied in pattern recognition and image processing, and have recently become a powerful tool to identify and classify patterns in Earth science data (Ham et al., 2019; Huntingford et al., 2019; Chattopadhyay et al., 2020; Lou et al., 2021). In our application, we trained a neural network using a model dataset, and the network was used to determine the goodness of fit of each vector in the surface currents to provide a quality flag along with the surface currents. We apply this strategy to Himawari-8 skin SST data to demonstrate the generation of surface currents using satellite data.

MATERIALS AND METHODS

Surface Current Generation

In this paper, we suggest a strategy that can be used to produce operational surface currents using data from a geostationary satellite. One possible data source is the SST from the Advanced Himawari Imager (AHI) onboard Himawari-8. The SST is estimated from the infrared (IR) bands centered at 3.9, 8.6, 10.4, and 11.2 μm whose spatial resolution in the raw data is 2 km. Validation performed against over 630,000 pairs with drifting and moored buoy data showed a root-mean-square difference of 0.59 K and bias of −0.16 K (Kurihara et al., 2016). The negative bias is due to the difference between the skin temperature that satellites sense and the bulk temperature that the buoy measures, and the bias of −0.16 K is consistent with the bias level reported for an advanced very-high-resolution radiometer (Donlon et al., 2002).

To generate a velocity field near the ocean surface from the geostationary data, we use the PIVlab Matlab code (Thielicke, 2014; Thielicke and Stamhuis, 2014; Thielicke and Sonntag, 2021) that implements the Particle Image Velocimetry (PIV) technique (Wereley and Meinhart, 2010; Xu and Chen, 2013). It is a standard experimental strategy that generates an instantaneous velocity field in the laboratory, where the particles (herein, equivalent to scalar tracers SST or Chla) in the cross section of the water channel (herein, satellite coverage) are illuminated by a laser sheet (herein, the sun), and the particle movement is recorded by a camera (herein, a satellite sensor). The PIV algorithm generates a cross-correlation plane by taking the FFT between two same-sized interrogation windows obtained individually from two successive images, and an optimized displacement vector is determined in a way that maximizes image matching. By virtue of its ability to derive a wide range of velocity scales, the PIV has been applied to analyzing micro-fluid (Santiago et al., 1998), river discharge (Legleiter et al., 2017), supersonic flows (Avallone et al., 2016), the atmospheric flow

of Jupiter (Tokumaru and Dimotakis, 1995), and the flow rate of the Deepwater Horizon oil spill (McNutt et al., 2012). Our application aimed to generate a basin-scale velocity field across the satellite coverage by applying the PIV technique to two satellite images, followed by evaluating the velocity field by the deep learning CNN.

Evaluation of Surface Current by Convolutional Neural Network

The CNN architecture consists of multiple layers (input, output, and other hidden layers). In this calculation, the hidden layers include multiple convolutional layers: max pooling layer, activating layers (batch normalization, PreLu, and softmax layers), fully connected layer, and classification layer. The batch normalization, Parametric rectified Linear unit (PreLu), and max pooling layers are used after each convolutional layer. The final layer, the classification layer, uses the probabilities returned by the softmax activation function for each input to assign the input to one of the mutually exclusive classes and calculate the loss. After defining the network structure, the dataset is trained with the specific options: stochastic gradient descent with momentum (SGDM), constant learning rate of 0.01, and maximum number of epochs of 60. The convolutional layers are established with a padding and stride of 1, the size of filter at 11, and the number of filters at 128. The images are categorized into two classes (i.e., good and bad, each with 80,000 images), and the deep learning CNN[1] is used to train and validate the velocity data.

In this paper, the evaluation of the surface current consists of three steps: preparing ground truth data (model SST field and corresponding model velocity field), training a neural network using the ground truth dataset, and applying the network to model SST and Himawari-8 SST to demonstrate a quality flag in the satellite data.

First, to train the deep learning network, we prepared the ground truth data from the ocean model and synthesized it by image translation. We used model SST from the Ocean Predictability Experiment for Marine environment (OPEM) based on the GFDL Modular Ocean Model (MOM) version 5 with a horizontal resolution of 1/24° (Kim et al., 2015). We interpolated the raw data to a 2-km grid to match the resolution of Himawari-8 SST in the area of the East/Japan Sea (**Supplementary Figure 1**). We used the model SST snapshots (300×300) at 12 different times through the 9-month simulation to train the deep learning network. We translated each image of model SST (I_1) by a spatially constant velocity field (V_{true}) to create a new deformed image (I_2). Then, the PIV algorithm processed the two images (I_1 and I_2) to generate a calculated velocity field (V_{cal}). Three calculated velocity fields (SST-R, SST-G, SST-G^2) were considered: SST-R is surface currents from the raw SST (SST-R), SST-G is surface current from the spatial gradient of raw SST, and SST-G^2 is surface current from the double gradient of raw SST. By comparing V_{true} and V_{cal}, an error between model (true) and PIV (calculated) velocity fields was estimated to evaluate the performance of the PIV algorithm at every vector. To ensure the deep learning network could cope with various cases, instead of using the model velocity field corresponding to the model SST field, we used various velocity fields that differed in amplitude (0.05, 0.1, 0.2, 0.4, and 0.7 m/s) and direction (0 to 330° at intervals of 30°), which provided 60 times more data (approximately 1.8 million vectors) for training than using the model velocity fields. To validate the network trained using 80% of the vectors, we estimated the classification accuracy (validation accuracy) using the remaining 20% vectors.

We implemented three types of error (weighted relevance index (WRI), weighted magnitude index (WMI), and combined magnitude and relevance index (CMRI) used in Willman et al., 2020) to quantify the deviation of V_{cal} from V_{true}. Because typical indices such as the relevance index (RI) and the magnitude similarity index (MSI) are known to show problematic high sensitivity to low-amplitude vectors, we used these errors (WRI, WMI, and CMRI) to overcome the issue (Willman et al., 2020). The WRI is a metric of alignment evaluation, the WMI is a metric of magnitude evaluation, and the CMRI considers both evaluations of alignment and direction (Willman et al., 2020). These errors are defined as

$$WRI\left(x,y\right)=\left(\frac{1-RI\left(x,y\right)}{2}\right)\times\left(\frac{U_1\left(x,y\right)}{median\left(U_1\right)}\right)\times\left(\frac{U_2\left(x,y\right)}{median\left(U_2\right)}\right) \quad (1)$$

$$WMI\left(x,y\right)=\frac{\left|U_1\left(x,y\right)-U_2\left(x,y\right)\right|}{median\left(U_1,U_2\right)} \quad (2)$$

$$CMRI(x,y)=\frac{WRI(x,y)+WMI(x,y)}{2} \quad (3)$$

where x and y are two-dimensional coordinates, U_1 and U_2 are the magnitude of the true and calculated velocity vectors, RI is $[=(\overrightarrow{u_1}\cdot\overrightarrow{u_2})/(|\overrightarrow{u_1}||\overrightarrow{u_2}|)]$, and MSI is $(=1-(|\overrightarrow{u_1}-\overrightarrow{u_2}|)/(|\overrightarrow{u_1}|+|\overrightarrow{u_2}|)$, where u_1 and u_2 are the true and calculated velocity vectors, and *median* is defined as the statistical median of all components.

Second, we trained a neural network that was fed SST image data. The difference in the two images represents the temporal and spatial changes in a concise way, so the image difference (I_{2-1}) between I_1 and I_2 was chosen as the input to the network. Since it is trained such that the errors are paired up with the characteristics of I_{2-1}, the deep learning network allows the estimation of the goodness of fit of a PIV-derived vector associated with an arbitrary I_{2-1}.

Third, we evaluated the PIV-derived velocity field by applying the pretrained network to the arbitrary model SST field that accompanied the velocity field, from which the performance of the trained network was examined. The network was also applied to SST observation from the geostationary satellite (Himawari-8 SST) to demonstrate the generation of surface currents with deep learning-selected vectors. Due to the lack of ground truth data to train the network for evaluating satellite-based surface currents, the offline pretrained neural network should be prepared using synthetic data, as we did in this paper.

[1]MATLAB and Deep Learning Toolbox Release 2021b, The MathWorks, Inc., Natick, MA.

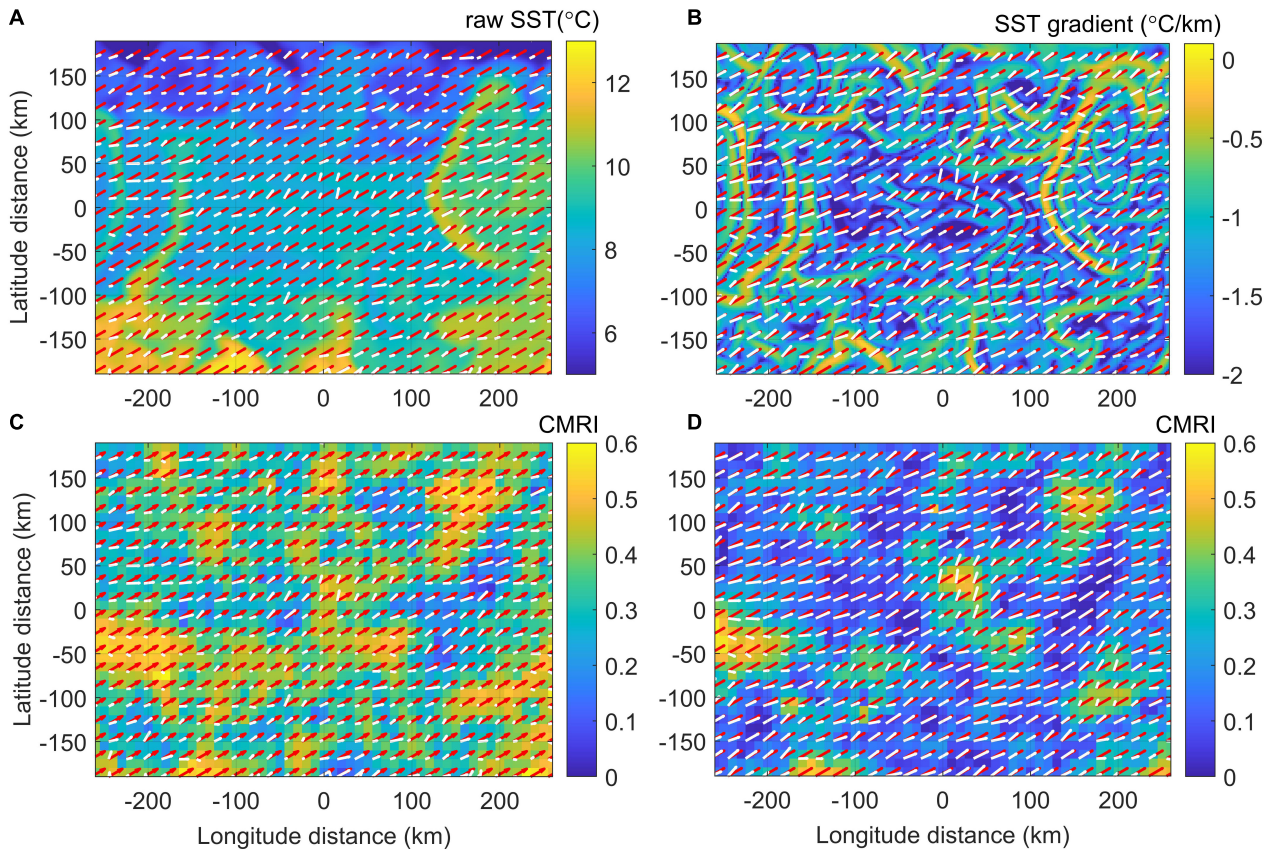

FIGURE 1 | Example comparison of true velocity field V_{true} in a 10 km-grid (red arrows) and calculated velocity field V_{cal} in a 10 km-grid (white arrows) for raw SST **(A)** and SST gradient **(B)**. Contours in panels **(C,D)** show CMRI errors corresponding to panels **(A,B)**, respectively.

RESULTS

Surface Current by Particle Image Velocimetry and Sea Surface Temperature

Figure 1 compares the idealized uniform velocity field and the calculated velocity field. Despite the uniform velocity field used to deform or translate the scalar field, the deviations in amplitude and alignment were not homogeneous, and they showed a bias linked to the spatial structures of the scalar field. For the SST-R, it tends to show poor agreement between V_{true} (red arrows) and V_{cal} (white arrows) over the region where the direction of V_{true} is aligned with the direction of the SST front [e.g., (x, y) = (−200, −50) and (150, 100)], while good agreement can be found in the region where the direction of V_{true} is perpendicular to the direction of the SST front [e.g., (x, y) = (150, −50)]. The spatially different errors can be more clearly identified when SST-G is considered. It is observed that the directions of the SST gradient and the CMRI error are strongly correlated when they are parallel or perpendicular to each other: a high CMRI for the parallel direction and a low CMRI for the perpendicular direction. For the other angles, the direction of V_{cal} is coherently biased toward the normal direction of the front, as demonstrated at (x, y) = (30,−120) and (120, 0) in **Figure 1B**.

The relevant spatially varying error inevitably occurs by the PIV method that applies to the smooth scalar image that does not include noise-like particles whose scale is much smaller than the interrogation window. Even the scale of features revealed in the scalar field we have was comparable to the grid size of the velocity field. In this case, the PIV algorithm misleadingly interprets the movement of a unidirectional front to the direction normal to the front. The smaller the features in the scalar field, the lower the CMRI error. This can be simply examined by adding a noise before performing PIV: if a random noise (maximum magnitude at 5% of STD) was added to the first image (I_1), the CMRI error in **Figures 1C,D** were reduced by 10% for SST-R and 50% for SST-G.

Figure 2 shows spatially averaged errors (WRI, WMI, and CMRI) that vary with different angles and magnitudes of V_{true} for SST-R, SST-G, and SST-G^2 (second-order gradient). For the SST-R case, the difference between two consecutive images is less distinct, which increases the uncertainty in determining the displacement vector in the cross-correlation calculation. WRI (**Figures 2A–C**), WMI (**Figures 2D–F**), and CMRI (**Figures 2G–I**) indicate that taking the gradient of SST is advantageous for both vector alignment and magnitude estimations. Emery et al. (1986) qualitatively showed that

using the SST gradient yields better results from raw SST; however, most works afterward utilized raw scalar fields to derive surface currents from satellite observations (Yang et al., 2014; Kim et al., 2016; Sun et al., 2016; Park et al., 2018; Choi et al., 2019). Nevertheless, when taking multiple gradients, the narrowing front becomes indistinguishable from random noise

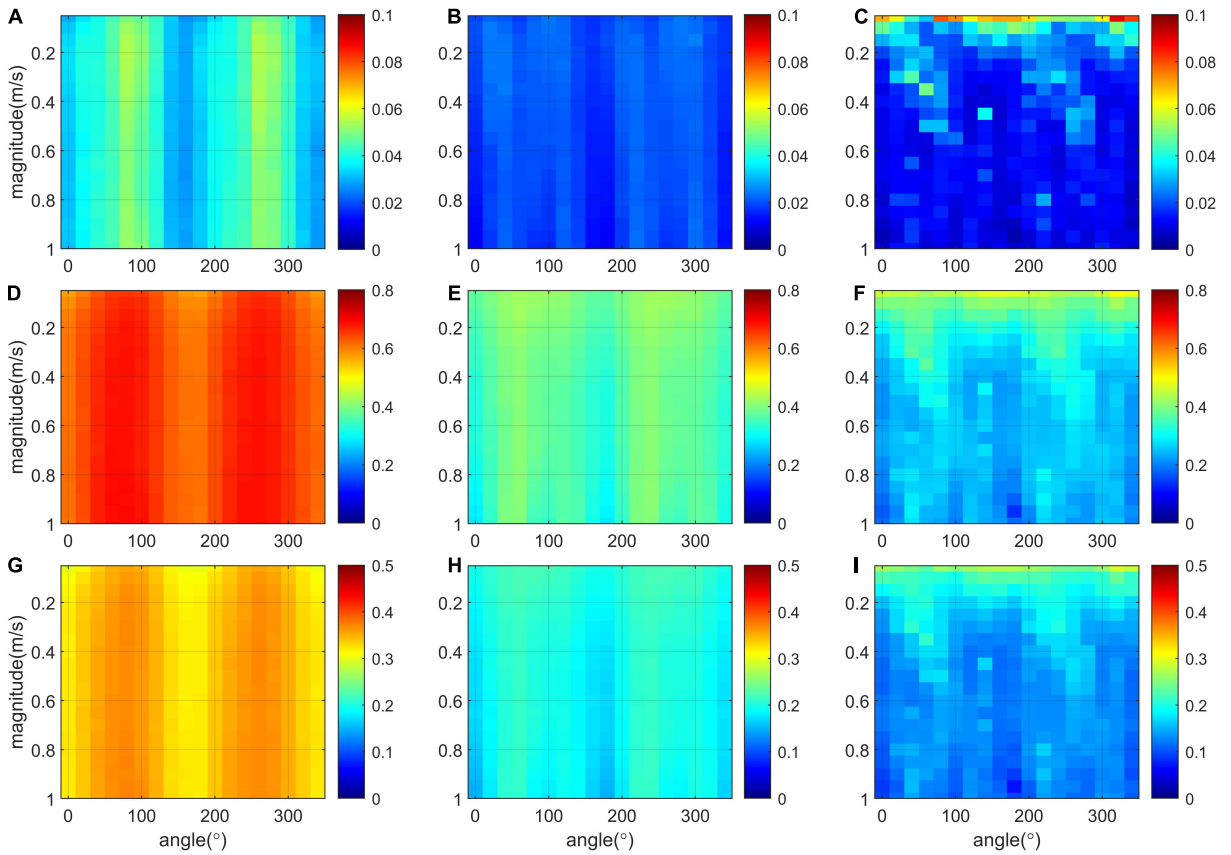

FIGURE 2 | Spatially-averaged WRI (upper panels), WMI (middle panels), CMRI (lower panels) errors for SST-R **(A,D,G)**, SST-G **(B,E,H)**, and SST-G^2 **(C,F,I)** depending on the magnitude and direction of V_{true}. SST-R, SST-G, and SST-G^2 indicate surface current generated from the raw SST, the spatial gradient of raw SST, and the second order spatial gradient of raw SST, respectively.

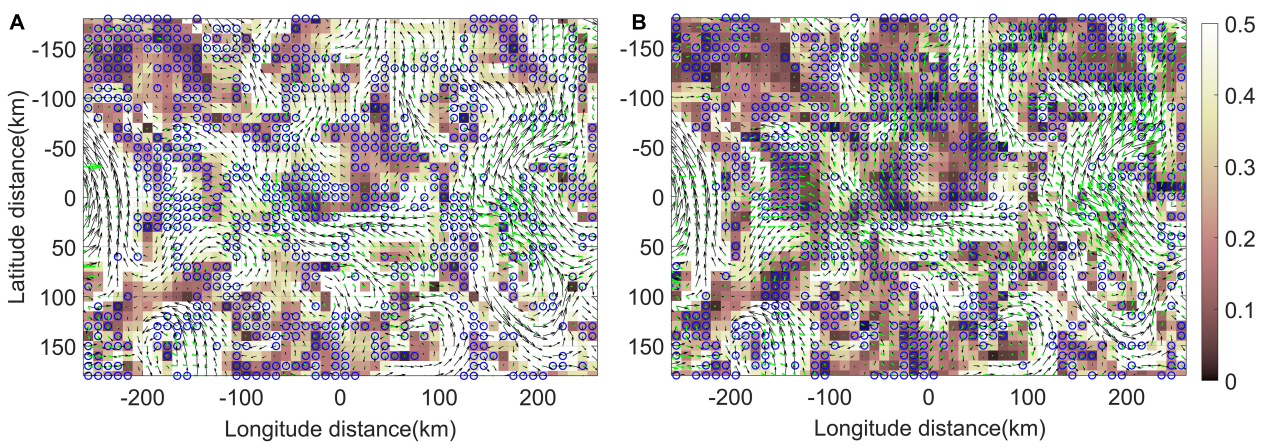

FIGURE 3 | Surface current reliability determination based on CNN evaluation for SST-R **(A)** and SST-G **(B)**. The black vector is the model surface current (true), and the green vector is the PIV surface current (calculated). The background color represents the difference (CMRI error) between the true value and the calculated value (0: lowest error / 1: highest error). The blue circles designate the vectors within top 30% having high reliability evaluated by deep learning CNN.

so that the error can be increased from the smallest grid size, as shown in **Figures 2C,F,I**.

The error is amplified near the angles around 90° and 270° (**Figure 2A**), and such observation indicates an anisotropy in the horizontal shape of mesoscale eddies and fronts that are elongated and aligned along the north–south direction over the East/Japan Sea, which appears more prominently in the WRI error. The spatial averages of CMRI were 0.34, 0.20, and 0.15 for SST-R, SST-G, and SST-G^2, respectively. Those for WRI (WMI) were 0.04, 0.02, and 0.02 (0.65, 0.37, and 0.28), respectively.

Convolutional Neural Network Training and Surface Current Evaluation

By applying the CNN to the training datasets SST-R and SST-G, we generated a network that classified the image difference into two classes, good and bad, based on the CMRI error. For the SST-R training dataset, the image difference for low CMRI $<$ 0.3 and high CMRI $>$ 0.4 were labeled as good and bad vectors, respectively, while for the SST-G training dataset, low CMRI $<$ 0.1 and high CMRI $>$ 0.3 were labeled as good and bad vectors (**Supplementary Figure 3**). The shape of the probability density function (PDF) of CMRI is skewed toward low CMRI for SST-R and Gaussian for SST-G. Those partitions were made to ensure the bad and good classes had similar amounts of data, and different datasets may have different partitions depending on the CMRI PDF. In most cases, images showing more coherent patterns are placed in the good class; however, the traits that lead a vector to be classified in the good or bad class are not determinable without performing deep learning-based examination. In this work, we trained only the SST-R and SST-G datasets for evaluating the surface current, and the final validation accuracies for those at 100 epochs were 85.8 and 89.7%, respectively. The accuracy and the results did not show significant changes after epoch 50.

Figure 3 shows the deep learning-based evaluation of the surface current using synthetic data generated simultaneously by SST and velocity fields on DOY 150 covering longitude 129°N–136.5°N and latitude 36.5°E–40.5°E in the OPEM model. The black and green vectors indicate the model surface current (V_{true}) and calculated surface current (V_{cal}), and the SST-R and SST-G datasets are sequentially displayed in **Figures 3A,B**.

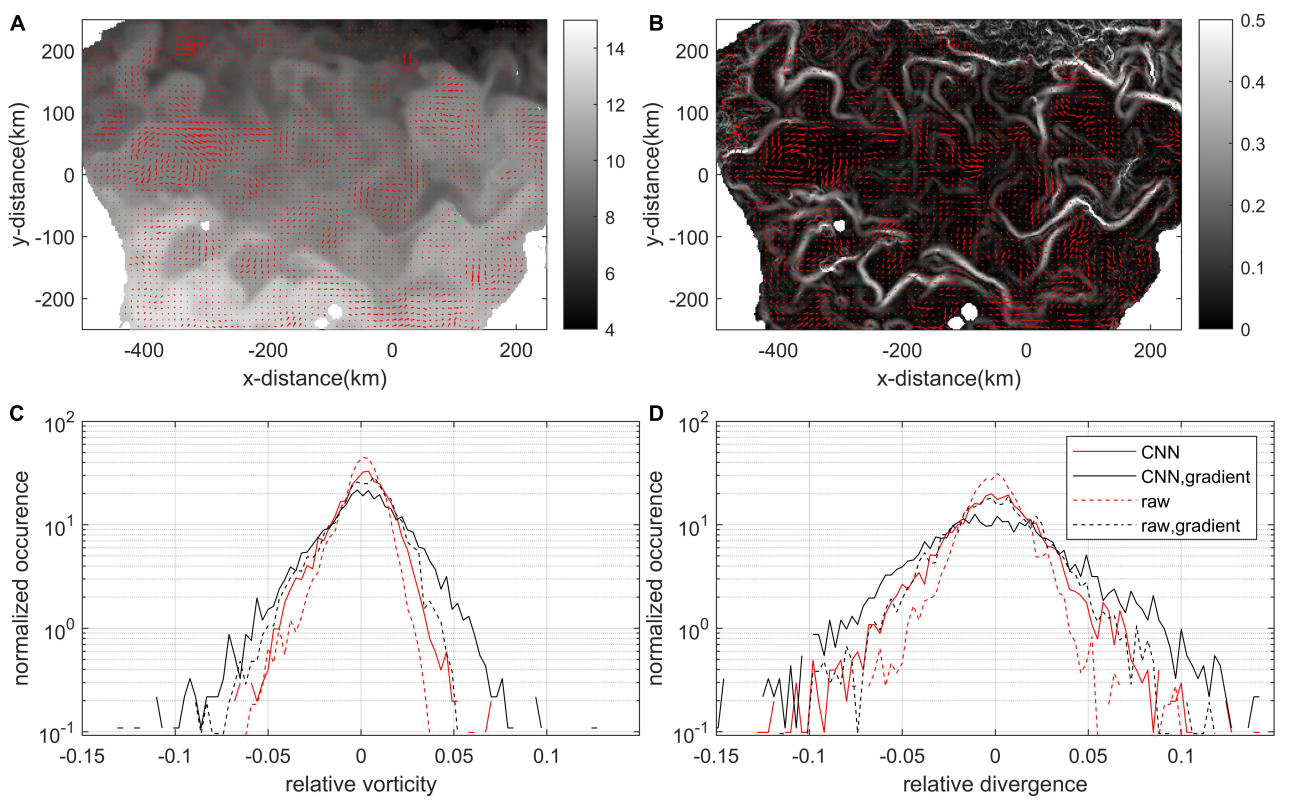

FIGURE 4 | One-day averaged surface current in a 10 km-grid in the East/Japan Sea on 25th March 2018 derived from Himawari SST **(A)** and Himawari SST gradient **(B)** and corresponding scalar fields. 22 hourly velocity fields derived from 23 consecutive SST images were used to calculate the mean surface current for that date. The scattered cloud area accounted for about 68%, and the area excluding the cloud area was used to calculate the mean velocity field. **(C,D)** Indicate vorticity and divergence PDF normalized by local Coriolis parameter. In the legend, "CNN" indicates 1-day averaged surface current using vectors filtered by CNN, "raw" indicates 1-day averaged surface current without CNN filtering, and "gradient" indicates surface current derived from SST gradient. The standard derivation (STD) of the PDF are 0.0158 (CNN), 0.0254 (CNN-gradient), 0.0117 (raw), and 0.0183 (raw-gradient) for relative vorticity, and 0.0288 (CNN), 0.0420 (CNN-gradient), 0.0181 (raw), and 0.0284 (raw-gradient) for relative divergence. The changes in STD show that flatter PDF (or smaller circulations) can be obtained by CNN-filtering and taking gradient of a scalar field.

The background color of the figure is the CMRI error showing the deviation between V_{true} deforming the original image and V_{cal} obtained by applying PIV to the original image (I_1) and the deformed image (I_2). The blue circles designate the vectors within top 30% having high reliability evaluated by deep learning CNN. The pretrained deep learning network classified good vectors (blue circles shown in **Figure 3**), mostly at low CMRI values. To quantify the performance of the network, the correlation coefficient (r) between V_{true} and V_{cal} was calculated (**Supplementary Figure 5**). For SST-R, u and v velocity components showed $r_u = 0.572$ and $r_v = 0.479$ while applying the trained network gave $r_u = 0.761$ and $r_v = 0.722$. For SST-G, u and v velocity components showed $r_u = 0.704$ and $r_v = 0.608$ while applying the trained network gave $r_u = 0.799$ and $r_v = 0.816$. We also calculated the correlation coefficient between δ_{true} and δ_{cal} (divergence) using the same velocity fields. For SST-R, applying the network increased r_δ from 0.366 to 0.401, and for SST-G, applying the network increased r_δ from 0.514 to 0.550. Overall, the surface current involved with SST-G resulted in a lower CMRI error than that involved with SST-R, and the pretrained network using the SST-G dataset showed better performance in identifying good vectors.

The same procedures of calculating the surface current and applying the deep learning pretrained network as above were implemented with the image pair of Himawari skin SST captured on March 25, 2018 over the area of the East/Japan Sea. We obtained V_{cal} in a 10-km resolution by applying PIV to two consecutive Himawari SST images in a 2-km resolution, and each vector was linked to a good or bad vector based on the evaluation by the deep learning network. **Figure 4** shows the 1-day average of the hourly surface currents from hourly Himawari SST (**Figure 4A**) and the Himawari SST gradient (**Figure 4B**). Only vectors within the top 30% accuracy evaluated by the deep learning network at each snapshot were used for the average, and the field were smoothed by a 3×3 mean filter. The surface current generated by the SST gradient contains slightly stronger velocity and dynamic features such that more distinct eddies can be identified.

Figures 4C,D show the PDFs of the vorticity (**Figure 4C**) and divergence (**Figure 4D**) fields normalized by the Coriolis parameter. The PDFs calculated from the PIV-derived current with CNN filtering (solid red lines) have heavier or flatter tails than the ones from the PIV-derived current without the CNN filtering (dashed red lines), and taking the gradient (black lines) also leads the tails to be flatter. Since heavier tail in a divergence and vorticity PDFs is indicative of realizing smaller-scale features (or stronger submesoscale circulations) (Barkan et al., 2017; Choi et al., 2017), it is considered that taking gradients of a scalar field along with filtering the vectors through CNN evaluation are considered helpful in realizing smaller features in the surface current. Due to the limited grid size of surface currents, the sub-grid circulations with a size less than 10 km cannot be considered in this study. However, applying the strategy to high-resolution scalar fields, such as 250 m-grid satellite products from the Geostationary Ocean Color Imager (GOCI), would provide submesoscale-resolving (∼3 km) features in surface currents.

CONCLUSION

The estimation of surface currents associated with geostationary satellite data, the PIV method, and deep learning networks has been conducted to suggest a strategy for the production of operational surface currents. Information of real-time surface currents can be very useful for practical and scientific applications. However, an operating system based on geostationary satellite observation that can cover marginal seas and sample at high spatiotemporal resolutions has not yet been developed.

We demonstrated the generation of surface currents from model SST. Applying PIV to the scalar field resulted in errors that were correlated with the direction of the front and true velocity field. To point out erroneous vectors, we conducted a deep learning-based evaluation of vectors, which was achieved by training the image difference between two consecutive scalar images. We found taking the gradient of the scalar field performed better in generating surface currents. We also applied the same procedure to Himawari SST to provide a quality flag indicating the surface current's reliability. Based on the quality flag that evaluated each vector, good vectors were chosen and used to generate an averaged velocity field showing clear dynamics of coherent mesoscale eddies, which was confirmed by heavy tails in the PDFs of kinematics. Although a limited amount of training data was generated and used for deep learning training, the trained network successfully discerned more accurate vectors of the calculated surface currents.

The strategy introduced in this paper can be applied to not only the Himawari satellite but also the newly launched GOCI-II geostationary satellite that just started generating ocean color scalar fields in a 250-m grid. Furthermore, this study can be extended to produce vast synthetic data (model and experimental data) to develop a pretrained network that can give the right vector in numerous situations and can be applied to different kinds of scalar fields.

DATA AVAILABILITY STATEMENT

The original contributions presented in the study are included in the article/**Supplementary Material**, further inquiries can be directed to the corresponding author/s.

AUTHOR CONTRIBUTIONS

JC: plan research, write paragraphs, and data analysis. WK: write paragraphs and research advice. TH: write paragraphs and data analysis. Y-GP: plan research and research advice. All authors contributed to the article and approved the submitted version.

FUNDING

This work was funded through the projects "Investigation and prediction system development of marine heatwave around the

Korean Peninsula originated from the subarctic and Western Pacific (20190344)" from the Ministry of Oceans and Fisheries, South Korea, and "Building Conceptual Design for Mid-size Integrated CCS Demonstration (20214710100060)" from the Korea Institute of Energy Technology Evaluation and Planning.

SUPPLEMENTARY MATERIAL

The Supplementary Material for this article can be found online at: https://www.frontiersin.org/articles/10.3389/fmars.2021.695780/full#supplementary-material

REFERENCES

Avallone, F., Ragni, D., Schrijer, F. F., Scarano, F., and Cardone, G. (2016). Study of a supercritical roughness element in a hypersonic laminar boundary layer. *AIAA J.* 54, 1892–1900. doi: 10.2514/1.J054610

Barkan, R., McWilliams, J. C., Shchepetkin, A. F., Molemaker, M. J., Renault, L., Bracco, A., et al. (2017). Submesoscale dynamics in the northern Gulf of Mexico. Part I: regional and seasonal characterization and the role of river outflow. *J. Phys. Oceanogr.* 47, 2325–2346. doi: 10.1175/JPO-D-17-0035.1

Berta, M., Griffa, A., Magaldi, M. G., Özgökmen, T. M., Poje, A. C., Haza, A. C., et al. (2015). Improved surface velocity and trajectory estimates in the Gulf of Mexico from blended satellite altimetry and drifter data. *J. Atmos. Ocean. Technol.* 32, 1880–1901. doi: 10.1175/JTECH-D-14-00226.1

Bjorck, J., Gomes, C., Selman, B., and Weinberger, K. Q. (2018). Understanding batch normalization. *arXiv* [Preprint]. arXiv:1806.02375

Boccaletti, G., Ferrari, R., and Fox-Kemper, B. (2007). Mixed layer instabilities and restratification. *J. Phys. Oceanogr.* 37, 2228–2250. doi: 10.1175/JPO3101.1

Bracco, A., Chassignet, E. P., Garraffo, Z. D., and Provenzale, A. (2003). Lagrangian velocity distributions in a high-resolution numerical simulation of the North Atlantic. *J. Atmos. Ocean. Technol.* 20, 1212–1220. doi: 10.1175/1520-04262003020<1212:LVDIAH<2.0.CO;2

Breivik, Ø., and Allen, A. A. (2008). An operational search and rescue model for the Norwegian Sea and the North Sea. *J. Mar. Syst.* 69, 99–113. doi: 10.1016/j.jmarsys.2007.02.010

Buesseler, K. O., Jayne, S. R., Fisher, N. S., Rypina, I. I., Baumann, H., Baumann, Z., et al. (2012). Fukushima-derived radionuclides in the ocean and biota off Japan. *Proc. Natl. Acad. Sci. U.S.A.* 109, 5984–5988. doi: 10.1073/pnas.1120794109/-/DCSupplemental

Cai, S., Zhou, S., Xu, C., and Gao, Q. (2019). Dense motion estimation of particle images via a convolutional neural network. *Exp. Fluids* 60:73. doi: 10.1007/s00348-019-2717-2

Chattopadhyay, A., Hassanzadeh, P., and Pasha, S. (2020). Predicting clustered weather patterns: a test case for applications of convolutional neural networks to spatio-temporal climate data. *Sci. Rep.* 10:1317. doi: 10.1038/s41598-020-57897-9

Choi, J., Bracco, A., Barkan, R., Shchepetkin, A. F., McWilliams, J. C., and Molemaker, J. M. (2017). Submesoscale dynamics in the northern Gulf of Mexico. Part III: Lagrangian implications. *J. Phys. Oceanogr.* 47, 2361–2376. doi: 10.1175/JPO-D-17-0036.1

Choi, J., Park, Y. G., Kim, W., and Kim, Y. H. (2019). Characterization of submesoscale turbulence in the East/Japan sea using geostationary ocean color satellite images. *Geophys. Res. Lett.* 46, 8214–8223. doi: 10.1029/2019GL083892

Corrado, R., Lacorata, G., Palatella, L., Santoleri, R., and Zambianchi, E. (2017). General characteristics of relative dispersion in the ocean. *Sci. Rep.* 7:46291. doi: 10.1038/srep46291

Dalziel, J., and Pelot, R. (2019). "Maritime emergency preparedness and management," in *The Future of Ocean Governance and Capacity Development* (Leiden: Brill Nijhoff), 473–478. doi: 10.1163/9789004380271_082

Dohan, K. (2017). Ocean surface currents from satellite data. *J. Geophys. Res. Oceans* 122, 2647–2651. doi: 10.1002/2017JC012961

Dohan, K., and Maximenko, N. (2010). Monitoring ocean currents with satellite sensors. *Oceanography* 23, 94–103. doi: 10.5670/oceanog.2010.08

Donlon, C. J., Minnett, P. J., Gentemann, C., Nightingale, T. J., Barton, I. J., Ward, B., et al. (2002). Toward improved validation of satellite sea surface skin temperature measurements for climate research. *J. Clim.* 15, 353–369. doi: 10.1175/1520-04422002015<0353:TIVOSS<2.0.CO;2

Emery, W. J., Thomas, A. C., Collins, M. J., Crawford, W. R., and Mackas, D. L. (1986). An objective method for computing advective surface velocities from sequential infrared satellite images. *J. Geophys. Res. Oceans* 91, 12865–12878. doi: 10.1029/JC091iC11p12865

Guo, T., Dong, J., Li, H., and Gao, Y. (2017). "Simple convolutional neural network on image classification," in *Proceedings of the 2017 IEEE 2nd International Conference on Big Data Analysis (ICBDA)*, (Piscataway, NJ: IEEE), 721–724.

Ham, Y. G., Kim, J. H., and Luo, J. J. (2019). Deep learning for multi-year ENSO forecasts. *Nature* 573, 568–572. doi: 10.5281/zenodo.3244463

Huntingford, C., Jeffers, E. S., Bonsall, M. B., Christensen, H. M., Lees, T., and Yang, H. (2019). Machine learning and artificial intelligence to aid climate change research and preparedness. *Environ. Res. Lett.* 14:124007. doi: 10.1088/1748-9326/ab4e55

Iwasaki, S., Isobe, A., Kako, S. I., Uchida, K., and Tokai, T. (2017). Fate of microplastics and mesoplastics carried by surface currents and wind waves: a numerical model approach in the Sea of Japan. *Mar. Pollut. Bull.* 121, 85–96. doi: 10.1016/j.marpolbul.2017.05.057

Kim, W., Moon, J. E., Park, Y. J., and Ishizaka, J. (2016). Evaluation of chlorophyll retrievals from Geostationary Ocean color imager (GOCI) for the north-east Asian region. *Remote Sens. Environ.* 184, 482–495. doi: 10.1016/j.rse.2016.07.031

Kim, Y. H., Hwang, C., and Choi, B. J. (2015). An assessment of ocean climate reanalysis by the data assimilation system of KIOST from 1947 to 2012. *Ocean Model.* 91, 1–22. doi: 10.1016/j.ocemod.2015.02.006

Kurihara, Y., Murakami, H., and Kachi, M. (2016). Sea surface temperature from the new Japanese geostationary meteorological Himawari−8 satellite. *Geophys. Res. Lett.* 43, 1234–1240. doi: 10.1002/2015GL067159

Kwon, K., Choi, B. J., Kim, K. Y., and Kim, K. (2019). Tracing the trajectory of pelagic *Sargassum* using satellite monitoring and Lagrangian transport simulations in the East China Sea and Yellow Sea. *Algae* 34, 315–326. doi: 10.4490/algae.2019.34.12.11

LaCasce, J. (2008). Statistics from Lagrangian observations. *Prog. Oceanogr.* 77, 1–29. doi: 10.1016/j.pocean.2008.02.002

Lancewicki, T., and Kopru, S. (2019). Automatic and simultaneous adjustment of learning rate and momentum for stochastic gradient descent. *arXiv* [Preprint]. arXiv:1908.07607

Laxague, N. J., Özgökmen, T. M., Haus, B. K., Novelli, G., Shcherbina, A., Sutherland, P., et al. (2018). Observations of near−surface current shear help describe oceanic oil and plastic transport. *Geophys. Res. Lett.* 45, 245–249. doi: 10.1002/2017GL075891

Leese, J. A., Novak, C. S., and Clark, B. B. (1971). An automated technique for obtaining cloud motion from geosynchronous satellite data using cross correlation. *J. Appl. Meteorol. Climatol.* 10, 118–132. doi: https://doi.org/10.1175/1520-0450(1971)010<0118:AATFOC>2.0.CO;2

Legleiter, C. J., Kinzel, P. J., and Nelson, J. M. (2017). Remote measurement of river discharge using thermal particle image velocimetry (PIV) and various sources of bathymetric information. *J. Hydrol.* 554, 490–506. doi: 10.1016/j.jhydrol.2017.09.004

Liu, F., Zhou, Z., Samsonov, A., Blankenbaker, D., Larison, W., Kanarek, A., et al. (2018). Deep learning approach for evaluating knee MR images: achieving high diagnostic performance for cartilage lesion detection. *Radiology* 289, 160–169. doi: 10.1148/radiol.2018172986

Lou, R., Lv, Z., Dang, S., Su, T., and Li, X. (2021). Application of machine learning in ocean data. *Multimed. Syst.* 1–10. doi: 10.1007/s00530-020-00733-x

Lumpkin, R., and Pazos, M. (2007). "Measuring surface currents with surface velocity program drifters: the instrument, its data, and some recent results," in *Lagrangian Analysis and Prediction of Coastal and Ocean Dynamics*, Vol. 39, eds A. Griffa, A. D. Kirwan, A. J. Mariano, T. Özgökmen, and H. T. Rossby (Cambridge: Cambridge University Press), 67. doi: 10.1017/CBO9780511535901.003

Mahadevan, A. (2016). The impact of submesoscale physics on primary productivity of plankton. *Annu. Rev. Mar. Sci.* 8, 161–184. doi: 10.1146/annurev-marine-010814-015912

McNutt, M. K., Camilli, R., Crone, T. J., Guthrie, G. D., Hsieh, P. A., Ryerson, T. B., et al. (2012). Review of flow rate estimates of the Deepwater Horizon oil spill. *Proc. Natl. Acad. Sci. U.S.A.* 109, 20260–20267. doi: 10.1073/pnas.1112139108

Molemaker, M. J., McWilliams, J. C., and Capet, X. (2010). Balanced and unbalanced routes to dissipation in an equilibrated Eady flow. *J. Fluid Mech.* 654, 35–63. doi: 10.1017/S0022112009993272

Osadchiev, A., and Sedakov, R. (2019). Spreading dynamics of small river plumes off the northeastern coast of the Black Sea observed by Landsat 8 and Sentinel-2. *Remote Sens. Environ.* 221, 522–533. doi: 10.1016/j.rse.2018.11.043

Park, K. A., Lee, M. S., Park, J. E., Ullman, D., Cornillon, P. C., and Park, Y. J. (2018). Surface currents from hourly variations of suspended particulate matter from Geostationary Ocean Color Imager data. *Int. J. Remote Sens.* 39, 1929–1949. doi: 10.1080/01431161.2017.1416699

Pinaya, W. H. L., Vieira, S., Garcia-Dias, R., and Mechelli, A. (2020). "Convolutional neural networks," in *Machine learning* (Cambridge, MA: Academic Press), 173–191. doi: 10.1016/B978-0-12-815739-8.00010-9

Rocha, C. B., Chereskin, T. K., Gille, S. T., and Menemenlis, D. (2016). Mesoscale to submesoscale wavenumber spectra in Drake Passage. *J. Phys. Oceanogr.* 46, 601–620. doi: 10.1175/JPO-D-15-0087.1

Rypina, I. I., Kirincich, A. R., Limeburner, R., and Udovydchenkov, I. A. (2014). Eulerian and Lagrangian correspondence of high-frequency radar and surface drifter data: effects of radar resolution and flow components. *J. Atmos. Ocean. Technol.* 31, 945–966. doi: 10.1175/JTECH-D-13-00146.1

Santiago, J. G., Wereley, S. T., Meinhart, C. D., Beebe, D. J., and Adrian, R. J. (1998). A particle image velocimetry system for microfluidics. *Exp. Fluids* 25, 316–319. doi: 10.1007/s003480050235

Sklar, F. H., and Browder, J. A. (1998). Coastal environmental impacts brought about by alterations to freshwater flow in the Gulf of Mexico. *Environ. Manag.* 22, 547–562. doi: 10.1007/s002679900127

Sun, H., Song, Q., Shao, R., and Schlicke, T. (2016). Estimation of sea surface currents based on ocean colour remote-sensing image analysis. *Int. J. Remote Sens.* 37, 5105–5121. doi: 10.1080/01431161.2016.1226526

Thielicke, W. (2014). *The Flapping Flight of Birds – Analysis and Application.* Ph.D. thesis. Groningen: Rijksuniversiteit.

Thielicke, W., and Sonntag, R. (2021). Particle image velocimetry for MATLAB: accuracy and enhanced algorithms in PIVlab. *J. Open Res. Softw.* 9:12. doi: 10.5334/jors.334

Thielicke, W., and Stamhuis, E. J. (2014). PIVlab – towards user-friendly, affordable and accurate digital particle image velocimetry in MATLAB. *J. Open Res. Softw.* 2:e30. doi: http://dx.doi.org/10.5334/jors.bl

Tokumaru, P. T., and Dimotakis, P. E. (1995). Image correlation velocimetry. *Exp. Fluids* 19, 1–15. doi: 10.1007/BF00192228

Walker, N. D., Wiseman, W. J., Rouse, L. J., and Babin, A. (2005). Effects of river discharge, wind stress, and slope eddies on circulation and the satellite-observed structure of the Mississippi River plume. *J. Coast. Res.* 21, 1228–1244. doi: 10.2112/04-0347.1

Wereley, S. T., and Meinhart, C. D. (2010). Recent advances in micro-particle image velocimetry. *Annu. Rev. Fluid Mech.* 42, 557–576. doi: 10.1146/annurev-fluid-121108-145427

Willman, C., Scott, B., Stone, R., and Richardson, D. (2020). Quantitative metrics for comparison of in-cylinder velocity fields using particle image velocimetry. *Exp. Fluids* 61:146. doi: 10.1007/s00348-020-2897-9

Xu, D., and Chen, J. (2013). Accurate estimate of turbulent dissipation rate using PIV data. *Exp. Ther. Fluid Sci.* 44, 662–672. doi: 10.1016/j.expthermflusci.2012.09.006

Yang, H., Choi, J. K., Park, Y. J., Han, H. J., and Ryu, J. H. (2014). Application of the Geostationary Ocean Color Imager (GOCI) to estimates of ocean surface currents. *J. Geophys. Res. Oceans* 119, 3988–4000. doi: 10.1002/2014JC009981

Yanovsky, I., Holt, B., and Ayoub, F. (2020). "Deriving velocity fields of submesoscale eddies using multi-sensor imagery," in *Proceedings of the IGARSS 2020-2020 IEEE International Geoscience and Remote Sensing Symposium*, (Piscataway, NJ: IEEE), 1921–1924. doi: 10.1109/IGARSS39084.2020.9323797

Yoo, J. G., Kim, S. Y., and Kim, H. S. (2018). Spectral descriptions of submesoscale surface circulation in a coastal region. *J. Geophys. Res. Oceans* 123, 4224–4249. doi: 10.1029/2016JC012517

Zavialov, P. O., Grigorieva, J. V., Möller, O. O. Jr., Kostianoy, A. G., and Gregoire, M. (2002). Continuity preserving modified maximum cross−correlation technique. *J. Geophys. Res. Oceans* 107:3160. doi: 10.1029/2001JC001116

Conflict of Interest: The authors declare that the research was conducted in the absence of any commercial or financial relationships that could be construed as a potential conflict of interest.

Advantages of publishing in Frontiers

OPEN ACCESS
Articles are free to read for greatest visibility and readership

FAST PUBLICATION
Around 90 days from submission to decision

HIGH QUALITY PEER-REVIEW
Rigorous, collaborative, and constructive peer-review

TRANSPARENT PEER-REVIEW
Editors and reviewers acknowledged by name on published articles

Frontiers
Avenue du Tribunal-Fédéral 34
1005 Lausanne | Switzerland

Visit us: www.frontiersin.org
Contact us: frontiersin.org/about/contact

REPRODUCIBILITY OF RESEARCH
Support open data and methods to enhance research reproducibility

DIGITAL PUBLISHING
Articles designed for optimal readership across devices

FOLLOW US
@frontiersin

IMPACT METRICS
Advanced article metrics track visibility across digital media

EXTENSIVE PROMOTION
Marketing and promotion of impactful research

LOOP RESEARCH NETWORK
Our network increases your article's readership